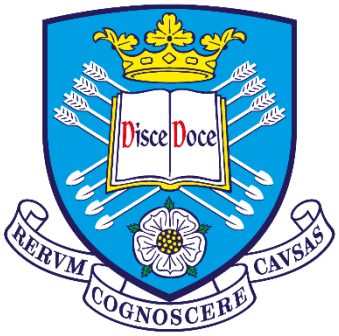

The University Of Sheffield.

Cold Sintering of Functional Ceramics and Glasses

Jessica Andrews

A thesis submitted in partial fulfilment of the requirements for the degree of Doctor of Philosophy.

Supervisor:
Professor Ian M. Reaney

The University of Sheffield
Faculty of Engineering
Department of Materials Science and Engineering
March 2021

Acknowledgements

I would firstly like to thank my academic and industrial supervisors, without whom this project would never have happened. Prof. Ian Reaney, for his advice and support throughout my PhD, and the numerous opportunities he has created for me to further both my research and personal development. Jonathon Booth and Hong Ren for many interesting and helpful discussions throughout the project and all those at Johnson Matthey who have contributed to this work. Thanks are also due to Nicole Kelly and Dr. John Hanna (University of Warwick) for their assistance in obtaining NMR data and to Dr. George Bullock and Prof. Cheryl Miller (University of Sheffield) for enabling the cytotoxicity study of cold sintered Bioglass.

There are so many people and groups who have supported me along the way, even if they did not realise they were doing it and for that I will be forever grateful. Members of the Functional Materials and Devices community past and present, who have been constant source of knowledge and reassurance. A special mention must go to Kerry and George – whose unwavering patience, support and belief has kept me going in the final stages of writing up. A huge thank you to occupants and frequent visitors of the office, in the before times, for many a welcome distraction over the years and to Ben and Joe for lockdown coffee breaks. The 'Material Girls' for numerous trips to Nando's to celebrate birthdays and successes, to rant about life and sometimes just to enjoy some peri-peri chicken and have a laugh. The Unicorns Netball for adding a bit of sparkle to my Monday and Wednesday nights and to many other parts of life – you are a truly amazing group of women.

And last but not least, my Family, for always being encouraging, believing in me, putting up with me and making many trips "up north" since I first came to Sheffield - yes, it is *still* cold up here.

Abstract

Ceramic and glass materials have had been used for millennia and have become ubiquitous in applications including communication, electronic and biomedical devices. Traditionally, ceramics are sintered at very high temperatures approaching ~80% of melting temperature. The high temperatures required to produce dense ceramics not only makes a significant contribution to processing energy but also limits the potential for development of novel ceramic and glass components which integrate polymeric materials and non-noble metals.

A novel method of densification, known as 'cold sintering', utilises a transient liquid phase, pressure, and temperatures up to 300 °C to achieve the consolidation and densification of ceramics. In addition to energy reduction, benefits include the ability to co-sintering a broad variety of materials, greater control of component dimension and the final microstructures. This work demonstrates the application of the cold sintering process to three materials – lithium molybdate, a borosilicate glass frit and Bioglass® 45S5.

The properties of lithium molybdate after cold sintering, heat treatment and conventional sintering are compared with heat treated and conventionally sintered samples. No residual water or secondary phases were found in cold sintered samples although some evidence of an amorphous grain boundary phases is seen. Lithium molybdate - bismuth molybdate composites were also fabricated and shown to remain as distinct phases within the component. The room temperature permittivity of the composites is reported and discussed. Coatings of lithium molybdate on glass substrates are produced by cold sintering, demonstrating the capability of the process to create well-adhered coatings on glass at very low temperatures.

A glass frit provided by Johnson Matthey is also densified *via* the cold sintering method and compared to conventionally sintered materials. The effect of sintering conditions (cold and conventional) on the impedance behaviour is discussed. The creation of coatings and adhesive layers on steel and PTFE are also demonstrated.

Bioglass® 45S5 is well-known for its bioactive responses driven by the ability to dissolve in the body and stimulate bone regeneration. Its solubility makes it an ideal candidate for densification using the cold sintering method. Bioglass powders are produced *via* flame spray pyrolysis and densified by cold sintering at 100 °C. NMR studies of the materials as received, wetted and after cold sintering provide insight into

the potential mechanisms of the cold sintering of Bioglass. Bioglass-polymer composites are produced with a broad range of compositions and are shown not to be cytotoxic. Coatings of Bioglass on titanium have also been achieved. These results are promising steps towards a simple method of creating biomedical components utilising Bioglass-polymer composites and coatings thereof.

The outcome of this work is to gain further understanding of the difference between properties of cold and conventionally sintered materials and to demonstrate the potential applications of cold sintering in areas beyond electroceramics.

Novelty and Significance

The study of cold sintered lithium molybdate presented here contributes to the understanding of how the cold sintered process affects the structure and microstructure.

This thesis has demonstrated for the first time the densification of silicate glass components from powders at very low temperatures and expands the current applications of the process into a new class of materials. The intrinsic solubility of a silicate glass produced by Johnson Matthey (JM5430F) in acidic environments has been utilised to achieve dense pellets by cold sintering.

The cold sintering of Bioglass® 45S5 has been achieved at 100 °C, composites with PLA and coatings on titanium plate have also been produced. Cell culture work indicates that the cytotoxicity of Bioglass-PLA composites after pre-conditioning is within acceptable levels and similar to materials formed from conventional Bioglass.

Work described in chapters 5 and 0 on the densification of glasses, forms the basis of a patent application entitled "Method of forming glass coatings and glass coated products", filed by Johnson Matthey.

Thesis Outcomes to Date

Journal Article:

- **J. Andrews**, D. Button, and I. M. Reaney, "Advances in Cold Sintering" Johnson Matthey Technol. Rev., no. 2, pp. 219–232, 2020 doi: 10.1595/205651320x15814150061554.
- **J. Andrews,** G. Bullock, C. A. Miller, E. Christian, J. Booth, H. Ren, N. L. Kelly, J. V. Hanna and I. M. Reaney, "Cold Sintering of Bioglass and Bioglass/Polymer Composites", *In Preparation*

Patent Application:

- J. Booth, E. Christian, H. Ren, I. M. Reaney, **J. Andrews**, C. Miller, G. Bullock Method of forming glass coatings and glass coated products. Patent Application Number: GB2005268.4 (2020)

Conference Presentations:

- **J. Andrews,** "Cold Sintered Bioglass and Bioglass-Polymer Composites" Johnson Matthey Academic Conference 2020, Online

- **J. Andrews**, "Developments in Cold Sintering" IOM3 Future Materials Conference 2019, Leeds, UK

Contributions

Chapter 4:	Collection of TEM images and SAD patterns of cold sintered lithium molybdate performed by Dr. Ali Mostaed at the University of Sheffield.
Chapter 5:	Raw material (JM5430F) and EPMA data provided by Johnson Matthey.
Chapter Error! Reference	Raw Material (Bioglass® 45S5) provided by Johnson Matthey. Collection of NMR data Nicole Kelly and Dr. John Hanna (University of Warwick). Cytotoxicity experiments of Bioglass composites performed by Dr. George Bullock and Prof. Cheryl Miller (University of Sheffield).

source not
found.:

Contents

Table of Figures

1 Introduction

A crucial stage in the manufacture of ceramics products is sintering, where materials are heated to ~80 % of their melting temperature to drive mass transport and densification. Archaeologists have dated some of the earliest ceramic artefacts to 24,000 BC and sintering methods evolved empirically for thousands of years prior to the development of the relevant theoretical background [1].

A promising method for the densification of ceramics, cold sintering, utilizes a transient liquid phase, uniaxial pressure and heat to achieve densification [2], [3]. The maximum temperature typically used in cold sintering is <300°C, which is a dramatic reduction in compared to conventional methods for most materials (>1000 °C). There are numerous incentives to reduce the sintering temperatures used in ceramic processing, including reducing energy usage (which is a significant factor in final component cost), total processing time and allowing the integration of dissimilar materials [4]–[7].

First reported in 2016, the application of cold sintering is currently being explored to achieve densification of a broad range of functional ceramics [2], [3]. The development of a broad range new technologies is likely to be enabled by the process as the capability to densify new materials is demonstrated. Partial solubility of a material in a solvent is a strong indicator that it is possible to be densified *via* cold sintering. Much of the work to date has focused on functional ceramics for applications such as multilayer capacitors and antennae. This work aims to contribute to the understanding of the cold sintering process and broaden the application of cold sintering to other classes of material.

1.1 Aims and Objectives

This work aims to apply the cold sintering method to a number of functional materials, exploring how the process might affect the final properties. This work also aims to broaden the potential applications of the cold sintering technique by demonstrating the method on a class of materials which has not yet been reported in the literature – glasses. The thesis focusses on three main materials to achieve these aims, through the objectives below:

- Lithium Molybdate
    - Compare and contrast the properties of lithium molybdate produced *via* cold sintering, after heat treatment and conventional sintering.
    - Demonstrate the densification of lithium molybdate - bismuth molybdate composites.
    - Deposit dense layers of lithium molybdate on glass substrates.

- Johnson Matthey Silicate Frit – JM5430F
    - Demonstrate the feasibility of utilising the cold sintering process for glasses by densifying a glass produced by Johnson Matthey.
    - Compare microstructural and electrical properties of the glass densified by cold and conventional sintering.
    - Creation of coatings of JM5430F on steel substrates.

- Bioglass
    - Achieve the densification of Bioglass through cold sintering and develop an understanding of the mechanisms.
    - Investigate the potential for cold sintered Bioglass to be utilised in biomedical applications through cytotoxicity testing.
    - Demonstrate the application of a cold sintered coating on titanium, a commonly used biomedical implant material.

2 Literature Review

2.1 Sintering of Ceramics

Sintering is a crucial stage in the manufacturing of dense ceramic products from a green body and archaeologists have dated some of the earliest ceramic artefacts to 24,000 BCE [1]. Sintering was developed in a very empirical way for thousands of years prior to the development of relevant theories [1]. The density of ceramic materials significantly affects their dielectric and physical properties. High densities are, therefore, crucial in ceramic manufacture.

Traditionally, sintering of materials to create dense products has required them to be heated up to 0.8 T_m to promote the transport of material to eliminate pores; such high temperatures are not only energy intensive but can be restrictive in the manufacture of many functional ceramic devices. At high temperatures, there are several challenges for the integration of metallic and polymeric materials such as volatility and mismatch in coefficient of thermal expansion. This leads to complications in the production of components such as warping and the high cost of metallic materials able to withstand the harsh temperature environment.

Conventional sintering processes can be approximately divided into four different types, which are dependent upon to the volume fraction of solid, liquid and pore in the component [8]:

Solid state sintering, which occurs in systems of solid material and pores.
Liquid phase sintering, occurs when <20 vol.% liquid is added to the system.
Viscous composite sintering, requiring >20 vol.% liquid phase, and
Viscous glass sintering, occurring during the solidification a liquid melt.

These four types of sintering in relation to the amount of solid, liquid and pores present are shown in Figure 1. The type of sintering observed is largely dependent on the materials being sintered. The addition of secondary phases or additives with a lower melting temperature creates a liquid during sintering which allows high diffusivity into pores and aids densification [9], [10]. However, the properties of functional materials, such as permittivity (ε_r) and dielectric loss ($\tan\delta$) can all be affected by the use of sintering aids and this should be balanced by improvements gained by enhanced densification [11].

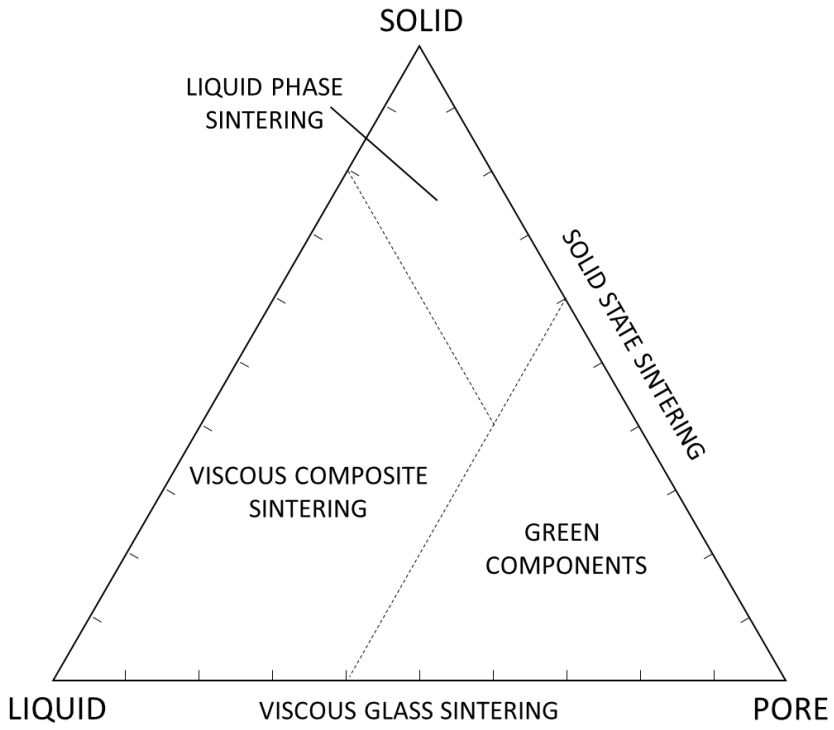

Figure 1: Ternary Solid-Liquid-Pore diagram showing when the different types of sintering occur, after [8]

2.2 Driving Forces of Densification

The driving force for densification is the reduction of Gibbs' free energy through the reduction in surface energy by eliminating solid-vapour interfaces and solid-solid interfaces with lower energy [12]. The transfer rate of material is affected by both the particle size and the radius of curvature of particles in particular. When curvature is small (on the order of microns), the rate of material transfer increases, fine particles are therefore often utilized in ceramic materials to ensure good sintering and densification behaviour [12].

When a large pore is surrounded by a large number of grains with convex surfaces, the pore can become metastable and begin to grow, causing residual porosity in the sintered samples [13]. The relationship between the dihedral angle (the angle between the surface of particles) and the number of grains surrounding that pores is shown in Figure 2. If the number of grains surrounding a pore is greater than the critical value (N_c) indicated by the curve in Figure 2 for a given dihedral angle, pores will grow during sintering [13].

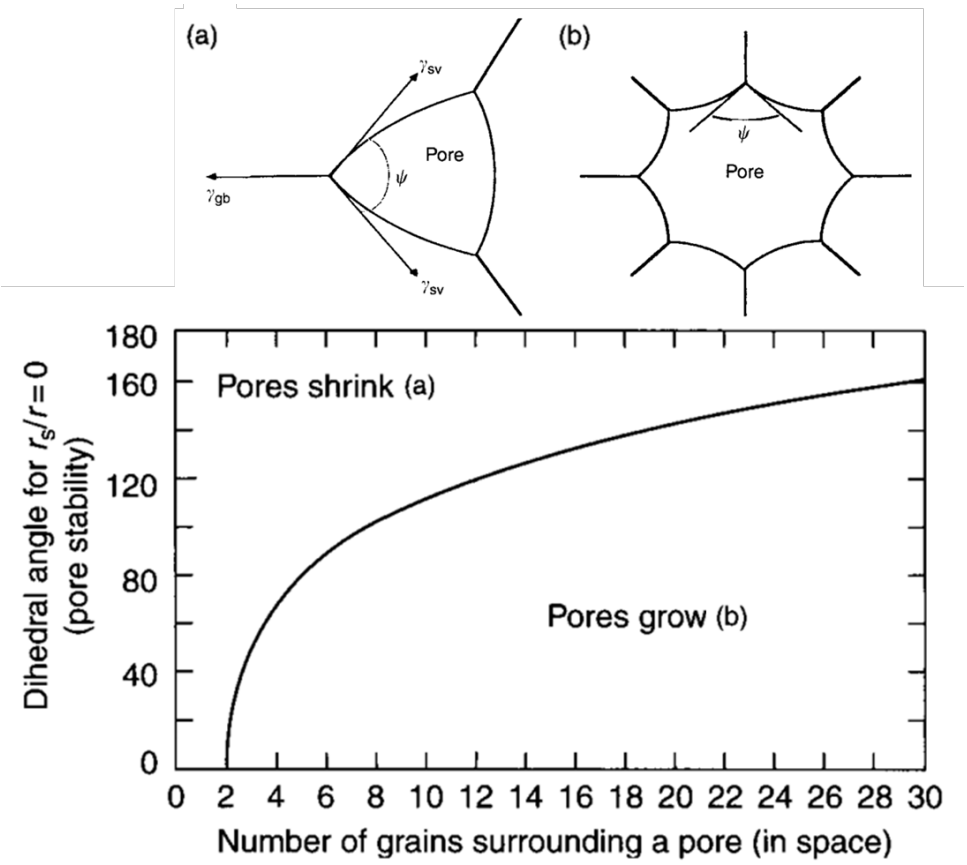

Figure 2: Stability of pores determined by the dihedral angle and pore coordination number, after [13]

There are several non-densifying material transport mechanisms which can occur alongside sintering which reduce the driving force of sintering and cause coarsening of the microstructure. It is therefore important to avoid processing conditions where these mechanisms are highly active [13].

2.2.1 Solid State Sintering

Solid state sintering is the method most understood and is utilized in several industries [9]. For solid state sintering to occur, a ceramic powder is compacted and heated to very high temperatures, usually greater than half the melting point of the material. High temperatures are required to allow reaction and mass transport between particles, schematically represented in Figure 3 [13]. During the sintering of polycrystalline materials there are a number of diffusion, vapour transport and plastic flow processes, which and are shown in Figure 3 [10], [13]–[15]. Densification is caused by plastic flow, grain boundary and lattice diffusion from the grain boundary, causing the formation of a neck between particles. During solid state sintering, non-densifying mechanisms create significant microstructural changes and grain growth, as material from particle surfaces moves to necking regions and that from convex grains is transported to concave grains [13], [15], [16].

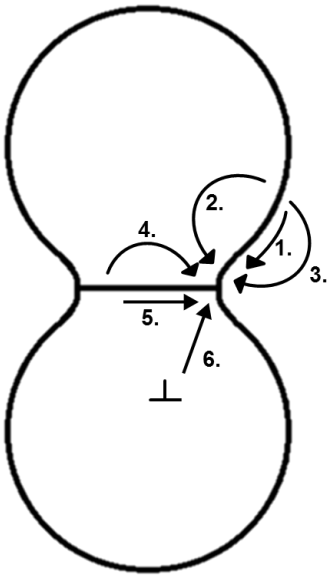

Non-Densifying Mechanisms:

1. Surface Diffusion
2. Lattice Diffusion (from surface)
3. Vapour Transport

Producing microstructural change without causing shrinkage

Densifying Mechanisms:

4. Lattice Diffusion (from grain boundary)
5. Grain Boundary Diffusion
6. Plastic flow (via dislocation motion)

Causing shrinkage by removing material from the grain boundary region

Figure 3: Schematic representation of mass transport systems contributing to sintering of crystalline particles, adapted from [10], [13]–[16].

The rate of sintering can be altered by the presence of aliovalent dopants and impurities which alters the diffusion coefficients. The precise role of dopants and impurities is complex and is determined by segregation at grain boundaries, boundary energy and the potential for secondary phase formation [13]. The addition of sintering aids is often utilized to reduce conventional sintering temperatures. Lithium doping of $BaTiO_3$ (BT) has been shown to successfully reduce sintering temperatures, Kimura *et al*. demonstrated a reduction from 1300℃ to 1000℃ [17] and Randall *et al*. achieved a reduction of sintering temperature to 750℃ with <0.3 mol.% Li by the addition of 15 mol.% LiF [18]. Many other sintering aids have been investigated, but no others are able to reduce the BT sintering temperatures to below 900℃ [6], [19]. However, this temperature remains too high to allow for the full integration of a wide range of materials with ceramics and the reduction in sintering temperature must be balanced with any effect on properties [20].

During sintering, volatile elements can evaporate causing changes to the stoichiometry of the final materials which in turn have an impact the electrical properties [21]. Co-sintering of ceramic materials with polymeric and metallic materials *via* a solid-state method presents a range of challenges. Thermal stability, rate of shrinkage and the physical and chemical compatibility of materials at high temperatures must all be considered and often precludes the integration of ceramic materials with low melting point electrodes, semiconductors and polymeric materials [22]–[24].

2.2.2 Liquid Phase Sintering

Sintering temperatures have often been reduced by the addition of liquid phase additives or fluxes in a process called liquid phase sintering. Typically, these additives are able to reduce the sintering temperatures by approximately 10-20% [3]. The benefits of a reduction in sintering temperature by adding a liquid phase have to be balanced with the potential for reduction in the dielectric properties; reducing ε_r and increasing the tanδ [23], [24]. For full densification of materials through liquid phase sintering, a number of requirements must be met [8], [25]: i) Partial solubility of the solid in the liquid phase, ii) an appropriate volume of added liquid, usually <15 vol.% and iii) complete wetting of the solid particles by the added liquid

During liquid phase sintering, the extent of densification is depends on the capillary pressure in the inter-particle region due to the wetting of the solid particles [26]. The size of the solid particles, the space between the particle and the properties of the liquid phase all contribute to the capillary pressure, fine particles with small inter-particle capillary spaces are required to achieve sufficient pressure.[12], [13]. The theories of liquid phase sintering suggest there are three stages distinct stages observes during the densification of a material *via* LPS [8], [13], [26], [27].

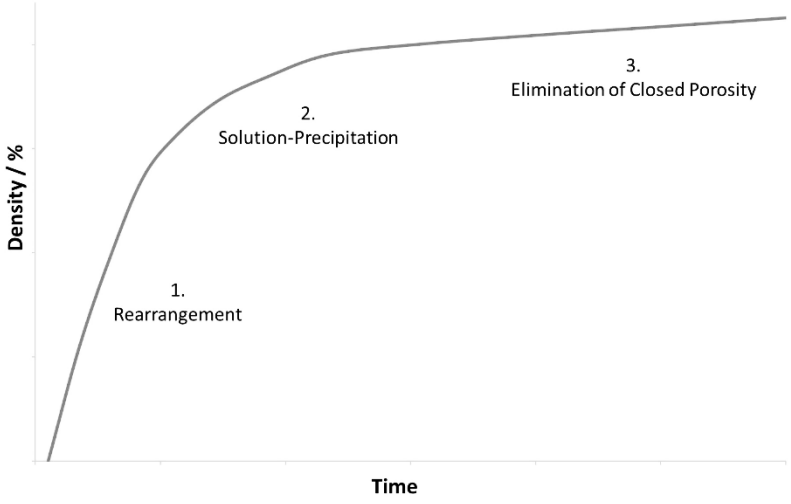

Figure 4 Densification curve showing the three main stages of liquid phase sintering [8], [13], [26], [27].

During stage one of liquid phase sintering, the solid material particles are wetted by the addition of a liquid or the melting of a flux phase. The material is rapidly densified in stage 1 as the particle are rearranged and the liquid is able to move into pores. [9], [25], [26]. The controlling factor for this step is the amount of liquid in the system, densification is achieved by sufficient wetting of the particles to allow for rearrangement of the particles [13]. Kingery calculated the liquid required to instigate

true liquid phase sintering to occur with particle rearrangement is 35 vol.% and this can lead to a volume shrinkage during sintering of up to 40%, as shown in Figure 5. When insufficient amounts of liquid are added to the system, other sintering methods, such as solid-state sintering are required to achieve densification [25].

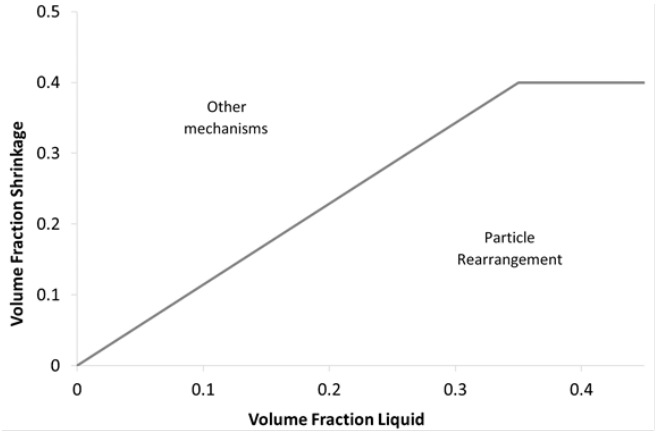

Figure 5: Effect of liquid fraction on shrinkage by rearrangement [25]

Solution-precipitation occurs in stage 2 after the initial particle rearrangement, the solubility and diffusivity of the materials then become the dominant effects in densification [9], [26]. During solution-precipitation a significant amount of microstructural coarsening occurs. Smaller grains dissolve into the liquid phase due to their higher relative solubility; this material then diffuses into the larger grains causing them to grow, increasing density [9], [26].

The final densification stages in liquid phase sintering are solid state controlled in which closed porosity is eliminated in the samples. Due to its slow rate, the solid-state controlled portion of densification is only significant in the later stages of sintering after the liquid has been removed. The properties of liquid phase sintered materials are often degraded by the solid-state process so this is usually kept short. [9], [26]

2.2.3 Processing Routes with Reduced Sintering Temperatures

Microwave sintering, flash sintering, spark plasma sintering, and high-pressure sintering are among techniques which have been used to efficiently sinter ceramics by utilising electrical energy, high pressure, and controlled heating steps. In these techniques, the sintering temperature often remains above 400°C, which, whilst considerably lower than conventional sintering temperatures is still too high for co-firing with polymers and other materials [4], [5].

Incentives for the reduction in sintering temperatures include the reduction in energy requirements and processing times as well as the ability to integrate other materials into ceramic products. The use of high temperatures requires a significant amount of energy which becomes the dominant factor in the cost of final components [6], [7]. The energy required to sinter $BaTiO_3$ conventionally is 2800 kJ/g, a comparison of energy consumption for several sintering methods is shown in Table 1. A significant reduction in energy consumption can be achieved through various methods, by reducing processing temperatures, with cold sintering thought to represent a 99% energy reduction for sintering of $BaTiO_3$ [6].

Table 1: Comparison of energy consumption of sintering techniques after [6]

Sintering method	Energy consumption (kJ/g)
Solid State	2800
Liquid Phase	2000
Field Assisted	1050
Microwave	540
Fast firing	130
Cold	30

As sintering temperatures have been reduced to save energy, reduce processing time and allow for integration, processing temperatures have been classified into a number of categories: High 1200-1800°C; Low 900-1000°C; Ultra-low 400-700°C and Cold <200°C. Figure 6 illustrates these alongside compatible metallic elements used in co-firing ceramic technologies.

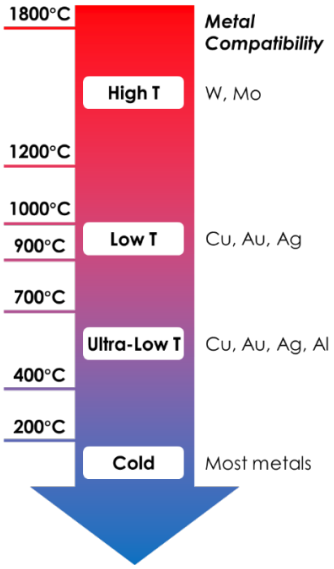

Figure 6: Sintering temperature classifications with compatible co-firing materials [28]

Ceramic components are commonly tape cast, printed with conductive patterns and stacked to produce multilayer components and then sintered at 900-1000°C, whilst this is considered 'low temperature' there are still a number of issues such as warping, cracking and other defects can occur due to thermal mismatch, which affects the performance of components [24], [29]. Recently, "cold sintering" has been developed for ceramic densification below 200°C utilizing a transient liquid, which aims to avoid some of the issues of traditional sintering methods [2], [3].

2.2.3.1 Microwave Sintering

The use of microwave radiation in the processing of ceramics has been explored since the 1950's and work towards utilising microwaves for densification began in the 1970s [30]. Reported advantages of the process over conventional sintering include: rapid heating and short cycle times, which in turn reduces processing cost, improved microstructural control and improvements in mechanical properties [31]–[34].

Conventionally sintered samples are indirectly heated via radiation, conduction and convection, whilst in microwave sintering, heat is generated within the materials. Dielectric loss is a crucial factor in the use of microwaves to densify materials as energy absorbed from the electromagnetic wave dissipates through the material as heat. There is a broad range of microwave absorption characteristics amongst ceramic materials, and for low loss materials such as ultra-pure alumina, "hybrid" sintering is [30], [31]. The hybrid method utilises conventional heating to ensure the work piece has sufficient microwave absorption to achieve densification. Hybrid microwave sintering allows for the heat distribution within a work piece to be tailored which can be used to aid microstructural control [30], [34]–[36].

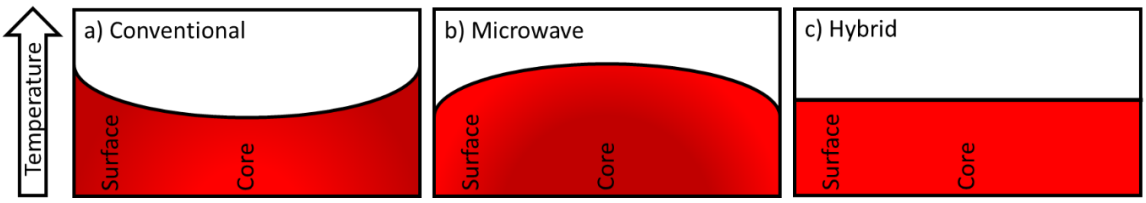

Figure 7: Temperature profile within a) conventional, b) microwave and c) hybrid sintered samples adapted from [35]

Alumina is highly refractory with a sintering temperature of over 1600 °C, whilst hybrid sintering has been shown to achieve >95% relative density at 1400 °C (Figure 8). Whilst still requiring temperatures of over 1000 °C, reducing sintering temperatures by several hundred degrees could yield significant improvement in processing time and therefore achieve significant energy and cost benefits.

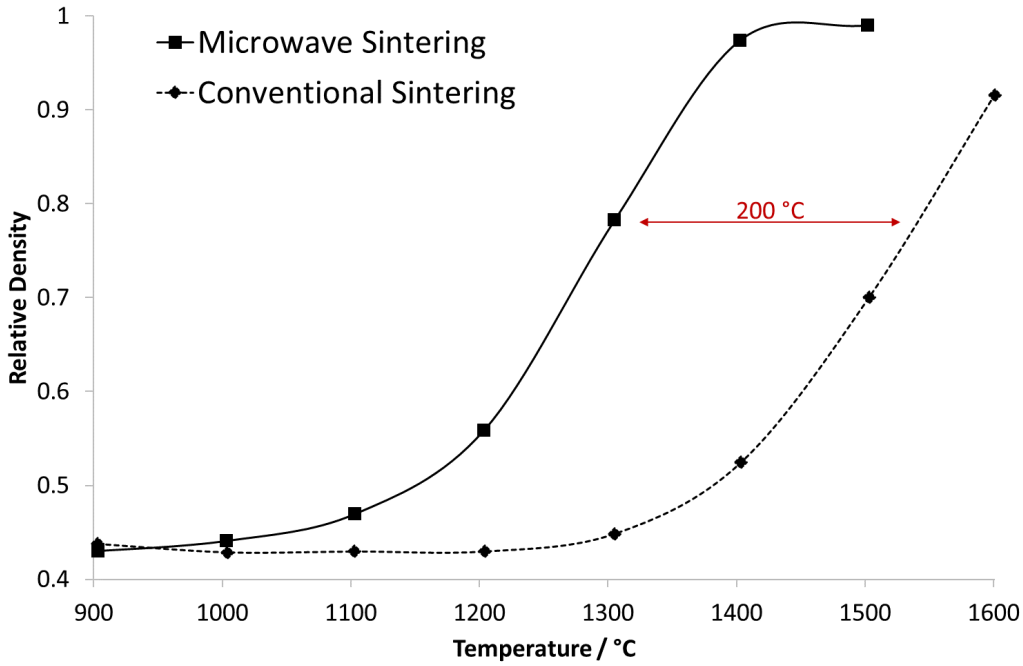

Figure 8: Sintered Density vs. Temperature for microwave and coventionally sintered alumina, adapted from [31]

2.2.3.2 Flash Sintering

Flash sintering, reported in 2010 utilises a combination of applied electrical field and elevated temperatures to densify oxide materials very rapidly [37]. Densification occurs at specific combinations of temperature and applied field, with onset temperature lowering with increased field strength. [38]. The flash sintering event is characterised by thermal runaway of Joule heating, a change in the electrical conductivity of the sample and the emission of bright light [37]–[40]

There are a significant number of variables (summarised in Figure 9) which affect the Flash sintering process, many of which are interrelated and therefore finding the optimum processing parameters for each materials can be complex [38].

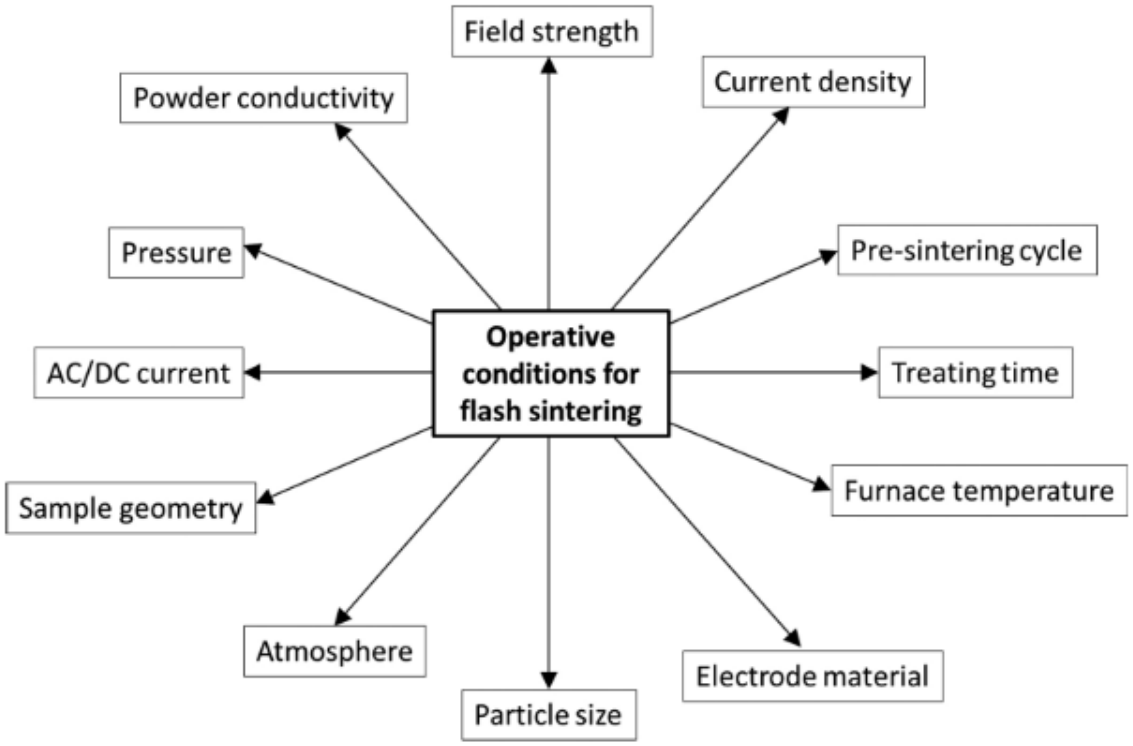

Figure 9: Processing parameters which must be considered in the flash sintering process, from [38].

Lab based trials of flash sintering are commonly performed on 'dog-bone' shaped samples suspended from platinum wire within a furnace, however these samples are complex to form and the final microstructure is complex due to field distribution in the sample [37], [40]. In smaller samples the electric field and current density can be easily controlled, however the ability to control these in larger work pieces may be a barrier to commercialisation [40].

It has been noted that the microstructure within flash sintered samples can vary, not only with applied field strength but also with distance from the anode. Figure 10 shows fracture surface micrographs of zinc oxide (ZnO) samples flash sintered at low (3.9 A/cm2) and high (15.4 A/cm2) current density [41]. Zhang *et al.* flash sintered ZnO with a particle size of ~0.5μm a with very little grain growth achieved in the low current density sample whereas a significantly larger grain size is seen in the samples sintered with a high current density. Grains nearer the anode were comparatively larger than those at the cathode in both cases and has been attributed the accumulation of electrons aiding the transport mechanisms which lead to grain coarsening [41].

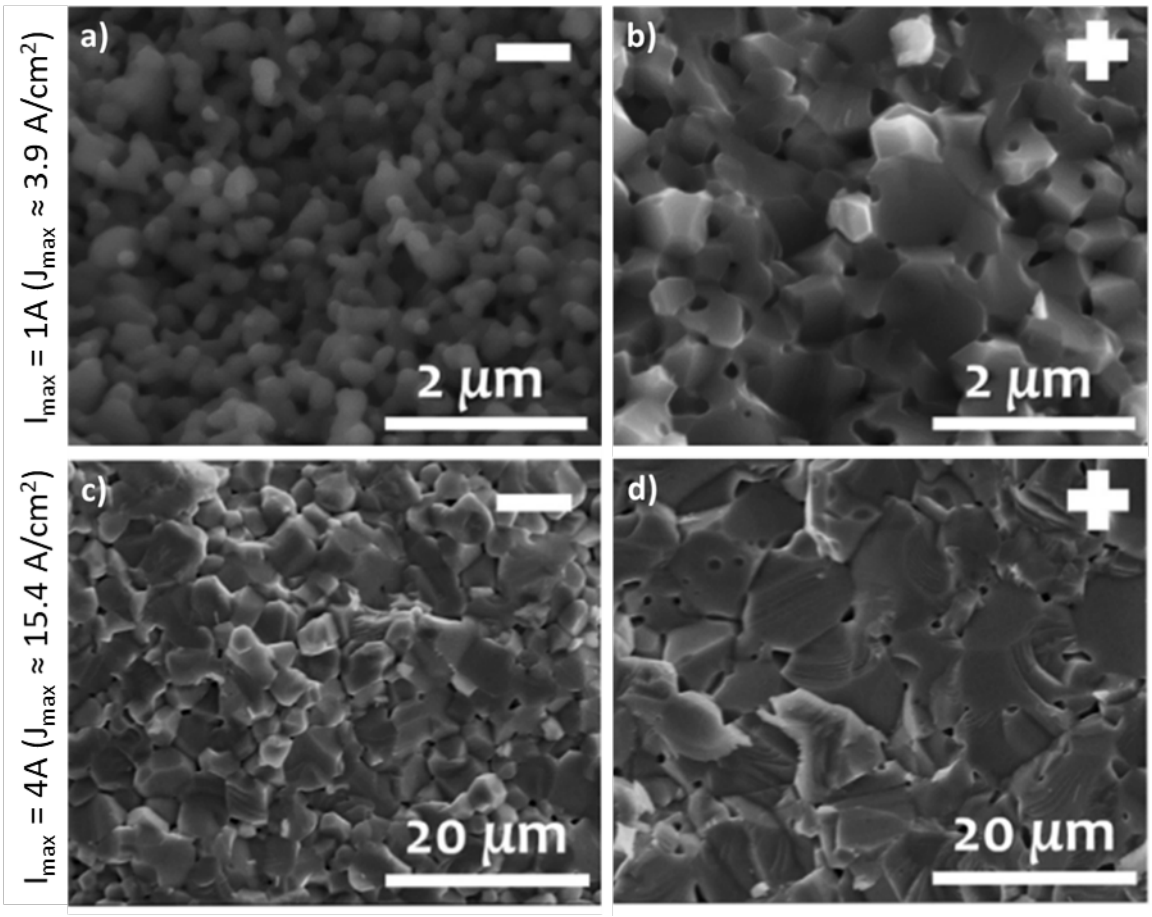

Figure 10: Fracture surface SEM micrographs of flash sintered Zinc oxide at a), b) low current density and c) d) high current density at the cathode (-) (a and c) and the anode (+) (b and d), adapted from [41]

Significant efforts have been made in electro-ceramics industry to develop a facile route for the production of functionally graded components. The asymmetric grain growth observed in ZnO and Yttria-stabilised zirconia by Zhang *et al.* and *Kim et al.* under applied electric field could be a potential avenue to achieve this. However, for applications where microstructural homogeneity is important, this phenomenon must be better understood in order to overcome the grain size distribution in the final products.

2.2.3.3 Spark Plasma Sintering

Used to consolidate a wide range of materials, spark plasma sintering uses uniaxial force and pulsed DC currents at low atmospheric pressure to achieve densification [42][43]. As current passes through the material, coulomb discharge and Joule heating effects cause significant heating at the contact points between powder particles, which promotes densification with limited grain growth [42], [44], [45]).

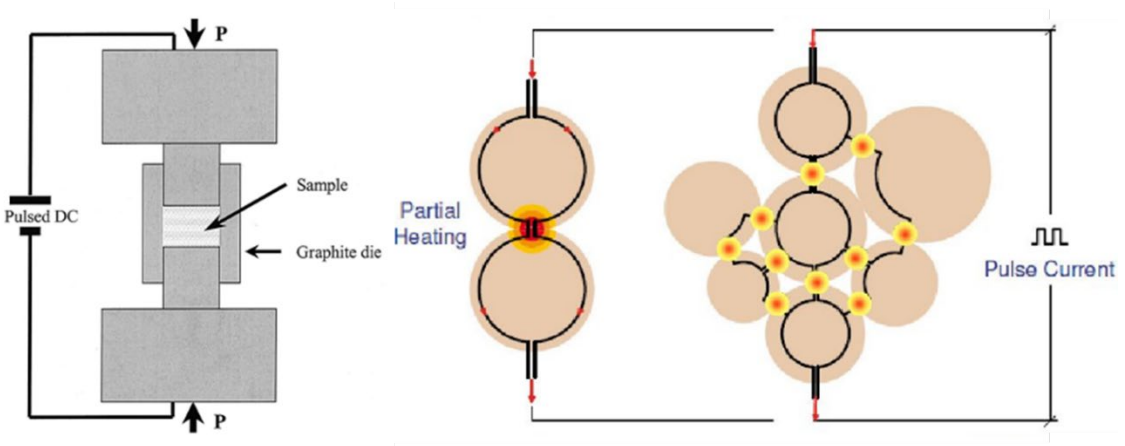

Figure 11: Schematic drawing of SPS apparatus, left (from [43]*), and visualisation of the flow of pulsed current and energy dissipation through powder particles during SPS, right (from* [45]*).*

Reducing sintering temperatures and times is a major step towards reducing the overall energy consumption of ceramic processing, and spark plasma sintering has been demonstrated in a broad range of ceramic materials from cutting tools to bio ceramics [45]. Elissalde *et al.* investigated the use of spark plasma sintering for zirconia (ZrO_2) ceramics from different precursor materials to reduce sintering temperatures, control the microstructure and prevent the formation of the detrimental cubic phase [46]. Using $ZrOH_4$ as a precursor, sintering at 350 °C with applied pressure of 600 MPa, achieved relative densities of 70-80 % in just 10 minutes [46]. Bioglass® 45S5 glass-ceramics have also been densified *via* the SPS method, achieving high relative density and improved mechanical properties when compared with conventionally densified material, Figure 12 [47]. Ion release studies in distilled water of the resulting glass-ceramics attributed higher rates of sodium dissolution to lowers densities amongst samples sintered at lower temperatures, but may also be attributable to the extent of crystallisation as discussed in sections 2.7 and 2.8 [47].

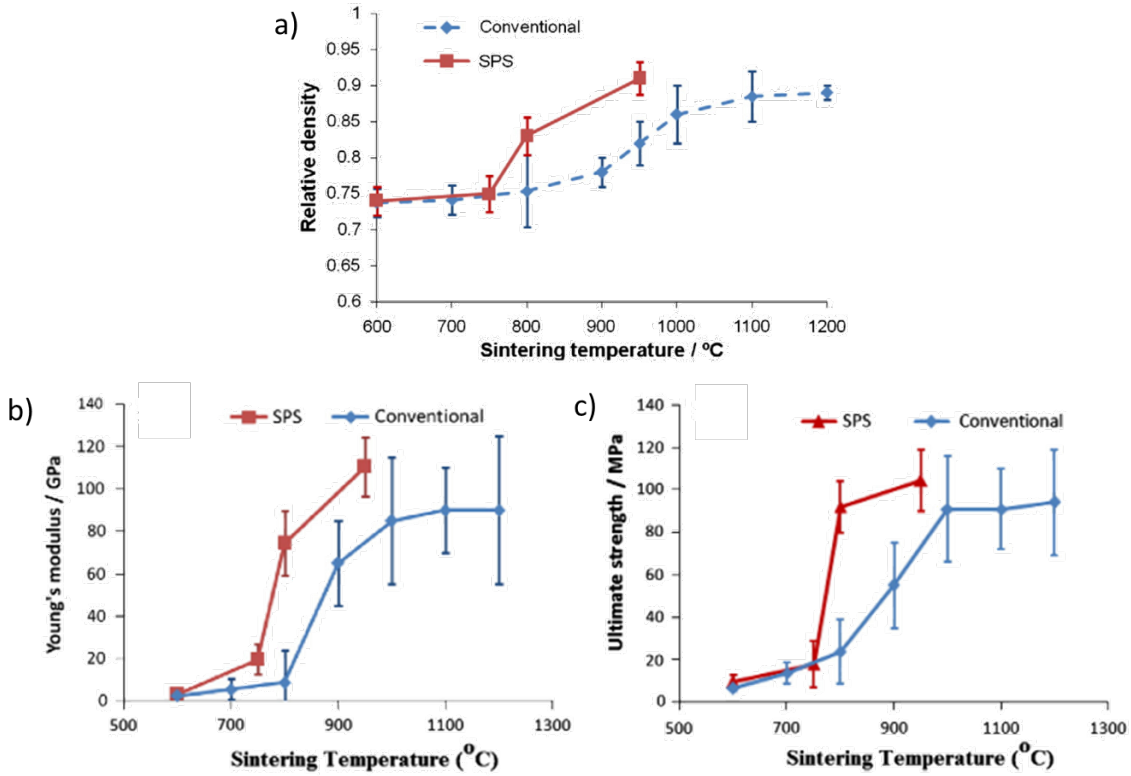

Figure 12: Relative density (a), Young's modulus (b) and ultimate compressive strength (c) of Bioglass® 45S5 glass-ceramics after densification via *conventional heat treatment and SPS, adapted from* [47]

There are numerous potential benefits to SPS over conventional sintering methods. Due to the rapid rate of sintering, it is likely that unwanted reactions and significant grain growth can be avoided. Shrinkage is also limited to the dimensions parallel to the applied pressure, allowing for greater control of the final component dimensions.

2.2.3.4 High-Pressure Sintering

During conventional sintering, pressure is not applied to the sample during densification and can therefore be considered pressureless sintering. During high pressure sintering, samples are heated whilst under and applied pressure >1 GPa[48]–[52]. Whilst in most cases the sintering temperature remains high, this technology allows the densification of otherwise difficult to prepare materials [51], [53], [54].

One application for high-pressure sintering is the production of cutting tools from diamond-SiC composites and boron nitride [51], [52]. Sintering of diamond–SiC composites at 1400-1600 °C with applied pressure of 6 GPa for 1 hour achieved samples with ~99 % relative density, with homogenous microstructures at higher temperatures and Knoop hardness over 40 GPa [52]. Cubic boron nitride is difficult to

prepare through conventional means and has been densified by Lv *et al.* at 1300-1700 °C with applied pressure of 5 GPa for 20 minutes [51]. The Vickers hardness of the resulting samples initially increases with temperature and then begins to decreased, which the authors attribute to the formation of secondary phases

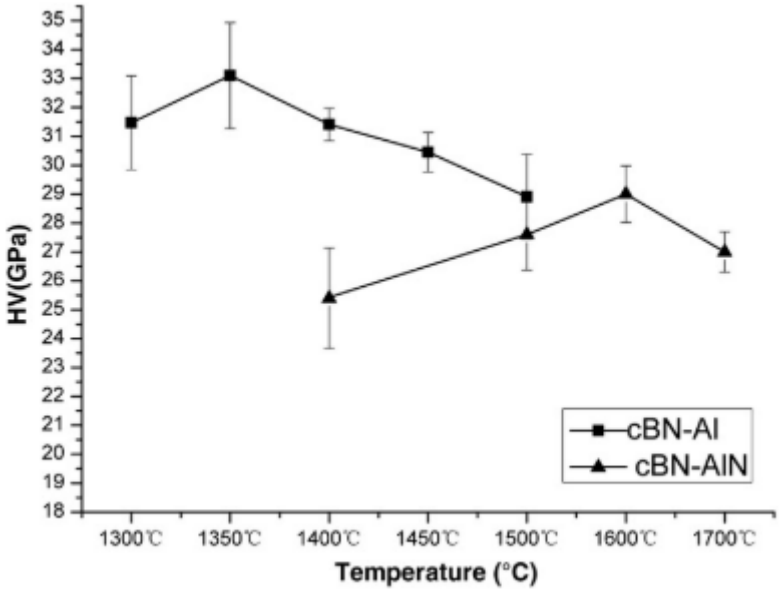

Figure 13: Comparison of Vickers hardness for cubic boron nitride sintered with 15 wt.% Al (—■—) and 20 wt.% AlN (—▲—), from [51]

High-pressure sintering has also been utilised in functional materials to achieve electrical/thermal property combinations that are difficult to achieve through conventional processes, such as thermoelectric devices. Good thermoelectric materials should have high electrical conductivity and Seebeck coefficient whilst maintaining low thermal conductivity to achieve a high figure of merit (ZT) [21]. $CoSb_3$ and BiCuSeO are thermoelectric materials which have been consolidated using high-pressure sintering [48]. For $CoSb_3$, Mei *et al.* reported higher electrical conductivity at lower pressures (2 GPa) attributed to Sb impurities, whilst the Seebeck coefficient was highest after higher pressure sintering (5.7 GPa) due to increase grain size [49]. Zhu *et al.* report a significant increase in ZT for BiCuSeO when prepared *via* high pressure sintering (3 GPa) at the same temperature (700 °C) compared to pressureless sintering, Figure 14 [48]. This was attributed to a low crystal defect concentration within the samples and restricted grain growth leading to a fin final microstructure.

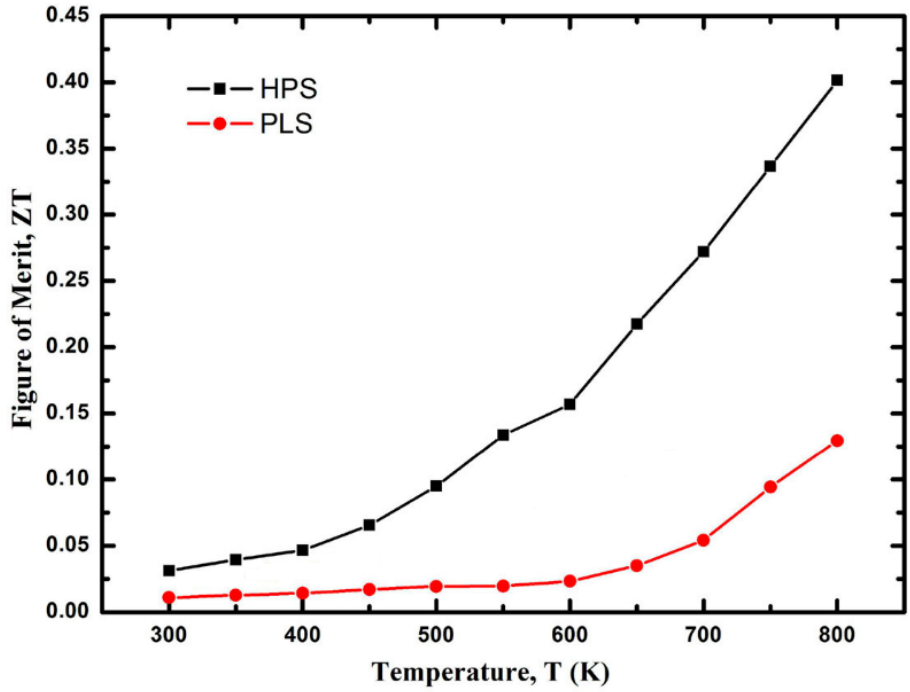

Figure 14: Temperature dependence of ZT for BiCuSeO prepared by conventional (PLS) and high pressure (HPS) sintering, adapted from [48].

Although high pressure sintering is performed at relatively high temperatures, it often enables a slight temperature reduction or the improvement of material properties which may not have been otherwise achieved. An understanding of the role of pressure during high-pressure sintering may also prove useful in further reducing processing temperatures.

2.3 Cold Sintering

Cold sintering is a promising method for the densification of a wide range ceramics, which utilizes a transient liquid phase, uniaxial pressure and heat to achieve densification [2], [3]. During cold sintering, powdered material is mixed with a transient liquid in which it is partially soluble, introducing a liquid phase at particle-particle interfaces. The moistened powder is then placed into a die, pressure (100–500 MPa) and heat (<300°C) are then applied to aid rearrangement of the particles and the re-precipitation of the solid material from the solution [2], [3], [28], [29], [55], [56]. The maximum temperatures typically used in cold sintering is 300°C, which is a dramatically reduced sintering temperature compared to conventional methods for most materials. The general process of cold sintering is shown in Figure 15. Factors that can affect the efficacy of the process include particle size and distribution; pressure; temperature; volume of transient liquid and solubility of powdered material in the transient liquid.

Development of the process has mainly been on a material-by-material basis, optimising parameters empirically. Therefore, for each material-solvent combination densified *via* cold sintering, a significant amount of trial and error occurs before achieving sufficiently dense materials.

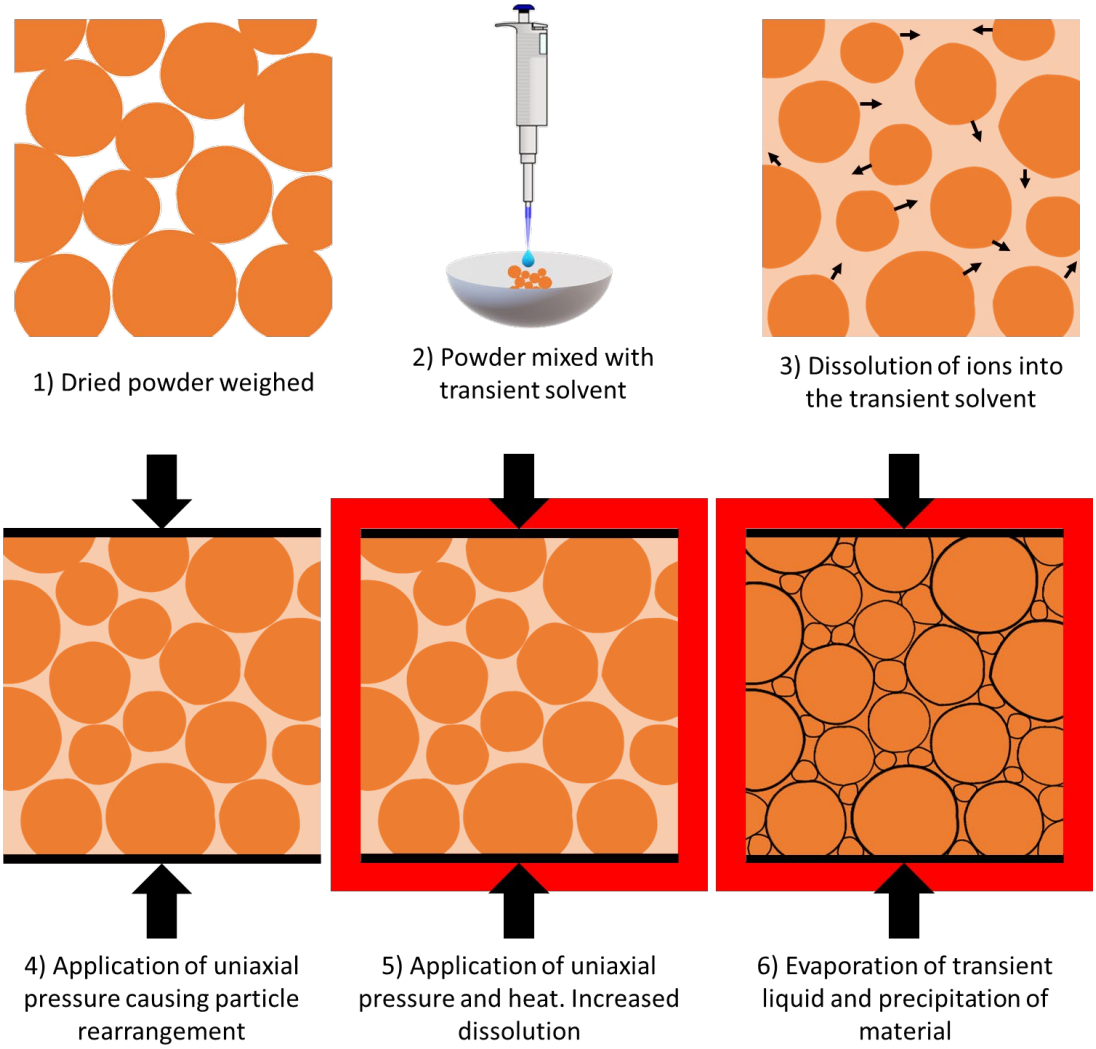

Figure 15: Stages in the Cold Sintering process

The proposed mechanisms of cold sintering are closely related to those observed in liquid phase sintering, comprising of two-stages [6]. The initial stage is dominated by particle rearrangement and compaction whilst the second is dominated by dissolution, grain growth and precipitation. The application of uniaxial pressure to the moistened powder allows for rearrangement of the particles in the initial stage of cold sintering, aided by the liquid phase which lubricates the movement of solid particles and fills small voids. In the majority of cases, pressure is applied before the temperature is increased, however, papers by H. Guo *et al.* and Baker *et al.* have reported preheating the die or pressing platen prior to application of pressure [3], [57]. In stage two, the uniaxial pressure is maintained whilst applying heat, further

aiding densification as the solubility of the materials in the liquid is enhanced as the system is heated. As the materials are heated further, the liquid evaporates, leading to precipitation of the solute onto the surfaces of the remaining particles. The liquid used for cold sintering can be used to create a saturated solution *via* the dissolution of the starting powder or be pre-loaded with a liquid phase containing the materials of interest [58].

Prior to research emerging from Randall *et al*. at Pennsylvania State University, Yamasaki *et al*. described a combined process of hydrothermal processing with isostatic pressing referred to as "hydrothermal hot pressing" to densify ceramics at 200-300 °C in 1986 [59]. The process was used to demonstrate the densification of a range of materials including silicates, cements, barium titanate, porous anatase, hydroxyapatite ceramics and low-level nuclear waste [59]–[61]. Initially, HHP generated interest as a method of bonding hydroxyapatite with metal and densifying ceramics which decompose at low temperatures. Cold sintering has many similarities with HHP such as the requirement for a liquid phase to facilitate mass transport and the occurrence of dissolution and precipitation reactions. HHP was inspired by natural geological phenomenon and is now considered to be a subset of the broader definition of CSP [58].

Table 2 shows a summary list of the materials that have been reportedly cold sintered. Molybdate, tungstate and vanadate ternary compounds are promising for cold sintering, with many having already demonstrated potential for processing *via* this route. Many of the compounds presented in Table 2 (such as Li_2MoO_4) are hygroscopic or highly soluble in water, making cold sintering using distilled water as the solvent possible. Other compounds such as $BaTiO_3$ require solutions containing constituents of the final material to allow cold sintering to occur.

Table 2: Compositions reported to have been cold sintered [29], [62]–[64]

Binary		Ternary			Quaternary	Quinary
Al_2O_3	Bi_2Te_3	$BaMoO_4$	$AgVO_3$	Li_2CO_3	$LiFePO_4$	$Li_{1.5}Al_{0.5}Ge_{1.5}(PO_4)_3$
Bi_2O_3	PbTe	$Gd_2(MoO_4)_3$	$BiVO_4$	Na_2ZrO_3	$LiCoPO_4$	$Li_{0.5x}Bi_{1-0.5x}Mo_xV_{1-x}O_4$
MgO	ZnTe	$K_2Mo_2O_7$	$LiVO_3$	$NaNO_2$	KH_2PO_4	$Na_{3.256}Mg_{0.128}Zr_{1.872}Si_2PO_{12}$
MoO_3	CuCl	Li_2MoO_4	KPO_3	$SrTiO_3$	$Ca_5(PO_4)_3(OH)$	
V_2O_3	NaCl	$Na_2Mo_2O_7$	$Mg_2P_2O_7$	CsH_2PO_4	$(LiBi)_{0.5}MoO_4$	
V_2O_5	AgI	$ZnMoO_4$	$Ca_3Co_4O_9$		$Pb(Zr,Ti)O_3$	
WO_3	CsBr	Cs_2WO_4	$Na_xCo_2O_4$		$Li_2Mg_3TiO_6$	
ZnO	ZrF_4	Li_2WO_4	$BaTiO_3$		$Na_{0.5}Bi_{0.5}MoO_4$	
ZrO_2		Na_2WO_4	$CsSO_4$			

The cold sintering process has been shown to be simple and effective in materials which readily dissolve congruently in water, including NaCl, NaF, alkali molybdates and phosphates. The process becomes more complicated in materials which dissolve incongruently in water or are insoluble. $BaTiO_3$ (BT) is one of the most used electroceramic materials and Ba^{2+} ions are known to preferentially leach out of the solid material when water is added, creating particles with Ti^{4+} rich exterior layer. In the case of BT, high quality nanoparticles have been used with a supersaturated solution of Ba and Ti sources to inhibit dissolution [65] [29].

Due to the low temperatures involved, cold sintering can be utilized to produce components from ceramic-polymer composites and with integrated metallic layers such as multi-layer ceramic capacitors and compact filtering-radiating modules for microwave communication [5], [22], [29]. There is a broad range of compositions that can be cold sintered, with over 50 inorganic compositions reported to have achieved densification *via* CSP by Guo *et al*. [29] and Baker *et al*. [2], [66]. As well as densification of bulk inorganic ceramic materials, a range of polymer/ceramic and organic/inorganic composites have also been investigated.

2.3.1 Water Soluble materials

LMO is conventionally sintered at 540 ℃ but *via* cold sintering it can be densified at 120℃ with the addition of 2-10 wt.% distilled water under applied pressure [58], [67], [68]. The properties of cold sintered LMO are comparable with conventional samples but a slight increase in dielectric loss is thought to relate to residual hydroxyl groups at the grain boundaries [68].

Lithium molybdate (LMO) has a phenacite-type crystal structure consisting of corner sharing tetrahedrons (Figure 16) [29][68][69]. LMO has been reported to melt incongruently at 698°C according to DSC studies by Moser *et al.* [72]. Denielou *et al*. and Brower *et al.* reported melting points of 701±2°C and 700±2.5°C respectively [73], [74]. Lithium molybdate (Li2MoO4, LMO) is a hygroscopic material which is congruently soluble in water and was one of the first materials used to demonstrate cold sintering. [18], [66], [67].

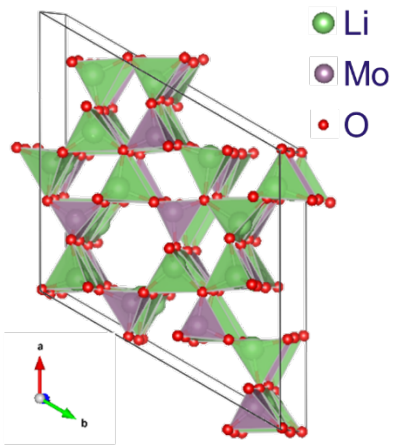

Figure 16 Phenacite structure of lithium molybdate [70], [75]

Conventionally, lithium molybdate is produced *via* solid-state synthesis by mixing stoichiometric amounts of Li_2CO_3 and MoO_3 and calcining at temperatures ranging from 500-620°C [68], [70], [76]–[78]. Lower temperature manufacturing could reduce costs and prevent volatile compounds being lost during calcination and there are reports in the literature of low temperature production of lithium molybdate.

Inagaki *et al.* prepared Li_2MoO_4 at 'room' temperature *via* a precipitation method from an aqueous solution of $(NH_4)_6Mo_7O_{24}$ and LiOH which is heated to 100°C to remove ammonium and then precipitate in ultrasonically agitated ethanol [78]. They investigated several processing parameters and their effect on the final materials, including the concentration of the aqueous solutions, quantity of ethanol, frequency of agitation and sintering duration. The particle morphology and morphology were highly sensitive to small alterations in the process. Zhang *et al.* followed a similar solution method to Inagaki substituting ethanol for distilled water. $(NH_4)_6Mo_7O_{24}{\cdot}H_2O$ and $LiOH{\cdot}H_2O$ were dissolved in deionized water and held at 60°C until the water had completely evaporated. The resulting dried powder was then ground using ethanol as a dispersant [79].

Yip *et al.* claim to have produced highly crystalline lithium molybdate by mixing $LiOH{\cdot}H_2O$ and MoO_3 to form a paste and then leaving the paste to dry at room temperature [80]. The particle size and morphology of room temperature Li_2MoO_4 was found to be smaller and more regular when compared to that of conventionally calcined material produced from Li_2CO_3 and MoO_3.

The dielectric properties of lithium molybdate have been shown to vary with production method and sintering conditions. Kahari *et al.* densified lithium molybdate

by pressing with 2-3 wt.% distilled water followed by drying at room temperature, 120°C or sintering at 540°C and found all samples had a permittivity of 4.6-5.2 at 9.6 GHz [68]. They also measured the Q_f which increased as a function of sintering temperature due to removal of residual water in the samples. Zhou *et al.* reported dielectric properties of Li_2MoO_4 sintered at 540°C as ε_r 5.5 (±0.05), Q_f 46,000 (±1000)GHz and a TCF of -160(±10)ppm/°C [76]. Zhang *et al.* reported slightly higher permittivity and Q_f values (5.58 and 49,328 GHz) in lithium molybdate manufactured *via* their aqueous solution method due to a reported reduction in impurity concentration compared to conventional solid state synthesis [79]. Cold sintering of lithium molybdate has been shown to increase the relative permittivity (5.61) but also to reduce the quality factor (30500 GHz) [66]. A decrease in Q_f values was also observed in other materials produced by Guo *et al. via* cold sintering, most significantly in $Na_2Mo_2O_7$ (Q_f of conventional material: 62,400 GHz, of cold sintered: 14,900 GHz) , although no explanation is offered [66].

Materials related to LMO such as sodium molybdate and potassium molybdate (Na_2MoO_7, NMO and K_2MoO_4, KMO) can also be densified *via* cold sintering. Whilst not hygroscopic, NMO and KMO are highly soluble in water (65.0 and 164.5 g/100ml respectively) making them ideal candidates for cold sintering [81], [82] . Sodium molybdate is conventionally sintered at 610 °C, whilst the material can be cold sintered at 150 °C with the addition of 5-10 wt.% water and the application of 200 MPa of pressure. Wang *et al*. achieved relative densities of 87% after conventional processing but 96% after cold sintering. The dielectric properties of NMO are also comparable between conventional and cold sintered. An increase in ε_r is observed (Conventional: 11.6 CSP: 12.7), due to increased density whilst residual hydroxyl groups increased dielectric loss [83], [84]. For KMO, a relative density of 100 % was achieved by cold sintering with 5-10 wt.% deionized water at 150 °C, 200 MPa for 30 minutes, followed by a 24 h drying step at 120 °C [85].

2.3.2 Water Insoluble Materials

Using water as the transient solvent in cold sintering limits the process to only water-soluble materials. To widen the applicability of the technique, a range of other liquids have been investigated. Transient liquids utilised to achieve cold sintering include acids/alkalis or solutions which upon heating decompose to form the desired chemical phase.

Funahashi *et al*. studied the cold sintering process for ZnO, utilising a 1M acetic acid solution to encourage dissolution, densification and grain growth of the material under cold sintering [56]. They achieved samples with >90% density and grain structures similar to that of conventional sintered materials (1400°C) after pressing at 378MPa followed by sintering at a pressure of 77MPa and temperatures between 88 and 305°C [56].

Gonzalez-Julian *et al*. used kelvin probe force microscopy (KPFM) to investigate the role of different solvent chemistries and the mechanisms occurring during cold sintering [86]. Samples were produced *via* cold sintering and a combined cold sintering/SPS method. For both CSP and CSP-SPS, powders were moistened with 1.6-3.2 wt.% distilled water or a 0.5% Zn-Ac solution and sintered according to parameters in Table 3. The use of a Zn-Ac solution as the transient solvent was found to significantly reduce the onset temperature of densification from 90-130 °C to ~25 °C at all applied pressures. This demonstrates the crucial role of powder dissolution in densification *via* cold sintering.

Table 3: Parameters used by Gonzalez-Julian et al. to create CSP and CSP-SPS samples

	CSP	CSP-SPS
Solvent content	1.6 - 3.2 wt.% H_2O 3.2 wt.% H_2O + 0.5 wt.% ZnAc	1.6 wt.% H2O 1.6 wt.% H_2O + 0.5 wt.% ZnAc
Temperature ramp rate	20 °C/min	100 °C/min
Holding Temperature	250 °C	250 °C
Pressure	150, 300 MPa	100, 125, 150 MPa

The surface potentials of samples sintered *via* CSP-SPS at 150 MPa were assessed using KPFM. The addition of water increased surface potential compared to the as-received powder, indicating an increased defect concentration. With the addition of Ac-H_20, a contrasting effect is seen, surface potentials are reduced indicating a lower defect concentration, attributed to grain growth during sintering. The increase in surface potential indicates that the solvent phase promotes transport and as OH^- and H^+ ions diffuse into the surface of the crystal structure, defects are created which lower the activation energy and raises sintering potential [56], [86], [87].

Induja *et al*. cold sintered the naturally occurring mineral sillimanite Al_2SiO_5 with distilled water at 120°C and using NaCl as a sintering aid [88]. Sillimanite has low permittivity (4.43), high Q_f value (41,800) and a TCF of -17 ppm/°C, however it sinters

poorly *via* conventional methods and converts to mullite at 1500-1650°C so cannot be manufactured into component by conventional methods. The dielectric properties of the resulting composite samples matched those calculated from the rules of mixing with ε_r = 4.52, Q_f = 22,350 GHz and TCF -24 ppm/°C [88].

Unlike lithium molybdate, MoO_3 has limited solubility in water (1g/L @ 20°C) and whilst cold sintering using 4 wt.% water as a transient solvent achieves some improvement in density it is below the desire >95% for commercial MW ceramics. Molybdenum oxide has been used to demonstrate new approaches to cold sintering of materials. Varghese *et al*. reports that conventional sintering of MoO_3 at 650°C (no time specified) achieved a relative density of 88%, whilst Zhou *et al*. achieved 64% density after sintering at 680°C for 2 hours and 76.8- 83.7% % *via* cold sintering [89], [90]. The cold sintering processes adopted by Zhou *et al*. compared the use of water and a solution of ammonium molybdate tetrahydrate as transient solvents, sintering at 100-150 MPa and 120-150 °C following by an annealing step. Ammonium molybdate is highly soluble in water and decomposes to form MoO_3 at high temperatures, 10 wt.%. $(NH_4)_6Mo_7O_{24}{\cdot}4H_2O$ was mixed into the MoO_3 powder prior to the addition of 4wt.% water and cold sintering at 150 °C with a 600 °C anneal. After the initial 150 °C CS step, the $(NH_4)_6Mo_7O_{24}{\cdot}4H_2O$ remains as a secondary phase and is observed in XRD. Heat treating at 600 and 700 °C removes the secondary phase and improves density. Cold sintered samples were found to have higher permittivity and lower Q_f values than conventional sintering, likely due to the increased density and smaller grains present in cold sintered samples [91].

2.3.3 Non-Congruently dissolving materials

In cases where the powder dissolves incongruently, a method of hydrothermal assisted cold sintering is applied where the transient liquid forms reactive intermediate phases. The transient liquid is often a solution containing a deep eutectic reaction precursor which forms the desired products at temperatures below that of a solid state calcination process [28], [92]–[94].

Guo *et al*. and Ma *et al*. utilised barium titanate nanoparticles and a hydrothermally inspired $Ba(OH)_2/TiO_2$ suspension in deionized water to cold sinter $BaTiO_3$ (180 °C, 430 MPa) [94], [95]. When particles of $BaTiO_3$ are exposed to water, Ba^{2+} ions leach from the surface, leaving a Ti-rich layer [96]. The composition of the transient liquid prevents the dissolution of Ba^{2+} from the powder particle surfaces. A post-sintering annealing step at 700-900 °C is applied to the cold-sintered material,

which whilst significantly lower than the conventional sintering temperature, causes significant grain growth and increases relative density by 1-5% [3]. During hydrothermal synthesis of barium titanate, $BaCO_3$ is a commonly reported by-product, which was seen in XRD as an impurity phase in the as-cold-sintered material by both Guo *et al*. and Ma *et al*. [94], [97]. Post sintering heat treatment allows the removal of this impurity phase by reaction to form $BaTiO_3$. TEM and chemical analysis revealed the presence of a carbonate rich, amorphous, intergranular phase which crystallizes during annealing. The improvements reported by Guo *et al*. in dielectric properties achieve after heat treatment are shown in Figure 17. Dielectric loss is significantly reduced and room temperature dielectric constant (1kHz) increases from ~70 after cold sintering to ~1800 after 900 °C annealing [95]. Ma *et al*. reported a room temperature permittivity of 2332 (1kHz) in samples cold sintered for 60 minutes and annealed for 3 hours at 900 °C [94].

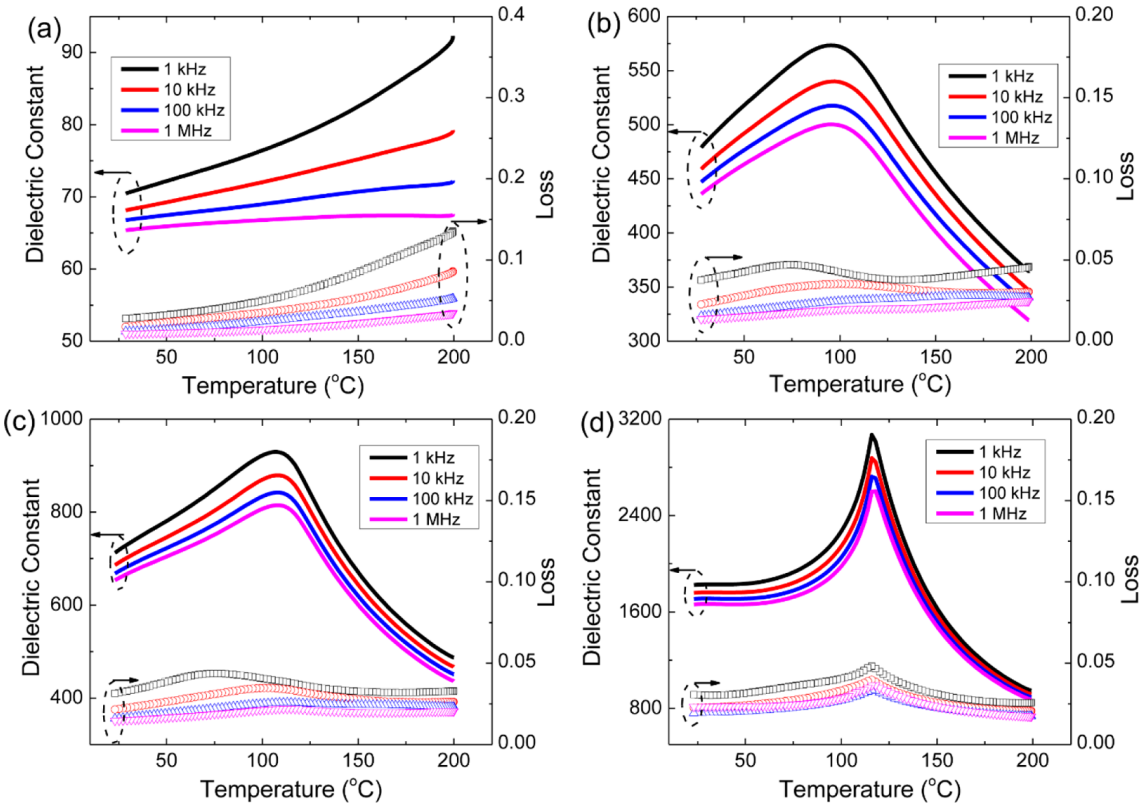

Figure 17: Temperature-dependence of dielectric constant and loss for (a) cold-sintered ceramics at 180 °C, and subsequently annealed at (b) 700 °C, (c) 800 °C and (d) 900 °C reported by Guo et al. [95]

$SrTiO_3$ is conventionally sintered at over 1400 °C, Boston *et al*. developed a method to cold sinter $SrTiO_3$ which utilises reactive intermediate phases [92], [98]. Micro- and nanoscale $SrTiO_3$ and TiO_2 powders were mixed with 0.2 ml of a 1.5 M $SrCl_2$ aqueous solution. The mixture was pestle and mortared to produce a free-flowing powder which was then pressed at 750 MPa for 10 minutes at room temperature before

increasing to 180 °C for 60 minutes. After cold sintering, a 4 h heat treatment at 950 °C promotes micro-reactions between $SrCl_2$ and TiO_2 intermediate phases, forming $SrTiO_3$. The elimination of the intermediate phases is demonstrated in Figure 18, where peaks in the XRD spectrum attributed to $SrCl_2$ and TiO_2 are seen after cold sintering and are not seen after heat treatment [92].

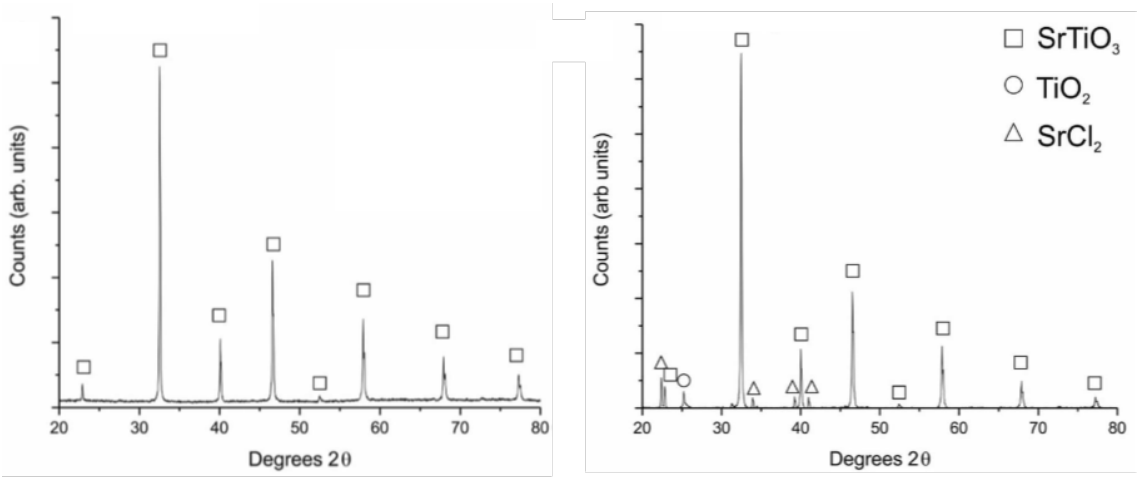

Figure 18: XRD spectra of a cold sintered ceramic using solid state powder as a starting reagent before (right) and after (left) heat treatment at 950 °C after [92].

Electrical testing of cold sintered $SrTiO_3$ showed similar trends to conventionally sintered materials, however the relative permittivity values were lower and exhibited frequency dependence. Particle size in the conventionally sintered samples is shown to affect the permittivity and loss whereas the properties of cold-sintered samples appear less dependent on particle size (Table 4).

Table 4: Range of relative permittivity and tan δ values measured across 25-250°C temperature range [92]

	Nanoscale		Micron-Scale	
	Permittivity	tanδ	Permittivity	tanδ
Conventional	130-210	0-0.55	120-180	0-0.14
Cold	70-120	0-0.21	70-120	0-0.21

2.3.4 Post-Sintering Annealing

Amorphous grain boundary phases have been reported in some polycrystalline ceramic materials after cold sintering [3], [28], [66], [95]. The formation of amorphous phases is controlled by a number of factors including the condensation rate of the solute due to solvent evaporation and the level of super-saturation prior to condensation [66]. The temperatures and times involved in cold sintering are insufficient to allow for total recrystallisation of grain boundaries and heat treatments are often utilised after cold sintering to remove moisture, aid recrystallization, and achieve further densification.

For $BaTiO_3$ the annealing temperatures used are 700-900°C, after cold sintering at 180°C, which is significantly lower than the conventional sintering temperature, but causes significant grain growth and increases relative density by 1-5% [3].

Densification of yttria doped ZrO_2 is typically achieved at temperatures of ~1400°C but Guo *et al.* have reported 85% theoretical density in 3 mol% Y_2O_3-doped ZrO_2 after cold sintering at 180°C for 30 minutes and 95% density after annealing at 1000-1100°C. In ZrO_2 with 8 mol.% Y_2O_3 doping (YSZ), the cold sintered density is much lower (56%) before heat treatment [62][66]. As most metallic electrodes melt or oxidise as high temperatures, the annealing processes required for some materials is a barrier to co-firing of components unless it is below ~900°C [24]. Therefore, development processes and materials which achieve full density is required before co-firing.

Whilst the use of heat treatments may seem to contradict the energy savings achieved by cold sintering, temperatures utilised are significantly lower than required in conventional sintering. The removal of secondary grain boundary phases and grain growth can lead to improvements in properties in materials such as $SrTiO_3$ and $BaTiO_3$, discussed in 2.3.3

2.3.5 Effect of Particle Size on Cold Sintering

Control of particle size can also be utilised to improve cold sintering of non-soluble materials, although competing ideas about the optimum particle size and size distribution exist. Kähäri suggests that greater particle sizes produce better results in hygroscopic Li2MoO4, due to water being more evenly distributed, preventing clumping and warpage [67]. Whereas Guo *et al*. cite the use of nano-particles as a

method to improve density in other non-hygroscopic material systems due to higher reactivity and surface to volume ratio [3]. A bimodal system, utilising nanoparticles in combination with coarser particles created a thermodynamically unstable system, which encourages the process of surface area reduction [65]. However nanoparticles tend to have a higher concentrations of defects, which could have a negative impact on mechanical and electrical properties [99]. When investigating the potential of new materials to be cold sintered, a number of factors should be considered, including solubility and particle size of the starting material and effect of sintered particle size on properties.

2.3.6 Cold Sintered Ceramic-Ceramic Composites

LMO, NMO and KMO are readily densified *via* cold sintering and have therefore been used as a starting point to create many composites with other ceramic materials with more favourable properties, but which are harder to cold sinter such as barium hexaferrite, sodium bismuth molybdate and bismuth lithium vanadium molybdate [83], [100], [101]. Several two-component cold sintered ceramic composites have been demonstrated with temperature stable MW properties using LMO, NMO and KMO to encourage densification [83], [85], [100], [101]. The ability to create highly dense ceramic composites with varying compositions allows for properties to be tailored, demonstrating compositional design that would not be easily achieved by conventional methods.

Wang *et al.* produced $Na_{0.5}Bi_{0.5}MoO_4$-Li_2MoO_4 (NBMO-LMO) composite samples by mixing NBMO and LMO powders with 5-10 wt.% of deionized water and pressing pellets 30 min at 150 °C and 200 MPa. Sintered pellets were dried for 24 hours at 120 °C to remove any residual moisture [101]. The NBMO-LMO ceramic composites in this study showed no chemical reaction between the phases occurs during cold sintering. Figure 19 shows the properties of the individual phases after conventional sintering and cold-sintered composites. The significantly lower permittivity and Q_f of cold sintered NMBO can be attributed to the lower density achieved. Near zero TCF was achieved at 20% LMO with ε_r = 17 and Qf = 8000 GHz [101].

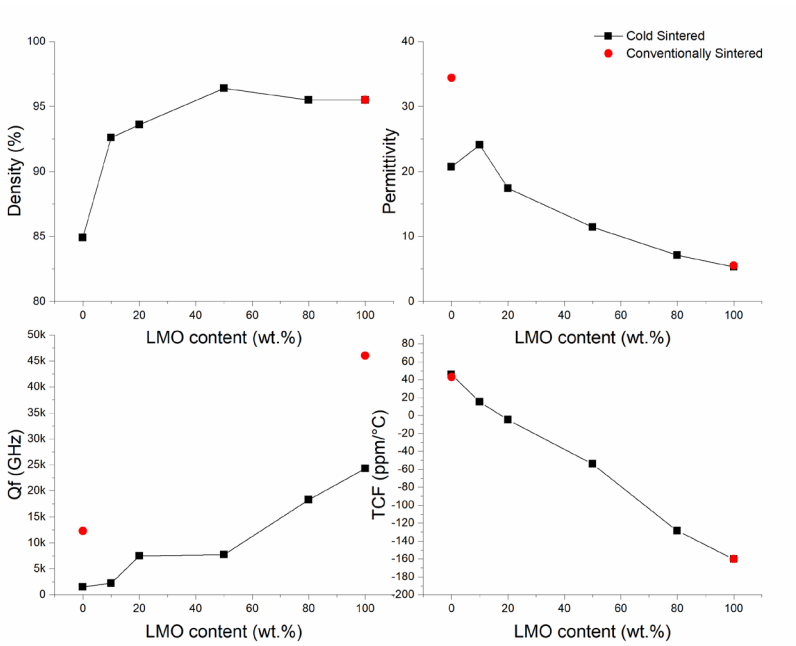

Figure 19: Properties of NBMO-xLMO composite ceramics produced by cold sintering, comparing permittivity to conventional samples produced and measured by Zhou et al. [22], [76], [83], [101], [102]

$(Bi_{0.95}Li_{0.05})(V_{0.9}Mo_{0.1})O_4$-$Na_2Mo_2O_7$ (BLVMO-NMO) composites were also sintered by combining the mixtures with 5-10 wt.% of deionized water, and hot pressing for 30 min at 150 °C & 200 MPa. A post sintering drying step of 120 °C for 24 hours was performed to remove residual moisture [83]. Electrical and microwave analysis of the BLVMO-NMO showed similar trends to the NBMO-LMO and near zero TCF was obtained at 20 wt.% NMO with $\varepsilon_r \sim 40$ and Qf = 4000, as shown Figure 20. Although the Q_f values of these composites do not compete with conventionally sintered ceramics for resonator applications, their properties, ease of integration and low energy consumption show promise for a wide range of novel devices.

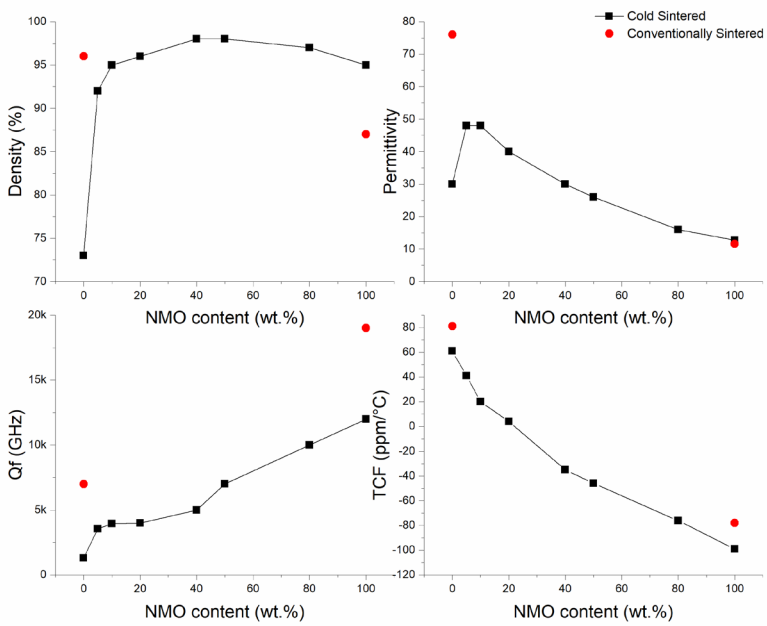

Figure 20: Properties of cold sintered BLVMO-NMO composite ceramics (Black) and conventionally sintered BLVMO and NMO (Red) [83].

Composites of BLVMO-NMO (20 wt.% NMO) were also used to produce multilayer ceramic capacitor *via* cold sintering. Ceramic layers were tape cast and Ag electrodes applied *via* screen printing which were stacked and laminated at 80 °C for 20 min, with an applied pressure of 10MPa. Binder burnout was performed at 180 °C for 3 hours and resulting stacks were exposed to water vapour in a sealed beaker at 80 °C. The moistened stacks were then cold sintered at 150 °C under 100 MPa of pressure for 30 minutes. The MLCC produced by this method was well densified, well laminated, and un-warped as shown in Figure 21. The silver electrodes (Figure 21c) appear well defined indicating no reaction at the metal-ceramic interface. EDS mapping also shows that grains of BLVMO and NMO are randomly distributed in each layer (Figure 21b-h) [84].

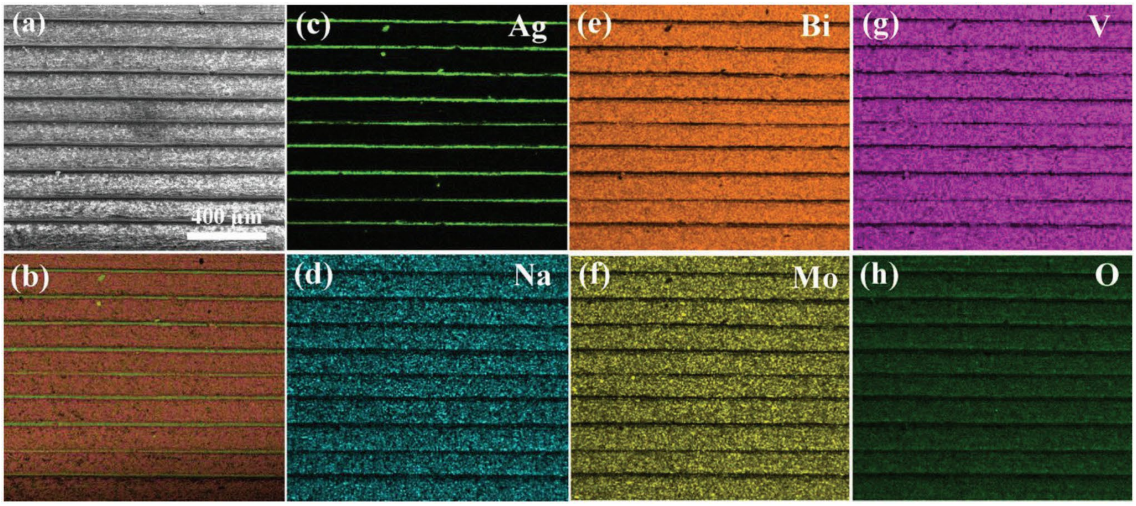

Figure 21: SEM (a) and EDS elemental mapping (b-h) for a cross-section of BLVMO-NMO MLCCs, from [84]. .

The room temperature ε_r and dielectric loss at 1 MHz were found to be 39 and 0.01, respectively and TCC was within 0.013% up to 150 °C. This indicates that the BVLMO-NMO MLCC's produced *via* cold sintering conform to property limits for C0G capacitors of TCC <0.01% of room temperature value (Figure 22). Current commercially available C0G capacitors are fabricated at approximately 1100 °C from $CaZrO_3$-based dielectrics with sintering aids and Ni electrodes.

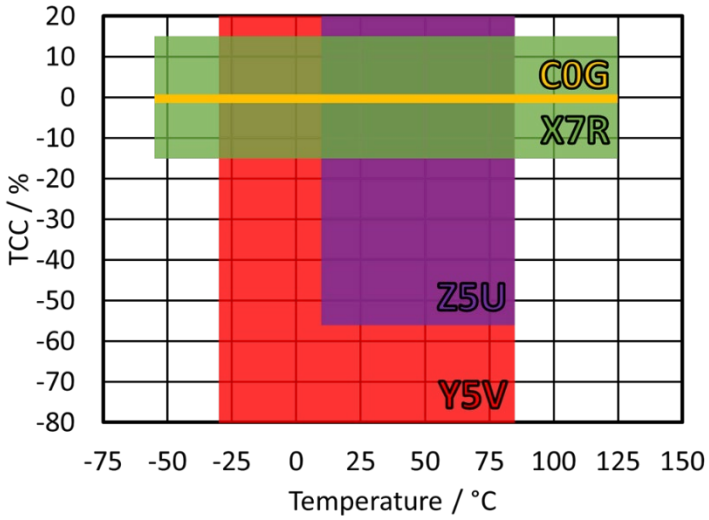

Figure 22: Comparison of commonly used capacitor categories, according to temperatures coefficient of capacitance and temperature [62][84]

Wang *et al*. cold sintered a series of calcium titanate-potassium molybdate (CTO-KMO) composites and produced a microstrip patch antenna substrate. Composites were produced at 150 °C under a uniaxial pressure of 200 MPa for 30 min. High densities were achieved for all KMO containing compositions, with 100 % relative density in compositions >70 wt.% KMO (Figure 23). From energy-dispersive X-ray

spectroscopy (EDS) mapping, the authors showed that two chemically discrete regions are present in the composites after cold sintering indicating that no reaction occurs between the two phases during sintering [85].

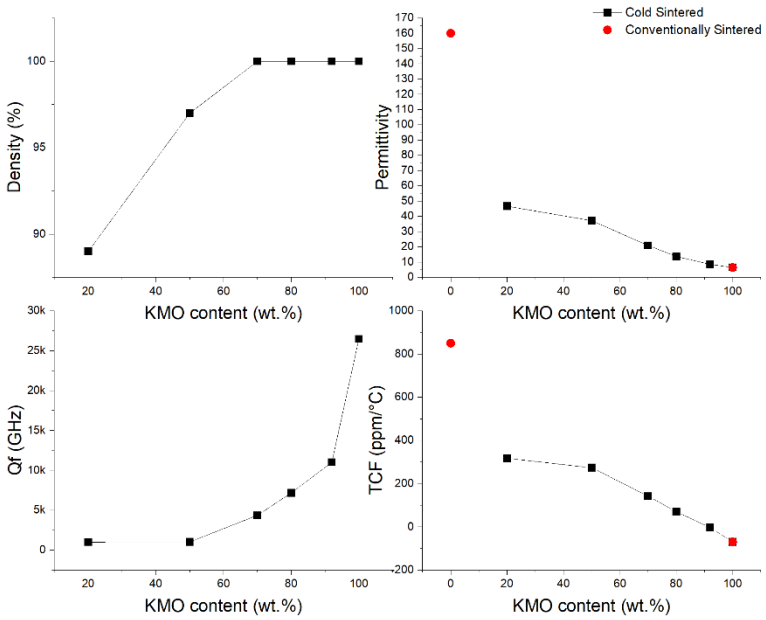

Figure 23: Properties of cold sintered CTO-KMO composite ceramics (Black) and conventionally sintered (Red) [85]

Materials for 5G antenna substrates should have ε_r <15, a near-zero TCF and high-quality factor [85], [103]. CTO-KMO composites produced with 92 wt.% KMO achieved TCF ~–4 ppm °C^{-1}, ε_r = 8.5 and Q_f ~11,000 GHz, which was then used to create a cold sintered microstrip patch antenna, operating at 2.51 GHz with a 62 % radiation efficiency. The combination of high antenna performance and low temperature densification demonstrates the potential for the direct fabrication of antenna substrates onto printed circuit boards [85].

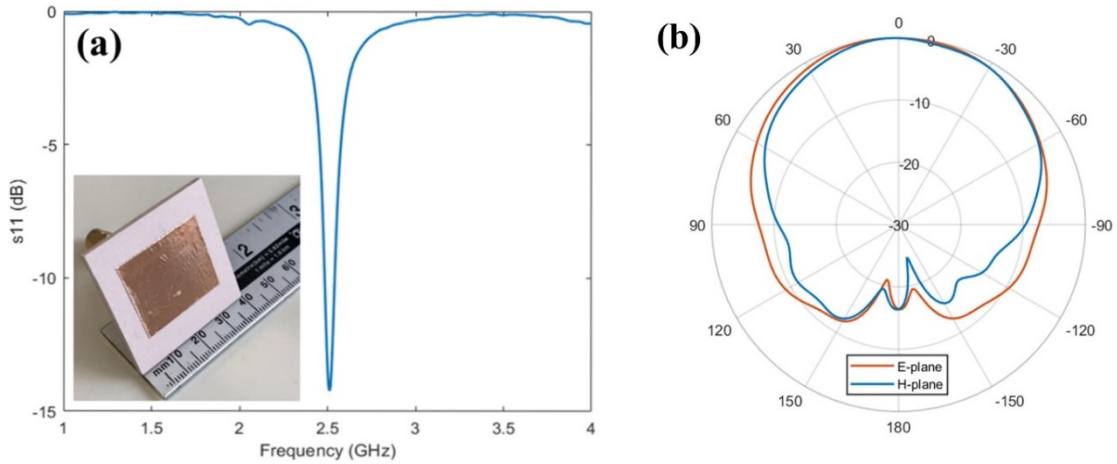

Figure 24: (a) Efficiency and (b) radiation pattern of a microstrip patch antenna fabricated from cold sintered CTO-KMO and shown inset (a) [85].

2.3.7 Cold Sintered Ceramic-Polymer Composites

The relatively low temperatures used during the cold sintering process allows for the integration of polymeric materials, which have significantly lower working temperatures than conventional ceramic processing temperatures. The advantages of combining polymers and ceramics are varied and could allow for the tailoring of electrical, thermal, or mechanical properties. A number of polymeric materials, including PTFE, PVDF-HFP, PEDOT:PSS and PEI have been co-sintered with ceramics to demonstrate a number of potential applications such as microwave communications, semiconductors and multi-layered circuits [22], [29], [104]–[107].

2.4 Screen Printing

To produce a range of components with more complex geometries, ceramic powders are commonly mixed with binders to produce slurry for tape-casting, screen printing or stereolithography. The final properties of components manufactured *via* these methods is very dependent on the slurry and processing parameters [81][82].

Screen-printing is commonly used to create relatively thick films (10-100μm) of ceramic materials and is used to produce a wide range of components [110]–[117]. During screen printing a slurry or 'ink' is applied to the screen, a flood bar then spreads the slurry across the printing area. The 'squeegee' is then lowered and moved across the screen, forcing the slurry through the mesh onto the substrate. This process can be performed multiple times to create thicker samples. Screen printing slurry is generally produced by mixing a powder of the materials to be printed with binder, solvent and dispersant [110]. Slurrys should be shear thinning such that the viscosity is reduced when pressure is applied by the squeegee allowing it to flow through the mesh and when printing is finished the pattern is maintained [83][91].

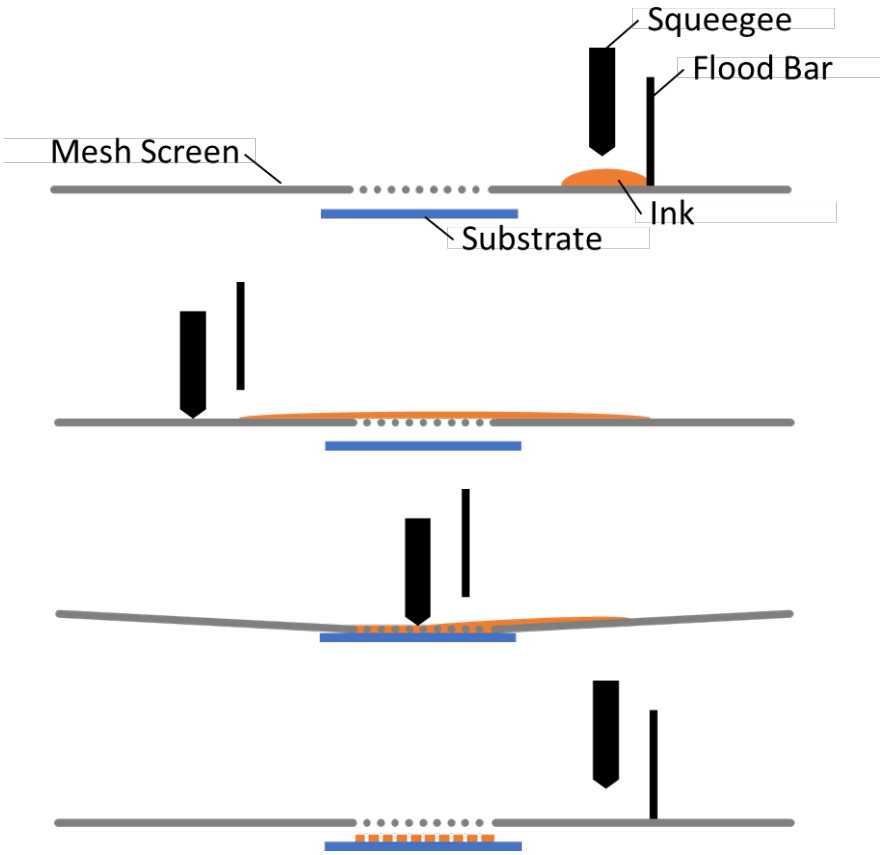

Figure 25: Stages of screen printing

There are several parameters that can be altered in both ink production and the screen-printing process that influence the final quality of the screen-printed materials. Several authors have discussed screen-printing parameters for producing high quality screen prints. These include the squeegee load, speed, angle and geometry and the type of mesh and the distance the mesh is from the substrate [114]. If the printing ink is very viscous and 'tacky' increasing the squeegee load whilst also reducing the speed of printing will improve film quality, however too low a speed causes flow out from the mesh pattern [83][87][89]. Figure 26 shows screen printed samples of doped ZnO produced by Rudež *et al.* with common screen-printing defects caused by slurry characteristics and printing parameters [83].

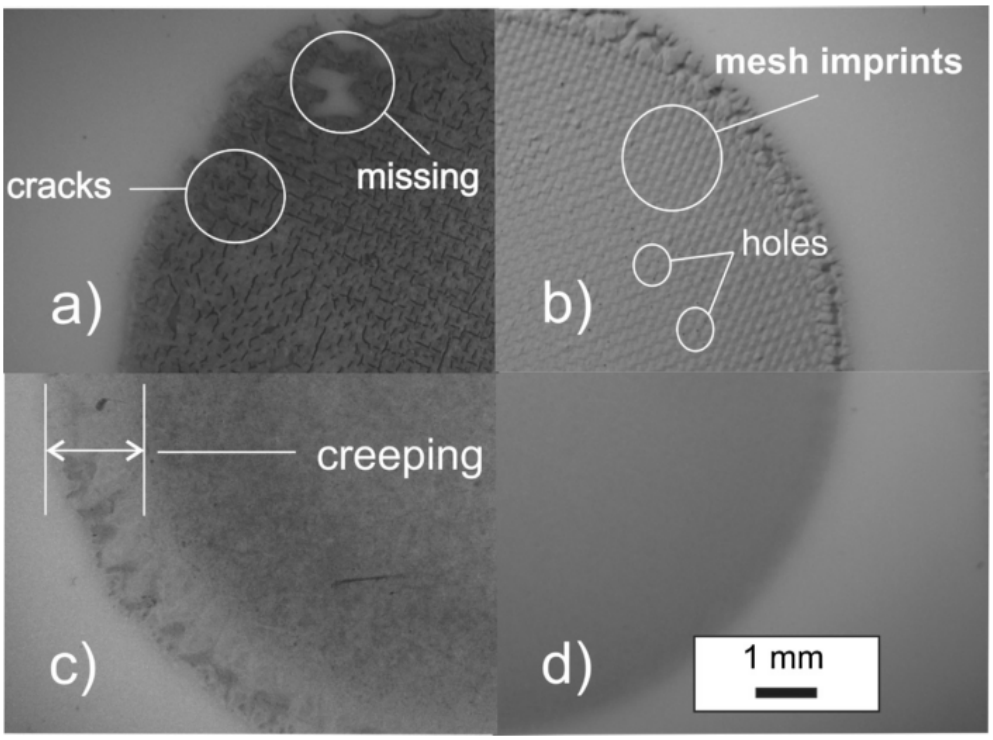

Figure 26: Optical microscope images of screen printed film surfaces displaying common defects (a-c) and an example of a well printed surface (d) [110]

The rheology of the printing ink has a significant impact on the quality and density of screen-printed samples and there have been several studies in this area relating to the manufacture of a number of different products. Increased binder content has been found to increase the green and sintered density of cermet films [112]. Mücke *et al.* studied the correlation between particle size of the powder and the green density of thick films produced *via* screen printing [119]. They showed that slurry produced using finer powder particles has higher viscosity and lower shear rates, due to the increased specific surface area the particles are wetted less completely. They also concluded that that using coarser particles in the ink produced denser samples [119]. Wu *et al.* manufactured Al_2O_3 based ceramics *via* stereo lithography followed by de-binding and sintering steps. In their work, denser samples could be produced using starting powders with bimodal particle size; however different sintering temperatures were used for samples containing particles of different sizes, potentially contributing to the observed difference in density [109].

Screen printing onto polymeric and metallic substrates has been used in conjunction with cold sintering for lithium molybdate [2]. A printing ink was made to the quantities in Table 5 and homogenized using a planetary centrifugal mixer, it was then printed through a 200 or 400 mesh onto nickel foil or PET substrates.

Table 5: Screen printing formulation for lithium molybdate [2]

		Wt.%
Lithium molybdate (LMO)		66
Ethylene glycol diacetate (EGD)		11
Benzyl Butyl Phthalate (BBP)		0.9
Printing Vehicle	QPAC40	3.3
	EGD	18.7

.

After screen printing, binder burnout was performed at 150 °C for nickel substrate samples and 175 °C for PET substrate samples for 6 hours. Cold sintering was then performed by exposing the green printed samples to water vapour to encourage water absorption prior to pressing the samples in a 120 °C preheated platen at 100MPa for 12-15 mins. Figure 27 shows the cross section of a single layer capacitor structure after cold sintering, the microstructure consists of fine grains, consistent with the low driving force for grain growth at such low sintering temperatures. To achieve consistent sintering, a variety of sintering aids were trialled in this study, such as paper and PTFE.

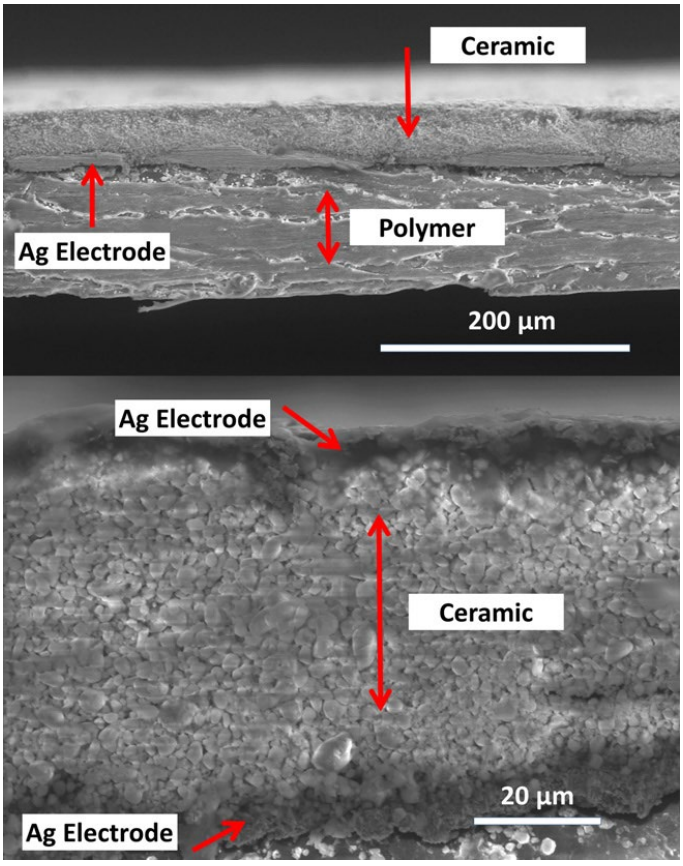

Figure 27: Cross-Sectional SEM image of lithium molybdate cold sintered onto a PET substrate in a single layer capacitor structure, reproduced from [2]

2.5 Microwave Dielectric Materials

There are a wide range of applications for microwave dielectric materials, such as microwave telecommunication, and satellite broadcasting [11]. With the continued growth of the telecommunication industry, research has been driven by the requirement for materials with properties which can enable the manufacture of smaller, more cost efficient components [11], [103], [120]

Ceramic materials have been widely utilized as filters and resonators in antennas for microwave communication since their commercial introduction in the 1980's. Dielectric resonator antennas consist of a high permittivity material, which exhibits resonance for a narrow range of electromagnetic frequencies, mounted on a ground plane and fed by a coaxial probe [121], [122]. Figure 28 illustrates how microwave ceramic technology developed between 1995 and 2005, with handset and base station technologies diverging due to differing requirements [103].

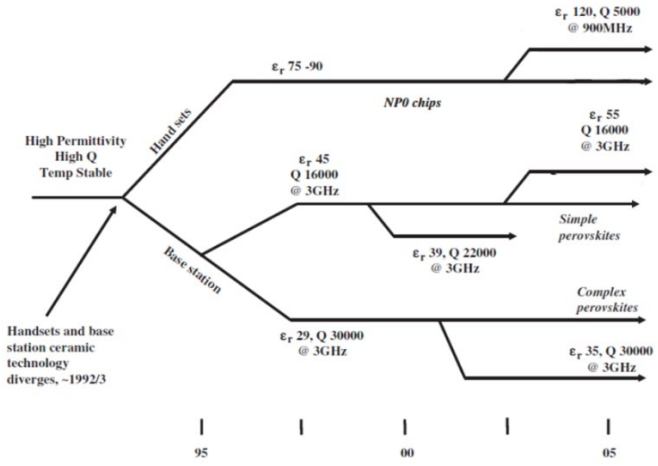

Figure 28: Ceramic resonator development through the 1990's and 2000's [103]

Early mobile technology was reliant on large, metallic invar air cavity resonators in base-stations and handsets, limiting the size and therefore practicality of mobile phone usage [24], [123]. Dielectric resonator antennas often used for satellite navigation offer a number of advantages including reduction in size and weight alongside radiation efficiency and ease of integration [121], [123]–[125]. For base stations, the emphasis is on producing extremely low loss materials rather than reducing size, so materials with high Q values and moderate ε_r are utilised to produce acceptable components.

There are a large number of possible of configurations for dielectric resonator antennas, making them highly versatile [126]. Ceramic pucks are suitable for use as single mode resonators, where a standing wave of specific resonant frequency is

sustained within the material [103]. Despite the concept being relatively simple, controlling the physical dimensions and phases during processing and sintering is more complex; small differences between batches of material affecting final properties [103].

Patch or microstrip antennas consist of a conducting layer on a low-loss dielectric slab. A variety geometries are easily manufactured by mass-production of printed circuit techniques where ground planes and strip conductor are deposited on the dielectric substrate by screen printing and other techniques [127], [128]. Figure 29 shows a simple, approximately square microstrip antenna configuration. The physical dimensions and relative permittivity of the dielectric slab determine the guide wavelength, which in turn affects the size of the conducting patch [129].

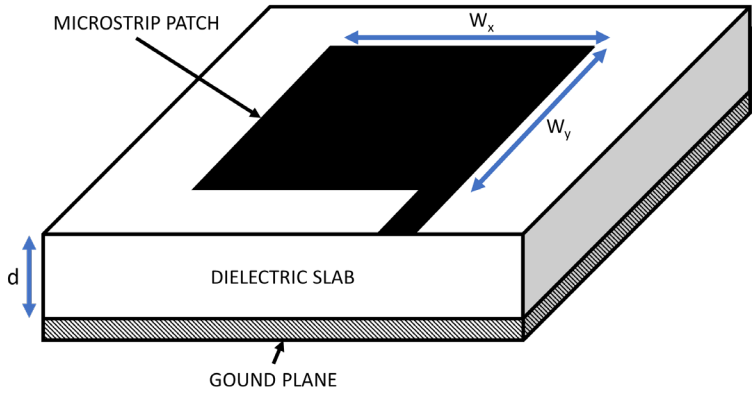

Figure 29: Schematic of a simple square microstrip patch antenna [129]

2.5.1 Polarization and Permittivity

Relative permittivity (ε_r) is the measure of a materials ability to store charge under an applied electric field, compared to the energy storage capacity of a vacuum. Permittivity is the macroscopic property of a material, caused by polarization. Polarization occurs when an electric field is applied to a material, causing small displacements of charge creating dipole moments within the material.

All materials exhibit atomic/electronic polarization (α_e), where electrons move relative to the nucleus of an atom. In ionic materials, the relative displacement of anion and cation lattices causes ionic polarization (α_i). In polar molecules such as water, the electric field acts to orient the molecules creating dipolar polarizability (α_d). Space charge polarization (α_{sc}), is caused by the movement of charge carriers in a materials until they are halted at a potential barrier such as a grain or phase boundary [12],

[130]. Figure 30 provides a visual representation of the four mechanisms discussed above.

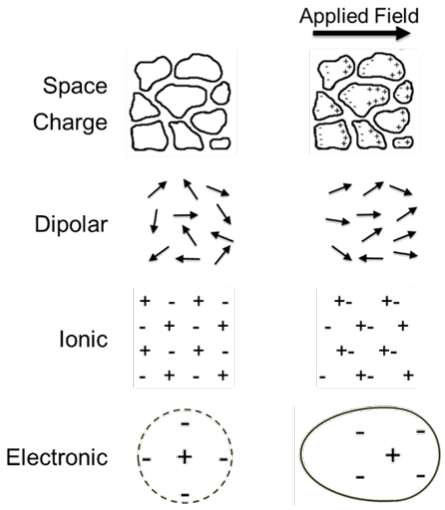

Figure 30: Schematic representation of the four polarization mechanisms [12], [130].

These four mechanisms all contribute to the overall polarization (α) of a material according to equation 1 [12]:

$$\alpha = \alpha_e + \alpha_i + \alpha_d + \alpha_{sc} \quad (1)$$

Each mechanism of polarization contributes to the ε_r of a material at different frequencies of applied field. As shown in Figure 31, all mechanisms of polarisation contribute to the polarisation of a material at frequencies lower than ~10^3 Hz. As the frequency is increased to ~10^4 Hz space charge effects begin to relax out, with dipolar effects being lost at frequencies higher than 10^{10} Hz. Electronic and ionic polarization mechanisms are the main contributors to ε_r at microwave frequencies (10^{11}-10^{13} GHz).

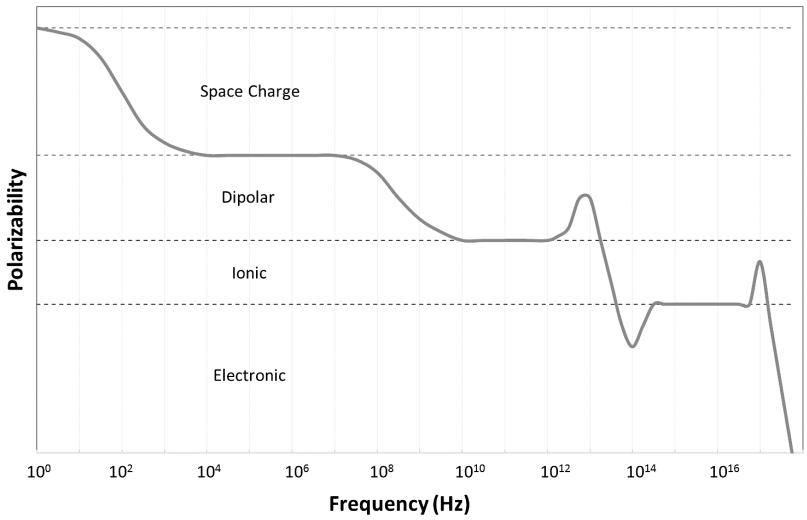

Figure 31: Schematic representation of the frequency dependence of polarization mechanisms contributions to the total polarizability of a material [11], [12].

The relationship between the ε_r and its resonant frequency (f_0) is shown in equation :

$$f_0 \approx \frac{c}{\lambda_d {\varepsilon_r}^{1/2}} \approx \frac{c}{D {\varepsilon_r}^{\frac{1}{2}}} \quad (2)$$

where c is the speed of light in a vacuum and λ_d is the length of the standing wave induced along the diameter (D) of a dielectric resonator [11], [12]. Utilizing higher permittivity materials therefore allows the same resonant frequency to be maintained whilst the resonator size is reduced proportionally to $\left({}^{1}/_{\varepsilon_r}\right)^{1/2}$ [11], [12], [131]. Therefore compared to a vacuum cavity ($\varepsilon_r = 1$) a dielectric component with $\varepsilon_r = 36$ is only 1/6 of the size but would have the same resonant frequency [120].

Materials with permittivity in the range of 4-12 are applicable in millimetre communication and as substrates for integrated microwave circuits [123]. Base stations require materials with $35 \leq \varepsilon_r \leq 55$, whereas miniaturized GPS antennas require $75 \leq \varepsilon_r \leq 120$ [131]. ε_r of a non-polar, non-conductive material with a highly symmetrical ionic structure can be estimated using the Clausius-Mossotti relationship:

$$\frac{\varepsilon_r - 1}{\varepsilon_r + 2} = \sum_i \frac{N_i \alpha_i}{3\varepsilon_0} \quad (3)$$

where *N* is density, α is the polarizability of the ionic species in the material [130]. The dielectric polarizability of a number of ions were derived by Shannon from the dielectric constants of oxides and fluorides [132]. The value obtained using the Clausius-Mossotti equation is idealised, with deviations in materials due high symmetry or caused by extrinsic defects such as cracks, pores and impurities [11], [130], [133].

Porosity has a significant effect on the ε_r of a ceramic puck, therefore experimental samples should be produced with high relative density. Penn at al. produced an equation to calculate the actual permittivity of a material (ε_m) corrected for fractional porosity (P) from experimental values (ε') in alumina [133]:

$$\varepsilon' = \varepsilon_m \left(1 - \frac{3P(\varepsilon_m - 1)}{2\varepsilon_m + 1}\right) \quad (3)$$

2.5.2 Dielectric Loss

The dissipation of electrical energy in a material due to physical processes such as conduction, relaxation and resonance is called the dielectric loss (tan δ) [134]. Losses are caused by the delay in change of polarisation as the applied electric field changes due to a combination of intrinsic and extrinsic factors. Losses occur intrinsically due to the crystal structure, temperature, or frequency of electric field change. Extrinsic losses are associated with impurities and microstructural features such as lattice defects and porosity [11], [130], [134], [135]. Increasing frequency normally increases losses due to higher energy dissipation within the material and dielectric leakage demonstrated by Figure 32.

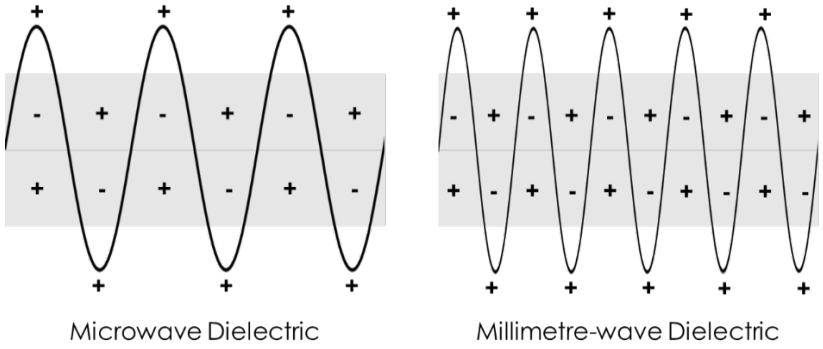

Figure 32: Increase of dielectric loss caused by increased number of polarisations over time and volume with increased frequency [131], [136]

Although the contribution of grain boundaries to extrinsic loss was shown to be very limited in work on MgO by Breeze *et al.* [135], grain size is reported to create a variety of effects in different systems [133], [135], [137]–[139]. Increasing grain size is found to reduce loss in (Zn,Mg)TiO_2 and $Ba(Mg_{1/3}Ta_{2/3})O_3$ and to increase tanδ in polycrystalline alumina [133], [138], [139].

Dielectric loss is an important factor to be considered in microwave dielectric materials and is given as a ratio between the two complex quantities dielectric permittivity, ε_r' and electric loss factor, ε_r'' [12], [71]:

$$\tan\delta = \frac{\varepsilon_r''}{\varepsilon_r'} \tag{4}$$

The Quality factor (Q_f) of a microwave dielectric material is commonly reported and is approximately the reciprocal of the tan δ value [131]. High quality factors reduce cross talk within a given frequency range [123]. Four types of loss are present in microwave resonators – dielectric, conduction, radiation and external, which are related to the loaded quality factor by equation 5 [11], [140]:

$$\frac{1}{Q_L} = \frac{1}{Q_d} + \frac{1}{Q_c} + \frac{1}{Q_r} + \frac{1}{Q_{ext}} \tag{5}$$

As frequency increases, the losses in a system normally increase, making Q_f frequency dependant. The Quality factor is determined experimentally, by measuring the half power bandwidth (width of the resonance curve 3dB below maximum peak) at resonant frequency (as shown in Figure 33) and applying equation 6 [11], [103] :

$$Qf = \frac{f}{\Delta f} \tag{6}$$

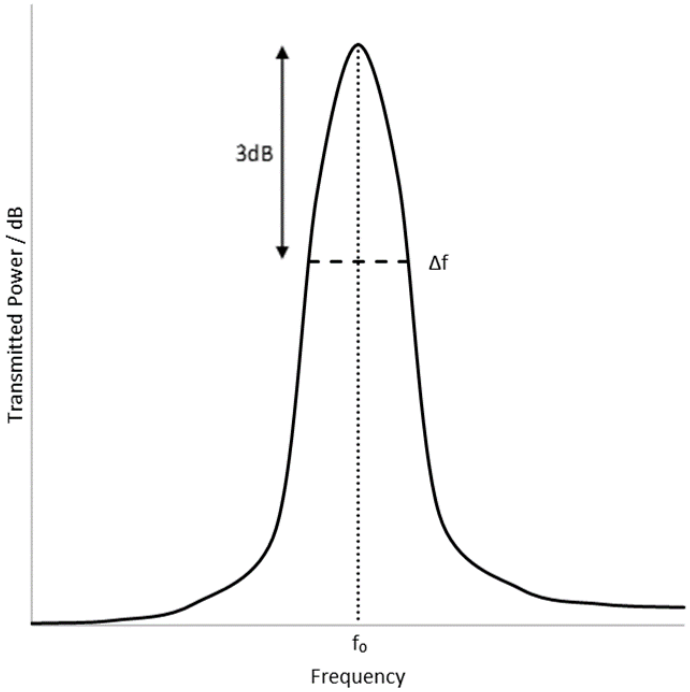

Figure 33: Resonance peak of a microwave dielectric material, with the resonant frequency and half bandwidth indicated [11], [103]

2.5.3 Temperature Stability

Changes in permittivity due to temperature are given by the temperature coefficient of permittivity, τ_ε, which is reported in parts per million per degree (ppm/°C or ppm/°K). The temperature coefficient of resonant frequency (τ_f) is related to the temperature coefficient of relative permittivity (τ_ε) and the linear expansion coefficient (α_L) by equation 7 [11], [123], [130], [131], [141]:

$$\tau_f = -\alpha_L - \frac{\tau_\varepsilon}{2} \tag{7}$$

Thermal stability is very important in microwave dielectric ceramics, as operating temperatures for common practical applications range from -30 to +80°C [24], with a requirement being that the magnitude of τ_f is lower than 10 ppm/°C from -40 to 100 °C [120] for most applications Experimentally, τ_f is determined my measuring the shift in resonant frequency as the temperatures is varied. The τ_f is then calculated from the slope of the resulting plot of resonant frequency against temperature using equation 8 [11]:

$$\tau_f = \frac{f_{Tmax} - f_{Tmin}}{f_{Tmin}(Tmax - Tmin)} \tag{8}$$

where f_{Tmax} and f_{Tmin} are the resonant frequencies measured at the maximum and minimum temperatures, respectively.

2.5.4 Factors affecting dielectric properties

The properties of dielectric materials can be altered by adding dopants to the composition or by utilizing different processing routes [125]. Plotting ε_r of zero τ_f resonator materials against $\log_{10}Qxf_0$, and against temperature coefficient of capacitance when $\tau_f \gg \alpha_L$results in trend lines that are straight [103], [142]. Although there is a wide range of commercial materials from $5<\varepsilon_e<90$ with high Q, zero τ_f, ceramics with $45<\varepsilon_r<75$ have not been developed [103], [143]. Qxf_0 is dependent on composition, processing and structure and is mainly improved by reducing sources of extrinsic loss [103].

Control of particle size is a critical factor in controlling the final properties of materials. Calcination rates are highly dependent on the mobility of the ions which can be improved by using smaller particle sizes [14], [21], [134]. Smaller particle sizes have higher surface area and therefore more potential reaction sites during calcination, allowing the formation of homogenous materials at shorter processing times. In conventional sintering, smaller particle sizes tend to improve sintering behaviour and densification, particularly when the curvature of the particle is on the order of a few microns [12]. This can aid in producing materials with high density and ε_r and Qxf_0 which are close to the materials theoretical maximum [15], [71], [130]. Nanoparticles have been shown to improve sintering rates and reduce sintering temperatures in some systems but the green density is often lower and the presence of contamination increases due to the higher surface area [13].

The ε_r of some materials is effected by the final grain size within the sintered materials, which is related to the initial powder size and subsequent processing [144], [145]. Figure 34 shows the effect of grain size on ε_r of barium titanate between -50°C and 175°C measured by Arlt *et al*. with grain sizes 0.28-6.8 µm [145]. $BaTiO_3$ with an average grain size of 6.7 µm showed the lowest ε_r at room temperature. Initially, decreasing the grain size (0.7 µm) increases ε_r and shifts the transition temperatures higher, even finer grain sizes (0.28 µm) show a decrease in permittivity and a smoothing of the peaks associated with phase transitions. The authors attribute this to changes in crystal structure in the ferroelectric phase and in the domain structure. McNeal *et al.* also studied the effect of grain size in $BaTiO_3$ and ceramic-polymer matrix composites and found a similar size dependence of properties [146].

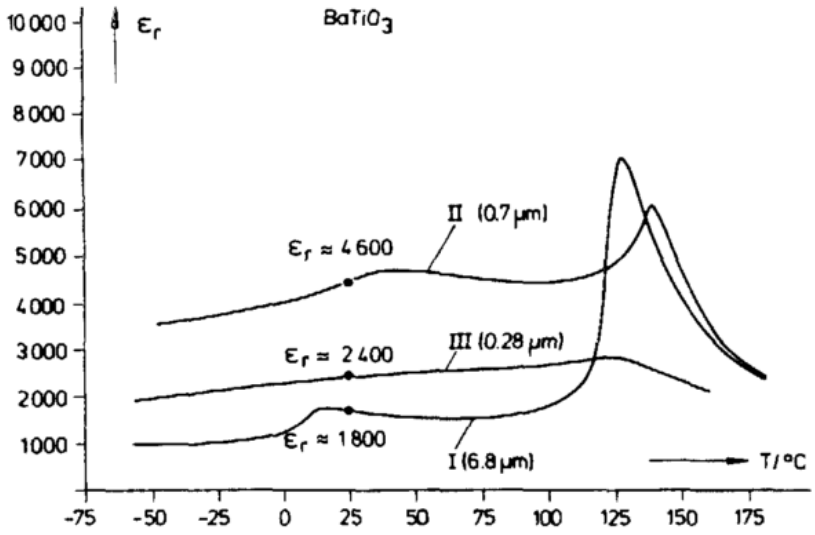

Figure 34: Temperature dependence of the relative permittivity of $BaTiO_3$ at grain sizes of (I)6.8µm, (II)0.8µm and (III) 0.28 µm [145].

However, grain size dependence has differing effects and is not present in all material systems. For example, in work by Ohata on alumina sintered at higher temperatures produces larger grain sizes and increase Qxf_e by ~300000 GHz but does not have a significant effect on ε_r or thermal stability [147].

Starting materials often contain low levels of impurities which in some cases can have a significant impact on sintering behaviour and final properties [14]. The effect of Fe_2O_3 and NiO on $(Zr_{0.8},Sn_{0.2})TiO_4$ was investigated by Wakino *et al.*. Adding just 0.5 wt.% Fe_2O_3 reduced the Qxf_0 from 7000 to 350 but for 0.5 wt.% NiO in conjunction with 0.5 wt.% Fe_2O_3, Qxf_0 remained relatively high (5000) [148]. This is

thought to be due to Ni ions supressing grain-growth and diffusion of Fe ions into the grains.

To prevent significant signal drift during operation and ensure communication systems are temperature stable, τ_f should be no more than ±2ppm/°C or 'near-zero' [125]. 'Tuning' is the term given to altering the τ_f to achieve a near-zero value; this is commonly achieved by mixing compounds with τ_f values of opposite sign [121], [149], [150]. Materials with high positive τ_f include TiO_2, $CaTiO_3$ and $SrTiO_2$ can be added to materials with negative τ_f to achieve a τ_f close to zero, these additions inevitably alter the permittivity and Quality factor, so the effects must be balanced [121], [125]. In complex perovskites, τ_f has been related to the tolerance factor (*t*) and the onset of octahedral tilt transitions, with cation substitution (used to alter the *t*) having a direct effect on the thermal stability [141], [151], [152].

2.6 Glasses

2.6.1 Structure of Inorganic Oxide Glasses

Glasses are often described as supercooled liquids, due to their lack of long-range order in the atomic structure. The amorphous structures of glasses are achieved by cooling between T_m and T_g sufficiently fast to avoid the nucleation and growth of crystalline structures (Figure 35) [153]. Conventionally, oxide glasses are produced by high temperature melting of precursors including oxides, carbonates and fluorides [153]. Other methods including sol-gel and pyrolysis have been used to decrease temperatures of manufacture and control composition.

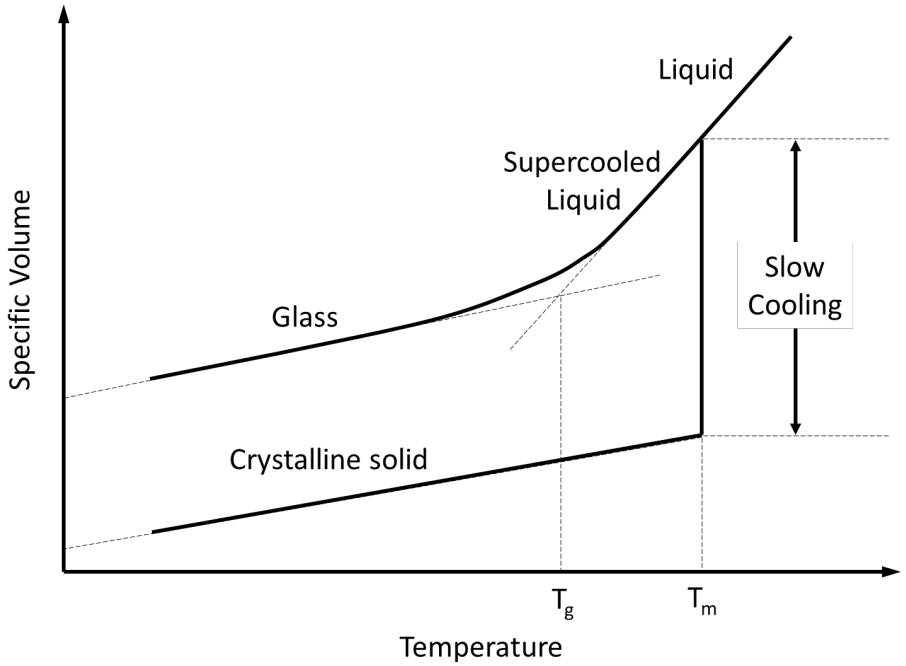

Figure 35: Schematic graph of specific volume vs. temperature of a glass, where Tg is the glass transition temperature and Tm is the melting temperature.

Glass compositions usually contain several different constituents, which depending on their electronic structure act either as network formers, modifiers, or intermediates. Network formers create a highly cross-linked, covalently bonded structure. Modifiers alter the network, bonding to oxygen and producing non-bridging oxygen, decreasing the *network connectivity* or degree of polymerization of the material. Intermediate ions, or conditional network formers can behave as both network formers and modifiers, depending on the composition of the glass. The network connectivity in glasses can be used to predict the reactivity, solubility, expansion coefficients and the likelihood of phase separation [153], [154].

Table 6: Behaviour of various cations in glass networks [155].

		Valence	M-O single bond strength
Network Formers	Si P B	4 5 3	106 88-111 119
Network Modifiers	Na Ca	1 2	20 32
Intermediates	Al Zr	3 4	53-67 61

Zachariasen's random network theory [156] details the required conditions for RO_2, R_2O_3 and R_2O_5 oxides to form a glass with a 3-dimensional network: Oxygen ions are not linked to more than 2 cations; coordination number of oxygen atoms around the cations is small; the corners of polyhedra are shared but not edges or faces and three or more polyhedral corners must be shared.

In pure SiO_2 all tetrahedra are connected in a 3D network with neighbouring tetrahedra *via* Si-O-Si bonds. The addition of network modifiers and intermediates to network formers alters the melt characteristic and physical properties; SiO_2 is chemically durable but requires high melting temperatures. Alkali oxide fluxes reduce melt viscosity and transition temperatures.

NMR spectroscopy can be used to characterize the structure of glasses, determining the local environment of constituents due to the presence of bridging oxygens. The speciation of the silicon within the glass can described by Si^n, where n is the number of bridging oxygens in the silica tetrahedra, as shown in Figure 36.

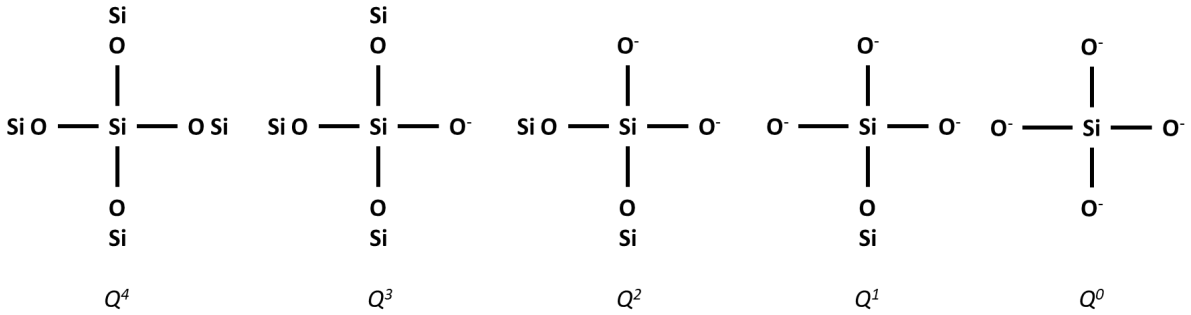

Figure 36: Q species of silica tetrahedra

Although Si^{4+} is the most common glass network former, other cations such as P^{5+} and B^{3+} can also form glasses. A similar notation can be used to describe phosphate tetrahedra as shown in Figure 37.

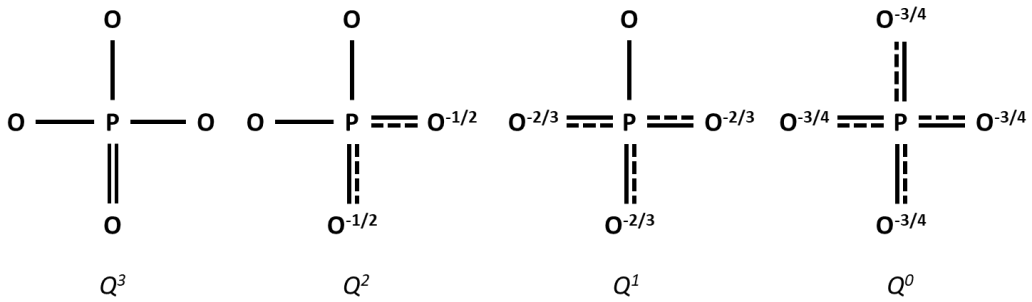

Figure 37: Q species of phosphate tetrahedra

2.6.2 Dissolution of Glasses and Its Potential Applications in Cold Sintering

Cold sintering of ceramics has been widely demonstrated and reported, although the technique could be applied to other material classes. The dissolution behaviour of glasses in a variety of conditions has been extensively investigated, especially for vitrified nuclear waste forms and bonding of optics required in extreme environments such as space.

The dissolution behaviour of glass is dependent on the composition of both the glass and solvent [157], [158]. As dissolution advances, the composition of the glass and solvent can change and alter dissolution behaviour; the leaching of alkali ions from multicomponent glasses into the solvent raises the pH and increases silica solubility [157]. Hench and Clark describe 5 classifications of glass dissolution behaviour, based on changes in surface and bulk composition and the development of films [158]:

Type I – Inert glasses which form limited hydration layers,
Type II – Durable glasses with a protective film,
Type III – Durable glasses with dual protective films,
Type IV – Glasses with a silica-rich film but poor durability,
Type V – Glasses that undergo total congruent dissolution.

The dissolution rate of quartz was investigated as a function of pH at 70°C by Knauss and Worley [159]. Up to ~pH 6, the dissolution rate was found to be independent of pH but above this value, dissolution rates increase with increasing pH due to increased influence of OH^- in the dissolution mechanism. The independence of dissolution rate is attributed to the breaking of Si-O bonds by water only [159].

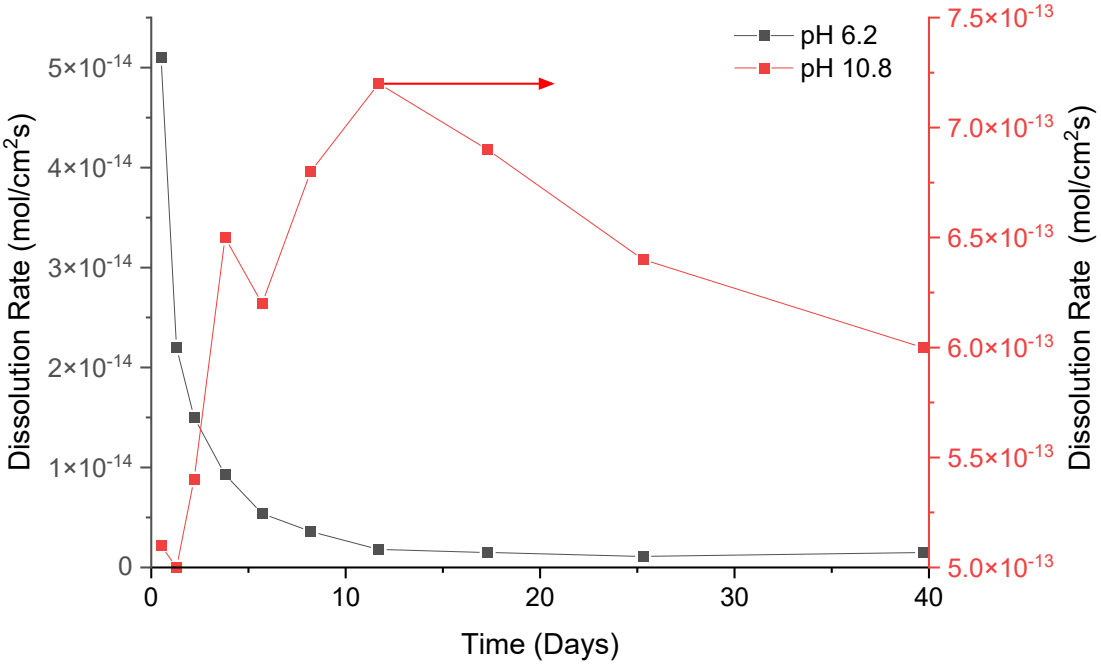

Figure 38: Dissolution rate of Quartz versus time at 70°C in aqueous, data plotted from Knauss and Worley [159]

There have been numerous studies on the dissolution of glasses with a variety of compositions for a wide range of applications. Whilst for most applications, highly durable glasses are required, glasses can be tailored to have specific dissolution characteristics. The controlled dissolution of glasses forms the basis for their use in biomedical applications and several glass processing techniques have been reported which utilise the partial solubility to achieve adhesion of bulk components or densification of powders. One of the key requirements for successfully cold sintering is the solubility of the material to be sintered in the transient solvent, or the decomposition of the transient phases during sintering.

Hydroxide catalysis bonding is a process first reported in 1998 (subsequently awarded a patent in 2001) that can be applied to the bonding oxide/oxidizable materials that are able to form silicate-like networks [160], [161]. In silica-based materials a three-step process of hydration, polymerisation and dehydration is observed [160]–[164]. During hydration, the hydroxide solution etches the surface and releases silicate ions:

$$SiO_2 + OH^- + 2H_2O \rightarrow Si(OH)_5^- \quad (9)$$

The release of silicate ions reduces the number of active OH^- ions in the bonding solution, decreasing the pH, and causing the disassociation of the silicate ions:

$$Si(OH)_5^- \rightarrow SiOH_4 + OH^- \quad (10)$$

Molecules of $SiOH_4$ then polymerize, forming siloxane chains and water:

$$2Si(OH)_4 \rightarrow (HO)_3SiOSi(OH)_3 + H_2O \quad (11)$$

The siloxane chains form the bond a rigid across the interface and during dehydration, the water evaporates or migrates away from the interface region. As dehydration progresses, siloxane forms a rigid 3D network and the strength of the bond increases. Heat treatments have also been shown to further increase the bond strength [164]

Producing amorphous silica usually requires significant temperatures, however a number of plants and marine organisms are able to form silica at very low temperatures through a series of polymerisation reactions [165]. A biologically inspired mechanism for the consolidation of silica at room temperature was outlined by Taveri *et al.* [166]. Slurries of silica were produced by adding distilled water or 0.5 mol NaOH to amorphous silica nanoparticles. The slurry was then placed into a leakproof, evacuating die, and subjected to pressure (450-600 MPa) for 5 minutes at room temperature. FTIR spectra of produced samples indicated the presence of a partially hydrated second phase after sintering. The mechanical properties achieved were reported to be comparable to sintered silica ceramics [166].

Ke *et al.* have developed a "Cold Isostatic Joining" process, inspired by hydroxide-catalysis bonding and the cold sintering process for the low-energy joining of bulk glass samples [167]. Solutions of NaOH (3-10 mol/l) were applied to the cleaned surfaces of fused silica disks and then the disks overlapped and placed into a cold isostatic press to control movement of the caustic solution. Samples were subjected to an isostatic pressure of 300MPa for 20 minutes at room temperature and dried at 60 °C for 24 hours and compared to a sample produced without pressure at room temperature (5mol/l) and a bulk fused silica sample. The shear strength of the joins initially improved with increased concentrations of NaOH, but decreases above 5mol/l. In line transmittance of a bulk sample (#8), samples produced using 5mol/l NaOH (#3 300MPa, 60°C and #7 pressure less, 25°C) are shown in Figure 39. The improved optical properties of #3 compared to #7 gives evidence for the importance of pressure in the removal of porosity and the extent of bonding between surfaces.

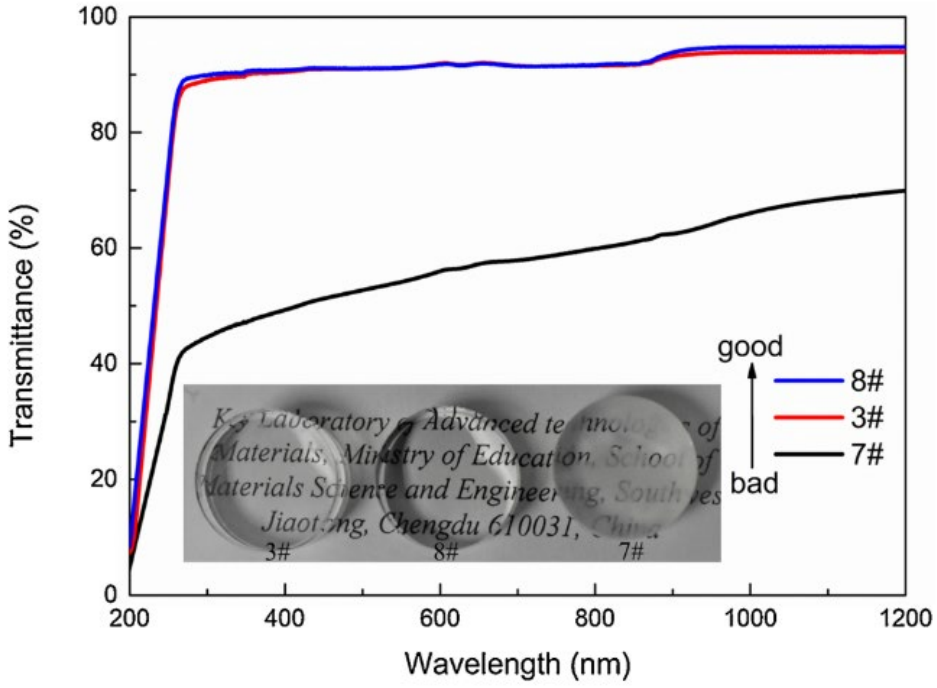

Figure 39: In line transmittance plots of 3#) a CIJ sample (300 MPa, 5 mol/l, 60°C), 7#) a pressure less cold joined sample 5 mol/l and 8#) a joint free bulk sample. All samples 8mm in thickness [167].

Hydrothermal sintering has also been shown to be applicable to silica [168], [169]. The role of water in hydrothermal sintering of silica was analysed by Ndayishimiye *et al.*, comparing the sintering properties of silica nanoparticles which are naturally hydrated due to absorbed water and after the addition of water. Increasing water content increases the relative densities achieved and contributes to changes in the sintered microstructure, the application of pressure causes mechanical-chemical effects such as increased dissolution, mass transport and precipitation which contributes to filling or porosity [168].

2.7 Bioglass

Bioactive glasses (bioglasses) were first developed by Hench and have seen significant study and development. Bioglass® 45S5 is the best known commercial biocompatible glass which is used to mimic normal bone and stimulate regrowth. Bioglasses are used extensively in a variety of clinical applications due to their high biocompatibility, bioactivity and easily tailored properties [170]. Bioglasses have silicate networks modified with sodium, phosphorous and calcium – the key compositional features of bioglasses are [171], [172]: lower than 60% SiO_2; higher Na_2O and CaO content, and high ratio of $CaO:P_2O_5$

Figure 40 shows the ternary compositional diagram of a glasses produced in the SiO_2-Na_2O-CaO system, with 6 wt.% P_2O_5 with corresponding reactivity/bone bonding levels. The viable compositions for a bioactive glass in this system are limited. Region I of Figure 40 show the range of compositions which achieve bone bonding. The reactivity in region II and III are too low and high respectively to bond to bone, whilst in region IV the SiO_2 content is too low to form a glass.

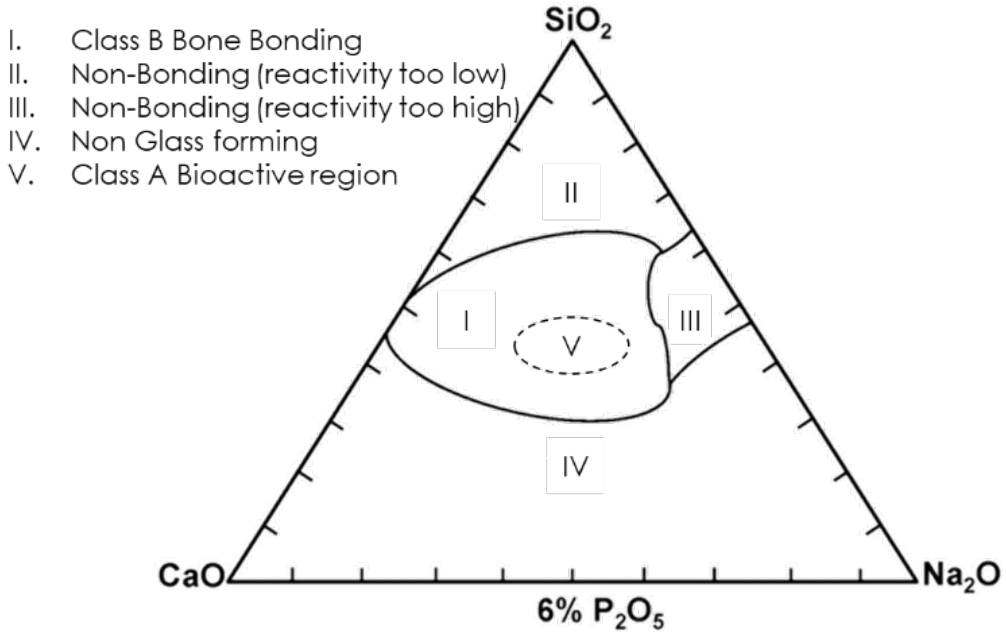

Figure 40: Ternary compositional diagram of the SiO_2-Na_2O-CaO system, with 6 wt.% P_2O_5 including bioactivity information.

Bioactivity is defined as conditions which elicit specific biological responses at materials interfaces. Bioactive materials are designed to be capable of forming interfacial bonds with surrounding tissues, and as such they can be used to improve implant fixation which in turn improves the expected lifetime of an implant [173], [174]. The surface active region in these bioactive materials has a composition similar to the mineral composition of bone tissues including calcium and phosphorus [172], [175]. The level of bioactivity of a material is measured by I_b the bioactivity index, which relates to the time taken (in days) for more than half of the interface to bond ($t_{0.5b}$) according to equation 12:

$$I_b = 100/t_{0.5b} \tag{12}$$

An I_b value between 0 and 8 indicates Class B bioactivity, when only osteo-conduction occurs and leads to bonding with bone but not soft tissues [176], [177]. Class A bioactivity is characterized by an I_b value over 8, inducing both osteo-induction

and osteo-stimulation leading to accelerated bone repair; Class A bioactive materials bond to both hard and soft tissues [176]–[178].

The composition of bio-active glasses must be tightly controlled; small deviations can prevent a glass from forming or completely alter the bioactivity. Additives act to change the network connectivity, reactivity, and the nature of dissolution products. The addition of less than 3 wt.% Al_2O_3 to Bioglass® 45S5 prevents bone bonding, a similar effect is also seen with the addition of Ta_2O_5, TiO_2, Sb_2O_3 and ZrO_2 [171], [172], [175]. Substantially increasing the proportion of P_2O_5 from 6 wt.% also prevents bone bonding [179]. Substituting 5-15 % B_2O_3 for SiO_2 increases the reactivity and using CaF_2 in place of CaO alters the surface activity and resistance to demineralization [175].

In vitro bioactivity is thought to be strongly influenced by network connectivity. Network connectivity is defined as the average number of bridging oxygens (BO) bound to network-forming cations and connect two network polyhedra [180]. Brauer *et al.* reported improved cell proliferation is seen in glasses with lower connectivity [153]. Most highly bioactive glasses have connectivity less than 2, with 45S5 having a network connectivity of 1.9, Eden *et al.* suggested the optimum network connectivity for bioactivity ranges between 2 and 2.6 [153], [154], [181]. More highly connected networks exhibit bioactivity due to the hydrolysis of the phosphorous-oxygen bonds [154]. Whilst network connectivity can give a good indication of bioactivity, the nature of network modifiers is not considered, and bioactivity is directly equated to dissolution. Glass dissolution is required for apatite formation, but the ions released such as Na^+ may not directly contribute to its formations.

Bioglasses can be created using a variety of methods including melt quenching, sol-gel and flame-spray pyrolysis, each method has its own advantages and disadvantages and can affect the network connectivity of the resulting glass [182]–[184]. Glasses have traditionally produced by melting at high temperatures in order to melt and react the reagents followed by shaping and cooling, the rate of which should be produced in order to limit the nucleation and growth of crystalline phases. Some bioactive glass compositions phase separate and crystallize.

Glass-ceramics are crystalline materials created *via* the devitrification of an amorphous glass. Whilst the mechanical properties of glass-ceramics are often superior to those of the parent glass, other properties such as solubility and bioactivity can be negatively affected. The dissolution of glasses is more uniform than glass-ceramics or

partially crystalline counterparts of the same composition [185]. Crystallization is known to reduce surface reactivity and therefore bioactivity of glass-ceramics compared to the parent glasses due to the decrease in Si-OH groups and the entrapment of Ca^{2+} ions by crystalline phases [186], [187]. In 45S5 based glass-ceramics, the rate of dissolution is significantly reduced and leads to the presence of remnant glass in the newly formed bone, a reduction in dissolution rate is also seen in A-W glass ceramics composed of an amorphous calcium-silicate phase with embedded apatite and wollastonite crystals [187], [188].

Whilst not suitable for forming larger components, sol-gel and flame spray pyrolysis methods of glass manufacture can be used to produce the desired compositions at lower temperatures. Organic precursors are reacted to create the desired composition, although attention must be paid to the removal of organics which could have a negative impact on the biological properties. The nano porous nature of sol-gel derived glasses created a far higher specific surface area, which due to the accelerated rate of ion release and increases in surface Si-OH groups display greater bioactivity [187]

The composition of Bioglass® 45S5 comprises a number of minerals found naturally in the body, Table 7 [176]. This modified composition creates a highly reactive surface when in contact with an aqueous medium [171], [172].

Table 7: Composition of Bioglass® 45S5 in wt.% [176]

	Wt.%
SiO_2	45.0
CaO	24.5
Na_2O	24.5
P_2O_5	6.0

When bioactive glasses are exposed to an aqueous solution, ion exchange of Ca^{2+} and Na^{+} with H^{+} and H_3O^{+} occurs rapidly, increasing the pH of the solution. A silica-CaO/P_2O_5-rich layer is formed, which within a few hours, mineralizes to form a layer of hydroxycarbonate. Hydroxyapatite is known to be both osteo-conductive and osteo-inductive, and the thickness of the layer increases with time and creates a "bonding zone" of up to 100μm [187]. *In vitro,* this hydroxycarbonate layer subsequently encourages the growth of bone after approximately 100 hours [175]–[177], [179], [189]–[192].

The surface reaction sequence shown in Table 8 is independent of the solution's composition. The rate of Si polymerization and formation of calcium phosphate is increased in the presence of Ca and P containing solutions such as simulated body fluid (SBF) [193].

Table 8: Stages of interfacial reactions occurring during the formation of bioactive glass bonding with bone [172], [174], [177], [179], [191]

Stage	Interfacial Reaction	Time (h)
1	Alkali ions exchange with hydrogen ions from body fluids	
2	Network dissolution and formation of SiOH bonds	
3	Silica-gel polymerization: SiOH + SiOH → Si–O–Si	1
4	Adsorption of amorphous Ca + PO_4 + CO_3	
5	Crystallization of the HCA layer	2
6	Biochemical adsorption of growth factors on HCA layer	10
7	Action of Macrophages	20
8	Attachment of stem cells	
9	Differentiation of stem cells	100
10	Generation of matrix	
11	Crystallisation of matrix	
12	Proliferation and growth of bone	

2.8 Materials for biomedical implants

All materials implanted into living tissues elicit some form of response and there are four categories of response: tissue death if the material is toxic; replacement of implanted tissue if the material is both non-toxic and soluble; formation of a fibrous tissue capsule if the materials is non-toxic and biologically inactive and formation of an interfacial bond if the material is non-toxic and biologically active [175], [179]

The human body is complex and creates a variety of environments, with pH of bodily fluids ranging from 1 to 9 and cyclic stresses applied to bones, joints and soft tissues [194]. Materials used therefore in biomedical implants should cause no adverse response in the tissues once implanted and have good wear and fatigue resistance and compatible mechanical properties with the surrounding tissues [195]. A variety of materials are used in biomedical application including metals, ceramics, polymers; coatings and composites thereof can be utilised to achieve optimal properties [194].

2.8.1 Bioactive glass and glass ceramic coatings

Titanium is used in biomedical implants due to its corrosion strength resistance, light weight and biocompatibility [196]–[199]. Without the application of a bioactive layer however, the bioinert implant does not bond to the surrounding bone, which can be detrimental to the fixation of the implant and the patient outcomes [198]. Hydroxyapatite ceramics and Bioactive glasses are often coated onto the surface of titanium implants in order to encourage bone bonding.

There are several challenges in creating bioactive coatings, such as the mismatch between the thermal expansion coefficient of substrate and coating materials. Commonly used materials are titanium and Bioglass® 45S5 with thermal expansions coefficient of 8.5-9 $x10^{-6}K^{-1}$ and 12.7-15.1 $x10^{-6}K^{-1}$ respectively [200][201]. Therefore, high degrees of control of the heating and cooling rates in implant manufacture to produce good quality coatings are required.

The dissolution rates and long-term stability of coatings is a key factor in design of both the composition and structure of the coating layers [200]. Plasma spray deposition is often employed to create hydroxyapatite coatings on titanium and this can lead to a number of issues, such as poor adherence, non-uniformity and control of the morphology and crystallinity [198], [202], [203].

The bonding of bioactive glasses and glass-ceramics involves a combination of physiochemistry and cell structure. Mechanical bonding arises from the interlocking of the materials at the interface due to surface roughness and is the basis of most traditional fixation methods. Subsequent ingrowth of bone to these crevices then provides permanent fixation between the implant and host bone [204]. The bond strength between bioactive materials and bone has been found to be greater than or equal to that of bone after 3-6 months and is attributed to the growth of nano-metric hydroxyapatite crystals which bond to collagen fibrils [173], [175]. The thickness of the bond has been found to be >100 μm after a few weeks and stabilizes after approximately 200-300 μm at six months [177].

2.8.2 Composites of Bioactive Ceramics, Glasses and Polymers

Bioactive ceramics and glasses exhibit good biocompatibility, compression and corrosion behaviours but suffer from brittleness and low fracture strength [182]. In contrast, polymeric materials have a wide range of physical characteristics are readily

processed into useful forms but are often too weak and flexible for some applications [170], [194]. Polymers used in biomedical applications should be either biodegradable with non-harmful products or non-biodegradable and durable such as polymethylmethacrylate (PMMA) used to fix implants [200]. The properties of synthetic biodegradable polymers (such as polylactic acid (PLA) and polyglycolic acid (PGA)) can be tailored and ideally the rate of resorption would allow a component to maintain function until the natural host material has completely healed [200].

Incorporating Bioglass into biodegradable polymers, such as polylactic acid can improve bioactivity and allow bone bonding of the material, Tsigkou *et al*. showed evidence for the formation of bone nodules after 14 days in culture for PDLLA/Bioglass composites [205], [206]. Composites of bioactive ceramic materials and biocompatible polymers are also produced to tailor mechanical properties [200]. These composites are produced by embedding bioactive materials into the polymer substrate, or by creating the desired structure and coating it, as shown in Figure 41.

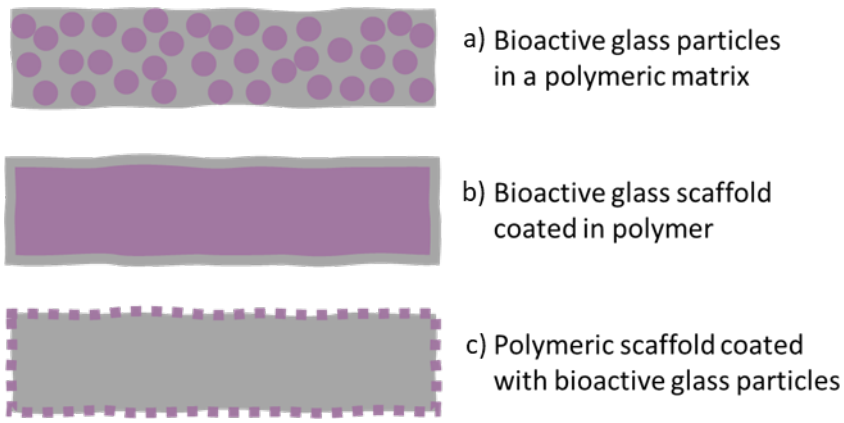

Figure 41: Schematic diagram showing several structural methods of combining polymers and bioactive glass particles [170].

Several methods for creating Bioglass/polymer composites have been reported in the literature. These include processes which produce samples with Bioglass embedded in a polymer matrix and coatings on solid and foam samples of polymer. When bioactive glass particles are used as a filler phase within a polymer matrix, they increase the stiffness of the polymer; at high volume fractions of HA particles in PE a number of researchers have shown brittle behaviour [207]. The application of the polymers onto a bioactive glass scaffold can improve toughness and compliance. The bioactive potential is sometimes reduced in composites, as the bioactive glass phase is not in direct contact with the surrounding media [207]. If the polymer and bioactive glass interfacial bond is weak, this will compromise the improvements in mechanical strength [208]. Some methods to produce composites are relatively simple and utilise

distilled/deionised water or the mixing of a polymer melt with powdered Bioglass. Other methods use a variety of organic solvents or require a complex experimental set up.

Work to create surgical sutures coated in bioactive glass by Stamboulis *et al*. encased Vicryl® sutures in powdered Bioglass and pressed at 100 and 160 MPa for 5 minutes [209]. Figure 42 shows the sutures before and after this process, while this method has creating a coating on the suture materials, the authors acknowledge that the structure and thickness of the coating is not uniform. Coated sutures were found to have a lower tensile strength than uncoated sutures, but to maintain a slightly higher proportion of tensile strength over time than uncoated samples. A slurry coating technique was also developed by the same group, where 47 wt.% Bioglass powder was placed in distilled water and magnetically stirred to prevent settling. Sutures were then placed into the "slurry" for three minutes before being carefully removed [210]. This method improved uniformity of the coating's structure and thickness, producing a stable coating. Figure 42 shows SEM micrographs of the suture materials before and after coating by the methods mentioned above.

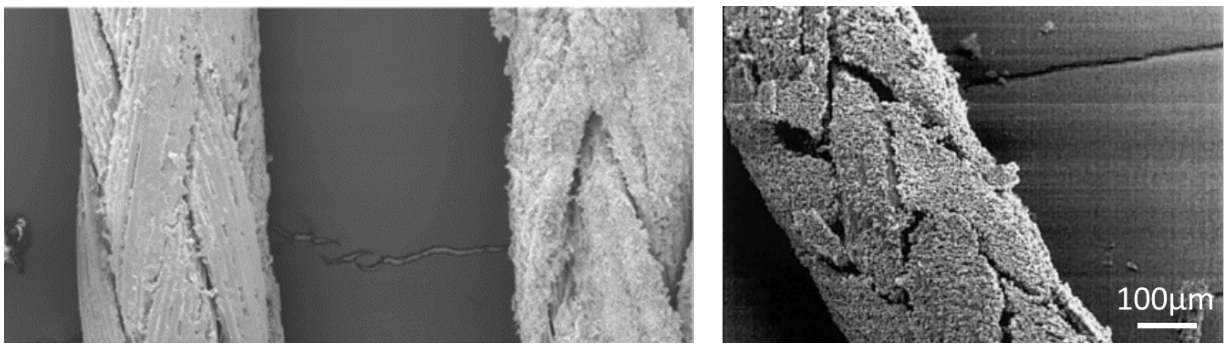

Figure 42: SEM micrograph of bioresorbable sutures as received (left) and after coating with Bioglass via dry-pressing (middle) and slurry dipping (right). From Stamboulis et al. and Boccaccini et al [209], [210]

A similar slurry-based technique was used by Roether *et al*. and compared to an electrophoretic deposition method. Distilled and deionised water was mixed with 42 wt.% Bioglass and placed in a EPD cell with the foam to be coated placed between stainless steel electrodes as shown in Figure 43 [211] The foam sample contained large tubular pores, which were oriented perpendicular to the surface of the electrode during EPD. The authors found that greater control of thickness and uniformity was achieved *via* the slurry dipping method and the polymer pore structure was maintained.

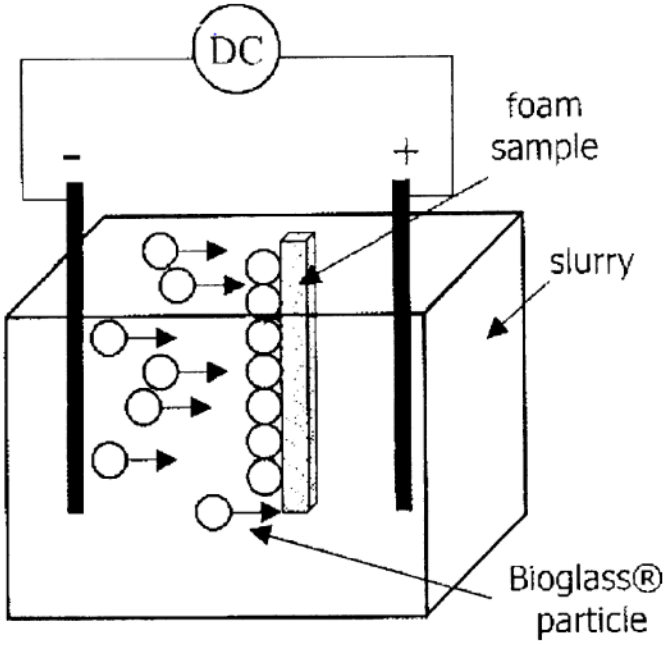

Figure 43: EPD cell used by Roether et. al to create Bioglass coated PDLLA foam composites [212].

Thermally induced phase separation (TIPS) is a commonly used method to produce polymers [213]–[219]. TIPS makes use of binary polymer-solvent or ternary polymer-solvent, non-solvent mixtures and their immiscibilty at low temperatures to produce polymeric foam structures. At high termperatures, a homogeneous polymer solution exists, as the temperatures is a lowered, a multiphase material is created, with regions of high and low polymer concentration. The rate of cooling between temperatures on the binodal and spinodal curves (Figure 44) can be used to control the structure and volume of pores in the material. A metastable region exists between the binodal and spinodal curves where the nucleation and growth mechanisms are slow and produce large pores. Below the spinodal curve seperation is quick and forms a network of small interconnected pores [217], [219].

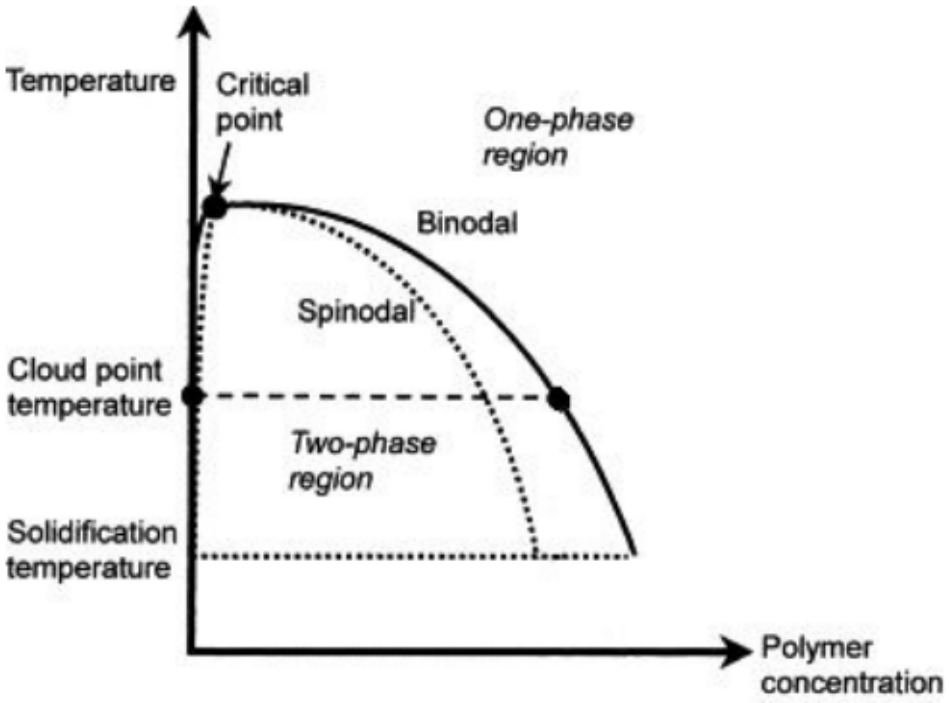

Figure 44: Phase diagram of a ternary system consisting of a polymer, solvent and non-solvent [217].

The use of TIPS to create highly porous PLGA foams with Bioglass embedded in the polymer matrix has been reported a number of times [213]–[218]. The polymer was dissolved in DMC (Dimethyl carbonate) and mixed with 5-50 wt.% Bioglass *via* sonication. The mixture is then cooled to -196 °C in liquid nitrogen and held at -10 °C to sublime the solvent and placed in a room temperature vacuum oven to completely dry [215], [216].

The advantages of for manufacturing composite porous scaffolds *via* TIPS reported by Boccaccini *et al.* are: the control over the volume, shape, size and orientation of porosity in the final component; the applicability of the technique to a wide variety of polymers; reproducibility and the ability to incorporate materials into the polymeric matrix [216].

PDLLA composites containing 5 and 40 wt.% 45S5 Bioglass were produced by Tsigkou *et al*., using chloroform to dissolve the PDLLA, before stirring for 2-3 hours and adding the Bioglass powder [206]. The solution was then pipetted onto a glass disc and dried at room temperature.

2.8.3 Biocompatibility, Bioactivity and Cytotoxicity

The biocompatibility of a material is its ability to perform with an "appropriate response in a specific application" [220]. Biocompatible materials do not elicit a toxic or immune response and are often examined using cell-cultures and dead/alive assays or assessing metabolic activity [220]. Prior to the clinical use of biomaterials within the human body, a series of *in vitro* and *in vivo* tests are performed to ensure components exhibit sufficient biocompatibility and bioactivity.

The *in vivo* bioactivity of materials is commonly related to the formation of apatite in simulated body fluid (SBF). A review by Zadpoor analysed the results of 33 studies which compared the *in vitro* to *in vivo* behaviour of a range of biomaterials (including glasses, ceramics and composites) [221]. In 8 of the 33 studies the *in vivo* performance was not correctly predicted by the *in vitro* results, with 5 of the 8 displaying better than expected bioactivity *in vitro* and 3 studies demonstrated hydroxyapatite formation *in vitro* but not *in vivo* [221]. The difference in *in vivo* behaviour has been attributed to chemical, biological and topographical mechanisms which cannot be easily replicated *in vitro* [221], [222]. Therefore, whilst monitoring the *in vitro* formation of hydroxyapatite is a simple way to assess the bioactivity of materials pre-clinical and clinical trials are required to ensure a beneficial response is elicited by implanted materials.

Material toxicity manifests itself in a number of ways including the presence of dead and dying tissues [223]. Cell cultures are especially sensitive to cytotoxicity caused by this change in pH and often overestimate the potential response seen in a complex organism such as the human body, where such effects would be buffered effectively by fluid movement [223], [224]. When bioglasses are subjected to aqueous media, there is significant exchange of alkali ions, which is found to increase the pH of the interfacial regions creating highly alkali regions. This can have a significant impact on *in vitro* cell viability tests for Bioglass, which when tested *in vivo* shows no evidence of toxicity [177], [178], [223], [224]. *In vitro* studies of the effect of bioactive glasses on cell behaviour therefore utilise a 'pre-conditioning' step. Pre-conditioning allows for the dissolutions of alkali ions which reduces the pH change observed during cell cultures, reducing cyto-toxicity [224]. Pryce *et al*. demonstrated the reduced change in pH of simulated body fluid caused by the addition of Bioglass powders (45S5 and 58S) subjected to pre-conditioning (Figure 45) [224]. There are several pre-conditioning methods which are used depending on the chemistries and morphologies of the materials [224].

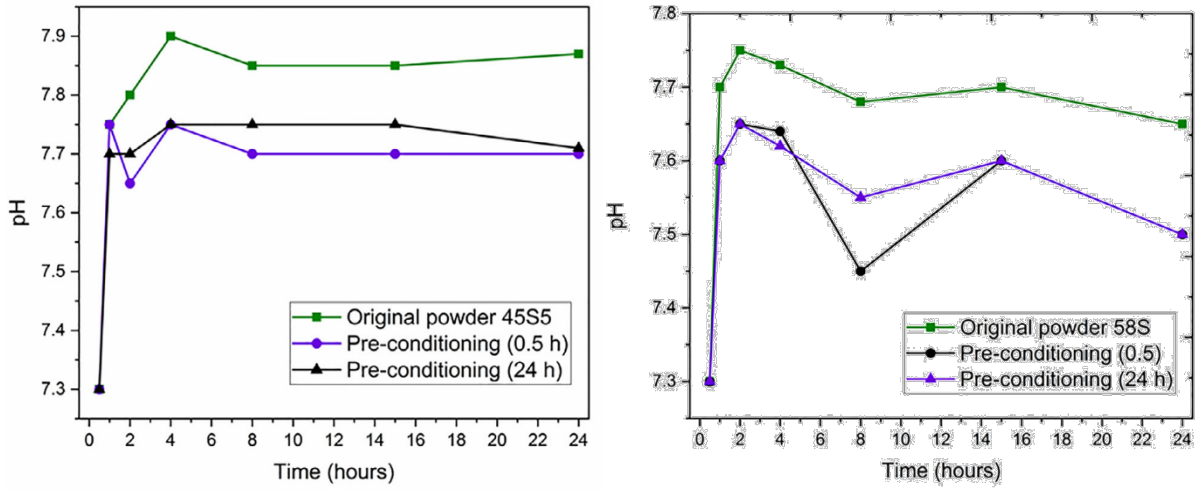

Figure 45: pH variation of SBF containing bioactive glasses (45S5 and 58S composition)

Tsigkou *et al*. created composites of PDLLA and 45S5 Bioglass (0, 5 and 40 wt.%) and pre-conditioned them in DMEM-F12 medium before biocompatibility testing. The composite containing 40 wt.% Bioglass significantly increased the pH in the first 24 hours (Figure 46). After the first 24 hours, none of the composites was found to further increase the pH of the surrounding media [206].

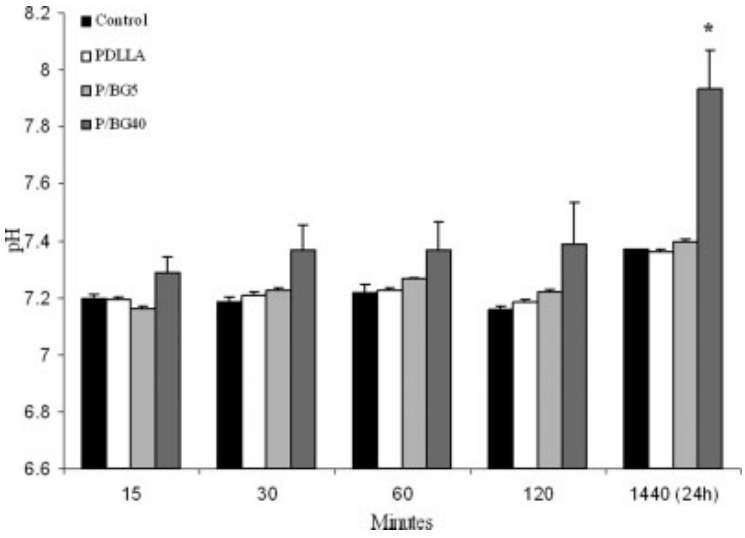

Figure 46 pH of DMEM-F12 medium with addition of PDLLA, and PDLLA/Bioglass composites after incubation at 37°C. DMEM-F12 medium used as control. [206]

The response of human foetal osteoblasts to PDLLA and 45S5 Bioglass composites produced using chloroform (0, 5 and 40 wt.%) was investigated by Tsigkou *et al.*. Live/Dead assays carried out on cell cultures after 6 days showed over 90% cell viability, indicating that the composite films are not cytotoxic. The metabolic activity of the composites was initially reduced compare to the control sample, but after 14

days the metabolic activity on all control and composite surface was found to be similar [206].

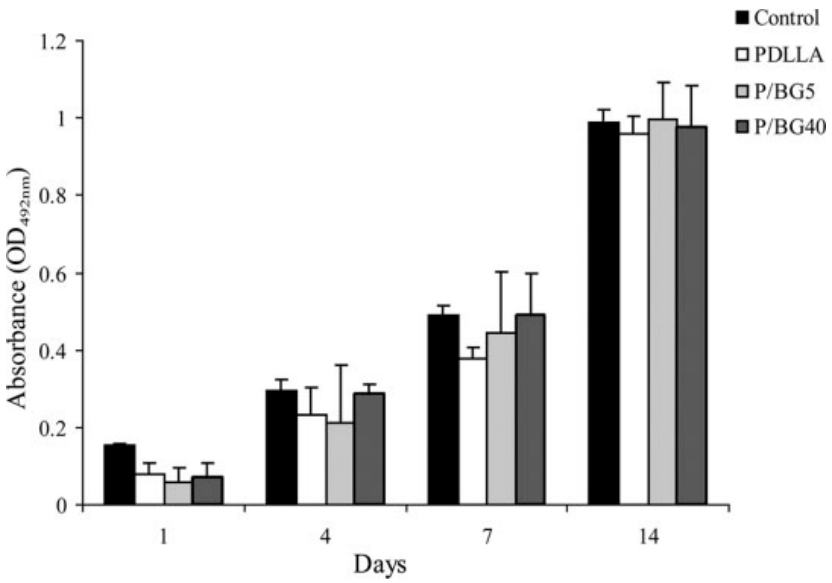

Figure 47: Cultured cell metabolic activity on cell culture plastic (control), PDLLA and PDLLA/Bioglass composites measured by MTS assay [206].

Testing of polyethylene-Bioglass composites by Huang *et al*. found no evidence of leaching of toxic materials during 24hr emersion. Samples were 1cm^2 and 1µm thick and had been polished and cleaned in an ultrasonic ethanol bath before testing [205]..

The cytotoxicity of polyethylene-Bioglass composites with up to 40 vol.% *via in vitro* cell cultures at 37°C for 24hr was also tested. No cytotoxic effect was observed and high viability in primary human osteoblast-like cells in Bioglass containing composites was observed compared to polyethylene polymer samples. The formation of hydroxyapatite was observed in thin films of the same composites when immersed in SBF, the XRD spectra in Figure 48 shows the development of crystalline apatite over 4 weeks [205].

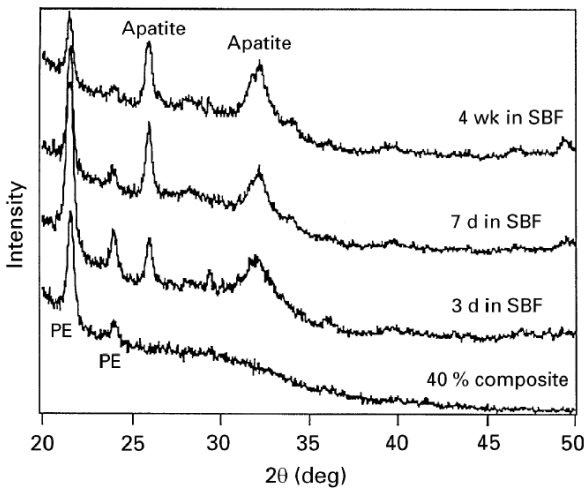

Figure 48: Thin film XRD of HDPE-40%Bioglass composites after immersion in SBF

The reactivity of bioactive glasses can be controlled particle size. Nano-are more reactive than micro-particles due to a higher surface area able to interact with body fluid [170]. The cytotoxicity of nano- and micron-sized Bioglass powder in solution at different concentrations was investigated by Rismanchian *et al.*. They indicate that the cytotoxicity of nano- and micro-powder is similar at low concentrations during the 48-hour test, whilst at ≥5 mg/ml nano powder is more cytotoxic. However, the Si-Ca-P compositions of the glass powders used in their experiments were not consistent, with the nano powder containing significantly more silicon and phosphorous and less calcium which was not addressed in the study, but could reduce cytotoxicity [225].

3 Experimental methods

3.1 Materials

3.1.1 Johnson Matthey Silicate Frit - JM5430F

JM5430F powder was produced at Johnson Matthey by grinding a melt-derived frit. The weighed raw materials in the correct ratios, mixed, heated in a ceramic crucible to 1400 °C, and maintained at 1400 °C for 1 hour before being quenched in water. The resultant coarse glass frit was collected and milled in water and then dried to achieve a d50 particle size around 5-10 μm. The composition is commercially confidential but approximate proportions of the constituent oxides is given in Table 9.

Table 9: Composition of JM5430F in weight percent

Oxide	Wt. %
SiO_2	30-60
ZnO	5-25
B_2O_3	5-15
TiO_2	0-10
Li_2O	0-5
Al_2O_3	0-5

3.1.2 Bioglass® 45S5

Bioglass powders were produced by Johnson Matthey *via* Flame Spray Pyrolysis. The reagents initially used in the precursor solution (1 molar) for FSP synthesis were:

Na 2 -ethylehexanoate
Hexamethylsdisiloxane (HDMSO)
Ca 2-ethylhexanoate
Tributyl Phosphate
Xylene
2-Ethylhexanoic acid (2-eha)

Subsequent powder batches replaced xylene with methanol/ethanol and Ca 2-ethylhexanoate with Ca acetate hydrate. The replacement of xylene reduced the

residual carbon in the FSP powder and Ca acetate hydrate is a significantly cheaper reagent. The final composition was not significantly affected, and materials behaved in a similar fashion during cold sintering.

3.2 Cold and Conventional Sintering of Pellets

3.2.1 Conventional Sintering

Pellets for conventional sintering were pressed using a Specac Uniaxial press, using a 10mm ø die. Samples were placed in an alumina crucible and heated to the sintering temperatures given in Table 10 at 5 °C/min and held for 4 hours before cooling to room temperature at a maximum rate of 5 °C/min.

Table 10: Conventional Sintering Temperatures

Material	**Temperature / °C**
Li_2MoO_4	540
JM5430F	500-600

3.2.2 Cold Sintering

Material to be cold sintered was first weighed and mixed with the appropriate amount of transient solvent in a pestle and mortar. The moistened powder was then placed into a steel die and placed into a Specac Uniaxial press, fitted with heating platens.

The parameters of cold sintering vary depending on the chemistry of the materials to be sintered. The cold sintering of lithium molybdate has been reported in the literature and therefore 10 wt.% distilled water was used in the sintering of pellets [58], [67], [68]. JM5430F and Bioglass have not previously been cold sintered and therefore a considerable number of trials were performed with varying solvent amounts in order to find the optimum conditions for cold sintering. Acetic acid was chosen for cold sintering of JM5430F as the materials is known to be susceptible to dissolution in acidic environments.

Table 11: Cold sintering parameters for pellets.

Powder Material	Solvent	Solvent Amount / wt.%	Temperature / °C	Pressure / MPa	Time / mins
Li_2MoO_4	Distilled water	10	120	250	60
JM5430F	Acetic acid (1mol)	36-57	100-180 then 250	250	10-30 then 60
Bioglass	Distilled water	80	100	250	30-60

3.3 Cold and conventional sintering of lithium molybdate onto glass substrates

An organic slurry of lithium molybdate was initially produced based on the composition reported by Baker *et al*. in Table 12 and mixed using a speed mixer at 1800 rpm for 5 minutes [2]. The resulting slurry was too viscous to be screen printed so the formula was altered by the addition of EGD.

Table 12: Lithium molybdate slurry formulation

		Wt.%	
		From [2]	This work
Lithium molybdate (LMO)		66	52.28
Ethylene glycol diacetate (EGD)		11	29.61
Benzyl Butyl Phthalate (BBP)		0.9	0.71
Printing Vehicle	QPAC40	3.3	2.61
	EGD	18.7	14.79

The ceramic slurry was deposited on the substrate via screen printing (DEK247 Screen Printer) with a squeegee pressure of 3 tonnes, each layer consisted of two passes of the squeegee followed by drying at 120°C for 15 minutes before subsequent layers are applied to create a sample of desired thickness.

The organic binder was burnt out at 300 °C with a dwell time of 6 hours, leaving a green layer of lithium molybdate. The LMO layer was then densified *via* two methods, conventional sintering (540°C for 2 hours) or cold sintering with the addition of distilled water.

Wetting of screen-printed samples for cold sintering was initially performed by producing water vapour in a sealed beaker at 40°C in a similar fashion to the paper by Baker *et al.* [57]. However, this method caused water droplets to form at the edges of

the printed area and produced an uneven water distribution. Therefore, to achieve better distribution, distilled water was sprayed over the samples using an atomizer. Due to the layer of LMO being very thin and to prevent the transfer of the wetted layer to the die during pressing, a sheet of non-stick silicone coated paper was placed between the printed layer and the die.

EPMA of the glass substrates after pressing at room and elevated temperatures were performed and Johnsons Matthey and information on the exact equipment and variables used is not available.

3.4 Cold sintering of JM5430F onto steel

Cold sintering of JM5430F onto steel substrates was performed by placing the putty-like mixture of JM5430F and acetic acid directly onto the substrate within a steel die. A sheet or disk of PTFE was then placed on top of the coating material before the upper die plunger. The sample was then sintered as for standard pellets, with applied pressures 55-250 MPa.

3.5 Pellet Dimension and Density

The Archimedes principle could not be used to calculate density due to the potential solubility of materials. Therefore, the pellet was weighed using a laboratory balance and a pair of digital callipers (accuracy ±0.005 mm) was used to measure thickness and diameter of each pellet. In order to reduce potential measurement error. measurements were taken at 3 points in each dimension and averaged. Density was calculated using the mass and volume of the samples according to Equation (13.

$$Density\ (\rho) = \frac{mass\ (g)}{Volume\ (cm^3)} \tag{13}$$

3.6 Particle Size analysis

Particle size of JM5430F and PLA was determined using a Mastersizer 3000 with a Hydro EV liquid dispersion unit, which uses laser diffraction to calculate particle size. Powder was placed into a 600ml beaker of distilled water and the dip-in sampling head lowered into the liquid. The liquid-powder mixture was then stirred at 3000 rpm before

sampling to reduce agglomeration and fully disperse the powder. Ten sampling cycles were then performed to achieve an average particle size.

Due to the solubility of Bioglass in water, a dry dispersion unit (Mastersizer 3000 Aero) was utilised to obtain particle size. Ten sampling cycles were then performed to achieve an average particle size.

3.7 Scanning Electron Microscopy

Scanning Electron Microscopy (SEM) was performed on both raw materials and sintered products to investigate particle size, grain structure, general microstructure, and differences in composition where appropriate.

Powdered materials were prepared for SEM by placing a small amount of powder onto a double-sided carbon sticky pad mounted on an aluminium stub, excess was removed using pressurised air.

Sintered pellet samples were prepared such that the face and fracture surface could be analysed under SEM. Sample faces were polished with SiC paper of increasingly fine grit size (P800, P1200, P2500, P4000). Samples were ground without liquid due to the potential for interactions between cold sintered samples and water. After grinding, samples were split in half to provide a fracture surface.

Bioglass-PLA composites imaged after cytotoxicity testing were not ground in order to preserve any surface phases that may have developed during testing. These samples were dried overnight in an oven (50°C) before mounting both face and fracture surface samples onto an SEM stub using double-sided carbon sticky tabs.

Mounted samples were coated with a conductive gold layer to avoid charging of the sample and allow Energy Dispersive Spectroscopy (EDS) to be performed. Samples were examined using an Inspect F (FEI, Hillsboro, Oregon, USA) SEM operating with spot sizes of 3.0-5.0 and 5-20 kV, depending on the sample.

3.8 Electrical Characterisation

3.8.1 LCR Measurements

LCR measurements were taken using an Agilent Precision LCR Meter. Readings were taken at 1kHz, 10kHz, 100kHz, 250kHz and 1MHz, every minute over a temperature sweep at 1°C/min from room temperature to 400°C.

Samples were prepared by polishing the flat surfaces of the pellet, before applying a gold coating *via* sputtering. Sputter coating was performed in an Agar Manual Sputter Coater AGB7340, for 5 minutes at 30 mA on each side. Prior to sputter coating, tape was applied to the sides of samples to prevent them from being coating and a short circuit being created. Prepared samples were then placed into an in-house manufactured jig and attached to the LCR meter *via* platinum wires. The jig is placed within a small conventional tube furnace to perform the temperature sweep.

3.8.2 Impedance Measurements

An Agilent Precision LCR Meter was used to take impedance measurements of all samples. Readings were taken at set temperatures over a frequency sweep between 20 Hz and 1 MHz. The temperature range for all readings were between room temperature and ~400°C, with measurement taken at smaller temperature intervals between 200 and 400°C.

The samples were prepared in precisely the same manner used for LCR measurements, above.

3.9 Structural Characterisation

3.9.1 X-Ray Diffraction

X-Ray diffraction (XRD) was used to analyse powder and bulk samples after cold and conventional sintering. In amorphous materials, diffractogram show diffuse scattering and leading a characteristic "amorphous hump" in the spectra, XRD was used in cold-sintered glass samples to evaluate any crystallisation occurring during processing. For Bioglass composite samples that had been left in a moist environment, XRD was used to identify the nature of thin crystallites which developed on the surface.

Diffraction data were obtained using a Bruker D2 Phaser (Karlsruhe, Germany) in Bragg-Brentano geometry with a Cu K_α radiation source (λ = 1.5408 Å), with 2.5 ° Soller slits and a 1 mm divergence slit at 30 kV and 10 mA. Data were collected across the 2θ range of 20 to 60°.

Pellet samples were mounted in Bruker PMMA holders using Apiezon putty and to avoid height displacement errors, the surface flattened in line with the top of the holder with a glass slide. Powder samples were placed into a zero background holder and pressed using a glass slide to ensure the specimen height was level with the holder.

3.9.2 Raman Spectroscopy

Raman spectroscopy was performed using a Renishaw inVia Raman Microscope. Spectra were acquired with a range 50-4000 cm^{-1}, laser power 100%.

3.9.3 NMR

Nuclear Magentic Resonance (NMR) spectroscopy is a technique which provides information of the chemical environment of nuclei from their electromagnetic properties. Nuclei have associated intrinsic spin, I, which produces a nuclear magnetic moment, μ_I [226]:

$$\mu_{I=\frac{g_I e\hbar I}{2m_p}}$$

Where g is a constant, the Landé splitting factor, e is the charge of an electron in coulombs, $\hbar$ is the reduced Planck's constant and m_p is the mass of a proton. The quantum states in which a magnetic moment exists is dependent on the orientation of a static applied magnetic field, B_o. The component of the spin vector parallel to the applied field in each quantum state is equal to $m\hbar$ where m is a value between $-I$ and $+I$ [226].

NMR Spectroscopy was performed at Warwick University, studying ^{29}Si and ^{31}P species within on Bioglass samples at various stages of the cold sintering process, to understand how the connectivity of silicon and phosphorus species changes within the material. Material was tested in the as received condition, after mixing with distilled water and after cold sintering.

The ^{29}Si MAS (Magic Angle Spinning) NMR data used in this study were acquired at 7.05 T using a using a Varian-Chemagnetics Infinity Plus-300 spectrometer operating at a ^{29}Si and ^{1}H Larmor frequencies (vo) of 59.6 and 300.13 MHz, respectively. Both single pulse (Bloch decay) 29Si MAS NMR and 1H-29Si CPMAS NMR experiments were performed using a Bruker 7 mm HX (dual channel) probe which enabled a MAS frequency of 5 kHz to be implemented. The 29Si pulse length calibration was performed on solid kaolinite ($Al_2O_3 \cdot 2SiO_2 \cdot 2H_2O$) from which a π/2 pulse time of 4.5 μs was measured. All single pulse ^{29}Si MAS NMR data were measured with a π/4 pulse time of 2.25 μs, a recycle delay of 240 s and a ^{1}H decoupling field of 80 kHz during data acquisition. The corresponding 29Si CPMAS NMR measurements were undertaken using an initial ^{1}H π/3 pulse time of 3 μs, a ^{1}H-^{29}Si contact duration of 5 ms, a recycle delay of 20 s and a ^{1}H decoupling field of 80 kHz during data acquisition. All reported ^{29}Si chemical shifts were externally referenced against the IUPAC recommended primary reference of Me_4Si (1% in $CDCl_3$, δ_{iso} = 0.0 ppm) *via* the secondary solid kaolinite reference (δ_{iso} = -92 ppm).[227]

The accompanying single pulse ^{31}P MAS NMR and ^{1}H-^{31}P CPMAS NMR data were acquired at 11.7 T using a Bruker Avance III-500 spectrometer operating at the ^{31}P and ^{1}H Larmor frequencies (v0) of 202.4 MHz and 500.13 MHz, respectively. These experiments were undertaken using a Bruker 3.2 mm HX (dual channel) probe which enabled a MAS frequency of 20 kHz to be implemented. The ^{31}P pulse length calibration was performed on solid ammonium dihydrogen phosphate ($(NH_4)H_2PO_4$) from which a π/2 pulse time of 3 μs was measured. All single pulse ^{31}P MAS NMR measurements were undertaken using a π/3 pulse time of 2 μs, a recycle delay of 45 s and a 1H decoupling field of 100 kHz during data acquisition, while the corresponding ^{1}H-^{31}P CPMAS NMR data were measured using an initial ^{1}H π/2 pulse length of 3 μs, a ^{1}H-^{31}P contact duration of 5 ms (consisting of a CP ramp from 50 - 100 %), a recycle delay of 10 s and a ^{1}H decoupling field of 100 kHz during data acquisition. The reported ^{31}P chemical shifts were externally referenced against the IUPAC recommended primary reference of 85% H_3PO_4 (δ^{iso} = 0.0 ppm) *via* the secondary solid $(NH_4)H_2PO_4$ reference (δ_{iso} = 0.99 ppm). [227]

Errors in the calculation of the intensity of each species from the MAS in NMR is usually 5-10 % and has been taken to be 10% in this work.

3.10 Cytotoxicity

All cell culture work was performed in Class II laminar flow hoods (Esco), which were sterilised prior to use with 70 % industrial methylated spirit (IMS) (Thermo Fisher Scientific). Incubation took place at 37 °C in 5 % CO_2.

Human osteosarcoma cells (MG-63) from passages 15 to 20 were used and cultured in Minimum Essential Medium Eagle - Alpha Modification (αMEM) with supplements as described in Table 13. Cells cultured in an incubator in T75 flasks (VWR), with passages occurring at least once weekly. When cells were over 80 % confluent, media was removed and cells were washed with phosphate buffered saline (PBS) (Oxoid), and then Trypsin-EDTA (Sigma-Aldrich) at a concentration of 5 mg/ml trypsin and 2 mg/ml EDTA was added. Cells were then incubated in Trypsin-EDTA until detachment, supplemented αMEM was subsequently added to deactivate the trypsin. Cells were centrifuged for 5 minutes at 1000 rpm, the media discarded, and the pellet resuspended in fresh medium. Cell counts took place using a haemocytometer (Hawksley) and cells divided into flasks as required.

Table 13: The composition of medium used for the cytotoxicity testing.

Solution	Concentration
Minimum Essential Medium Eagle - Alpha Modification (Sigma-Aldrich)	88 %
Foetal calf serum (Biosera)	10 %
L-glutamine (Sigma-Aldrich)	0.01 mg/ml
Penicillin/streptomycin	100 µg/ml
Non-essential amino acids	1 %

Bioglass samples were sterilised by placing in 70 % ethanol for 1 hour and rinsing in sterile PBS three times. Samples were then incubated for 7 days in fully supplemented αMEM, with a change of media on day 3. Samples were incubated on a Bibby Scientific rocking plate set at 45 rpm for 4 hours to ensure mixing of the new medium.

MG-63s cells were seeded into a 6 well plate at 5.2 x 10^3 cells per cm^2. A transwell insert with a 0.4 µm membrane was inserted into the well. The Bioglass was removed from the medium, washed thrice with sterile PBS, and placed into the inserts. Medium was then added to cover the Bioglass. Transwells without Bioglass were used as tissue culture plastic (TCP) controls. Transwells and Bioglass were also added to wells with no cells for normalisation.

Resazurin reduction assays were used to measure metabolic activity, resazurin sodium salt was dissolved in distilled water at a concentration of 251 µg/ml and sterilised with a 0.2 µm filter. This was stored at 4 °C, protected from light, for up to two weeks. Before each experiment, the stock solution was diluted 1 in 10 in media.

After incubation for 24, 72 and 168 hours, the transwells containing the Bioglass were moved and washed with PBS. The MG-63s were imaged using a phase contrast microscope (Motic AE2000), then the media was removed, wells washed with PBS twice and resazurin added to the wells followed by incubating for 4 hours. Samples of the resazurin media were then read in a fluorescence plate reader.

Values from wells containing no cells were subtracted from the other values to leave a no cell value of 0 and values were then normalised to the control wells on day 1. Prism 7 (GraphPad) was used to perform all statistical analysis, unless otherwise stated. Statistical significance was defined as $P \leq 0.05$. Standard deviation (SD) was used for all error bars. Statistical significance was determined using two-way analysis of variance (ANOVA) tests, with Dunnett's multiple comparison tests used to determine the significance between each Bioglass group and the control.

4 Lithium Molybdate

4.1 Introduction

Lithium molybdate (Li_2MoO_4, LMO) was one of the first materials to be used to demonstrate the densification of ceramics *via* the cold sintering method [18], [29], [66]–[68]. As a material which congruently dissolves in water, it is readily densified with the addition of a small amount of liquid (2-10 wt.%) and the application of pressure, as demonstrated by Kahari *et al.* [67], [68], [228]. Their research indicated that the application of pressure was the key driver for densification, with post processing heat treatments having minimal effect on density but nonetheless improving Qf values [68].

This chapter aims to cold sinter lithium molybdate and compare and contrast the resultant properties with post cold sintering, heat treated and conventionally sintered samples. As discussed in sections 2.3.6 and 2.3.7, cold sintering can be utilised to create a wide range of composites that allow for compositional design not easily achieved by conventional methods, thereby facilitating tailoring of properties [83]–[85], [100], [101]. This will be further illustrated through the fabrication of lithium molybdate - bismuth molybdate composites. In addition, low processing temperatures in cold sintering allow integration with dissimilar materials such as metals, glass, and polymers. Screen printing and cold sintering are therefore, used to demonstrate the ability to deposit dense layers of lithium molybdate on glass substrates.

4.2 Cold and Conventional sintering of LMO

Figure 49 shows SEM of as-bought lithium molybdate. The particles are of an irregular morphology and there is a broad size range, 25-100μm.

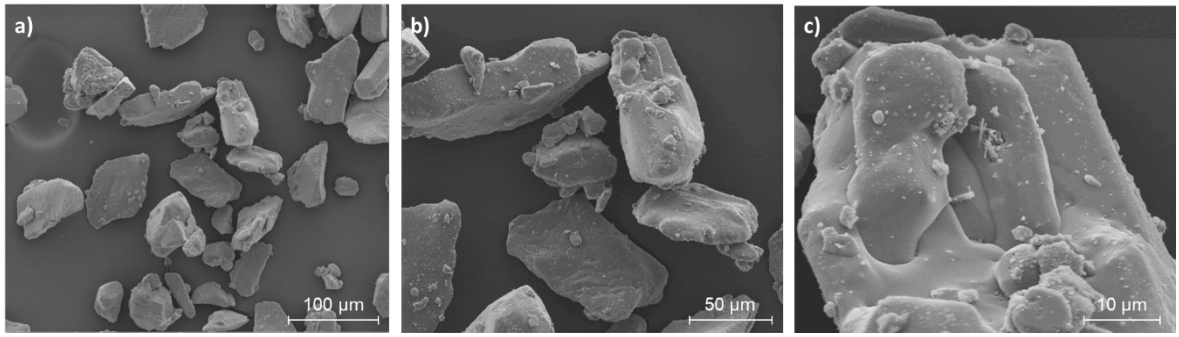

Figure 49: SEM of as bought lithium molybdate (Alfa Aesar)

Table 14 gives some representative values of sample densities produced *via* conventional and cold sintering. Lithium molybdate readily cold sinters to consistently produce pellets with a density of >90 % of the theoretical density (3.03 g/cm^3), whereas conventionally sintered pellets achieve various relative densities from 70 to 90 % [68], [78], [228]. Using attrition milled powder with a smaller particle size (<15 μm) shown in Figure 59, improved density of both conventional and cold sintered samples.

Table 14: Comparison of densities achieved by conventional and sintering with a) as bought powder and b) milled powder with <100 μm.

		Mass / g	Density / gcm^{-3}	Relative Density / %
1 [a]	Conventionally Sintered 540°C 4 h	4.88	2.40	79.2
		1.94	2.40	79.0
2 [a]	Cold Sintered 120°C 1 h	4.53	2.83	93.2
		1.78	2.78	91.6
3 [a]	Cold Sintered with 540°C, 4 h Heat Treatment	4.53	2.76	91.0
		1.80	2.76	91.1
4 [b]	Conventionally Sintered 540°C 4 h	0.63	2.75	90.7
		0.33	2.76	91.1
5 [b]	Cold Sintered 120°C 1 h	0.52	2.94	96.9

SEM of internal fracture surfaces of cold and conventionally sintered pellets are shown in Figure 50. A difference in porosity between conventional (a) and cold sintered (c) samples is evident. During cold sintering, some of the lithium molybdate dissolves into the distilled water, filling voids between larger particles and is then precipitated at the sintering temperature, leading to improved densification. In the conventionally

sintered samples, the temperatures are sufficient for significant grain growth and a final microstructure consisting of large grains is seen (Figure 50b). In contrast, the microstructure of the cold sintering sample consists predominantly of grains, similar in size and morphology to the starting powder surrounded by finer grains (Figure 50d).

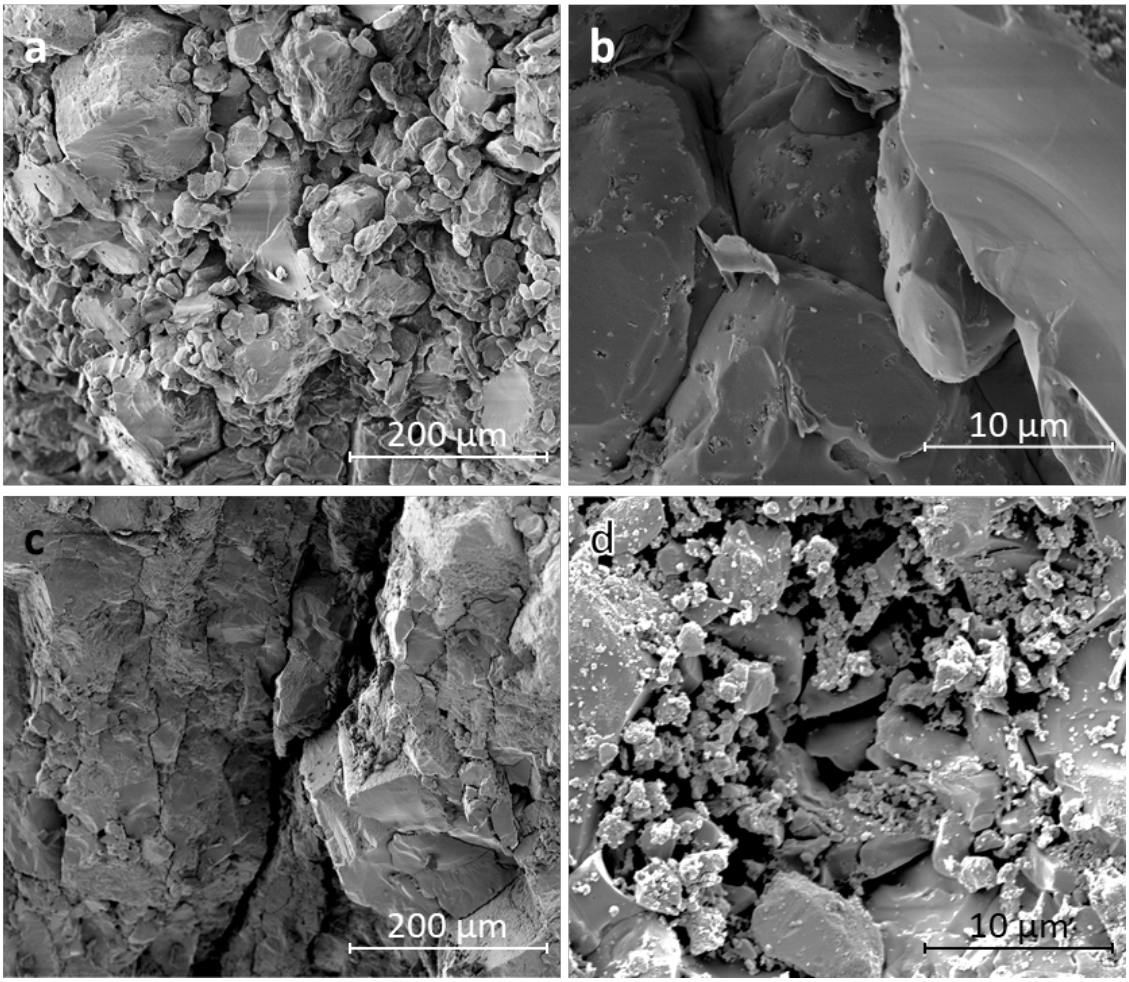

Figure 50: SEM of conventional (a, b) and cold (c, d) sintered lithium molybdate

X-Ray diffractogram of conventional and cold-sintered lithium molybdate are shown in Figure 51. All peaks in the diffraction profile may be indexed as lithium molybdate and have been normalised to the (220) peak at ~24.8°. No peaks from secondary phases are observed. The ratio of the (211) peak at ~ 21.1° to the (220) peak, however, is inconsistent between the cold and conventional samples. In cold sintered samples, there is very limited grain growth due to the low temperature, leading to samples having a high number of small, randomly oriented particles. In conventionally sintered samples, the (211) is overexpressed, indicating a significant grain growth and preferred orientation within the pellets.

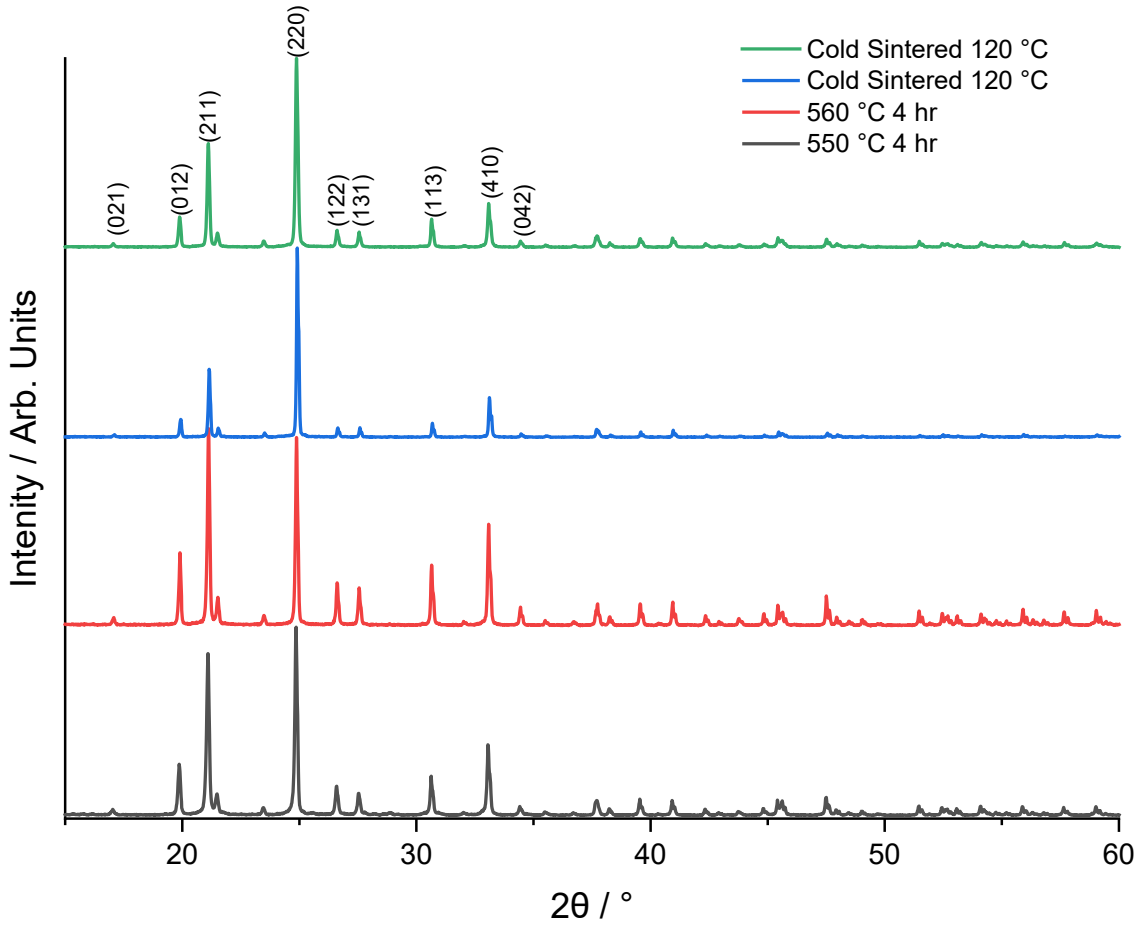

Figure 51: XRD of conventionally and cold-sintered lithium molybdate

Room temperature Raman spectra for lithium molybdate samples produced by cold sintering and cold sintering followed by a 4-hour heat treatment at 540 °C are shown in Figure 52 and Figure 53. Figure 52 shows the spectral regions 50-500 and 750-1000 cm^{-1}, which are the main regions of interest for lithim molybdate. The Raman shifts are in agreement with each other, and those reported in the literature for conventially and cold sintered LMO, indicating that the structure of lithium molybdate remains unaltered during the cold sintering process [229], [230].

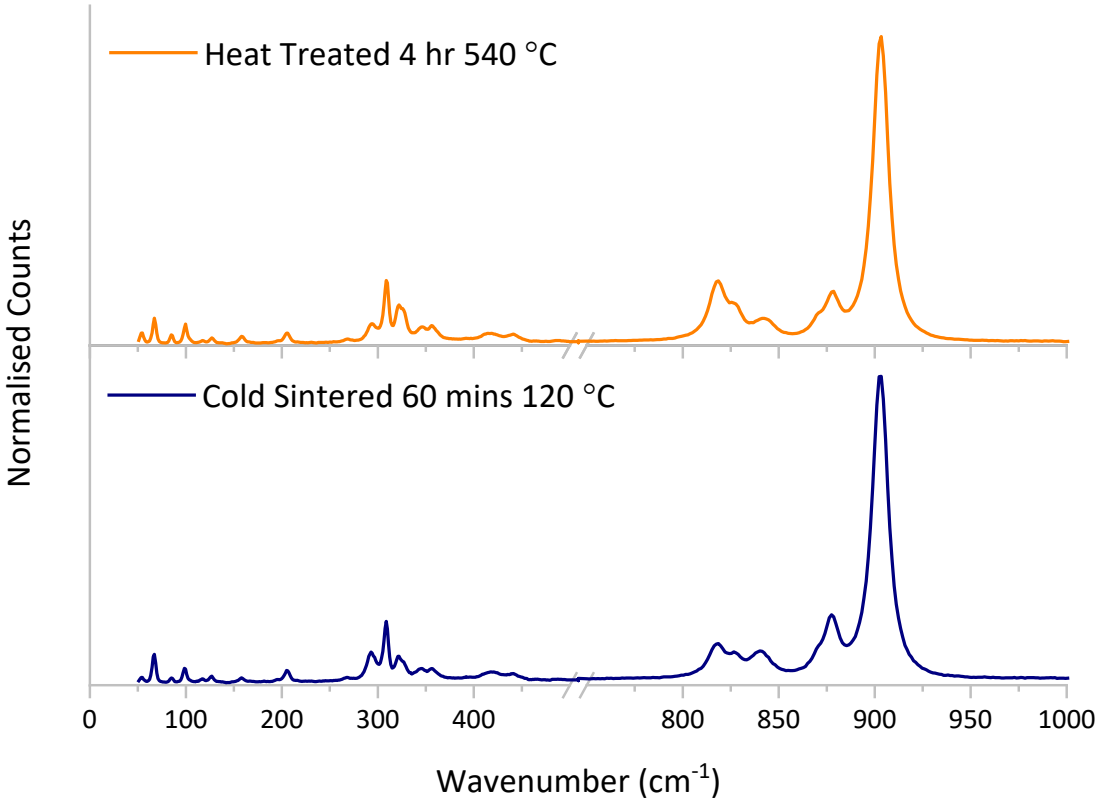

Figure 52: Raman spectra of Li2MoO4 after cold sintering and cold sintering with a post processing heat treatement at 540 °C, showing modes in the ranges 0-500 and 700-1000 cm -1

Kahari *et al.* attributed an improvement in Q_f values of samples produced *via* room temperature pressing of moist LMO powders followed by heat treatment to the removal of residual water [68], [228]. The Raman spectra of water shows a large, broad peak between approximately 2800 and 3800 cm^{-1} [231], [232]. No such peak is observed in Figure 53, which reveals the Raman spectra of cold sintered and cold sintered heat-treated samples from 50-4000 cm^{-1}, indicating that no detectable water is retained in lithium molybdate after cold sintering at 120 °C, nor after heat treatment. It is therefore likely that other factors are responsible for the change in Qf reported by Kahari *et al.*, such as increased grain size with increasing temperature of heat treatment, or the formation of a small volume fraction of smaller, possibly amorphous, grains in as-cold sintered ceramics at grain boundaries which are subsequently removed or crystallised during heat treatment.

Maria *et al.* suggested that using higher water content may lead to the formation of hydrated lithium oxide phases when cold sintering at 100 °C [58]. Gorelik *et al.* report that LiOH and $LiOH{\cdot}H_2O$ display a number of Raman shifts at lower frequencies, with significant peaks at ~193, 328 and 1090 cm^{-1} [233]. These peaks are not observed in the Raman spectra presented in Figure 52 and Figure 53, indicating

that hydrated lithium phases are not present or occur in such low volumes as to be undetectable.

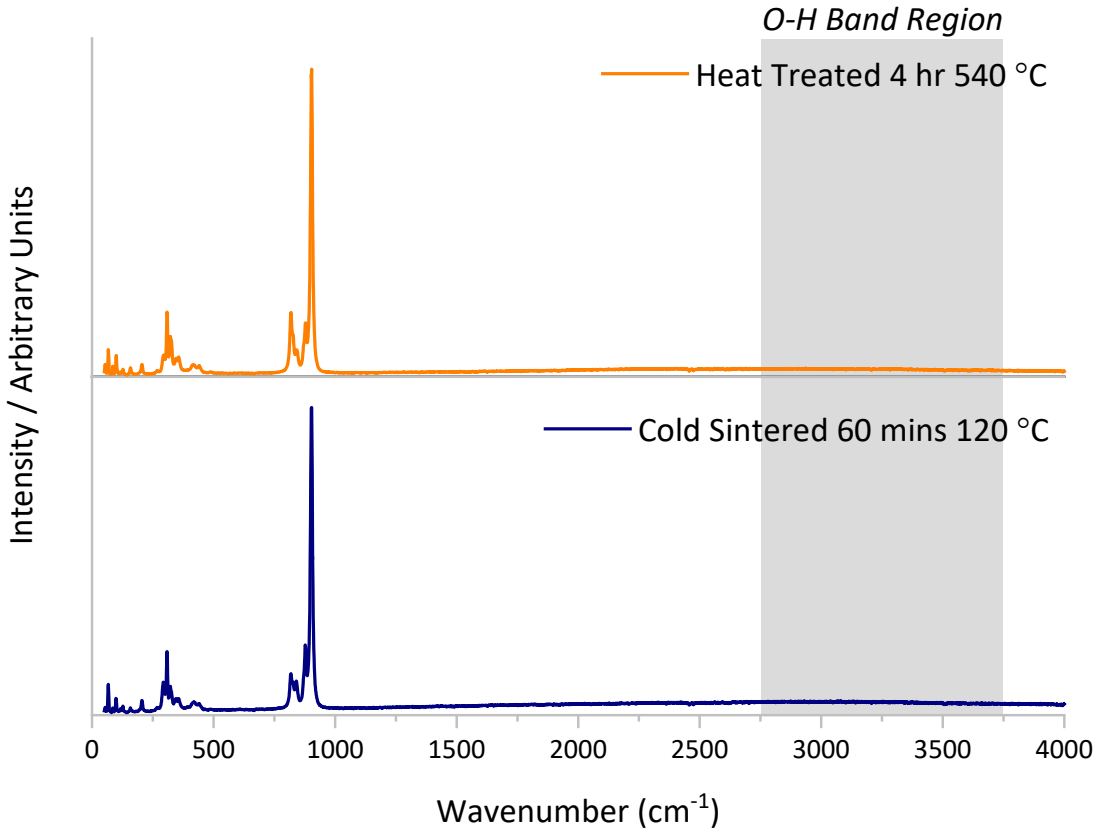

Figure 53: Raman spectra of Li2MoO4 after cold sintering and cold sintering with a post processing heat treatement at 540 °C in the range 0-4000 cm $^{-1}$

TEM and SAD of cold sintered lithium molybdate are shown Figure 56. The ring patterns observed in the SAD of the region shown in Figure 56c indicate the presence of highly disordered/amorphous material in the grain boundary regions between particles. X-Ray diffraction of the same cold sintered samples do not show the characteristic diffuse scattering hump expected within an amorphous material, indicating that the volume fraction of amorphous material is very low and not likely to occur at all interfaces. Work by Guo *et al.* on the cold sintering of sodium molybdate ($Na_2Mo_2O_7$) also observed the presence of a highly disordered intergranular phase at some interfaces, with most grain boundaries appearing abrupt without an intergranular phase [234]. These intergranular phases are likely to be the result of the short sintering time and low sintering temperatures utilised in cold sintering, which do not allow for full recrystallisation of the material that is dissolved and precipitated onto the particle surfaces.

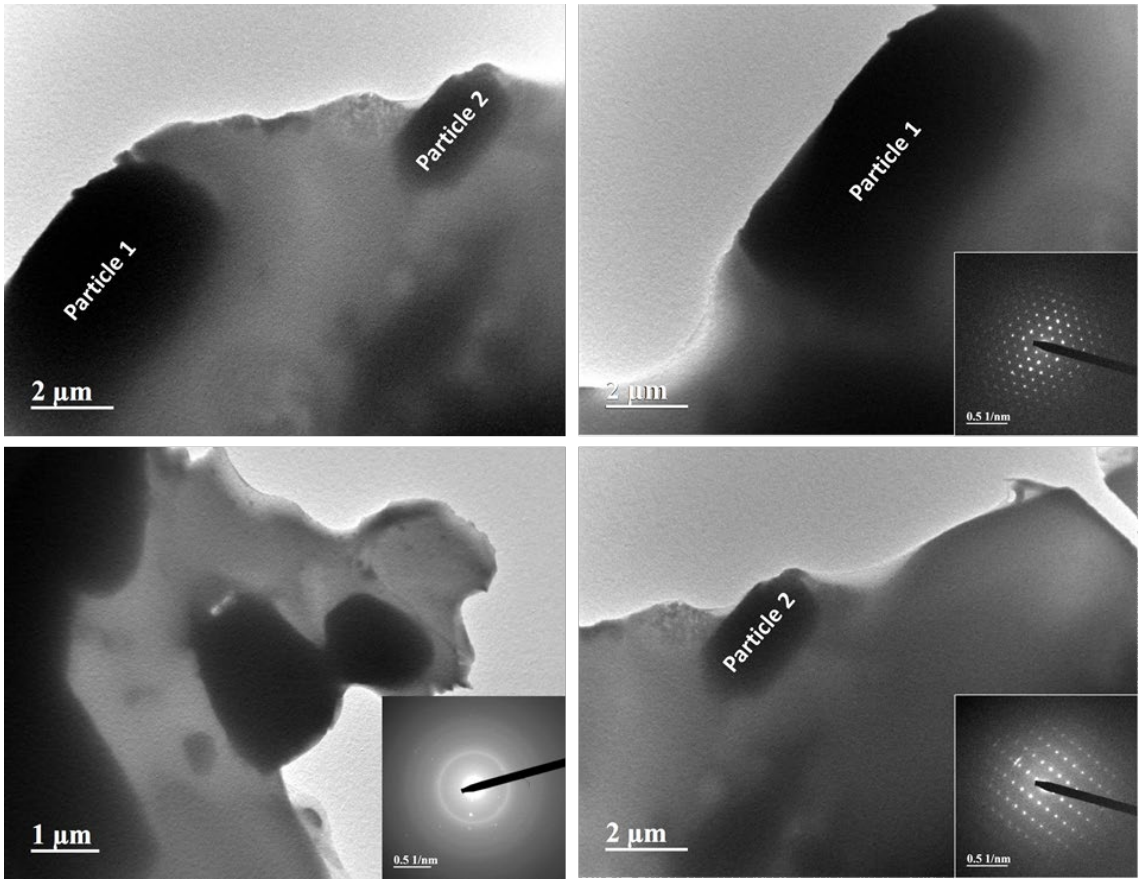

Figure 54: SAD-DF of cold sintered lithium molybdate

Secondary grain boundary phases have also been observed in the cold sintering of materials such as $BaTiO_3$ and $SrTiO_3$ which dissolve incongruently in water and are therefore, mixed with a hydrothermal processing inspired solvent [65], [92], [95]. TEM of "hydrothermally assisted" cold sintered barium titanate showed a significant amount of amorphous grain boundary material, which is then crystallised during a heat treatment at 700–900 °c (approximately 300-500 °C below conventional processing temperatures).

The ability to create dense ceramics at low temperatures during cold sintering is significant for several industries. Whilst the presence of secondary/amorphous phases at grain boundaries may be deleterious to electrical properties, in both lithium and sodium molybdate they are present at few grain boundaries and are unlikely to cause a significant effect. In materials where secondary phases are more common, annealing heat treatments can reduce their prevalence and therefore improve properties.

A combination of cold sintering followed by heat treatment could also be used to tailor material properties. Combining a low temperature sintering technique which

retains a grain size similar to that of the starting materials, with heat treatments to encourage controlled grain growth (and recrystallization where required) could enable the production of microstructures which are unfeasible *via* conventional methods.

4.3 Cold Sintered Ceramic-Ceramic Composites

Bismuth molybdate ($Bi_2Mo_2O_9$) is a dielectric ceramic with a conventional sintering temperature of 620-650 °C and a theoretical density of approximately 6.5 g/cm^3 [235]–[237]. Ceramic composites of lithium molybdate and bismuth molybdate (0, 20, 40, 50 and 100 wt.%) were produced *via* cold sintering using 10 wt.% distilled water added to the powder, 250 MPa and 150 °C for 30 mins. Pellets were then placed in a drying oven at 120 °C overnight to ensure all moisture had been removed. The measured, calculated theoretical density and relative densities as a function of composition are shown in Table 15.

Table 15: LMO-BMO composite compositions, including measured, theoretical and relative denstiy.

Composition	Measured Density g/cm^3	Theoretical Density g/cm^3	Relative %
LMO	2.82	3.03	93.1
0.8LMO-0.2BMO	2.68	3.39	79.0
0.6LMO-0.4BMO	2.52	3.85	65.4
0.5LMO-0.5BMO	2.44	4.14	59.0
BMO	1.99	6.51	30.6

As the bismuth molybdate concentration increases, the pellet density decreases, despite the higher theoretical density of BMO. The low relative density of "cold-sintered" bismuth molybdate implies that very little densification occurs within this end member of the composite. Compared to lithium molybdate, bismuth molybdate is much less soluble in water and is therefore likely to contribute less to the cold sintering process.

XRD spectra of LMO-BMO composites are shown in Figure 55. The cold-sintered bismuth molybdate displays the diffuse scattering expected of an amorphous material, this was also seen in the raw powder prior to cold sintering. It is likely that prolonged storage of the powder prior to use has led to the formation of an oxygen deficient phase, which has been reported as amorphous [238]. Spectra for cold sintered composites with 0-50 wt.% BMO are as expected for lithium molybdate and the

amorphous bismuth molybdate spectra contributes to slightly higher "background" scattering in composites with higher BMO concentration.

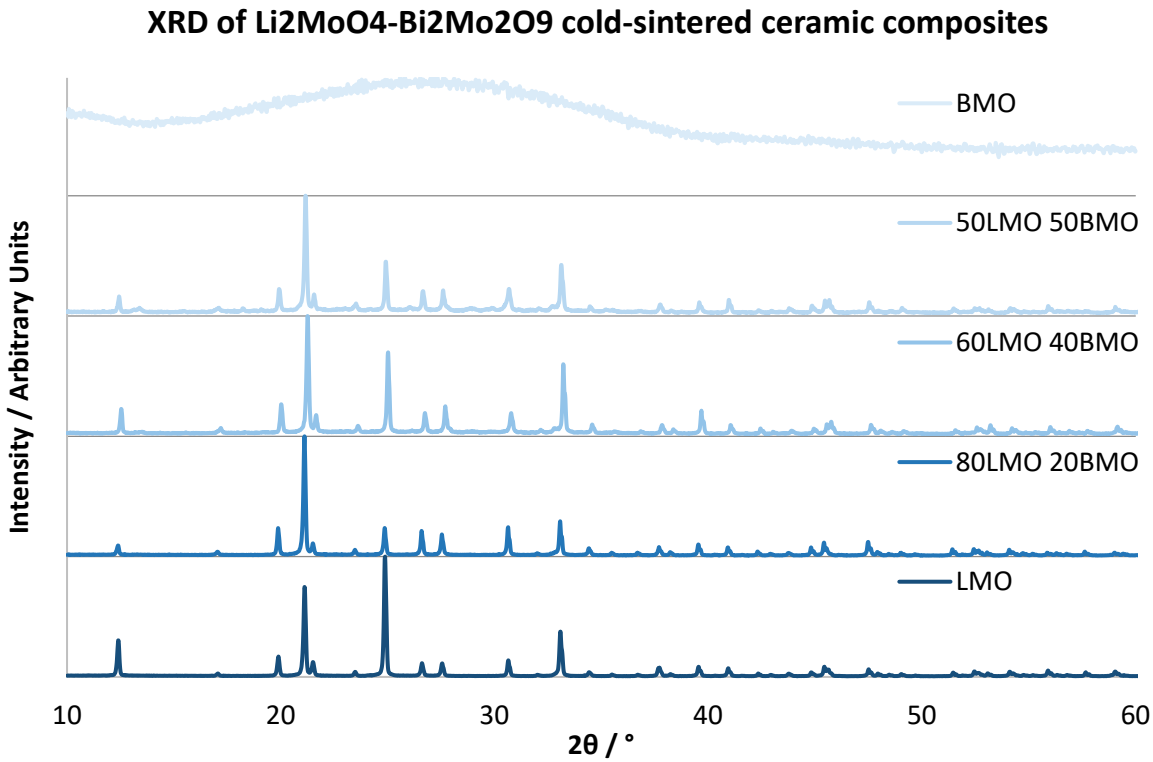

Figure 55: XRD spectra of lithium molybdate, bismuth molybdate and their composites.

Figure 56 and Figure 57 show SEM of ceramic-ceramic composite pellet surfaces and reveals that the two phases remain discrete in all samples. Larger lithium molybdate grains are surrounded by smaller bismuth molybdate particles which are well distributed throughout the composite pellets. Lithium molybdate grains appear lighter in Figure 56 and Figure 57, with darker grains of bismuth molybdate. The surface of cold sintered pellets depends on the surface finish of the dies which may contribute to the porosity observed on the surface of all samples. Due to the moisture sensitive nature of lithium molybdate, all polishing is performed without water and therefore, several surface scratches are still present.

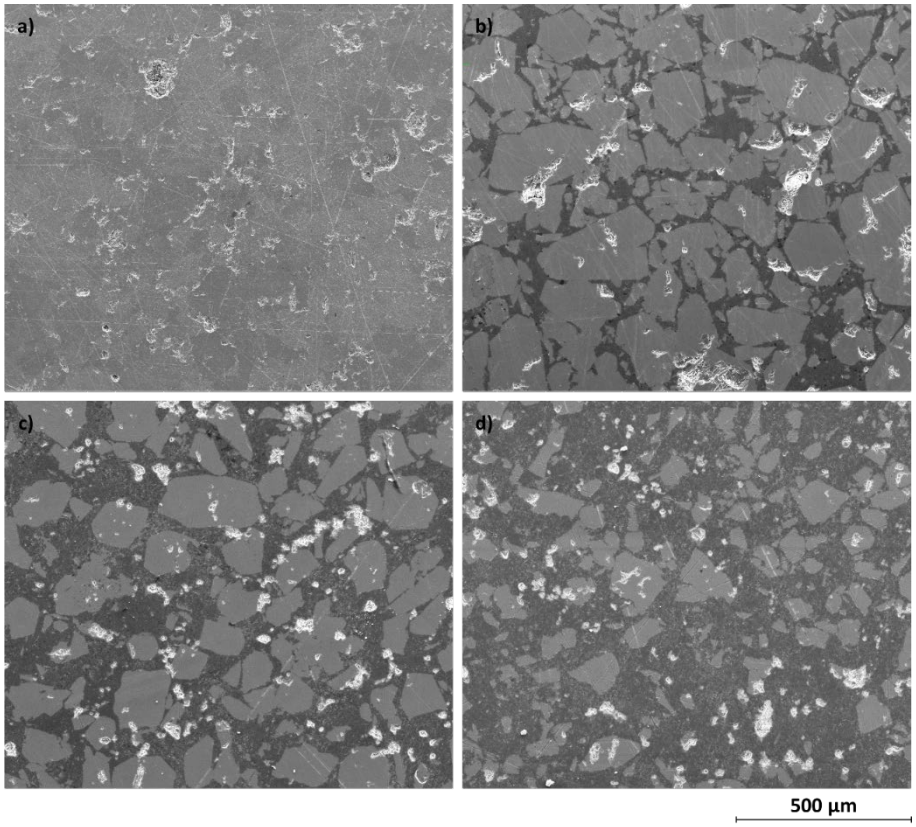

Figure 56: Surface SEM of LMO-BMO ceramic composites, with a) 100, b) 80, c) 60 and d) 50 wt.% lithium molybdate.

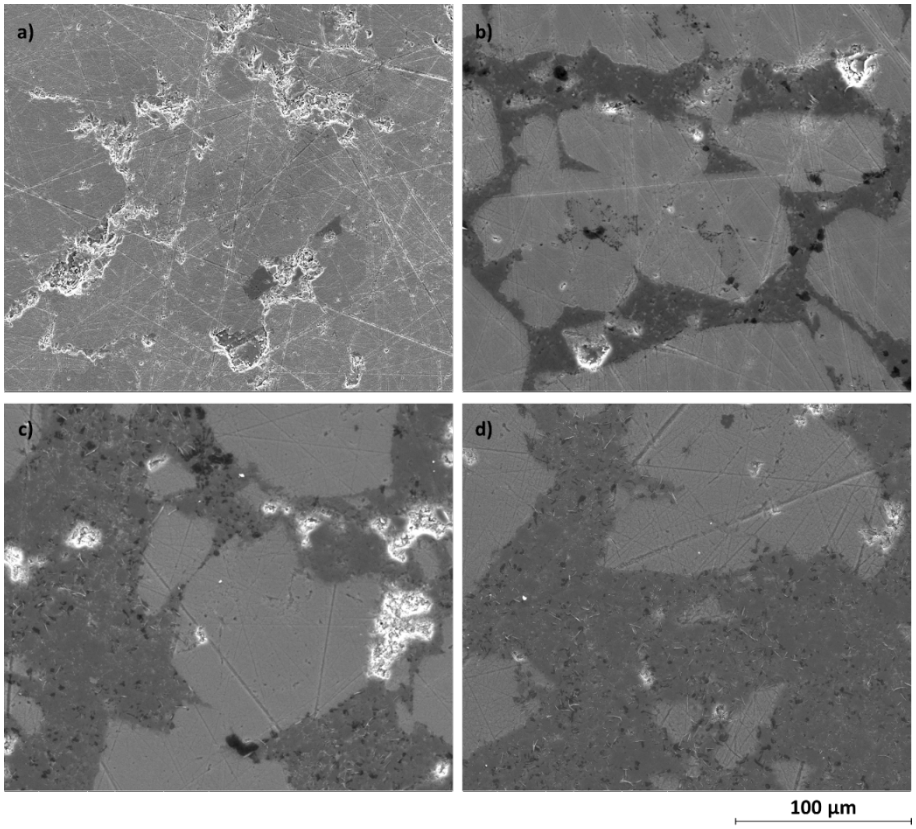

Figure 57: Surface SEM of LMO-BMO ceramic composites, with a) 100, b) 80, c) 60 and d) 50 wt.% lithium molybdate.

The relative permittivities of $Bi_2Mo_2O_9$ and Li_2MoO_4 have been reported to be approximately 38 and 5.5, respectively [67], [68], [235], [237]. Therefore, by creating composite samples of the two ceramics, it is, in principle, possible to achieve a broad range of permittivity. Figure 58 shows the relative permittivity of LMO-BMO composite samples. The permittivity of cold sintered lithium molybdate is similar to that reported in the literature and remains approximately constant with frequency. With the addition of 20 w.t% BMO, the permittivity increases but becomes frequency dependent, suggesting a strong contribution from space charge which typically has a large low frequency response. As discussed in 2.5.1, permittivity is caused by four mechanisms of polarization within the material, which contribute at different frequency ranges. The measured permittivity of the composites is highest at 1 kHz, indicating a strong contribution of space charge to the total permittivity in samples containing BMO.

As the BMO concentration is further increased, the permittivity decreases and remains frequency dependent. The reduction rather than the predicted increase in permittivity (BMO has a higher reported permittivity than LMO) is commensurate with the decrease in density as BMO concentration increases. [11], [130], [133]. The room temperature permittivity of cold sintered BMO is <1 at all frequencies, significantly lower than the reported values for conventionally produced samples. This likely due to the sample being highly conducting as a result of the low density with the low permittivity an artefact of the measuring process.

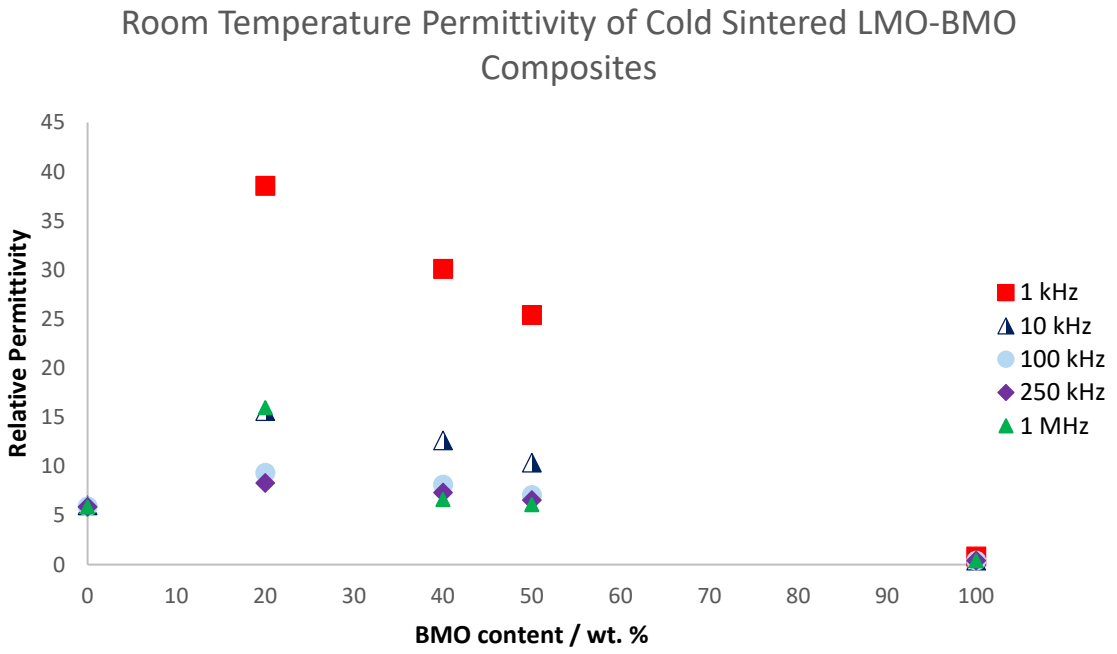

Figure 58: Room temperature relative permittivity of cold sintered LMO-BMO composites at 1, 10, 100, 250 kHz and 1 MHz.

4.4 Coatings of Lithium Molybdate

Lithium molybdate was attrition milled before slurry preparation to reduce particle size and passed through a 67 µm sieve. After attrition milling (Figure 59), the average particle size is significantly reduced and although some larger particles (10-15µm) are still present, most particles are <10 µm.

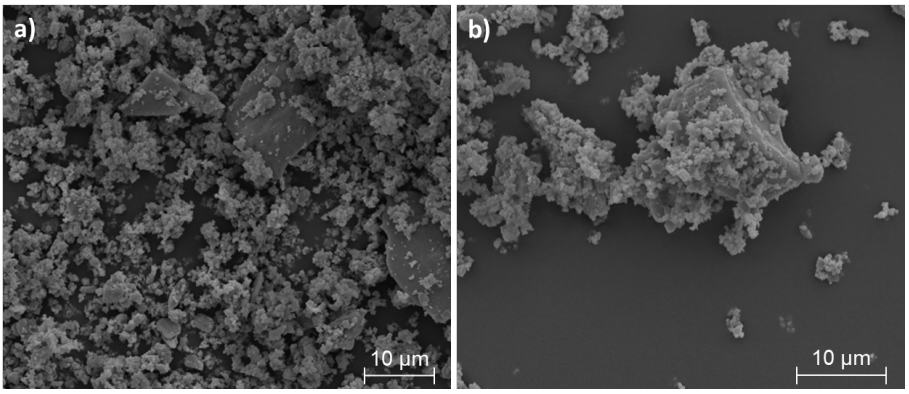

Figure 59: SEM of lithium molybdate (Sigma Aldrich) after attrition milling

The ceramic slurry was deposited onto a chemically toughened glass substrate *via* screen printing with a squeegee pressure of 3 tonnes, each layer consisted of two passes of the squeegee followed by drying at 120°C for 15 minutes before subsequent layers are applied to create a sample of desired thickness. The organic binder was burnt out at 300 °C with a dwell time of 6 hours, leaving a green layer of lithium molybdate. The LMO layer was then densified *via* two methods, conventional sintering (540°C for 2 hours) or cold sintering with the addition of distilled water.

Initial attempts at wetting printed samples for cold sintering was performed by producing water vapour in a sealed beaker at 40°C in a similar fashion to the paper by Baker *et al* [2]. However, this method caused water droplets to form at the edges of the printed area and produced an uneven water distribution. Therefore, to allow for better distribution on the LMO layer, distilled water was sprayed over the samples prior to cold sintering using an atomizer. To prevent the transfer of the wetted LMO layer to the die during pressing, a sheet of non-stick silicone coated paper was placed between the printed layer and the die.

Figure 60 shows screen printed layers of lithium molybdate on glass substrates before and after sintering. After binder burnout at 300 °C and prior to sintering (Figure 60a), the coating layer appears to have a consistent thickness and is opaque. There is

poor adhesion between the substrate and coating layer, which can be easily removed by light scraping. After conventional and cold sintering, the coating layer of ceramic became well adhered layers to the substrate. Layers produced by cold and conventionally sintering do not appear to have a consistent thickness, with thicker areas appearing opaque white and thinner areas greyer and partially translucent.

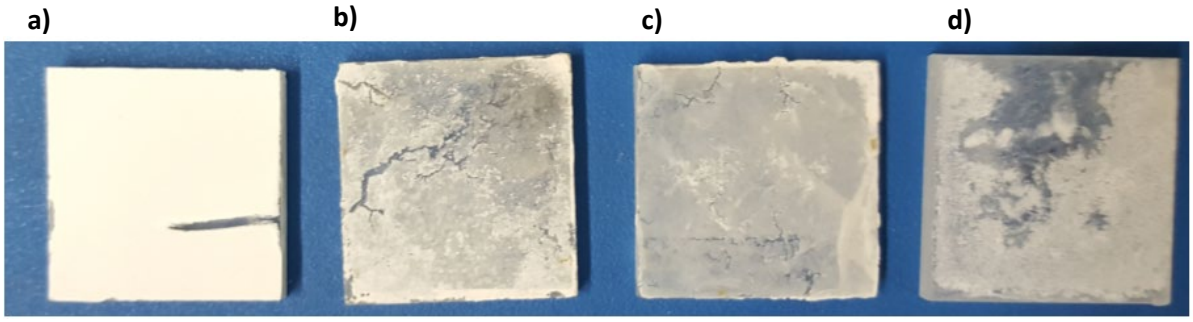

Figure 60: Screen printed samples after (a) binder burnout, (b) cold sintering at 120°C 10 MPa, (c) cold sintering at 120°C 5 MPa and (d) conventional sintering at 540°C.

The quality of the cold-sintered layers (Figure 60 b & c) appears to have been affected by the sintering pressure. Both samples have regions of brighter contrast near the edges/corners of the substrate which are likely to be thicker and created by imperfections in the die and the movement of material to the bevelled edges of the substrate from where it would be possible to escape through any gaps in the dies. There is also evidence of material on the edge of the substrates, which would not be subjected to the same sintering processes due to lower pressures and therefore, unlikely to have been densified.

The layer shown in Figure 60c, pressed at 5 MPa appears to be more consistent than the sample pressed at 10MPa (Figure 60b), fissure-like defects are also less significant in the coating layer of Figure 60c than b. The use of a lower sintering pressure allows the lithium molybdate to be densified, without being compressed in such a way that causes the coating to be forced out towards the die edges. The conventionally sintered sample shown in Figure 60d has a coating of inconsistent thickness, which attributed to screen-printing defects. In contrast to the cold sintered samples there are no thicker regions at the edges of the material or on the bevelled edges of the substrate.

Figure 61 shows the XRD patterns of the screen-printed layers after binder burnout and sintering. There is a small peak shift to the right in the cold sintered samples due to an error in sample height. Changes in intensity of a number of peaks

are also observed, most notably at 25°, where the conventionally sintered sample show a much greater intensity peak. This difference in intensity is due to the very large grain size, compared to the coating thickness and therefore the limited number of grains of different orientations in the sample detected during XRD.

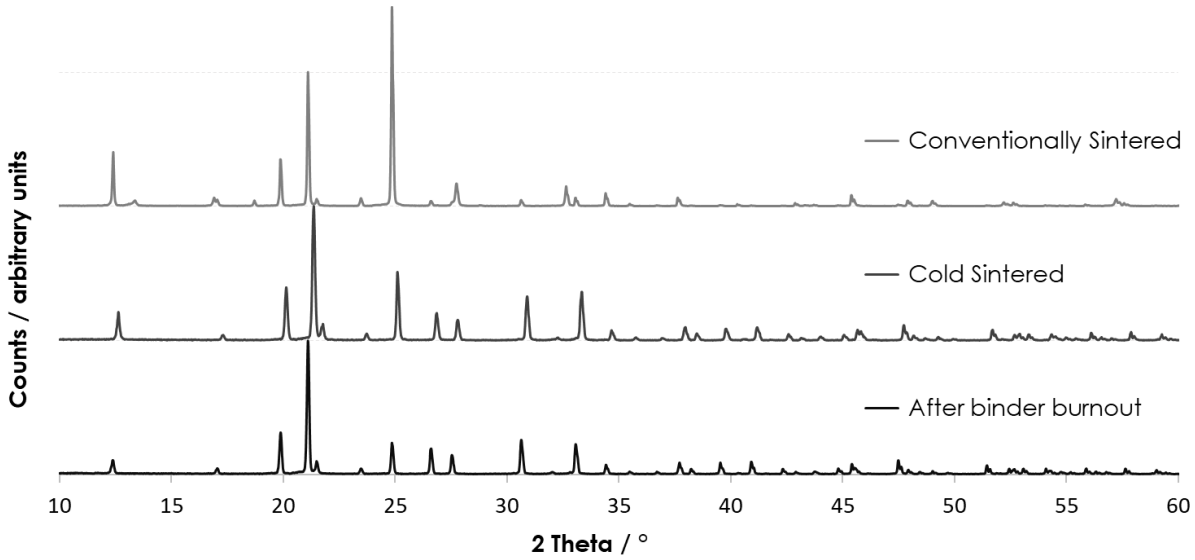

Figure 61: XRD of screen-printed layers after Binder burnout at 300°C, after cold sintering at 120°C and 5 MPa and conventional sintering at 540°C

Figure 62 shows SEM images of the cross-sectional fracture surface of a conventionally sintered screen-printed sample. The conventionally sintered layer is approximately 60 µm thick, has very low levels of porosity and consists of grains approximately 40 µm diameter. Significant grain growth is achieved during the sintering process; final grain sizes are larger than the starting powder used in the screen-printing slurry. The interface between the coating and the substrate is well defined, with very little porosity.

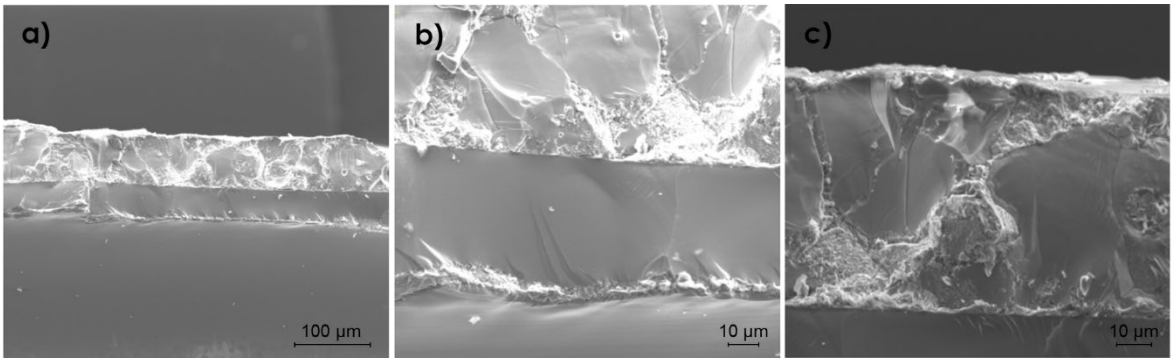

Figure 62: SEM of screen-printed lithium molybdate layer cross section after conventional sintering at 540°C

In Figure 62 (a & b) a defect can be seen in the glass lying approximately parallel to the glass-ceramic interface. The glass substrate is chemically toughened, as discussed below, with an ion-exchanged layer approximately 10-15 μm. Subsurface lateral cracks seen in chemically toughened samples are often larger than those seen in thermally toughened samples [239]. It is possible that the cracking observed in the substrate of the conventionally sintered sample occurs as a result of:

- Pre-existing defects in the near surface region which are larger or deeper than the toughened regions.
- The presence of a boundary between the compressive and tensile stresses within the material.
- Mobility of toughening ions at the conventional sintering temperature (540 °C) which is higher than temperatures used in chemical toughening, leading to stress relaxation [240]–[242]
- Heating/cooling rate during sintering creating thermal gradients within the substrate or differences in thermal expansion coefficient between the substrate and lithium molybdate.

Figure 63 shows a cold sintered screen-printed lithium molybdate layer. The cold sintered layer in Figure 63 is approximately 30 μm thick with grains ~5μm diameter. The final grain size depends on the initial powder size used to manufacture the printing slurry since, grain growth is restricted due to the low temperatures involved in cold sintering.

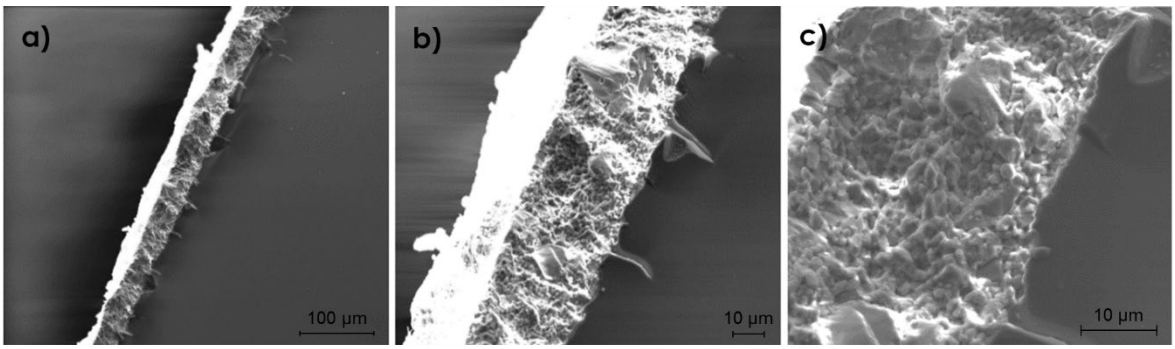

Figure 63: SEM of screen-printed lithium molybdate layer cross section after cold sintering at 120C, 10MPa

A crack parallel to the surface on the substrate is not seen in the cold sintered samples, indicating that the reduced sintering temperature avoids creating any of the conditions discussed above as potential causes of the crack in the conventionally sintered substrate. There are, however, several small (10-20 μm) cracks in the glass substrate running perpendicularly to the glass-ceramic interface. These cracks are

likely to be induced by the applied pressure of cold sintering, larger particles within the coating may act to indent the substrate and create regions of higher pressure.

During cold sintering, cracking of the chemically toughened glass substrate into several large pieces occurs. This is likely due to several different factors. No cracking occurred when ~50MPa uniaxial pressure was applied to a clean, uncoated glass substrate at room temperature in the same die used for cold sintering. This suggests that the toughened glass should be capable of withstanding the pressures applied during the cold sintering trials (5-10 MPa) and other factors contribute to the observed cracking.

The chemical toughening of glass is achieved through ion exchange, where ions such as sodium within the glass are replaced with larger potassium ions. This creates compression at the surface and tension in the bulk and toughens the glass [240], [241]. EPMA of silicon and potassium in the near surface region of the glass substrates after cold uniaxial pressing and cold sintering (120 °C) are shown in Figure 64. In both cases the chemical toughening of the substrates is evident, with comparatively high weight percentages of K at the near surface compared to bulk. This implies that the introduction of heat in the cold sintering process does not lead to de-toughening of the glass surface.

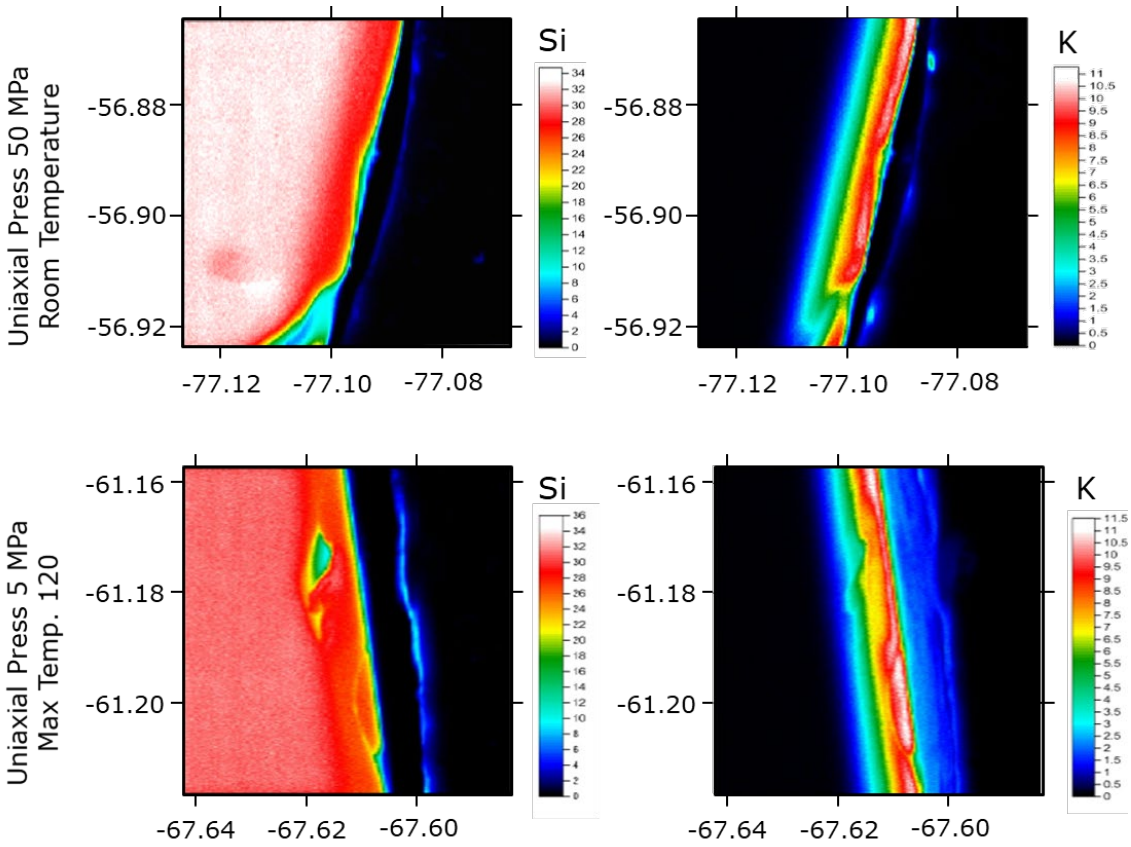

Figure 64: EPMA of silicon and potassium in the near surface region of the toughened glass substrates after cold and high temperature (120 °C) pressing

The EPMA spectral images in Figure 65 show the distribution of magnesium and aluminium in the substrates. The weight percentage of aluminium in the "bulk" region appears to be reduced in the hot-pressed sample compared to the sample pressed at room temperature. There are also indications that the near-surface distribution of magnesium is affected by hot pressing. A layer with lower magnesium content is present in both samples, which appears to be thicker in the hot-pressed samples.

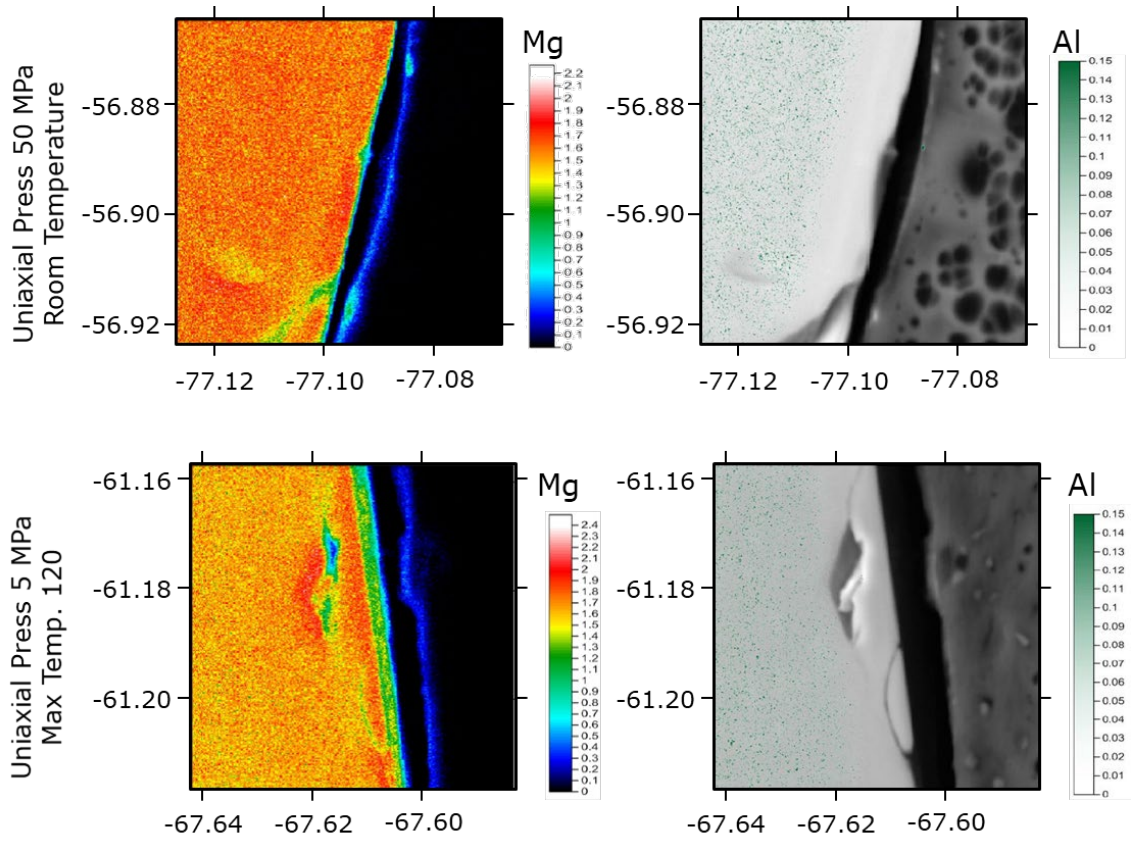

Figure 65: EPMA of magnesium and aluminium in the near surface region of the toughened glass substrates after cold and high temperature (120 °C) pressing.

Aside from the chemical distributions, the EPMA spectral images also indicate the presence of sub-surface defects in the glass, running approximately parallel to the surface and which are on the order of 0.01 mm. These are unlikely to be noticed on brief visual inspection of the substrate but could contribute to cracking observed in the samples during sintering. The application of heat is likely to exacerbate any stresses within the substrate caused by imperfections in the subsurface of the substrate.

Other possible causes of the substrate cracking have not been fully investigated. The edges of the substrate were bevelled and ground, any notches or scratches caused by this process could act an initiation point for cracks. The substrates were chemically toughened prior to cutting to the desired size and therefore, the effect of the toughening process would have been significantly reduced. Larger particles within the coating layer could have also acted to indent the surface and create initiation sites for cracking. As the samples are heated in the steel during cold sintering, there may be issues caused by the thermal expansion of the die pieces and substrate.

Applications for functional (electrical, chemical or mechanical) and decorative coatings on glass substrates are found in a broad range of industries [243]. There are

several barriers to using conventional processing methods to create ceramic coatings on glass substrates. Firstly, compatible materials are limited as the sintering temperature of the ceramic coatings and processing temperatures should not be above the softening or glass transition temperatures. When applying coatings to glass substrates which have been thermally toughened, there is a risk of de-tempering and losing the desired mechanical properties [240].

Numerous technologies, such as laser sintering and sol-gel spin coating, have been explored which allow for the densification of a glass-enamel coating whilst preventing damage the substrate beneath. Selective laser sintering uses a laser to induce localised heating to soften the frit and achieve densification, the application of this method is constrained to material combinations where the coating absorbs most of the energy provided by the laser, while the substrate absorbs very little of the remaining energy. Alongside the coating, the near-surface region of the substrate is still likely to be heated to temperatures which would prevent incorporation of heat sensitive components in either layer. Spin coating processes used for automotive windows require a sintering step after deposition, which can be incorporated into the shaping and thermal tempering regime of the substrate glass during manufacture [244]. This technique allows for the production of well adhered, durable glass coatings but must be performed prior to glass shaping and requires highly controlled heating regimes. This work has demonstrated the ability to create a functional ceramic coating layer on glass substrates at 120 °C *via* the cold sintering process. After cold sintering, the ceramic layers were found to be well adhered to the substrate and well densified.

5 Johnson Matthey Silicate Frit – JM5430F

5.1 Introduction

The cold sintering method has been applied to a variety of predominantly electroceramic materials. For a material to be a candidate for densification *via* cold sintering however, it need only be partially soluble in a liquid. The corrosion behaviour of glasses as they interact with the environment has been studied for several applications and is usually considered an undesirable process [245]–[247]. However, this corrosion behaviour could allow glass powders to be cold sintered and subsequently unlock a wide spectrum of potential applications.

Hydrothermal hot pressing and room temperature densification techniques have been applied to a number of glasses and a study by Ke *et al.* achieved the adhesion of two bulk silicate components utilising a "Cold Isostatic Joining" technique [167], [248]. This further indicates the potential for bulk glass components to be produced from powders *via* a cold sintering technique.

This chapter aims to densify a glass provided by Johnson Matthey, JM5430F, *via* the cold sintering method. A comparison of cold and conventionally sintered materials is presented and potential of this material to be used in the creation of coatings and adhesive layers on steel and PTFE are then demonstrated.

5.2 Cold Sintering of JM5430F

JM5430F is a borosilicate-based glass material and was supplied as a fine powder by Johnson Matthey. The precise composition is confidential, but the approximate range of weight percentages are given in Table 16.

Table 16: Composition of JM5430F in weight percent

Oxide	Wt. %
SiO_2	30-60
ZnO	5-25
B_2O_3	5-15
TiO_2	0-10
Li_2O	0-5
Al_2O_3	0-5

JM5430F powder was produced *via* a conventional process, with a melt temperature of 1400 °C for 1 hour, followed by quenching in water to form a frit. The resulting frit was then milled in water and dried to achieve a fine powder. Particle size analysis performed using a Mastersizer 3000, with powder suspended in distilled water, indicated a broad size distribution (0.5-200 µm), with an approximate d_{50} of 8 µm.

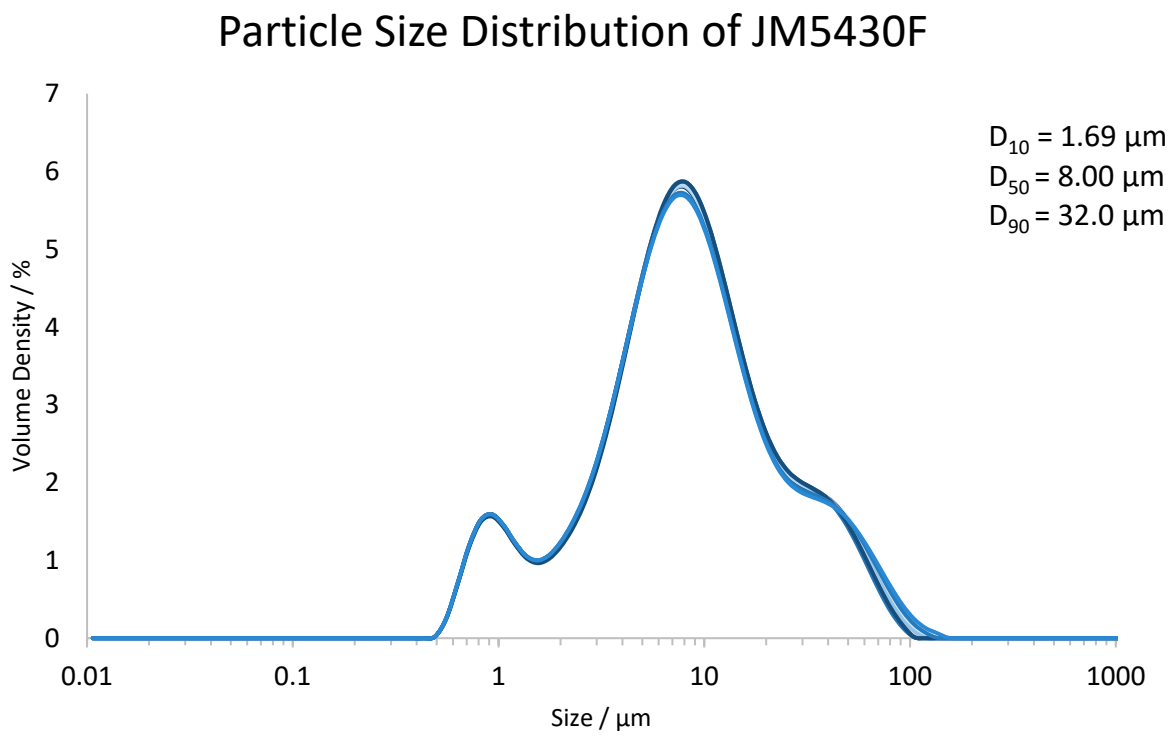

Figure 66: Particle Size analysis of JM5430F Powder

SEM of the powder (Figure 67) showed a non-uniform particle morphology and a broad range of particle sizes. A large number of very fine particles are seen on the surfaces of larger particles. Some large agglomerates, up to 40-50 μm, consisting of very fine (<1-5 μm) particles appear quite densely packed.

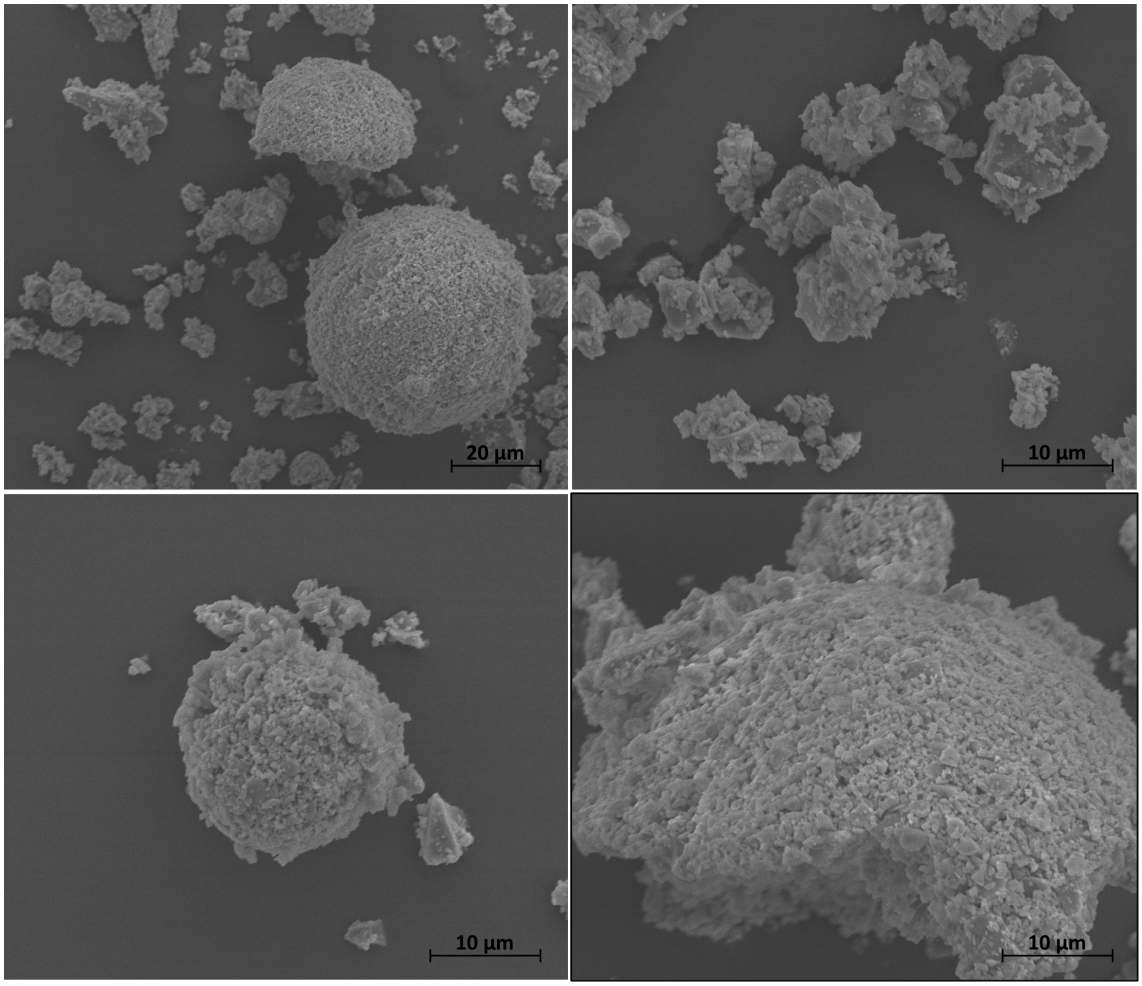

Figure 67: SEM of JM5430F powder

Powder of JM5430F was pressed in 10 and 2 0mm ø dies to create green pellets. The pellets were then conventionally sintered at various temperatures for 4 hours to determine optimum conditions. Samples sintered at 600 °C and 575 °C became lightly bonded to the crucible during sintering. At a sintering temperature of 500 °C the sample did not bond to the crucible but also had very low density (1.79 g/cm^3). Sintering at 550 °C created a well densified pellet (2.76 g/cm^3) which did not adhere to the crucible.

The composition of JM5430F is known to interact and be partially soluble in acids. Due to this and the relatively high content of ZnO in JM5430F, it was decided to follow a process of cold sintering developed from a method for pure ZnO by Funahashi

et al. [56]. Glacial acetic acid was therefore, diluted with distilled water to create a 1 M solution.

0.36-0.57 ml of 1 M acetic acid was added to 1 g of JM5430F glass powder and mixed in a pestle and mortar to ensure a homogeneous distribution of liquid over the surface of the solid samples. At higher levels of liquid, the mixture formed a 'putty'. The powder-acid mixture was placed in a 10 mm diameter steel die and pressed at 250 MPa for 5 minutes to allow particle redistribution. The temperature was then raised to 100 °C and held for 10 minutes before being raised again to 250 °C and held for 30-45 minutes. During densification, the pellet bonded to the steel die and was destroyed during removal. Therefore, a layer of silicone coated non-stick paper or PEEK was placed in the die ahead of the powder during subsequent sintering trials.

Figure 68 shows pellets created *via* cold and conventional sintering and indicates the significant difference in radial shrinkage from both conventional and cold sintering methods. In both cases, dies of 10 mm diameter were used during the pressing of samples. After sintering, the diameter of conventionally processed samples is 8.2 mm, whereas the cold sintered samples have a final diameter equal to the internal diameter of the die (10 mm). This is a very clear example of one of the major advantages cold sintering has over conventional processes. During cold sintering, shrinkage caused by densification only occurs in the direction of the applied pressure and final dimensions can be more easily controlled.

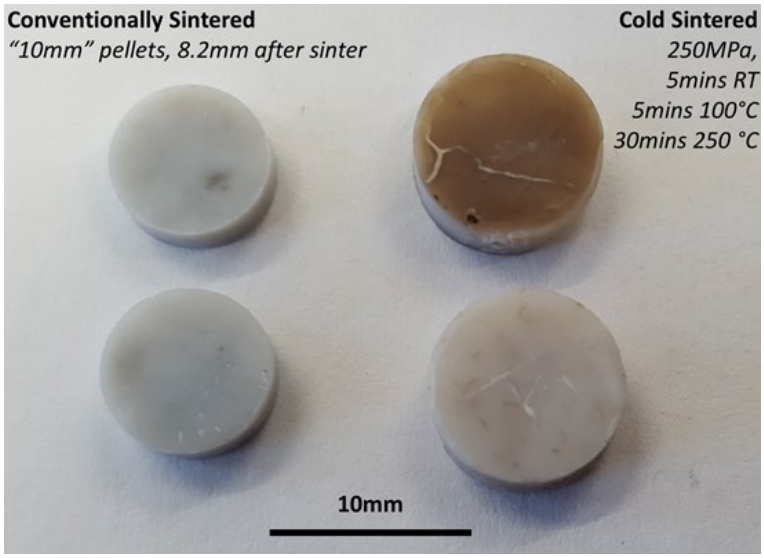

Figure 68: Difference in lateral dimensions of conventional and cold sintered samples after sintering.

Conventional sintering of the glass at 500 °C and 550 °C produced samples with density, 1.79 and 2.76 g/cm3, respectively. The difference in microstructure

between different processing parameters is shown in Figure 69. At the lower sintering temperature (500 °C, Figure 69a) very little densification has occurred. Particles of a similar size and morphology to the starting powder are still visible and appear to be only lightly bonded. In Figure 69b, after sintering the glass at 550 °C, the powder is well-densified and there is no discernible grain structure. However, there are a small number of pores present which are likely to have originated as voids within the green body.

Samples of cold sintered glass using 0.36 and 0.57 ml/g acetic acid achieved densities of 2.32 and 2.67 g/cm^3. In both cold sintered samples, the microstructure is made up of larger 10 μm particles bonded together by a boundary phase with a finer grain structure, comparable to that of the original powder morphology. Both cold sintered samples appear to have a higher density than the sample conventionally sintered at 500 °C, despite the significantly lower temperatures. Comparing the fracture surfaces of cold sintered samples shown in Figure 69 c and d, the intergranular material appears to create a better bond with the addition of higher concentrations of transient liquid. The increased liquid proportion is likely to have aided further densification by encouraging the rearrangement of particles during the appilication of pressure, accompanied by an increase in dissolution of smaller particles. This demonstrates how the concentration of transient liquid during cold sintering can be utilised to tailor the final density and grain structure.

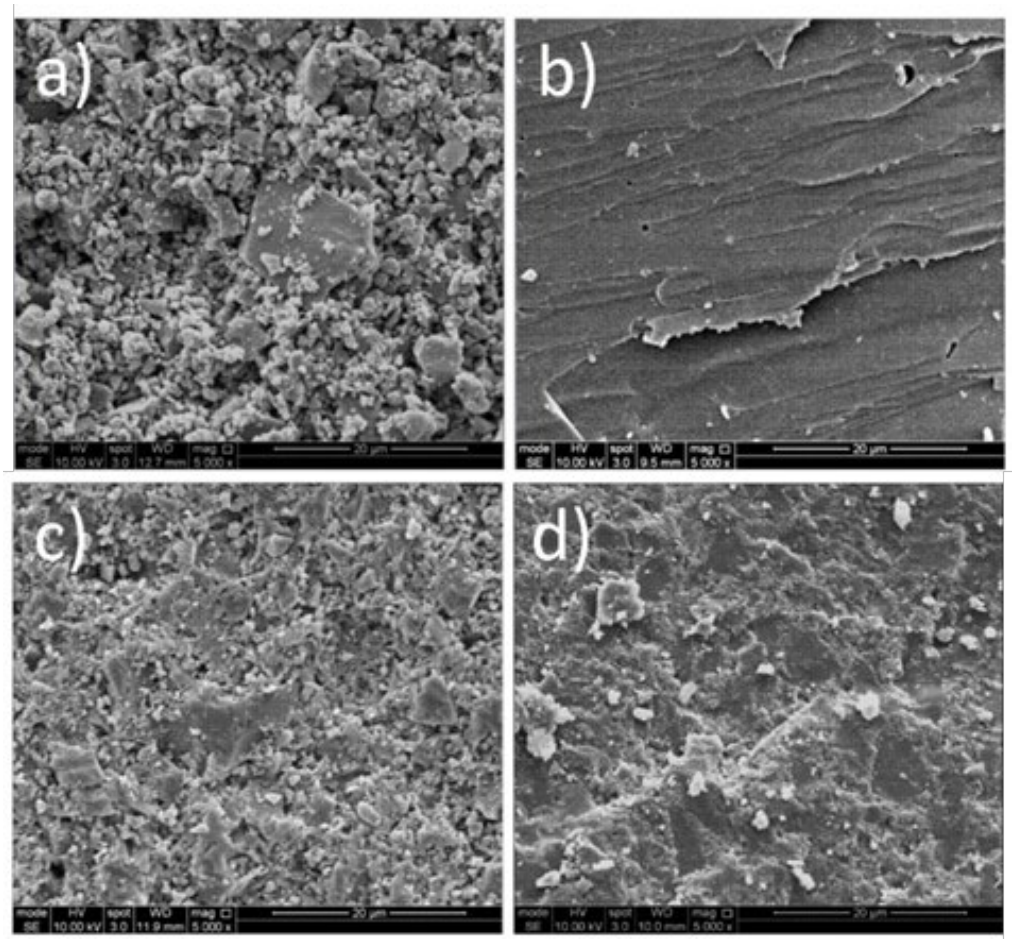

Figure 69: Fracture surface SEM of sintered glass samples with different processing parameters a) Conventional Sinter 500°C for 4 hours; b) Conventional Sinter 550°C for 4 hours; c) Cold Sintered using 0.36 ml/g acetic acid; d) Cold Sintered using 0.57 ml/g acetic acid (250 C)

From XRD analysis, Figure 70, the spectra of the initial powder and conventionally densified samples both show diffuse scattering patterns typical of an amorphous material. The XRD of cold sintered samples (0.57 ml/g) indicate that during cold sintering some crystallisation occurs. This crystalline phase is likely to have formed at particle boundaries. During heating, the liquid phase evaporates and the dissolved material precipitates to form a crystalline phase. Despite further XRD analysis, shown in Figure 71, the crystalline phase(s) could not be determined, and it is likely that several are present, possibly as acetates of dissolved cations.

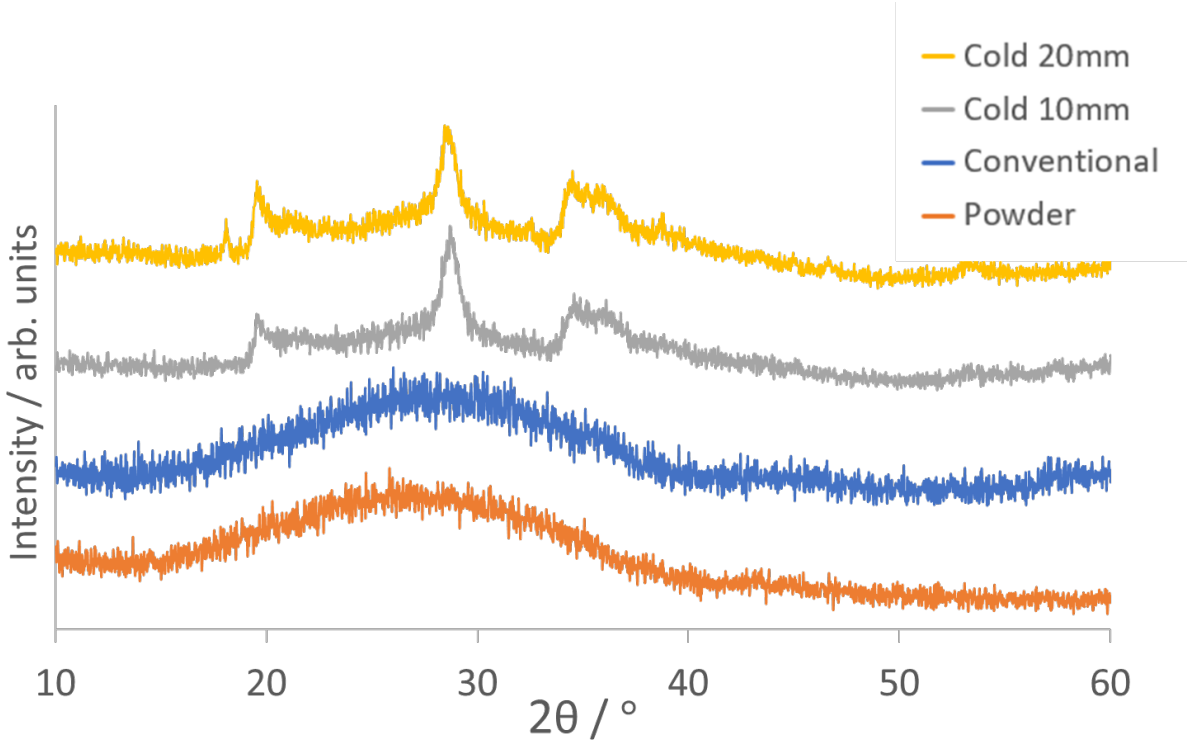

Figure 70: XRD of conventional and cold sintered glass.

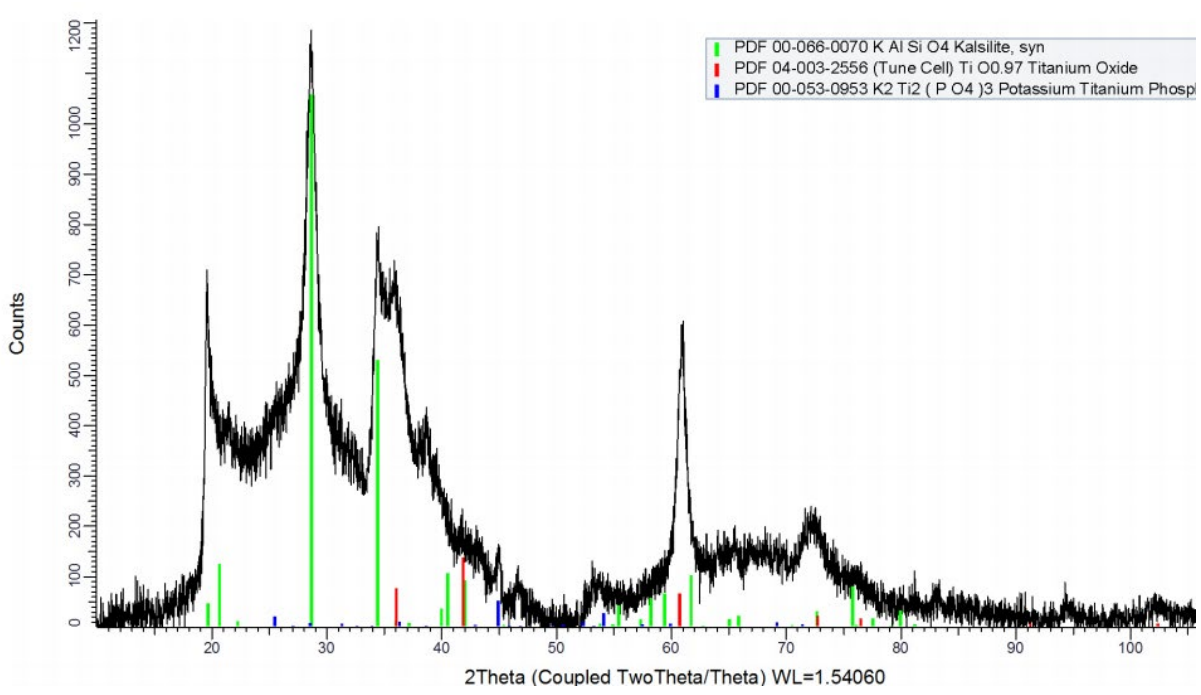

Figure 71: XRD of cold sintered JM5430F glass

EDX analysis of JM5430F, shown in Figure 72 and Figure 73, further confirms that there is compositional variation between the grains and intergranular phase after cold sintering. This indicates that dissolution of the glass powder is incongruent with

the acetic acid (most likely the acetate group) contributing to the creation of intergranular phase(s).

In Figure 72, analysis of the compositional distribution is hindered by the resolution of the maps compared to feature size. Zn appears slightly more prevalent in the intergranular phase but Ti and Al are evenly distributed. A few Al rich regions of an unidentified phase of very high brightness are observed. Na appears more concentrated within the large grains compared to the intergranular phase. During the cold sintering process, it is likely that the Zn^{2+} ions, which act as an intermediate within the glass are attacked preferentially, through the formation of Zn acetate. The mechanism has not been investigated for glass compositions but is likely to be analogous to the cold sintering of ZnO using acetic acid [62], [86], [249], [250].

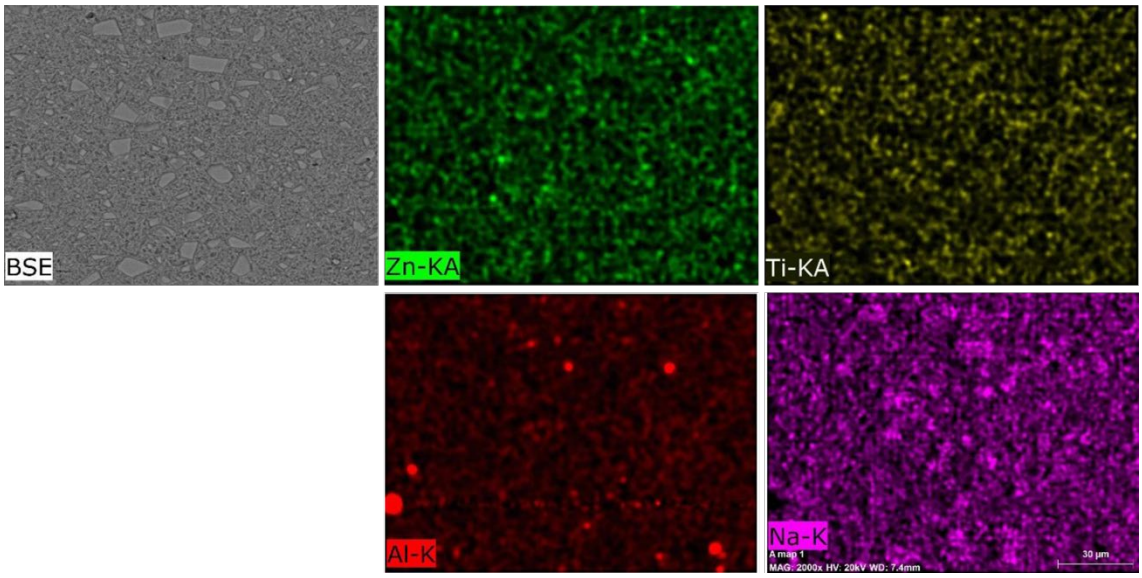

Figure 72: BSE image of cold sintered JM5430F and corresponding EDX maps of Zn, Ti, Al and Na.

The higher magnification EDX map in Figure 73 confirms that Na is more concentrated within the grains. Si is present throughout the grain and boundary phases, although the concentration is slightly higher within the grains. As in Figure 72, both Ti and Al are evenly distributed between the grain and boundary phases, with some regions of high Al concentration in the boundary phase.

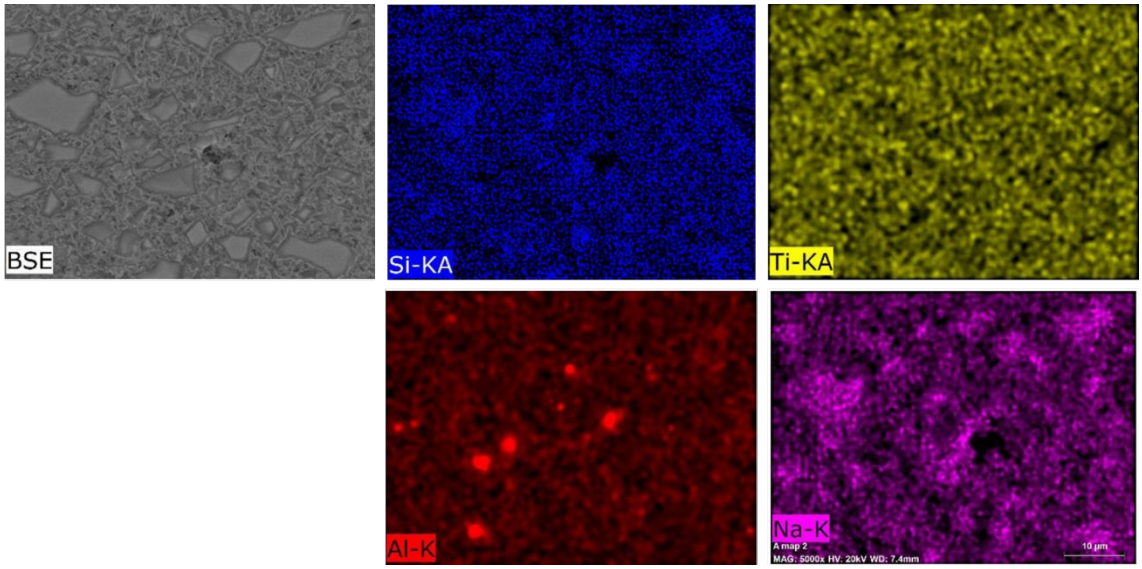

Figure 73: BSE image of cold sintered JM5430F and corresponding EDX maps of Si, Ti, Al and Na.

Impedance spectroscopy was utilised to further understand the effects of sintering methods and parameters on JM5430F. Samples were measured between 200 and 400 °C; however, a significant amount of noise is seen in data for conventional samples below 300 °C. The temperature dependence of bulk conductivity of cold and conventionally sintered samples are shown as Arrhenius plots in Figure 74. The activation energy of conduction is related to the gradient of the Arrhenius plots of conductivity in Figure 74 and are approximately 0.9-1 eV for both conventional and cold sintering samples. This indicates the addition of acetic acid, and the creation of a partially crystalline grain boundary phase during cold sintering does not affect the activation energy.

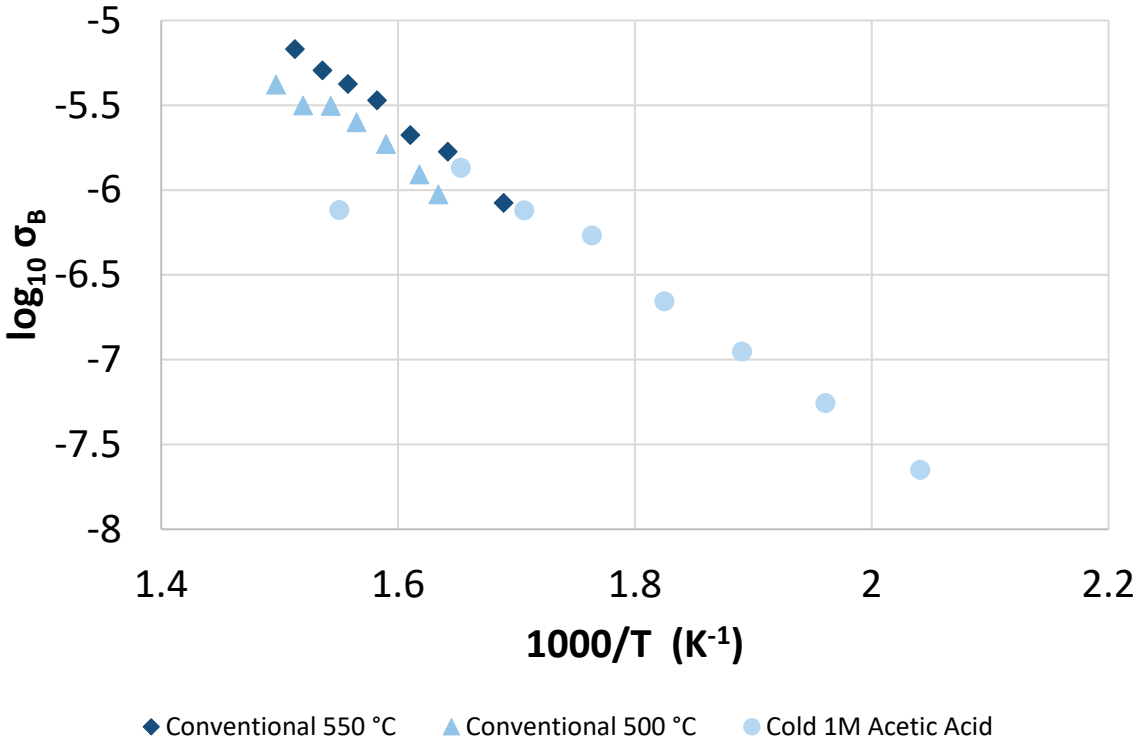

Figure 74: Arrhenius plot of conductivity versus temperature for samples produced via convention and cold sintering.

Figure 75 shows the Nyquist plots (Z", Z') of samples sintered conventionally (500 and 550 C) and cold sintered with 1M acetic acid, measured at ~ 315 °C. Low frequency data, below 500 Hz have been omitted from the plots, due to noise. The densities of the higher temperature (550 °C) conventionally sintered sample and the cold sintered sample are very similar (2.76 and 2.67 g/cm^3 respectively), whilst the lower temperature conventionally sintered sample was only 1.79 g/cm^3. The magnitude of the total impedance response is strongly influenced by the level of porosity [251][252]. The Nyquist plot of the low temperature conventionally sintered sample indicates a significantly higher total impedance, which can partly be attributed to the higher level of porosity in comparison with the higher temperature conventional and cold sintered samples.

Contributions to impedance of the grains (bulk) and grain boundaries occur at high and low frequencies, respectively. In the 550 °C conventionally sintered sample, which did not have a discernible grain structure (Figure 69), the impedance response is predominantly from the bulk. In both the cold sintered samples and the 500 °C conventionally sintered samples, there are contributions to the impedance response from grain and grain boundary regions. The bulk response of the cold sintered sample is of a similar magnitude to that of the higher temperature conventionally sintered sample, with a small grain boundary contribution. In the lower temperature

conventionally sintered sample, there is both a large grain and grain boundary contribution. SEM of the internal fracture surfaces of the cold and conventionally sintered samples shown in Figure 69 demonstrate that the densification of the small, 'intergranular' particles is limited in the 500 °C conventional sample compared to the cold sintered samples. The difference in ratio of the grain boundary responses compared to the bulk is due to the level of consolidation and necking in the smaller, inter-granular particles [253].

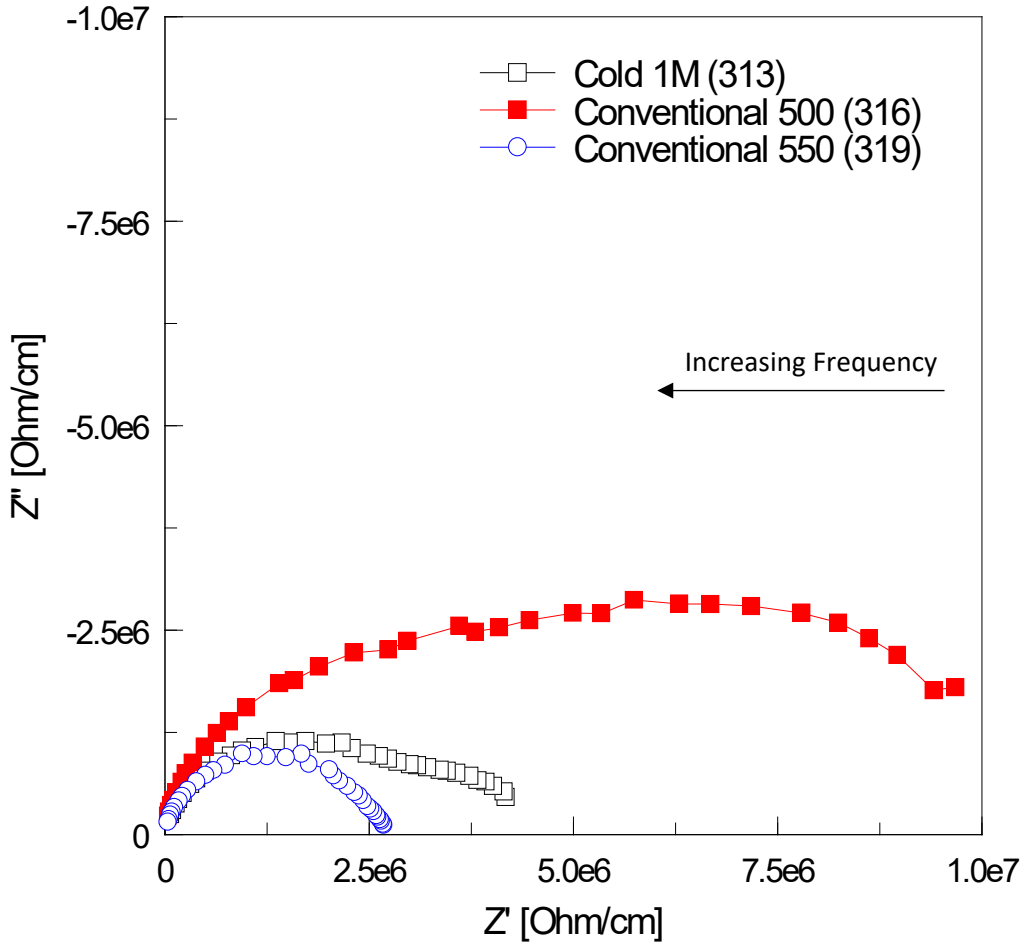

Figure 75: Nyquist plots of conventional and cold sintered JM5430F

The behaviour of the cold sintered pellet begins to change as the temperature is increased between 275 and 400 °C, as shown in Figure 76. The impedance measured between 215 and 332 °C decreases with increasing temperature and there is a significant contribution from the grain boundary phase(s). Above 332 °C, the impedance begins to increase, and the grain boundary contribution is significantly reduced. At higher temperatures (372 and 393 °C), the impedance increased, and a significant amount of noise is seen in the data.

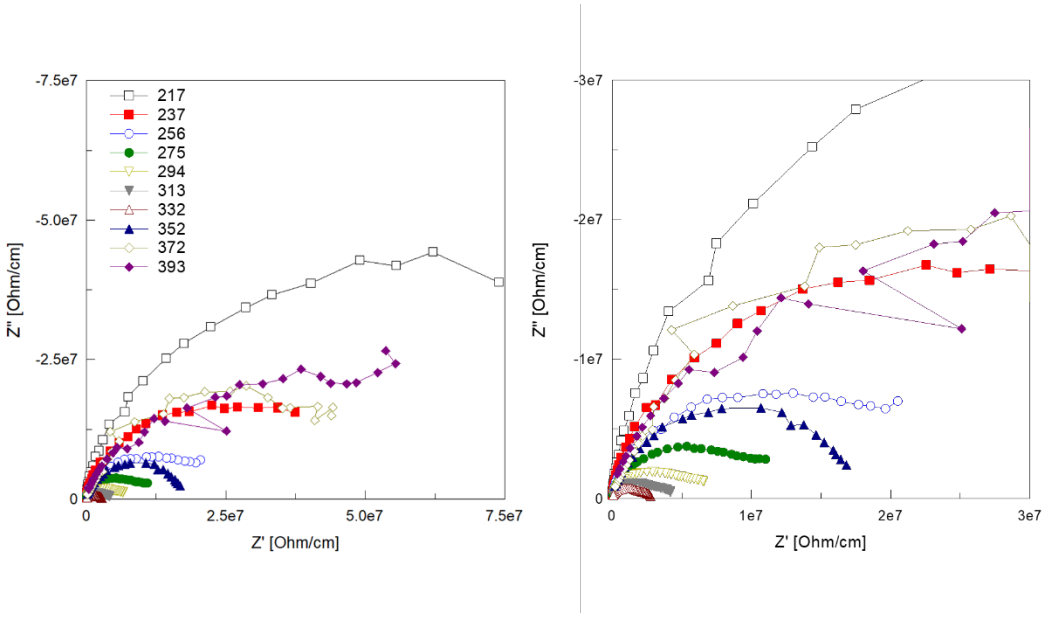

Figure 76: Impedance of cold sintered JM5430F between 215 and 400 °C

The impedance of conventionally sintered samples is shown in Figure 77. The total impedance of the sample sintered are 550 °C decreases with increasing temperature. The sample sintered at a lower temperature shows a decrease in impedance as the measurement temperature is increased between 316 and 375 °C. At 385 °C, the total impedance increases and is similar to that at °345 C, although the relative contribution from the grain boundary is significantly higher. As the temperature is further increased, the total impedance value reduces, with the grain boundary response remaining the dominant contribution.

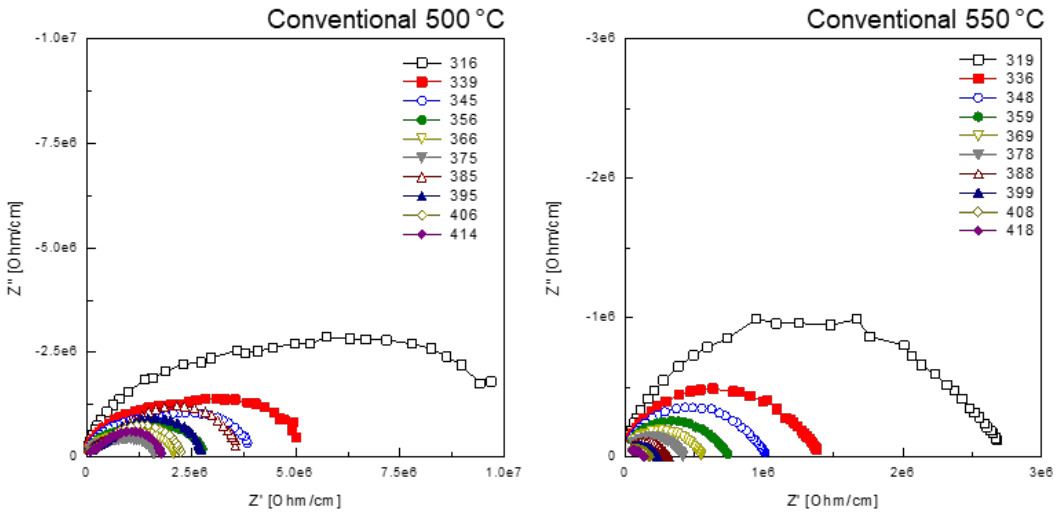

Figure 77: Impedance of conventionally sintered samples between 310 and 420 °C

In both cold and 500 °C conventional samples, the impedance initially decreases and then increases at higher temperature, implying that similar changes may occur in the two materials. The smaller intergranular particles seen in the microstructures may have begun to grow or further densify. In the 500 °C, however conventionally sintered samples, the impedance decreases as the sample is heated further, whereas in the cold sintered samples impedance continues to increase. During the cold sintering process, the maximum temperature applied to the material is 250 °C, the sample is taken above the cold sintering temperature and closer to conventional sintering temperatures. Secondary phases produced during cold sintering could contribute to this behaviour by beginning to react or decompose. It is likely that zinc acetates are formed as part of the cold sintering process, which has a reported thermal decomposition range 240-312 °C, with a significant dependence on heating rate [254]–[256]. This indicates that microstructural and electrical properties of a cold sintered material may change during service above their required sintering temperatures. This could prove detrimental during long term usage and therefore, any material to be used above its sintering temperatures should first be heat treated to at least the service temperature to ensure stability in properties.

5.3 Densification of JM5430F glass-ceramic on steel substrates

During cold sintering of pellets, there was significant adhesion to the steel dies which was prevented using layers of PTFE and/or silicone coated paper. The ability to sinter a glass onto a metallic substrate at low temperatures could be useful in several applications and was explored further. Steel samples were first ground to remove surface debris and to create a more uniformly roughened surface to encourage adhesion.

JM5430F powder was mixed with 1mol acetic acid at 0.57 ml/g and placed onto the steel substrate inside a die, with a PTFE layer to prevent adhesion to the die. The sample was then heated to 100°C for 60 minutes with an applied pressure of 55 MPa. The coating layer is partially densified; however, the white colour of the sample indicates that the relative density is not high and similar to samples sintered at 500 °C. These parameters did not achieve adhesion of the glass to the steel substrate but did achieve partial densification of the glass. The layer of JM5430F was easily removed from the steel and polymer and both the steel facing (a) and plastic facing (b) sides can be seen in Figure 78. There is significant discolouration on the metal side, which is likely due to the oxidation of the steel substrate caused by contact with acetic acid

at elevated temperature. The plastic facing side suffers indentation, where the plastic layer had creased, creating thin areas of the ceramic prone to cracking.

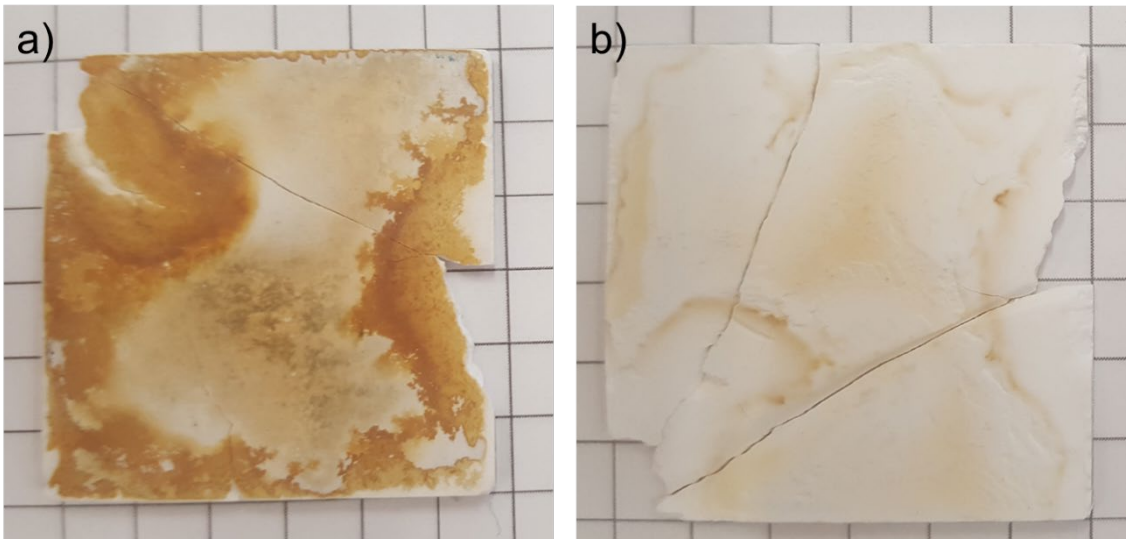

Figure 78: JM5430F layer cold sintered at 100 °C on a steel substrate.

A two-step heating regime with a 30-minute hold at 100 °C followed by 60 minutes at 250 °C (0.57 ml/g 55MPa), as used during the cold sintering of pellets, was also utilised. This was shown to improve the adhesion of the glass onto the steel substrate. The coating layer also adhered to the polymer layer used to prevent adhesion to the steel die, which caused damage to the coating during removal of the polymer (Figure 79).

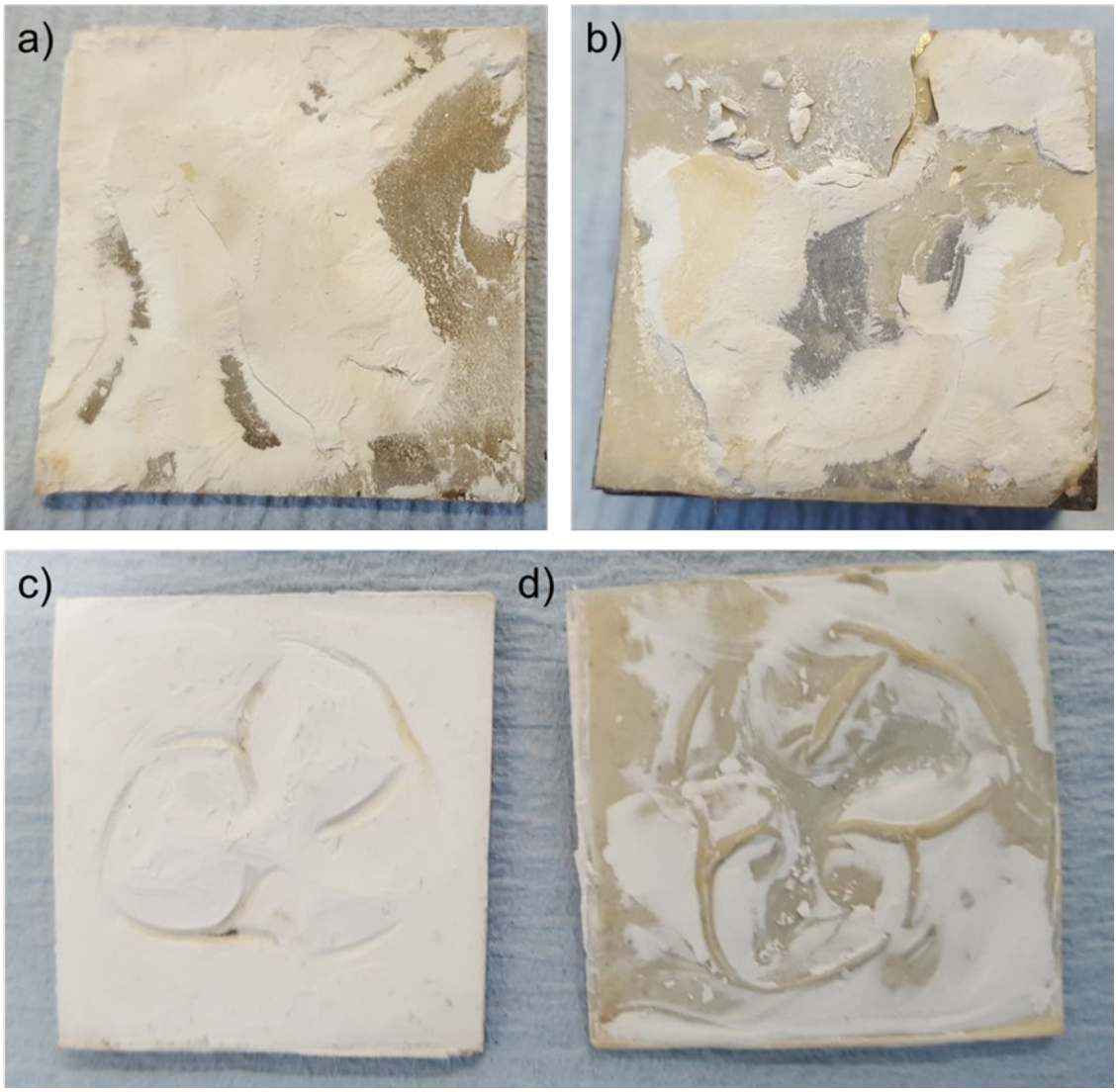

Figure 79: JM5430F layers cold sintered using a two stage process

As in Figure 78, the cold sintered ceramic layers in Figure 79 do not appear to be fully densified. The most significant reason is likely to be that the applied pressure (55 MPa) used in the coating sintering process is much smaller compared to standard pellets (250 MPa) due to the increased surface area.

The ability of JM5430F to intentionally adhere metallic and polymeric materials was further explored, using thicker pieces of PTFE (~3mm), which can be placed into the die without warping of the surfaces. Figure 80 shows a layer of JM5430F with approximately 3 mm thickness and 20 mm diameter, created using 1.5 g of powder, 0.85 ml 0.1 mol acetic acid. A higher pressure (250MPa) was used in order to understand the effect of the reduced pressure on the density in samples shown in Figure 78 and Figure 79. The layer was well adhered to both the metallic substrate and

the PTFE puck, the layer of JM5430F preferentially cracked with the attempted removal of the PTFE.

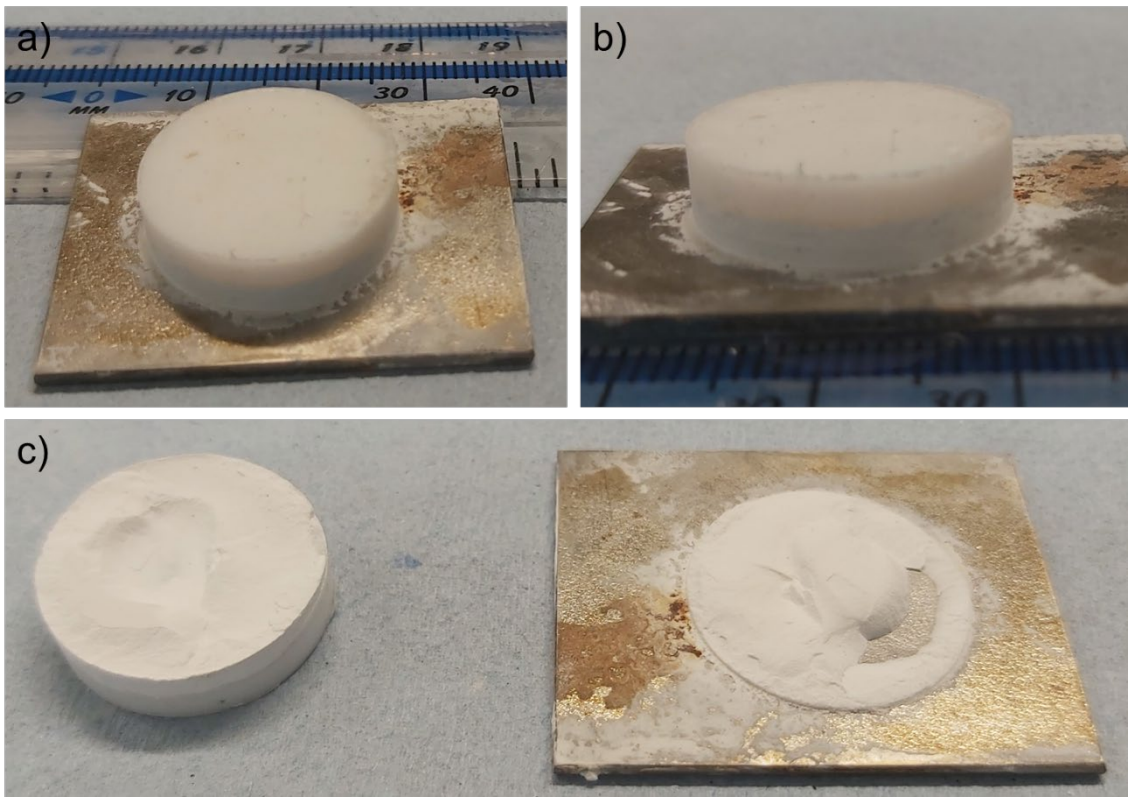

Figure 80: Layer of JM5430F between steel substrate and PTFE puck.

The layer of JM5430F which remained adhered to PTFE (Figure 80c) was sectioned to investigate the internal structure and interface between the two materials. From Figure 81, the layer appears to have been partially densified, with some regions of very low porosity. The microstructure of the JM5430F layers consists of large particles surrounded by a finer grain structure which appears to be well bonded. This is comparable with the cold sintered microstructures shown in Figure 69.

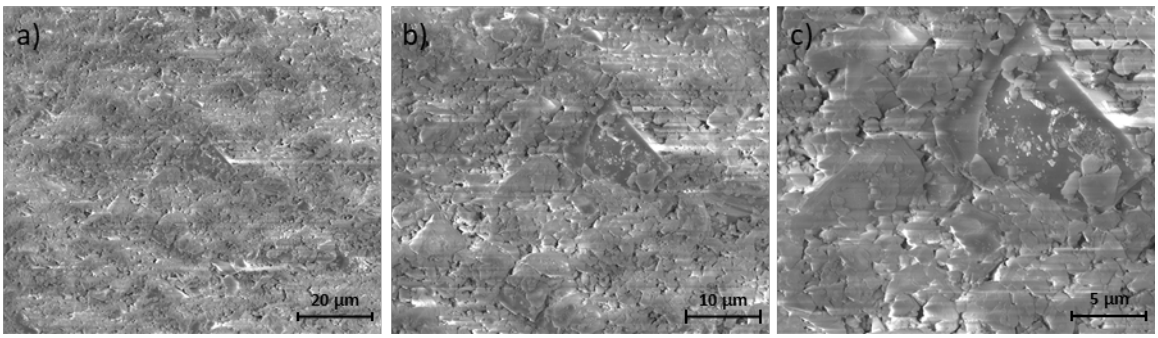

Figure 81: SEM of cold sintered JM5430F layer

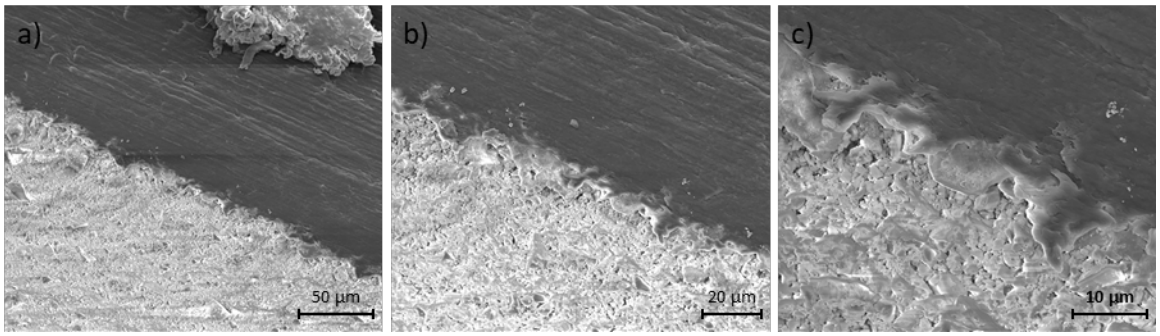

Figure 82: SEM of the interface between cold sintered JM5430F glass-ceramic and PTFE

When cold sintered JM5430F achieves a very high density, it appears similar to the higher temperature conventionally sintered samples. In all coatings produced above, the glass layer remains white indicating a low density more comparable to that seen in the 500 °C sintered samples. A number of factors are likely to contribute to the reduced densification, as there are a significant number of possible parameters during cold sintering. It was possible to densify a pellet with diameter 20 mm *via* cold sintering in a standard die and therefore, the dimensions of the coatings are not likely to contribute to reduced density. Increasing the pressure used to produce that sample in Figure 80 compared to the samples in Figure 78 and Figure 79 does not significantly improve densification but how the substrate fits within the die is likely to have a major effect on the rate that the transient liquid escapes. A poorly fitting substrate may allow the liquid to escape more quickly during the process, thereby inhibiting dissolution at higher temperature. There may also be some compliance in the steel substrate, which will affect the pressure applied to the JM5430F during the process which may be reduced by adopting the use of a higher quality steel (such as the tool steel used in the cold sintering dies).

The composition of JM5430F is related to a range of automotive enamels produced by Johnson Matthey, many of which are known to interact with acidic environments, causing degradation of the coating layer [257]–[259]. Decorative and functional enamels are traditionally applied to a substrate as a paste or liquid using processes such as screen-printing or spray coating. The frit layer is then heat treated to create a continuous glass coating by causing the particles to soften, flow and coalesce as a dense layer which is well adhered to the substrate. This process commonly requires firing temperatures above 550 °C, which can be undesirable in applications where this is close to the upper operating range of the substrate. Several issues are also observed when creating glass coatings on metallic substrates, such as coating cracking due to mismatching thermal expansion coefficients and the potential for increased oxidation of metals at heightened temperatures. During high temperature

processing, substrates may become damaged or misshapen, and mismatches in thermal expansions may contribute to warping, delamination or cracking. The densification of JM5430F at 250 °C demonstrated here represents a significant reduction in processing temperature – approximately half that of conventional processes. The low temperatures required may enable the creation of layered structures with materials of very dissimilar properties with little/no damage to either substrate. Achieving adhesion of two dissimilar materials in this way, with materials tailored to achieve the desired functional properties, could allow for greater integration of novel components during manufacture.

6 Bioglass® 45S5

6.1 Introduction

Since the cold sintering technique was first reported in 2016, research has predominantly focused on developing processing parameters for electroceramic materials. Results presented in chapter 5 and work on "Cold Isostatic Joining" published by Ke *et al.* demonstrate the possibility to use a cold sintering process on amorphous, silicate materials [167]. These developments indicate that the cold sintering process can be utilised in a broader range of materials, and therefore enable applications which have traditionally been hampered by the high processing temperature of materials.

This chapter aims to demonstrate the application of cold sintering to the densification of Bioglass® 45S5, which is commonly used in biomedical applications due to its solubility and subsequent bioactivity. In most cases, Bioglass is used as a coating material or as part of a composite system to achieve desired properties. This creates numerous compatibility issues such as those discussed in section 2.8.

A recently published review of Bioglass coatings by Oliver *et al.* cites significant barriers to further development in clinical applications; the most pressing of which are the differences in thermal expansion coefficient (Titanium 8.5-9 $x10^{-6}K^{-1}$ and Bioglass® 45S5 12.7-15.1 $x10^{-6}K^{-1}$) and the variety of different environments present within the human body [200][201]. Achieving densification of Bioglass at temperatures significantly lower than T_g through cold sintering could overcome the challenge of mismatching thermal expansion coefficients. Whilst the ability to produce composites of Bioglass with a range of other materials could enable the creation of implants which are specifically tailored to the application.

This chapter initially describes the use of cold sintering to densify Bioglass® 45S5. The potential for the cold sintering process to create Bioglass coatings on Titanium (a commonly used orthopaedic implant material) and Bioglass-polymer composites at low temperatures is then explored and the biocompatibility of the composite samples assessed.

6.2 Starting Materials

A 5 wt.% Bioglass in ethanol suspension was prepared and passed through a microfluidizer 5 times. Particle size analysis was conducted after each pass with the results are shown in Figure 83.

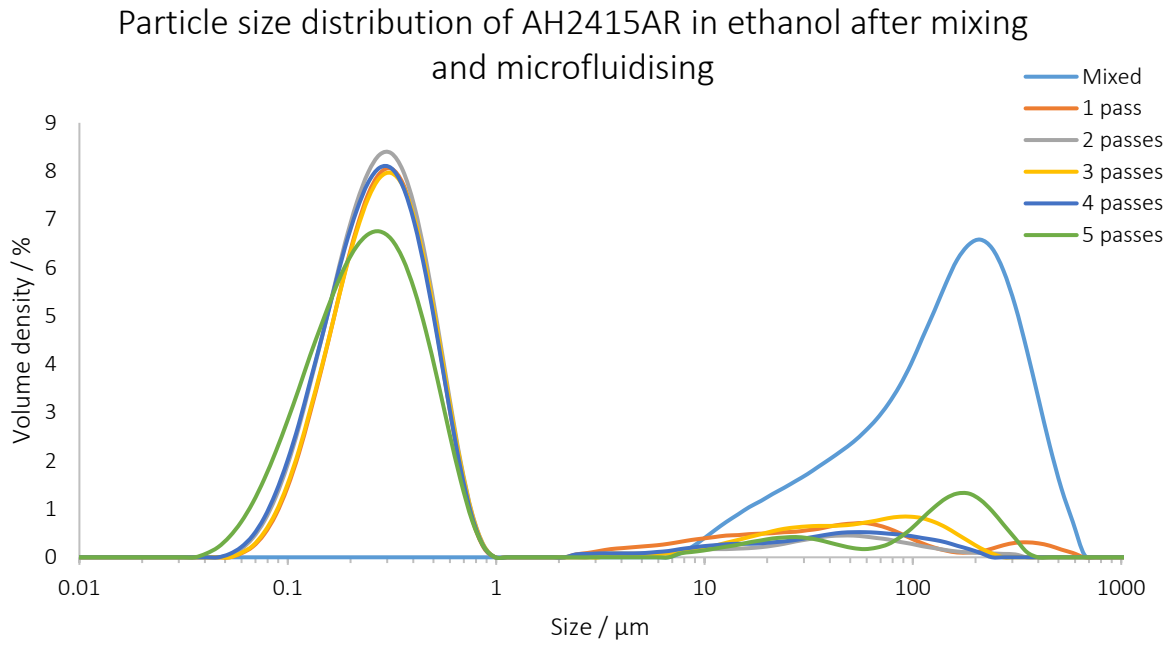

Figure 83: Particle size distribution of flame-spray bioactive glass (Batch: AH2415AR)

After being passed through a microfluidizer, most particles were between 0.1 and 1 µm (Average D_{50} of microfluidised samples 0.32 µm). Prior to microfluidising, the particle size analysis indicated the presence of a significant volume density of larger particles, which can be partly attributed to lightly agglomerated powder (Figure 84A), which are subsequently dispersed in the ethanol during microfluidisation. After 5 passes a small number of large particles are still observed, which are attributed to more compacted agglomerates (Figure 84B) and spherical particles (Figure 84).

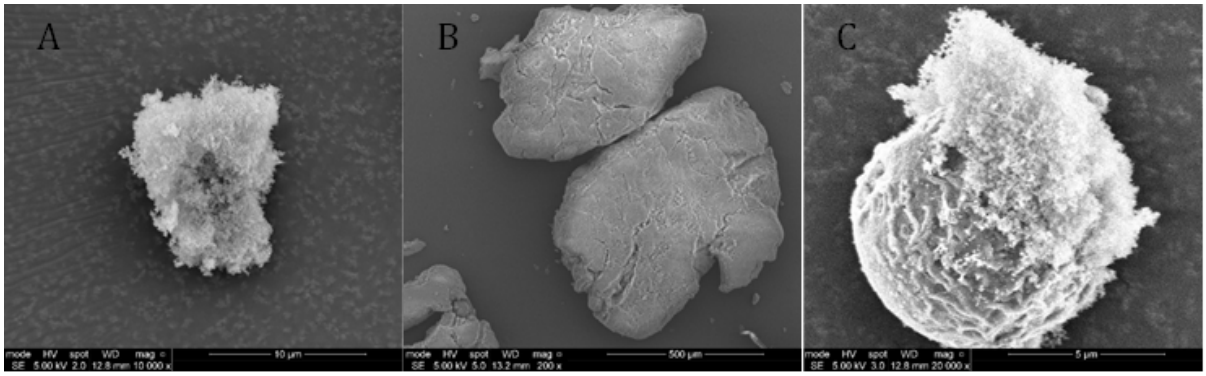

Figure 84: Examples of lightly (A) and densely (B) agglomerated material and spherical particles (C) observed under SEM of powder AH2415AR.

Cold sintering of the Bioglass (AH2415AR batch) with 80 wt.% water achieved mechanically stable pellets. SEM of the pellet surface and internal fracture surface of a cold-sintered pellet (Figure 85) show that the samples are well densified. The scratch-like surface features on the sample in Figure 85a, are caused by imperfections in the surface of the die. Some regions of the fracture surface appear to be more tightly bonded (Figure 85b), which is likely to be remnants of the agglomerates seen within the starting powder. The spherical particles seen in the as-received powder are still present in the sintered sample; these particles range from ~1-15 μm and are distributed randomly throughout as shown in Figure 85d.

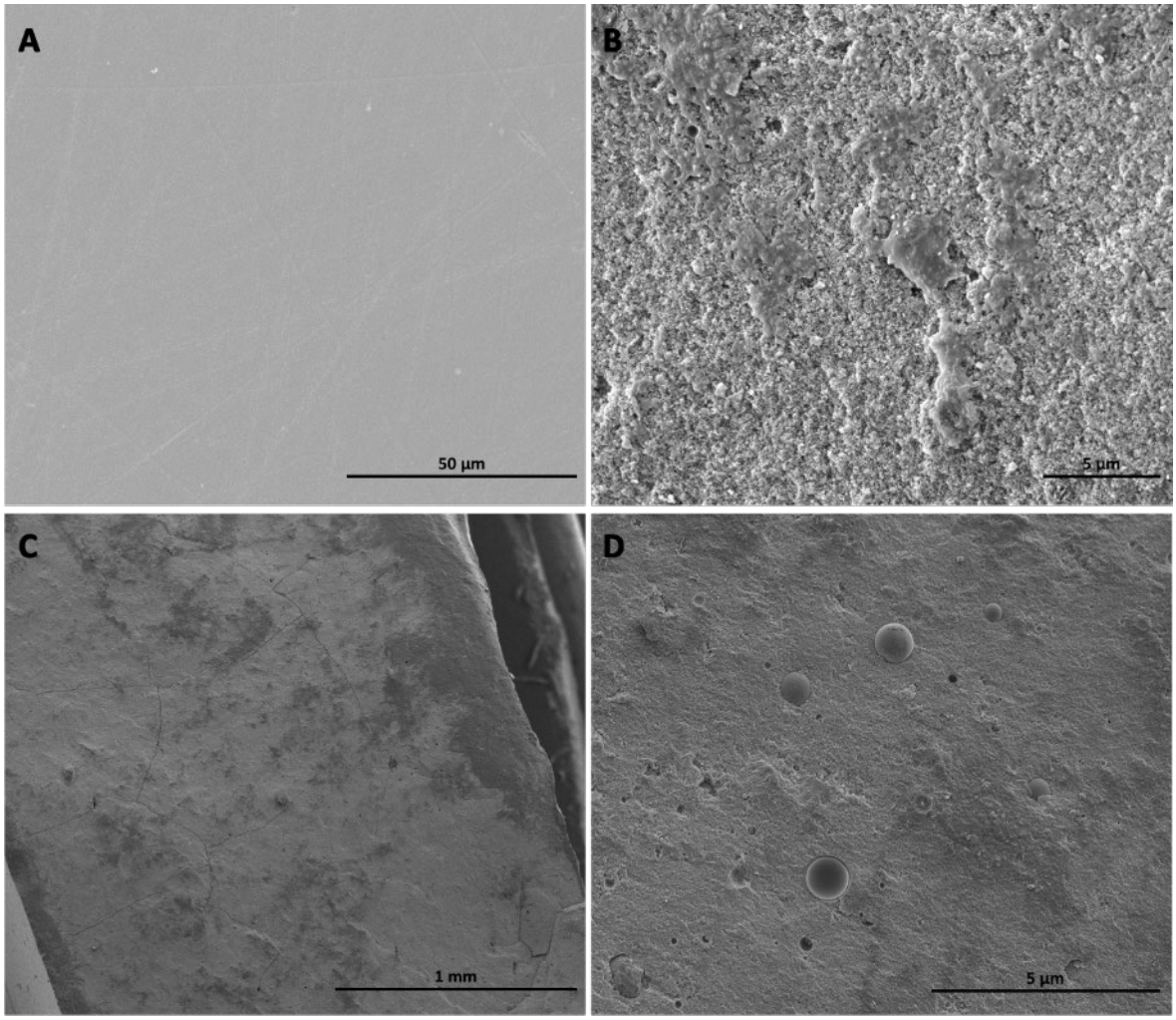

Figure 85: SEM of pellet surface (A, B) and internal fracture surface (C, D) of cold sintered Bioglass pellets

The spherical particles range in size and their morphology inconsistent with examples shown in Figure 86. The spheres can consist of hollow shells, which are either smooth and dense or lightly joined whilst some spheres have complex, partly filled structures. These particles are produced during flame spray pyrolysis (FSP) where the conditions emulate those in the related technology, flame-spheroidization.

Flame-spheroidization is commonly used to transform the morphology of a powdered material of a desired composition using a thermal spray gun. The addition of a porogenic material in the feedstock (such as calcium carbonate) can be used to tailor the internal structure of the spheres as it decomposes and encourages the formation of pores within the molten glass. It has been used by several researchers to transform calcium phosphate glass powders into microspheres with various morphologies using changes in feedstock size, ratio of porogen to glass and the nature of the oxy-acetylene flame [260]–[262]. The spherical particles seen within the AH2415AR batch of Bioglass indicates the presence of conditions within the flame spray

where gas or a thermally decomposing material becomes entrapped by molten glass. *Gupta et al*. also showed compositional variations between feedstock powders and microspheres caused by differences in boiling points of component materials and particle sizes [262].

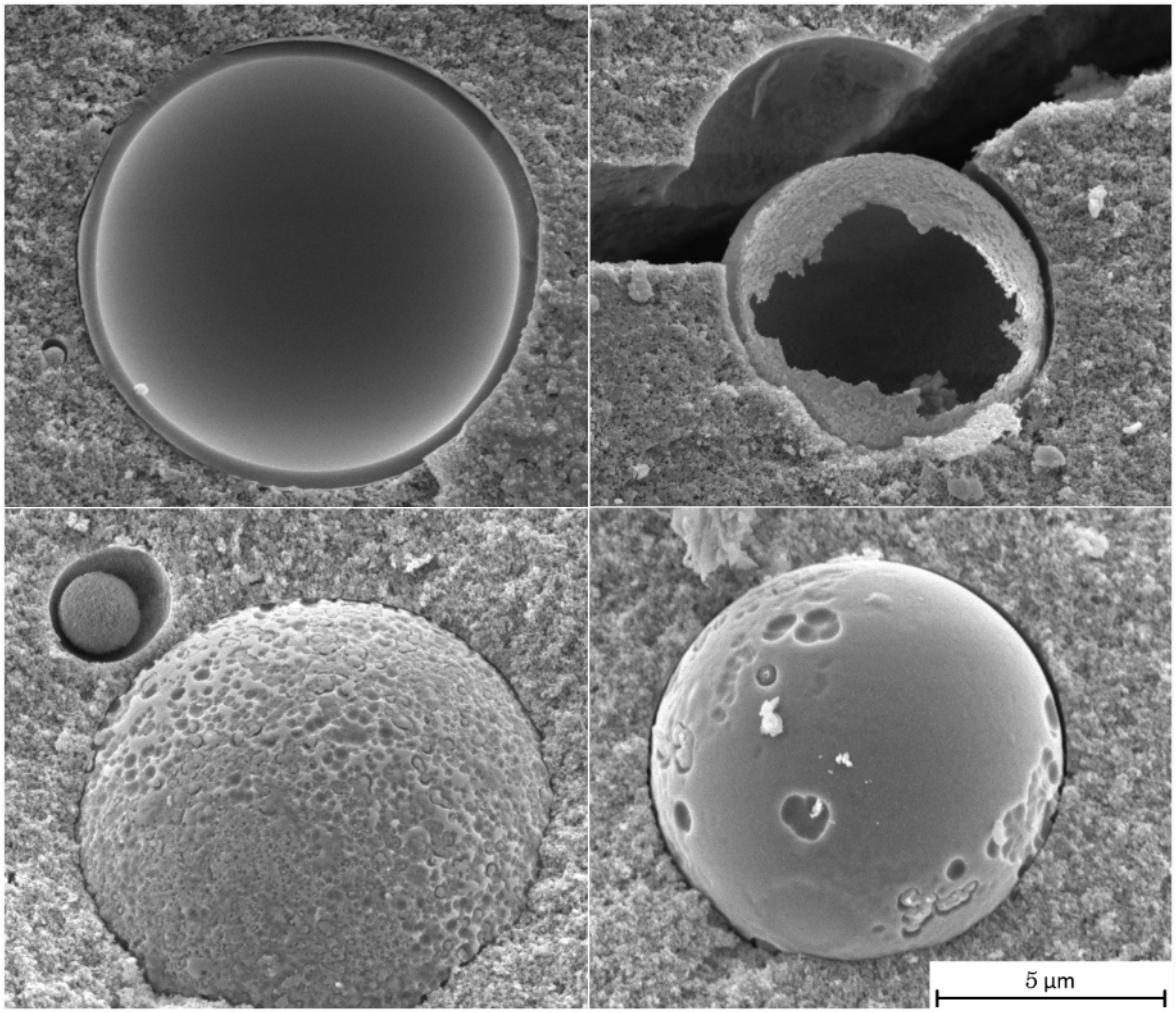

Figure 86: SEM of a number of different morphologies of the spherical particles observed in powder from the AH2415AR batch.

Although spherical particle morphologies are commonly produced *via* flame-spray pyrolysis and flame spheroidization, they were not the desired particle morphology in this case. The presence of these spherical particles at or near cracks (Figure 85 and Figure 86, above) in the cold sintered sample may indicate that they act as sites for crack formation and/or propagation. They could therefore potentially be deleterious to the structural integrity of the components produced. The starting reagents and processing parameters for flame spray pyrolysis were therefore altered for subsequent batches. Utilizing Methanol/Ethanol as an alternative to Xylene reduced residual carbon within the material, which is also likely to contribute to the reduction

in the prevalence of spherical particles as this indicates a minimization of CO_2 gas evolution which would act as a porogen.

SEM of the second batch of FSP Bioglass powder (17AH2416L) is shown in Figure 87. In this batch, no spherical particles were observed in the as-received powder, due to the change in processing parameters. A significant proportion of the powder appears to be agglomerated, as with the materials in Batch 1. However, the agglomerates are smaller than those observed in the initial batch, up to 200µm, compared to ~500 µm agglomerates, as shown in Figure 84b. Particles with a long, thin morphology are also observed within the agglomerated particles (Figure 87c).

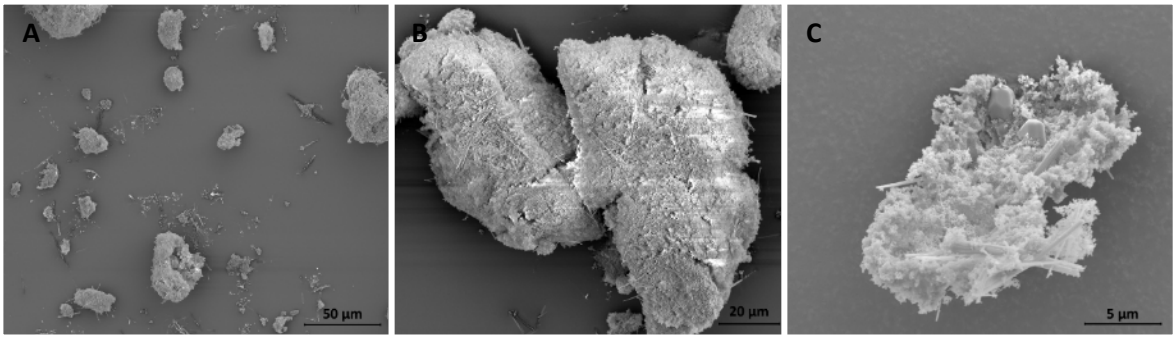

Figure 87: Particles within Bioglass® 45S5 batch 17AH2416L

The particle size distribution shown in Figure 88 of the second batch of Bioglass was performed on dry powder using a Mastersizer 3000 Aero. The average particle size within this batch is much larger (D_{50} = 14.9 µm), although the prevalence of very large particles and agglomerates is lower.

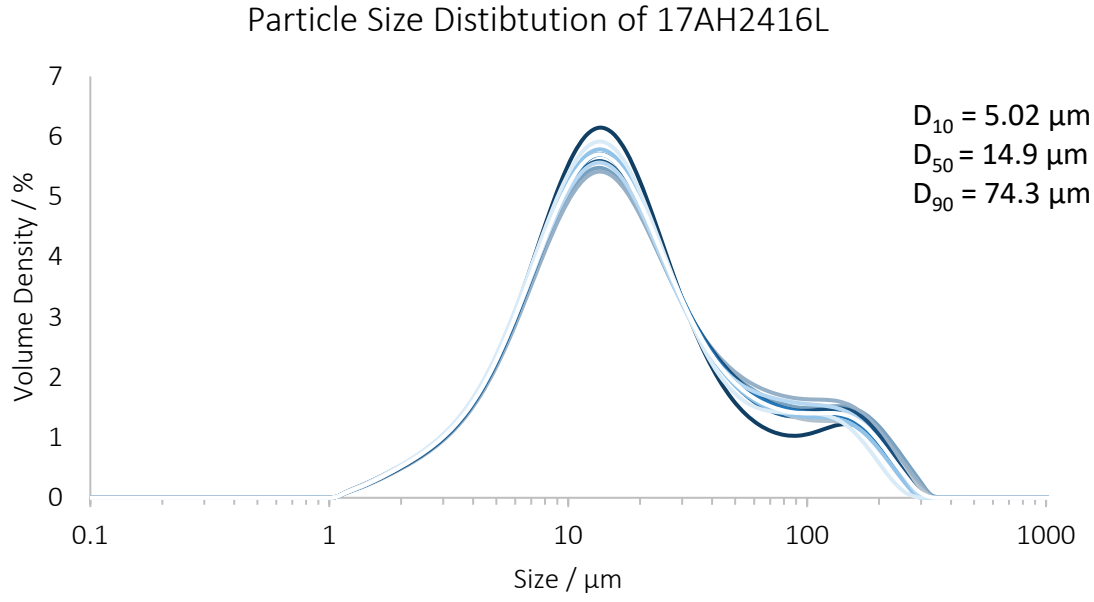

Figure 88: Particle Size Distribution of 17 17AH2416L

The cold sintered pellets using batch 17AH2416L were mechanically stable with good handling characteristics. The pellet surface structure is again highly influenced by the contact surface with the die faces, with any scratches or indentation being transferred (Figure 89a). Some surface regions appeared to have multi-scale porosity (Figure 89b). There is also evidence of the long, thin particles observed in the powder being retained through the cold sintering process, although their size has been reduced (Figure 89c). This reduction in size is due to particles of large aspect ratio being broken during the grinding stage required for the powder to become fully mixed with the distilled water.

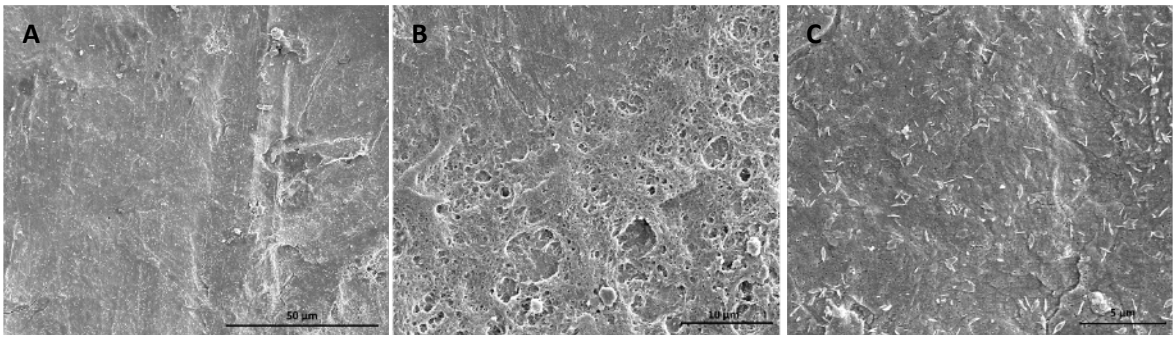

Figure 89: Pellet surface of cold sintered 17AH2416L

The fracture surface of cold sintered Bioglass, shown in Figure 90 indicates that the microstructure is not homogenous, with more compacted regions of diameter 5-10μm surrounded by finer grains. The regions which appear to be denser are of the same order of magnitude as agglomerate particles in Figure 87b and are therefore likely to be retained from the powder.

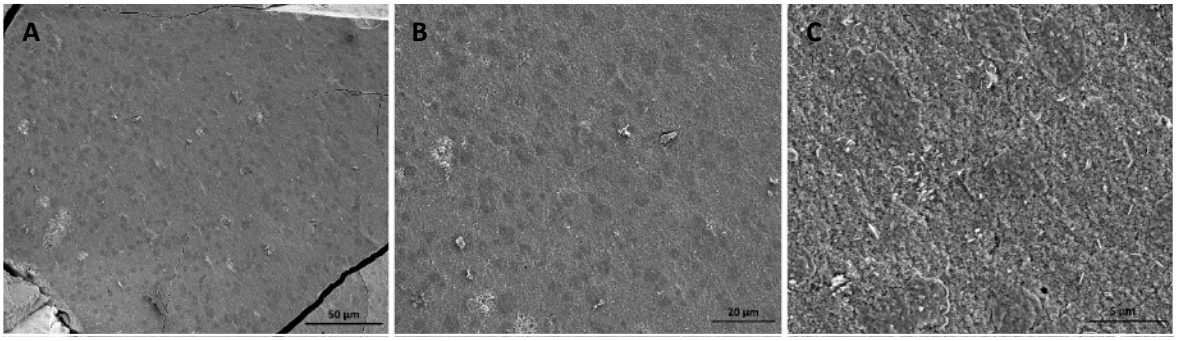

Figure 90: Internal fracture surface of cold sintered 17AH2416L pellet

Silicon and phosphorous NMR was performed on the two batches of Bioglass to better understand the effect of the changing processing parameters on the structures and network connectivity within the material. Comparing the ^{29}Si NMR of the as

received powders, shown in Figure 91, the network connectivity is significantly altered by the change in starting reagents and processing temperatures.

The number of Q_4 species is reduced by over half in the 2nd batch (17AH2416L), whilst all other Q species are increased. This higher proportion of Q_4 silica and the associated higher overall connectivity of the silica network indicates that the speherical particles observed within the AH powder are likely to be Si-rich regions.

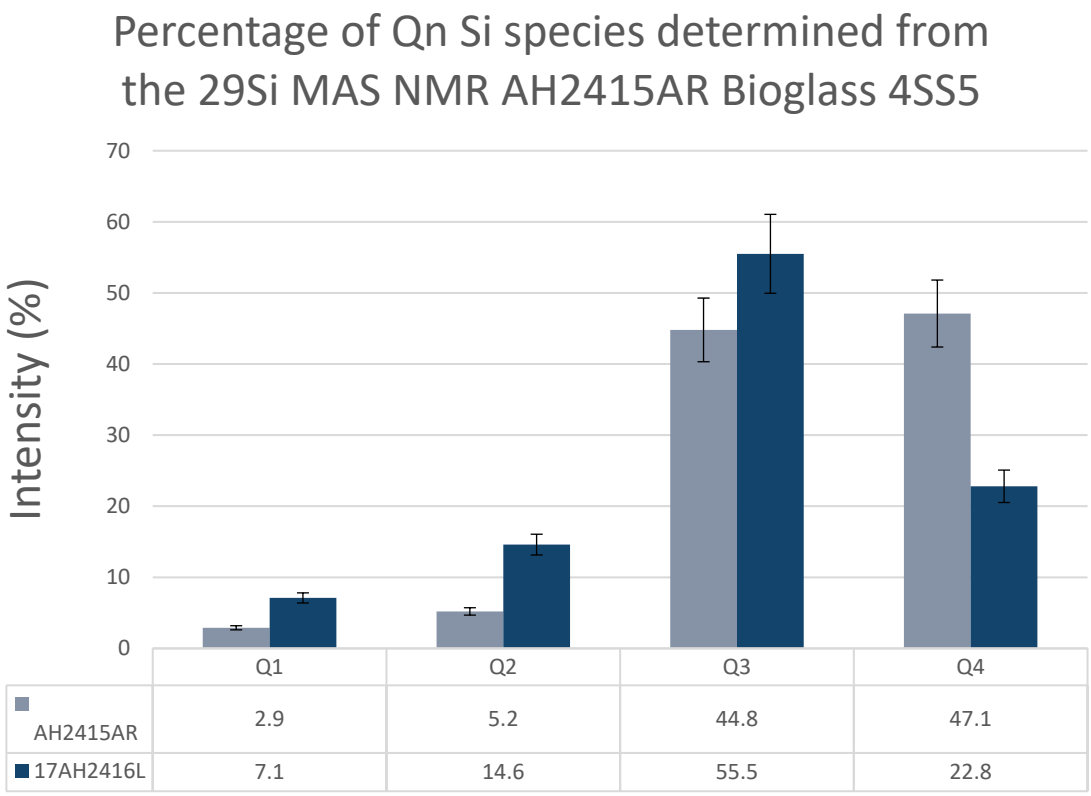

Figure 91: ^{29}Si NMR of as received materials

Similar to the Silicon NMR, the phosphorus species present in the material is affected by the changes in processing parameters and starting reagents. In the AH2415AR (Batch 1) material, the proportion of Q_1 and Q_2 is approximately equal (~48 %), with a very low amount of Q_3 tetrahedra. In contrast, the Q_1 species is the most prevalent within the 17AH2416L (Batch 2) material and Q_3 is increased, while Q_2 is significantly lower.

It is commonly reported that in phosphate containing Bioglasses, isolated orthophosphates are the predominant structural units. Tilocca *et al.* also report the presence of significant amounts of Q1 and Q2 species with increasing phosphorus content; the nature of the phosphorous bonding within the material being highly

dependent upon composition [263]. The ^{31}P NMR of FSP produced materials in this study (Figure 92) shows that in both batches, no orthophosphate (Q_0) is present in the as received state. This could indicate that a phosphorus network exists in very small, phase separated regions of the material. It is possible that the FSP method of manufacturing powder has led to this deviation from the reported structures due to rapid cooling from melt.

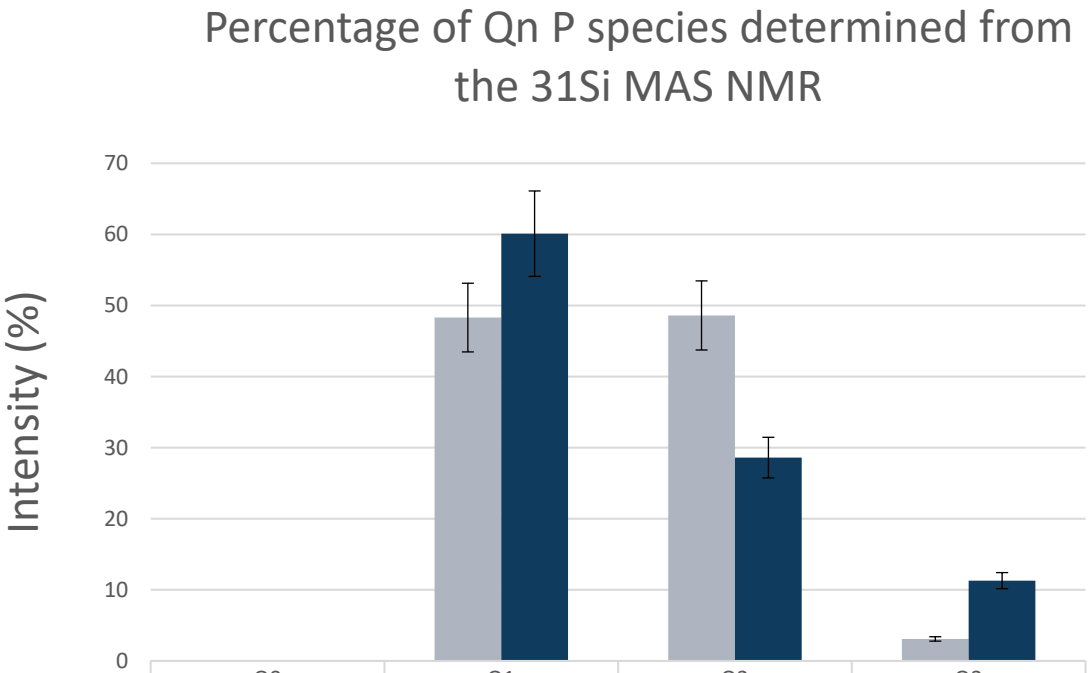

	Q0	Q1	Q2	Q3
AH2415AR	0	48.3	48.6	3.1
17AH2416L	0	60.1	28.6	11.3

Figure 92: ^{31}P NMR of as received materials

6.3 Understanding the mechanism of Cold Sintering Bioglass

To understand the mechanism of the cold sintering process and how it affects the structure within the Bioglass, ^{29}Si and ^{31}P NMR was also performed on wetted and sintered material of both AH2415AR and 17AH2416L batches. This has allowed a greater understanding to be gained of how the intrinsic solubility of Bioglass relates to its suitability for cold sintering.

The evolution of Q_n silica species within AH2415AR during the cold sintering process is shown in Figure 93. "Wetted" samples are weighed, and mixed with the appropriate volume of distilled water and mixed in a pestle and mortar. As distilled water is added to the powder, the Si network connectivity is reduced. This change in network connectivity is characterised by the significant reduction in Q_4 species and an increase in the proportion of Q_1, Q_2 and Q_3 species. After sintering, the Q_1 species percentage is reduced to below that of the as received powder, whilst there is a small reduction in the proportion of Q_2 and Q_3 remaining above the levels seen in the as received powder. There is an increase in the Q_4 after sintering, although it does not recover to levels seen in the as received powder, this indicates that the overall Si network connectivity is reduced by cold sintering of the powder.

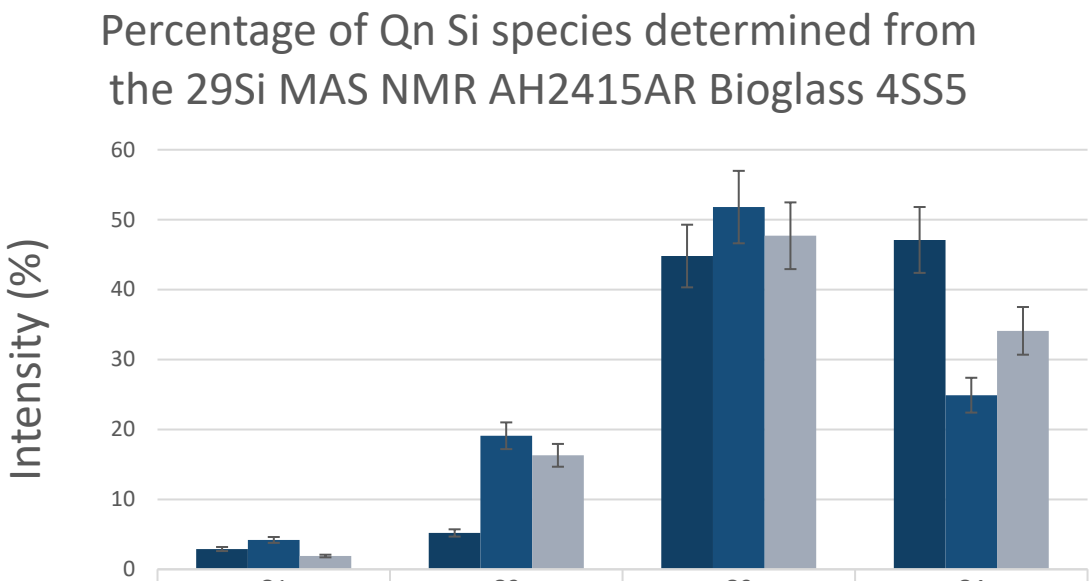

	Q1	Q2	Q3	Q4
As Received	2.9	5.2	44.8	47.1
"Wetted"	4.2	19.1	51.8	24.9
Sintered	1.9	16.3	47.7	34.1

Figure 93: ^{29}Si NMR data of as received, wetted and sintered AH2415AR powder.

The effect of the stages of cold sintering on the ^{31}P species observes in the AH2415AR batch are shown in Figure 94. There was no orthophosphate (Q_0) observed in the as received and sintered powder, the addition of distilled water releases a small amount of Q_0 phosphate ions. The proportion of Q_2 and Q_3 phosphate increases with the addition of distilled water, whilst the amount of Q_1 reduces. After sintering, the percentage of orthophosphate ions returns to zero. The Q_1 increases to above the levels observed in the as received powder in the cold sintered samples and the percentages of Q_2 and Q_3 are seen to decrease.

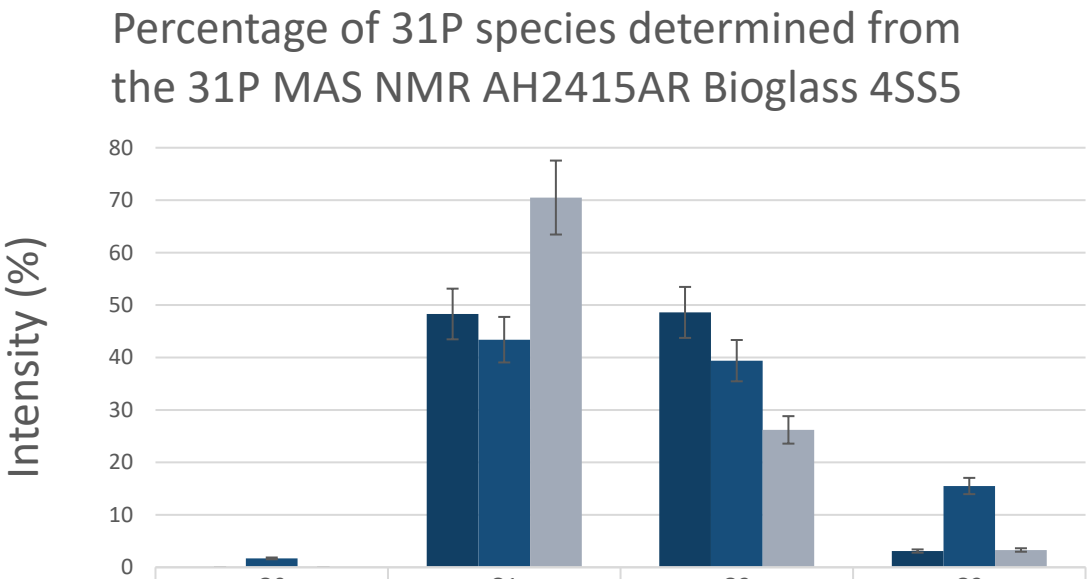

	Q0	Q1	Q2	Q3
As Received	0	48.3	48.6	3.1
"Wetted"	1.7	43.4	39.4	15.5
Sintered	0	70.5	26.2	3.3

Figure 94: ^{31}P NMR data of as received, wetted, and sintered AH2415AR powder.

Figure 95 shows how the proportion of the Qn silica species changes during the stages of the cold sintering process in the 17AH2416L batch. The powder wetted with 80 wt.% distilled water shows a significant decrease in Q3 species, whilst all other species increase. After cold sintering, the proportion of Q2 species continues to increase. Q1 and Q4 species decrease after sintering to levels below those seen in the as received powder. The amount of Q3 species increases but does recover to the level of the as received powder. The overall Si network connectivity is again shown to reduce when the powder is wetted and then increase again after the materials is sintered.

-

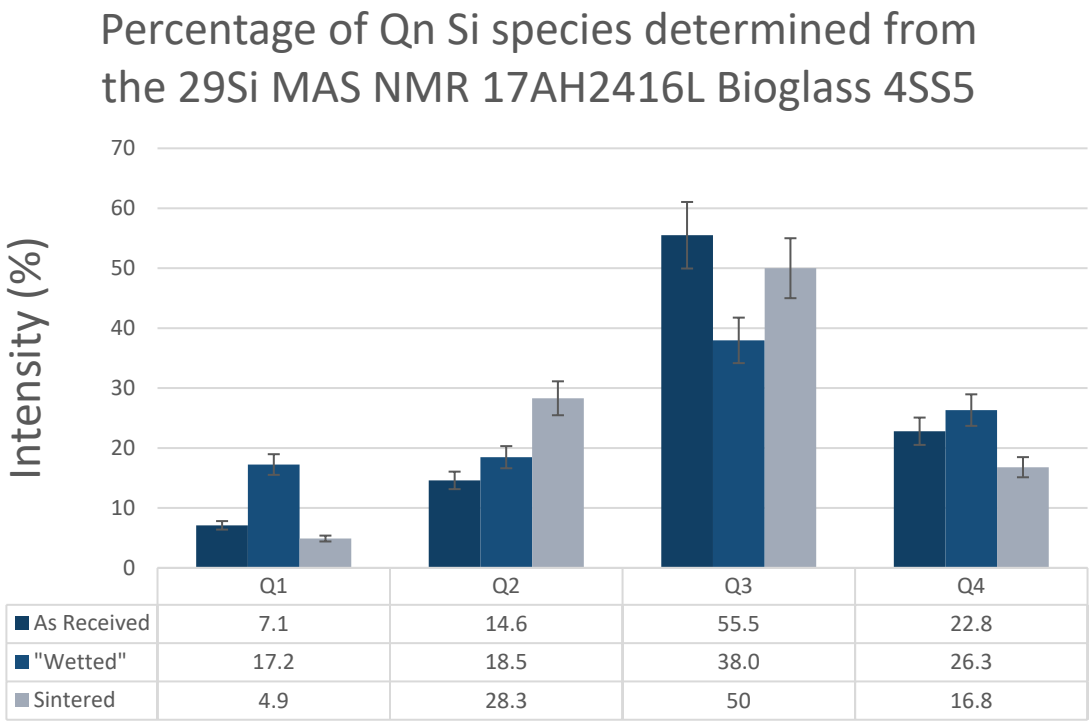

	Q1	Q2	Q3	Q4
As Received	7.1	14.6	55.5	22.8
"Wetted"	17.2	18.5	38.0	26.3
Sintered	4.9	28.3	50	16.8

Figure 95: ^{29}Si NMR data of as received, wetted and sintered 17AH2416L powder.

The proportions of ^{31}P Q species at the stages of cold sintering are shown in Figure 96. There was no orthophosphate (Q_0) observed in the as received and sintered powder, the addition of distilled water releases a small amount of Q_0 phosphate ions. The proportion of Q_2 and Q_3 phosphate increases with the addition of distilled water, whilst the amount of Q_1 reduces. After sintering, the percentage of orthophosphate ions returns to zero. The Q_1 increases to above the levels observed in the as received powder in the cold sintered samples and the percentages of Q_2 and Q_3 are seen to decrease.

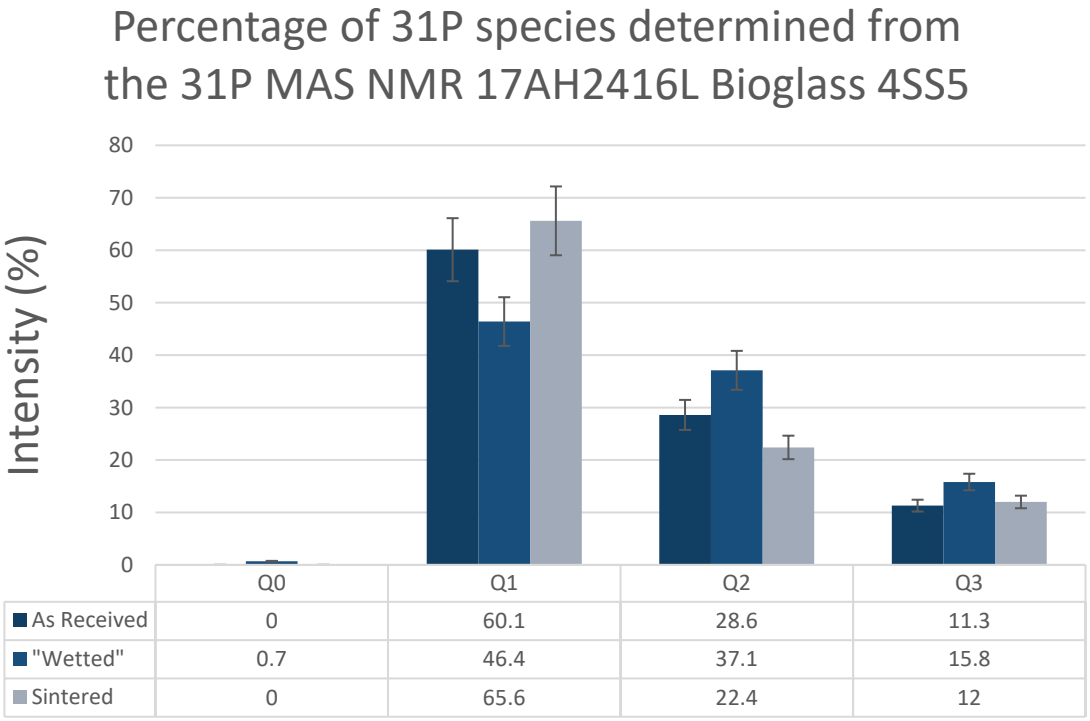

Figure 96: ^{31}P NMR data of as received, wetted and sintered 17AH2416L powder.

Bioglass® 45S5 is designed to interact with fluids within the body and has a well reported order of interfacial reactions, as discussed in section 2.7. These reactions are relevant to the mechanisms in cold sintering by the NMR due to the added water and the first five stages of interfacial reactions in Bioglass are presented again in Table 17 for ease of reference in the following discussion.

Table 17: First five stages of interfacial reactions of bioactive glass within the body leading to the formation of bonding with bone [172], [174], [177], [179], [191]

Stage	Interfacial Reaction	Time (h)
1	Alkali ions exchange with H^+ or H_3O^+ from body fluids	
2	Network dissolution and formation of SiOH bonds	
3	Silica-gel polymerization: SiOH + SiOH → Si–O–Si	1
4	Adsorption of amorphous Ca + PO_4 + CO_3	
5	Crystallization of the HCA layer	2

The NMR of wetted AH2415AR powder showed an increase in Q_1, Q_2 and Q_3 Si species compared to as received powder. A similar increase is observed in the Q_1 and Q_2 species of the 17AH2416L wetted powder. This increase in lower order Q species corresponds with an increase in non-bonding oxygens (NBOs), which in turn indicates

reduced connectivity in the network. This reduction in network connectivity can be attributed to network dissolution in the form of breaking Si-O-Si bonds and the formation of Si-O-H bonds. These changes are analogous to the mechanism proposed in the 2nd stage of the interfacial reactions of Bioglass during implantation and bonding. As soluble alkali ions are dissolved into the water from the powder they no longer act as network modifiers within the glass structure. The presence of dissolved alkali ions in the distilled water creates a solution with a higher pH, which in turn contributes to enhanced dissolution of the silica network.

The behaviour of Q_3 and Q_4 species of material is varied between the two batches and this is largely due to the difference in the structure of the as received powder. The speed of reactions in stages 2 and 3 is rapid and have been reported to overlap, which could also contribute to the differences between the Q species evolution in the materials; dissolution and repolymerisation reactions could be occurring simultaneously in different regions of the material [264]. The Q_4 increase in the wetted 17 batch material is indicative of the formation of a silica-rich regions due to the loss of alkali ions from the powder surfaces and condensation reactions leading to the formation of Si-O-Si bonds.

It is often reported that phosphorus in Bioglass® 45S5 is predominantly present as orthophosphate, however in this case the presence of orthophosphate was only detected within wetted powder and appeared to be reabsorbed into the main structure after sintering.

As with the silicon NMR, changes in the phosphorus species in both batches of Bioglass® 45S5 material also agree with the stages of interfacial reactions observed during the formation of bonding between bioactive glasses and bone. In stage 4 of these interfacial reactions, PO_4^{3-} and Ca^{2+} ions are adsorbed from the Bioglass and surrounding media, creating an amorphous layer of $CaO\text{-}P_2O_5$ on the silica-rich surface. This amorphous calcium phosphate layer subsequently crystallises in the 5th reaction stage to form HCA.

The general behaviour of the phosphorus within both batches of material is very similar although the magnitude of the changes in species varies. The evolution of Q_2 species differs with the addition of water between the two batches, with AH2415AR seeing a reduction and 17AH2416L seeing an increase. Levels of each of the species present in the as received powder is likely to affect this behaviour. In both batches, the "wetted" powder has very similar proportions of each species (Figure 97), despite

the differences in the as received powder. This could indicate that in the wetted powder, the species reach an energetically favourable distribution. The subsequent differences in the distribution of species within the materials after sintering is likely to have been influenced by the surrounding chemistry and the silica network structures.

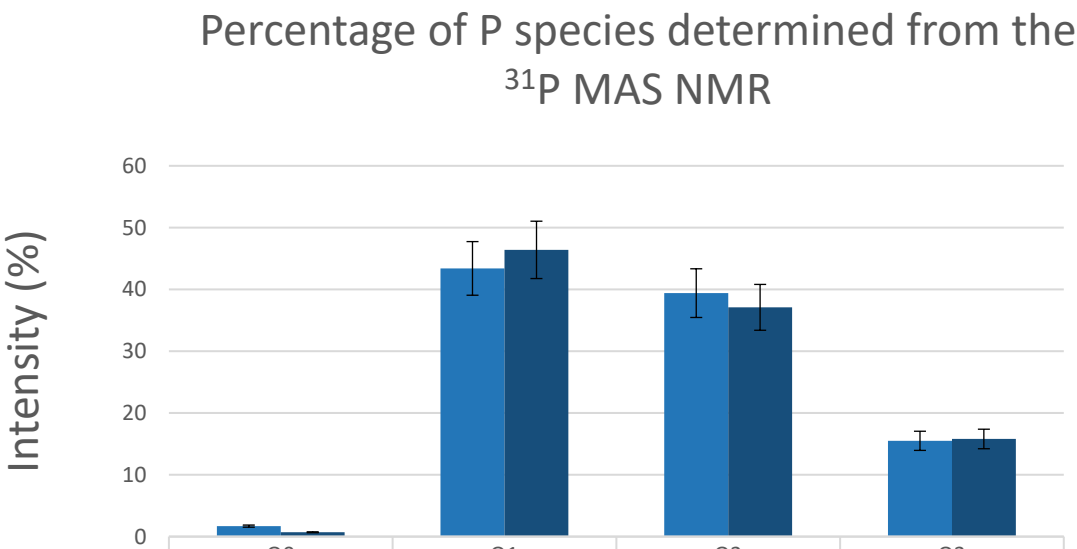

	Q0	Q1	Q2	Q3
AH2415AR Bioglass 4SS5	1.7	43.4	39.4	15.5
17 AH 24161 Bioglass	0.7	46.4	37.1	15.8

Figure 97: Phosphorus species within the wetted powder

The two batches of Bioglass produced by flame-spray pyrolysis demonstrate some variation in the structural changes occurring during the sintering process. This is due in part to the differences in the chemicals used in manufacturing and possibly the small sample sizes used for NMR. The five interfacial reactions presented in Table 17 occur rapidly in contact with aqueous solution and within the body, with a significant degree of overlap. It is therefore possible that the materials are measured at slightly different stages of the various reactions. However, in both batches of material, the structural changes can broadly be characterised by an initial reduction in the silica network connectivity with the addition of distilled water and a partial recovery of the network connectivity after the cold sintering stage. A reduction in silica network connectivity is expected in the wetted powder due to the creation of Si-OH bonds alongside the dissolution of alkali ions.

6.4 Cold sintered Bioglass

Cold sintering has been shown to produce mechanically stable, dense pellets of Bioglass using distilled water as the transient solvent. Figure 98 shows the XRD spectra of the as received powder and cold sintered pellets.

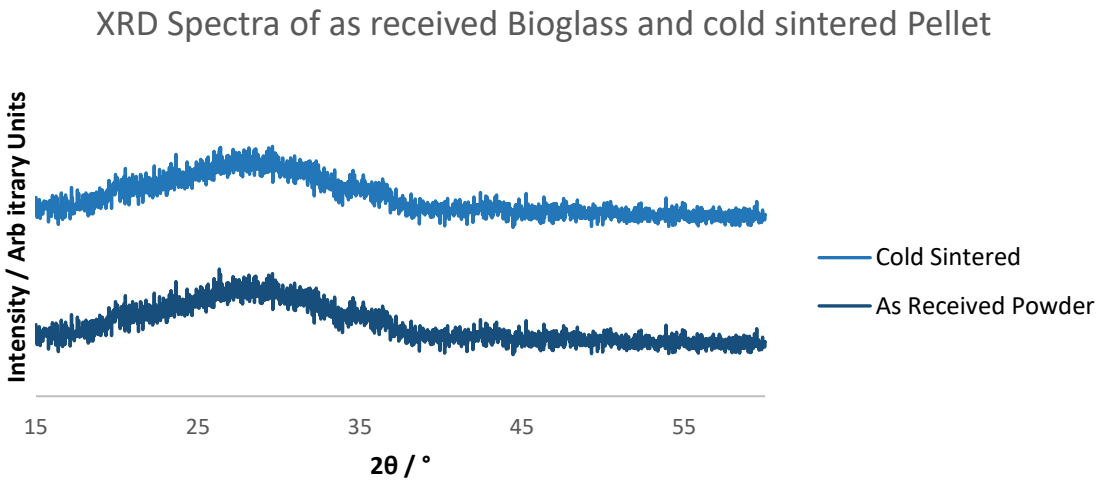

Figure 98: XRD of Powder and cold sintered pellet

The XRD spectra of cold sintered Bioglass are indicative of an amorphous material due to the diffuse scattering. From SEM however, there is some evidence of hydroxyapatite like phase beginning to form during the cold sintering process. Whisker-like structures with a morphology very similar to that of hydroxyapatite were seen across the samples, examples of which are shown in Figure 99, EDX indicated elevated levels of Calcium and Phosphorus in these structures compared to the surrounding material. Reflections associated with HCA are not present in the XRD spectra, this could be due to the low volume fraction within the material being below the detection limit of XRD (~5 vol.%) or the low time and temperatures not allowing for full crystallisation of the material.

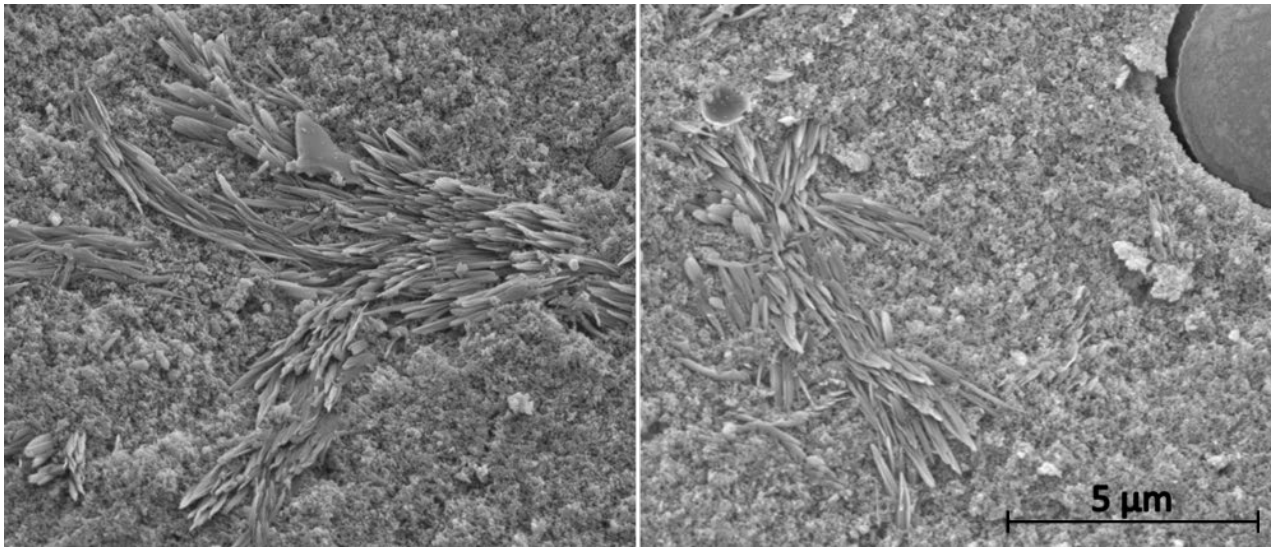

Figure 99: HCA-like structure on fracture surface of cold sintered pellets

Formation of HCA is often used as an indicator of bioactivity and numerous studies have been performed to investigate the effect of crystallinity on HCA formation [221]. The creation of Bioglass-based scaffolds and coatings is often dependent on high temperature deposition and sintering processes [265], [266]. These temperatures allow for the nucleation and growth required for the formation of a glass-ceramic, which can subsequently alter the bioactivity [191], [267]–[269]. Li *et al.* investigated how the proportion of residual glass in a heat treated bioactive glass (composition in wt.%: SiO_2 48, P_2O_5 9.5, Na_2O 20 and CaO 22.5) affected the formation of apatite in a synthetic physiological solution and reported decreases in apatite formation with reduction in weight percent of the amorphous phase [270]. Filho *et al*. observed the formation of crystalline HCA in the 45S5 system with up to 100 vol.% crystallinity, although the onset times are significantly increased as the amorphous content is lowered due to difference in ion exchange and silanol formation rates [267]. A similar delay in the onset of apatite formation has been reported in other bioactive glass compositions [271]. Dissolution has also been shown to be more uniform in amorphous glasses [185].

The low temperatures utilised in the cold sintering of Bioglass avoids the creation of conditions which would encourage high rates of crystallisation. Alongside the ability to densify the material without crystallisation, the use of significantly lower temperatures compared to conventional processing can enable a wide range of technological applications, such as the creation of polymer composite components, coatings and potentially components loaded with medicines to aid recovery [176]. Where appropriate, there is also scope to perform secondary heat treatments which

could allow for the tailoring of the rate of material dissolution through controlled crystallisation and subsequently the bioactivity of components.

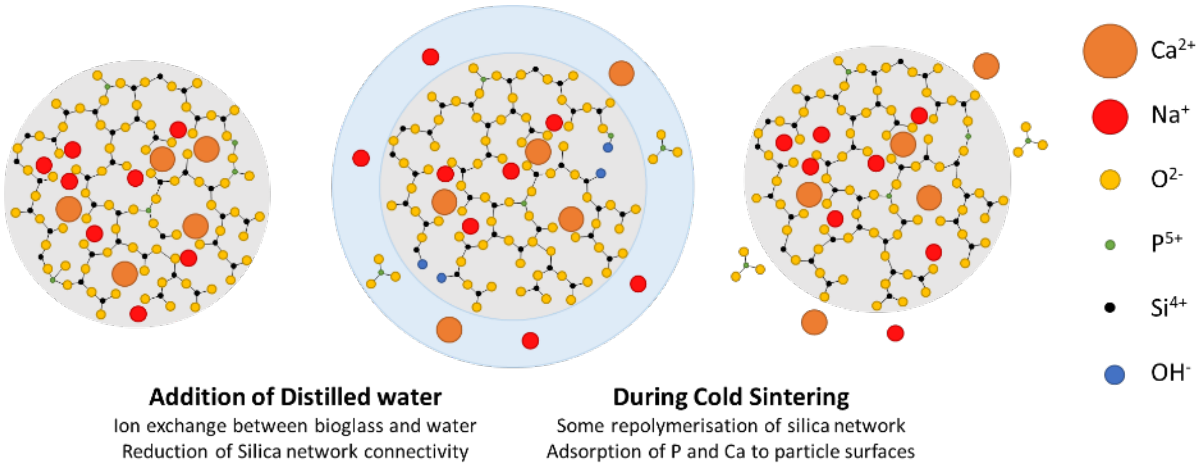

Figure 100: Schematic representation of the proposed mechanisms seen during the cold sintering of Bioglass® 45S5

6.5 PLA-Bioglass Composites

The mechanical properties of human bone vary considerably between trabecular (spongy) and cortical bone, and can therefore differ significantly from those of Bioglass® 45S5 ; a summary of reported values is given in Table 18. This mismatch in properties means that on its own, Bioglass® cannot be used as a direct replacement for bone in applications such as load bearing implant and polymer-Bioglass composites are commonly used, allowing for both mechanical and bioactive properties to be tailored.

Table 18: Comparison of the mechanical properties of trabecular bone, cortical bone, Bioglass after [191].

Material Property	**Trabecular bone**	**Cortical bone**	**Bioglass® 45S5**
Compressive Strength, MPa	0.1-16	130-200	500
Tensile Strength, MPa	n/a	50-151	42
Compressive Modulus, GPa	0.12-1.1	11.5-17	n/a
Young's Modulus GPa	0.05-0.5	7-30	35
Fracture Toughness MPa.m$^{1/2}$	n/a	2-12	0.7-1.1

A number of methods for producing Bioglass-polymer composites are discussed in section 2.8.2 Often these methods require a high degree of process control, specialised equipment and/or the use of solvents such as chloroform or DMC. Composites of electroceramic materials with polymers have been successfully produced using cold sintering and has been discussed in 2.3.7. Cold sintering of Bioglass is performed at 100 °C, which makes it an ideal candidate for producing composites with a wide range of polymers. PLA was chosen for this work due to it being a relatively low-cost material which is biocompatible and related to a wide range of commonly used polymeric biomaterials. The as received PLA powder has a broad particle size distribution of with a small number of particles smaller than 5 μm and most particles between 10 and 700 μm, as shown in Figure 101. The particles of PLA are therefore an order of magnitude greater than the Bioglass powder.

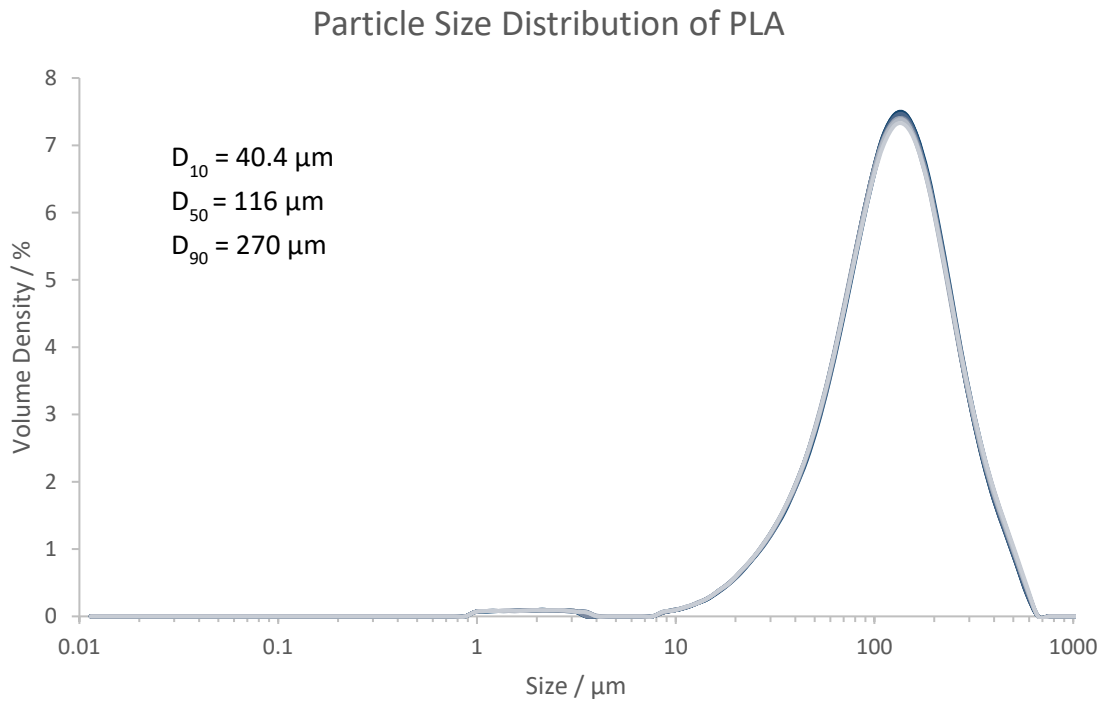

Figure 101: PSA of PLA powder

SEM of the PLA powder (Figure 102) shows that the particles have an irregular size and morphology, with a rough surface texture. There is also indication of "ribbons" of material extending from the surface of some particles [272]. Table 19 shows composite compositions produced from PLA and Bioglass.

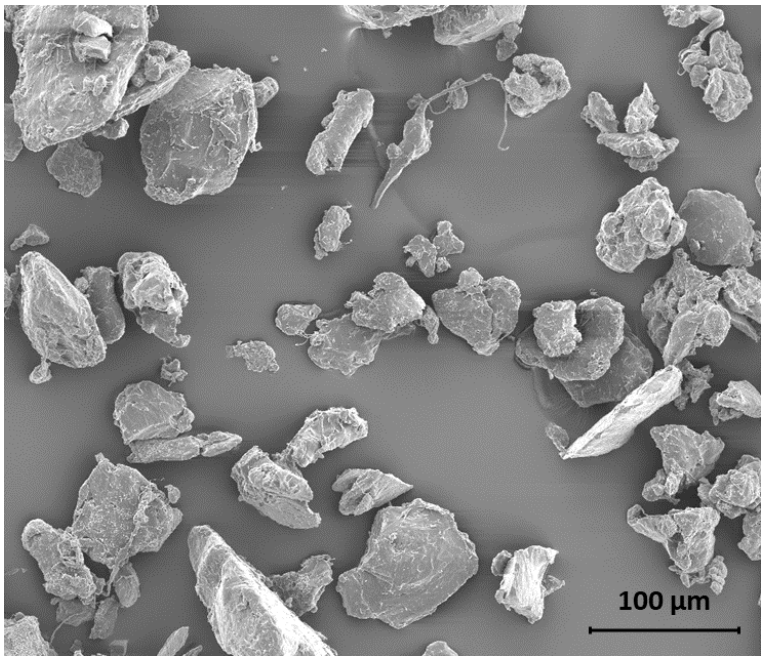

Figure 102: SEM of PLA Powder

Table 19: PLA-Bioglass composite compositions in mass % with approximate volume fractions.

	Polymer Mass %	Bioglass Mass %	Polymer Vol %	Bioglass Vol %	Cytotoxicity Testing
A	100	0	100	0	✓
B	80	20	90	10	
C	75	25	87	13	✓
D	60	40	77	23	
E	50	50	69	31	✓
F	30	70	49	51	
G	25	75	42	58	✓
H	0	100	0	100	✓

Optical images (Figure 103) show the surface of Bioglass/PLA composites after cold sintering. The pellets were mechanically stable and component materials appear to be well distributed within the samples. The homogeneity at smaller scales of the composites could be further improved by reducing the PLA particle size to be more comparable with the Bioglass powder. An attempt at cryomilling the powder did not successfully reduce particle size.

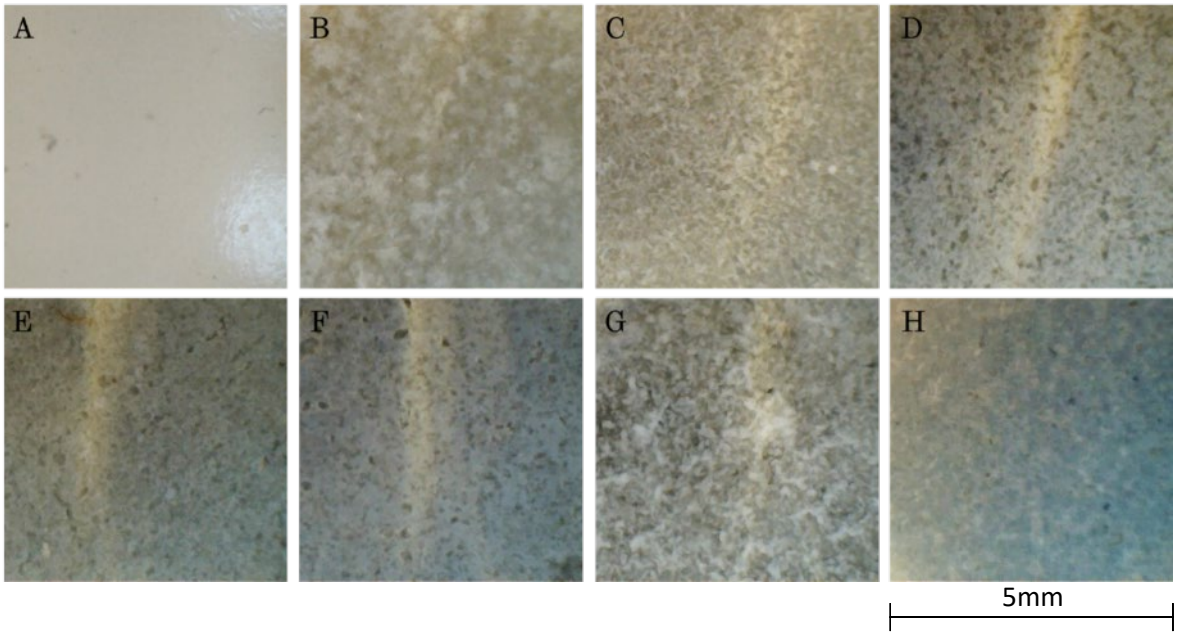

Figure 103: Optical images of cold sintered composite surfaces

Figure 104 shows SEM of the composite sample surfaces, which display regions of both the polymer and Bioglass phases. In the 100 wt.% PLA samples, the surface is predominantly smooth with a very low prevalence of pores. At the sintering temperature, the polymer particles have softened, and the applied pressure allows for a well densified material to be produced. As the content of Bioglass is increased isolated

Bioglass regions are seen on the surface which are similar in size to the agglomerates in the as-received material. Smaller particles of Bioglass are also seen attached to the surface of PLA particles. At 100 wt.% Bioglass, Figure 104h, the surface demonstrates some very fine pores and the presence of large aspect ratio particles as seen in the initial powder.

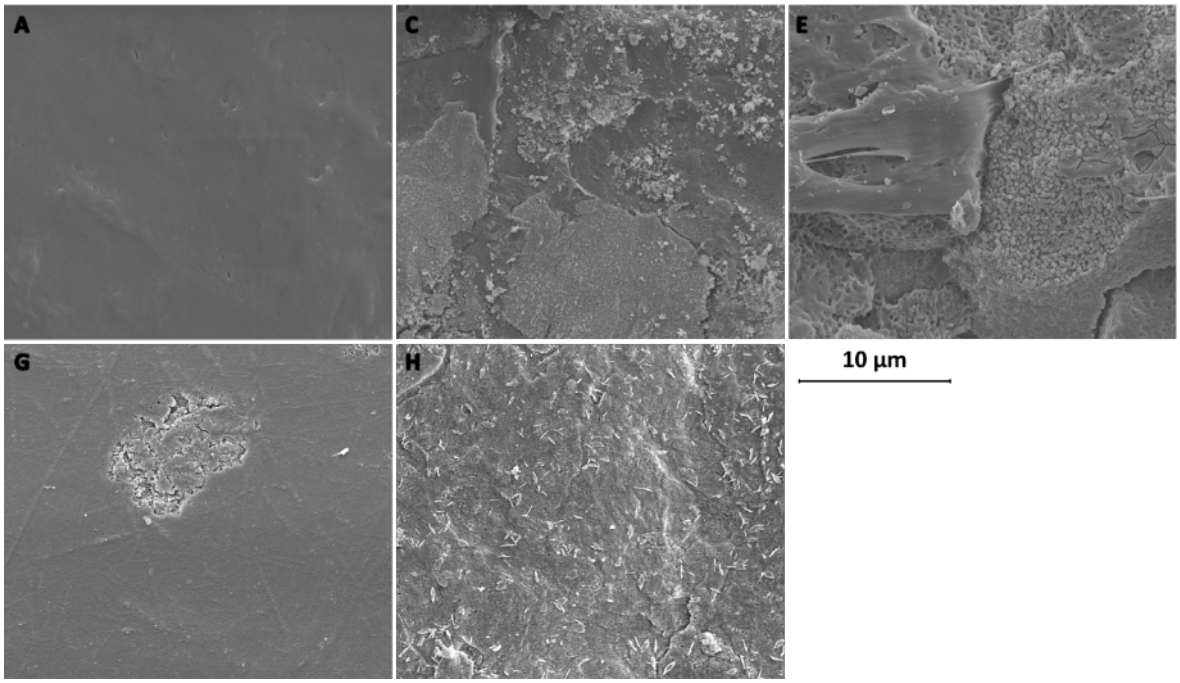

Figure 104: SEM of composite pellet surfaces. Inset figure labels are consistent with the sample designations in Table 19 and Figure 103.

Fracture surfaces of the composites shown in Figure 105 also aid the understanding of the interaction between the two component materials. The internal microstructure of the 100 wt.% PLA (Figure 105A) shows the particles have bonded together well and there is very low porosity. With increasing Bioglass content, as with the pellet surface, distinct regions of PLA and Bioglass can be seen on the fracture surface (Figure 105C, E and G). The large relative size of the PLA particles compared to the Bioglass is likely to contribute to the formation of these distinct regions, where the moistened Bioglass powder forms a layer around the particles on mixing and are then forced into the gaps between the PLA under applied pressure. In Figure 105G, where the Bioglass account for 60 vol.% of the pellet, the interface between the two materials is very distinct but the two particles of Bioglass appear to be well bonded the PLA surface.

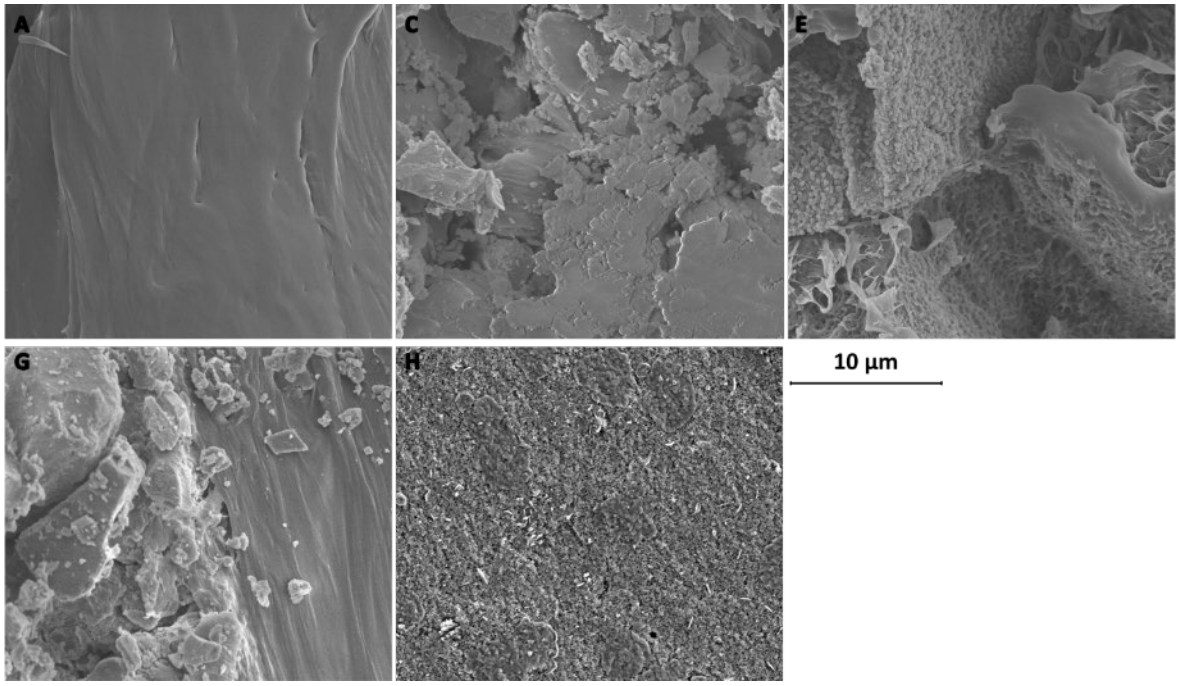

Figure 105: SEM of internal fracture surface of composite pellet. Inset figure labels are consistent with those in Table 19 and Figure 103.

Composites of PLGA/PDLLA and Bioglass produced by *via* TIPS by Boccaccini *et al.* and dissolution in chloroform by Tsigkou *et al*. the works have indicated the apparent upper limit of 50 wt.% Bioglass (approximately 30 vol.%) [206], [213]–[218]. This work has demonstrated the ability to produce a broader range of Bioglass-polymer composites, with up to ~60 vol.%. The cold sintering process for Bioglass-PLA composites is a relatively quick, simple process which would be capable of achieving higher volume percentages of Bioglass loading if required as both materials can be consolidated independently. A major advantage of the TIPS process to produce scaffolds is the ability to control the level of porosity and the morphology of the polymeric phase by altering processing parameters [217]. From SEM of the composites (Figure 104), the final microstructure appears to be strongly influenced by the morphology of the initial particles of the constituent materials. This suggests that if more complex, tailored microstructures are desired, this could be achieved by utilising alternative polymer particle morphologies.

Bone is a natural, hierarchical composite material which is exhibits anisotropic mechanical behaviours which can be complex due to structural heterogeneity [273], [274]. The cold sintering of multi-layered structures using electroceramics to create components with graded properties has been demonstrated by a number of authors [84], [105], [249]. Therefore, the ability to develop the cold sintering of Bioglass-polymer composites further to create biomedical components with graded properties

using a simple, adaptable process has great potential [275], [276]. By varying the composition of the composites, mechanical properties could be matched to the surrounding tissues whilst maintaining bioactivity which will encourage bone growth and subsequently stronger, longer lasting implant fixation.

6.6 Spontaneous behaviour of Bioglass: Polymer composites during ambient storage

When stored in a sample bag and stored in an ambiently humid environment for 3 days after sintering, some cold-sintered composite samples (17AH2416L) developed crystalline "whiskers" on the surface. The whiskers were long and thin, having relatively high levels of porosity as shown in Figure 106. These were most prevalent on the 50:50 weight fraction samples, where the polymer fraction may have acted to encourage growth by acting as nucleation sites for these crystallites.

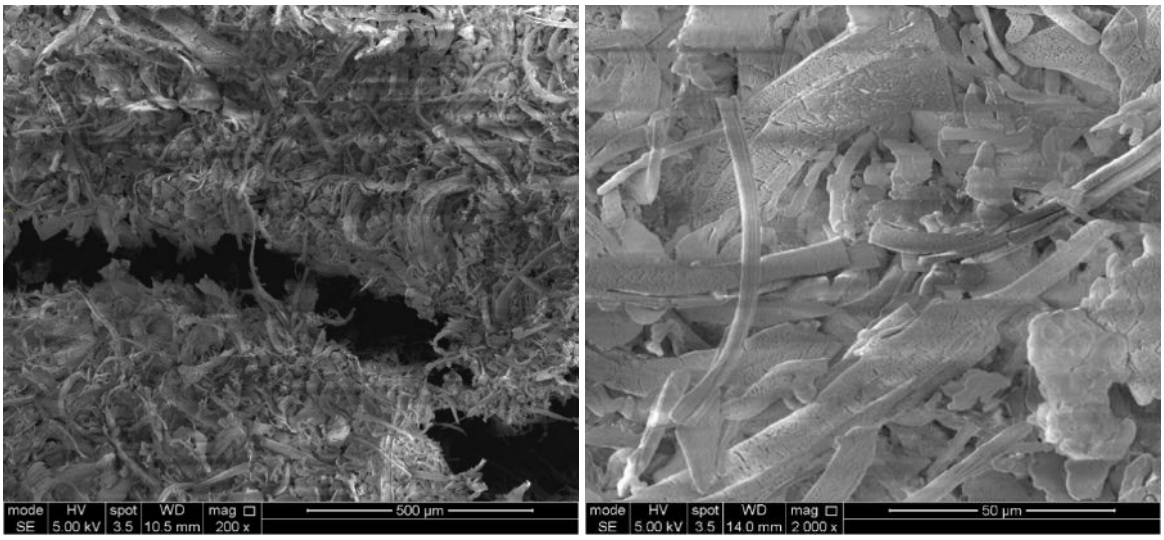

Figure 106: SEM of the crystalline phase which developed of the surface of the composite pellets.

The morphology of these whiskers is very different to that seen in the 100 wt.% Bioglass pellet fracture surface and indicates that the conditions with the cold sintering process are favourable to HCA formation. The development of these structures on the surface is a positive indication that the samples are highly reactive, even at low temperatures which would be beneficial to the rapid creation of interfacial bonding *in vivo*. Figure 107 presents XRD spectra of PLA, cold sintered Bioglass and Bioglass-PLA composites samples which had been exposed to the humid environment and produced the surface phase. Bioglass has previously been shown to maintain its amorphous structure after cold sintering (Figure 98), however, the Bioglass spectra in Figure 107 indicates the presence of a significant crystalline phase.

Due to the broadness of the peaks and comparatively low intensity, identifying the crystalline phases with confidence was not achievable. However, many of the reflections in the Bioglass spectrum correspond to a calcium carbonate ($CaCO_3$) phase, although this does not account for all the peaks. In the range of 2θ, PLA contains only a broad peak at 22.5°, from literature, further peaks also occur below the range measured here (approximately at 16 and 18°) with significant diffuse scattering [277]. In the 50:50 composite, as well as a significant amount of diffuse scattering, a large number of crystalline reflections are present. Some of these peaks can be attributed to the calcium carbonate phase seen in the Bioglass sample but determination of all phases present has not been possible.

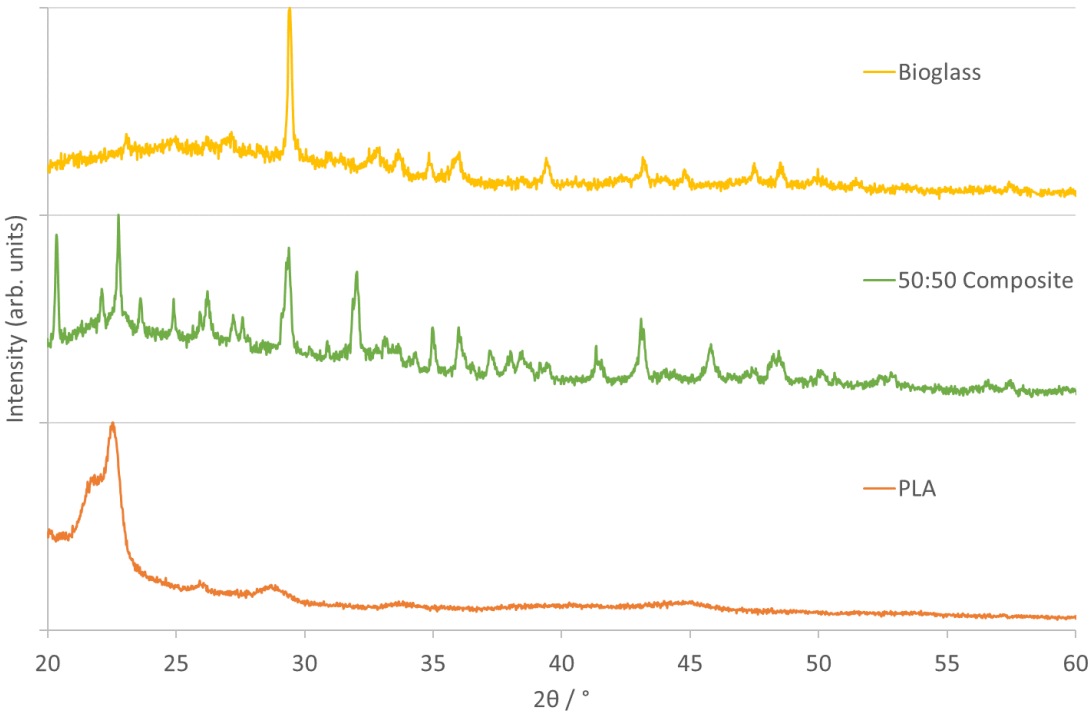

Figure 107: XRD spectra of 100 wt.% cold sintered Bioglass, 50 wt.% Bioglass composites and PLA

6.7 Cytotoxicity

Cytotoxicity testing was performed on cold-sintered PLA-Bioglass composite samples (as indicated in Table 19), with several iterations of testing required to achieve consistent results. To assess any potential cytotoxicity, sample are compared to tissue culture plastic (TCP) which is specifically designed to provide optimal conditions for cell culture work.

6.7.1 Test run 1

Cold sintered composite samples were initially sterilised in alcohol, which led to the yellow colour shown below (Figure 108a). This is due to the leaching of ions such as Ca^{2+}, Na^{+} and phosphate (PO_4^{3-}) from the samples, although the nature of the solution formed by the leaching was not investigated. When sterilised samples were added to the media, a colour change to pink/purple was observed (Figure 108b), indicating an increase in the alkalinity of the media. This change in pH is attributed to the continued leaching of Ca^{2+} and Na^{+} ions into the media. Such a significant deviation of the pH from the optimum level was likely to have a negative impact on the activity of the MG-63 cells.

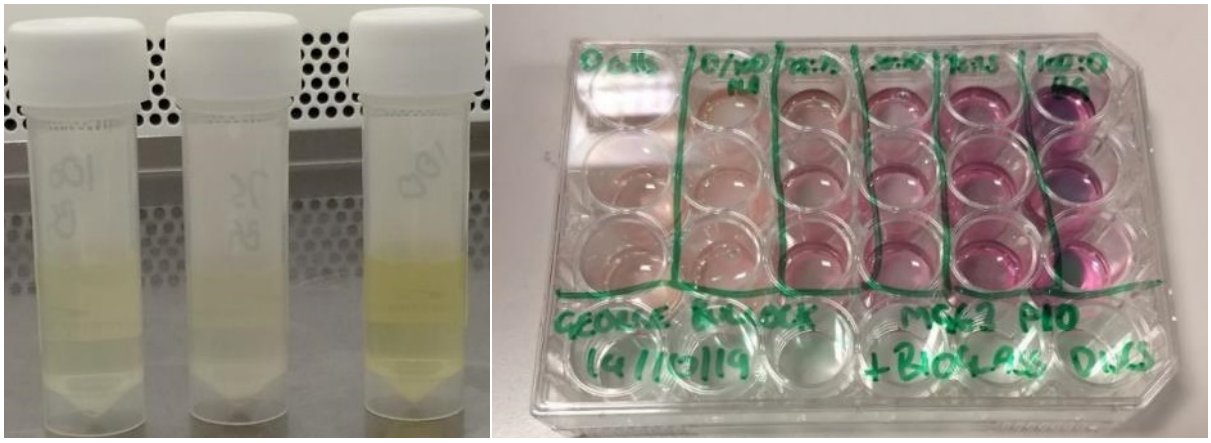

Figure 108: Example of alcohol after use to sterilise compoites (a), composite samples in seeding well with media (b)

Figure 109 shows the metabolic activity after 1 day. Due to an infection in a number of the wells, caused by contamination within the incubator, these results are not necessarily representative, and the test was terminated at 1 day. Further tests indicate that the infection in the wells was caused by an external factor and was not attributed to the samples. In Test 1, cells were seeded directly onto the surface of the composite samples.

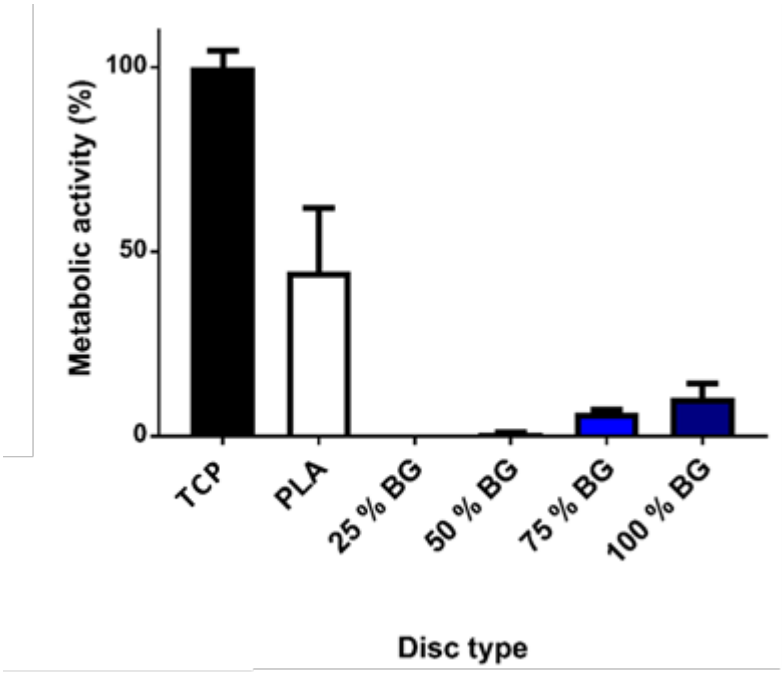

Figure 109: Metabolic activity after 1 day of incubation in test 1 n=3

6.7.2 Test run 2

Pre-conditioning of the samples in media should reduce the amount of leachable ions released during the cytotoxicity testing which should in turn lead to an improvement in metabolic activity. The metabolic activity of samples pre-conditioned overnight is shown in Figure 110.

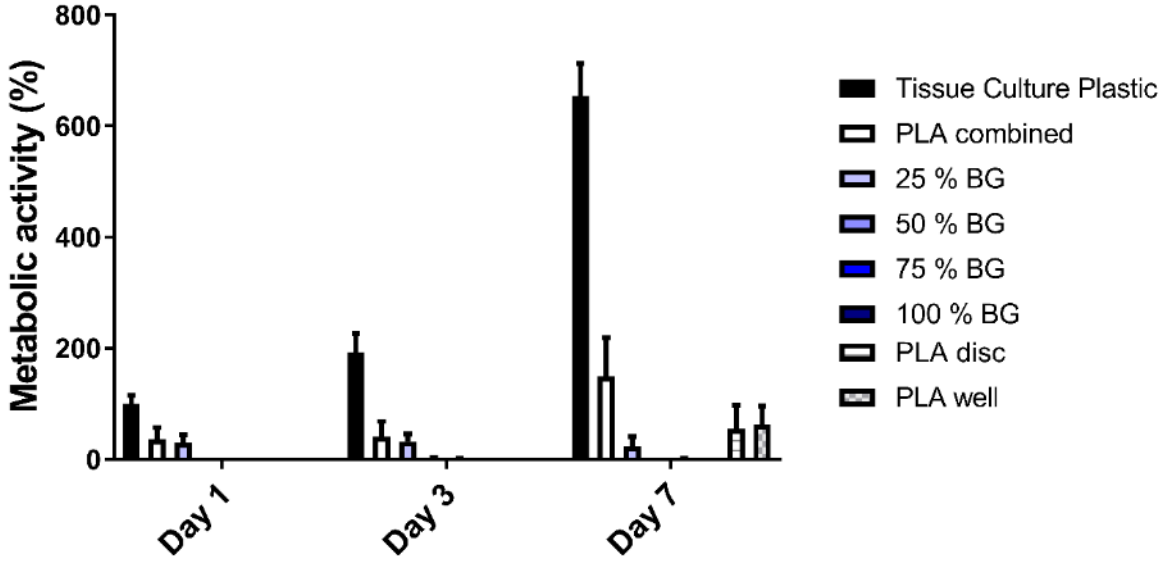

Figure 110: Metabolic activity at Day 1, 3 and 7 after an overnight pre-treatment in media n=3

A significant reduction of metabolic activity was seen in cells seeded onto cold-sintered samples when compared with TCP. The cells incubated with 100 wt.% PLA and 75:25 PLA-Bioglass composites show a small amount of activity. With increasing Bioglass mass fraction the activity continues to decrease, and very little activity is recorded, a number of factors may be contributing to the low levels of activity.

Pre-conditioning of Bioglass samples is commonly utilised in the assessment of cytotoxicity as *in vitro* testing is often performed in stationary systems and can be lead to unrepresentative results due to high concentrations of alkali ions. Ciraldo *et al*. preformed an extensive review of pre-conditioning protocols used in 29 studies of bioactive glasses and created a points system to recommend pre-treatment duration based on morphology and composition of the sample and the culture type and medium [224]. Based on this points system, it is recommended that the samples used for cytotoxicity testing in this study are pre-treated for at least 72 hours due to their low porosity, high sodium content and the use of α-MEM media in a static cell culture system [224]. This indicates that the overnight pre-conditioning step used was not sufficient to stabilise the pH of the media during incubation.

Table 20: Points system score sheet developed by Ciraldo et al. for the pre-treatment of Bioglass scaffolds for used in cell cultures adapted from [224].

Morphology	**Points**	**Medium/Buffer**	**Points**
Powder	1	TRIS	1
Monolithic, bulk	1	SBF	1
Low porous (<30%)	5	α-MEM	2
Highly porous (>31%)	10	DMEM	2
BG-Type	**Points**	**Culture type**	**Points**
<20 wt.% Na_2O	5	Highly dynamic	1
>21 wt.% Na_2O	10	Low dynamic	2
		Static	10

Total Points	**Recommended time of pre-incubation**
<10	1 h
11-20	24 h
21-24	48-72 h
>25	>72 h

This testing method also involved direct seeding of the cells onto the pellet surface. The surfaces of the composite pellets, consisting of larger polymer particles with regions of micron-sized Bioglass will have a significant level of roughness. Andrukhov *et al.* studied how roughness (R_a) of titanium, which is biologically inert,

affects the proliferation of MG-63 cells and showed significant reductions in cell growth with increased roughness, Figure 111 [278]. Roughness can contribute to low metabolic activity and/or cell growth as cells become entrapped [278], [279].

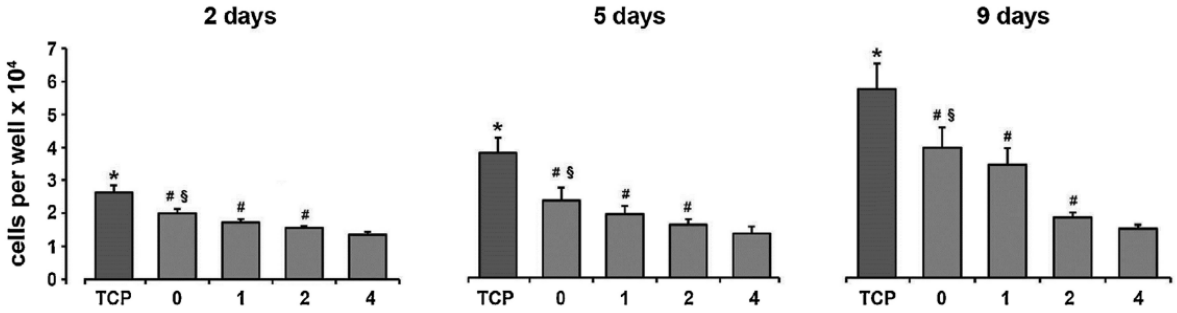

Figure 111: Effect of titanium surfaces with micrometre-scale roughness (R_a) on the number of MG-63 cells grown [278].

6.7.3 Test run 3

In the third test run, a 7-day pre-treatment was utilised to stabilise the release of leachable ions into the media during testing to ensure the pH stayed within a physiological range and remained suitable for the cell lines used. Indirect cell seeding significantly improved the observed metabolic activity as the well plate surface is smoother than the composite samples and allowed for the imaging of cells to assess morphology and proliferation.

Figure 112 shows the metabolic activity in the presence of the composite samples, after 3 sets (N = 3) of tests using 3 samples (n = 3) at each composition, normalised to the TCP values at Day 1. The red, dotted line in Figure 112 indicates 70 % of the control metabolic activity measured in the TCP well, which is taken as the level of at which the material is not cytotoxic [280].

After 1-day incubation, the metabolic activity of indirectly seeded cells in the presence of PLA composite samples with 0-75 wt.% Bioglass is at a comparable level to the TCP. The approximate range of metabolic activity for these samples is 90-110% of that observed in the TCP and all above the activity level which indicates that the sample are non-cytotoxic. Cold sintered samples made from 100 wt.% Bioglass show a 70% reduction in the metabolic activity at day 1, although the reduction at this time point is not significant.

Over the course of the study, the metabolic activity seen in the TCP control samples increases, indicating the proliferation of cells as expected. The metabolic activity recorded at Day 3 for samples made of PLA and composites with 25 and 50

wt.% Bioglass have a slightly lower metabolic activity than the TCP but are within 10 %. A reduction of approximately 45 % in the metabolic activity is seen in the 75 wt.% composite at day 3, though this was not significant. In the 100 wt.% Bioglass samples, the metabolic activity was found to be significantly reduced at this time point to approximately 10 % of the TCP control values.

Similar trends are observed at Day 7, with cold sintered composites containing 0-75 wt.% Bioglass all displaying good levels of activity compared to the controls with all the metabolic activity for all samples lying within 10 % of the TCP. Samples with 75 wt.% have approximately 80 % viability compared to the control. At day 7, the 100 wt.% cold sintered composite samples again show a significant reduction in the metabolic activity to around 10 % of the control. Higher levels of leachable ions are present within the samples before pre-treatment and are likely to remain at high levels as samples are placed into the media. These ions will continue to be released during the incubation period and could contribute to the reduction in metabolic activity due to changes in the pH of the media.

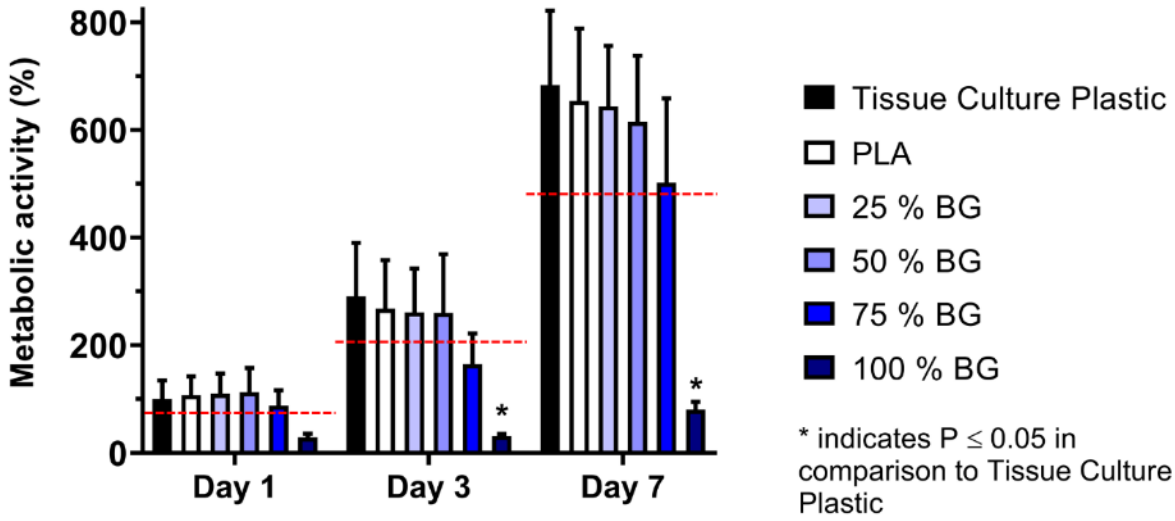

Figure 112: Metabolic activity at day 1, 3 and 7 for composite samples N=3 n=3.

Optical images (Figure 113) of indirectly seeded cells agree well with the metabolic activity. The number of cells observed on all plates increases over time, the presence of a bright 'halo' around a cell indicates that it has detached from the cell plate and is therefore either dividing or dead.

The morphologies of cells shown in Figure 19 are as expected for MG63 cells in all samples [222], [281], [282]. Cells are becoming so confluent in the presence of composite samples up to 75 wt.% Bioglass at Day 7 that the morphology is no longer clear. In 100 wt.% Bioglass samples, very low proliferation of cells at Day 1 and Day 3 is seen in the optical micrograph which agrees with the low metabolic activity data. At Day 7, the metabolic activity begins to increase, and the cell coverage also appears to increase in the optical micrograph, with a reduction in the proportion of cells which are surrounded by 'halos' indicating that rate of cell death may have reduced. This could be related to a reduction in concentration of alkali ions in the transwells after rinsing at each metabolic activity testing time point.

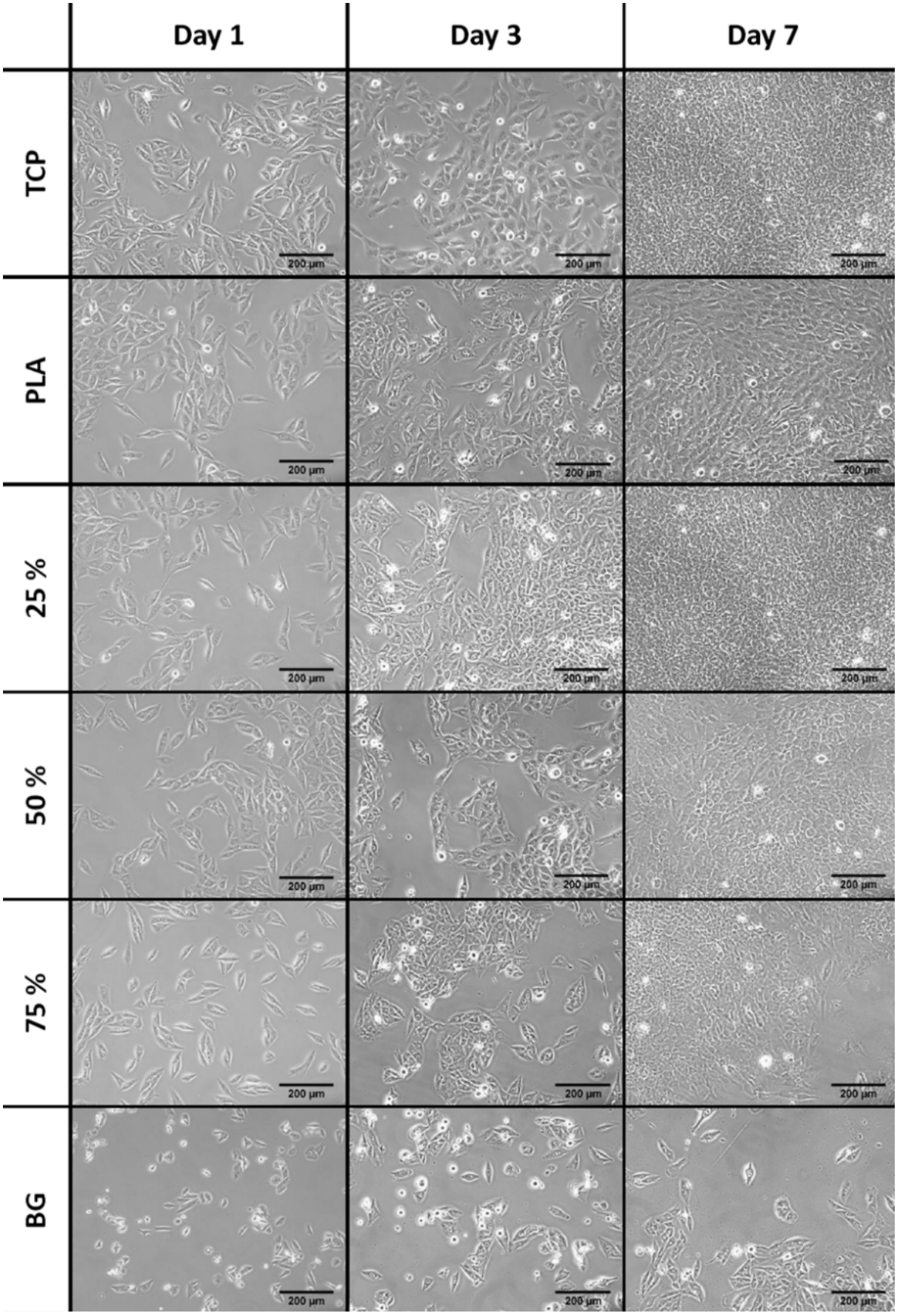

Figure 113: Optical micrograph of cells after 1, 3 and 7 days incubation

6.8 Cold sintering of Bioglass® 45S5 coatings on titanium

Conventional technologies such as plasma spray deposition used to coat orthopaedic implants with bioactive materials such as Bioglass often require high temperatures [198], [202], [203]. In this work, cold sintering has been used to show the potential to achieve coatings on titanium plate (Ti6Al-4V) at 100 °C, 55MPa. Figure 114 shows several developmental iterations of coatings produced to demonstrate the viability of coatings to be created on the surface of titanium.

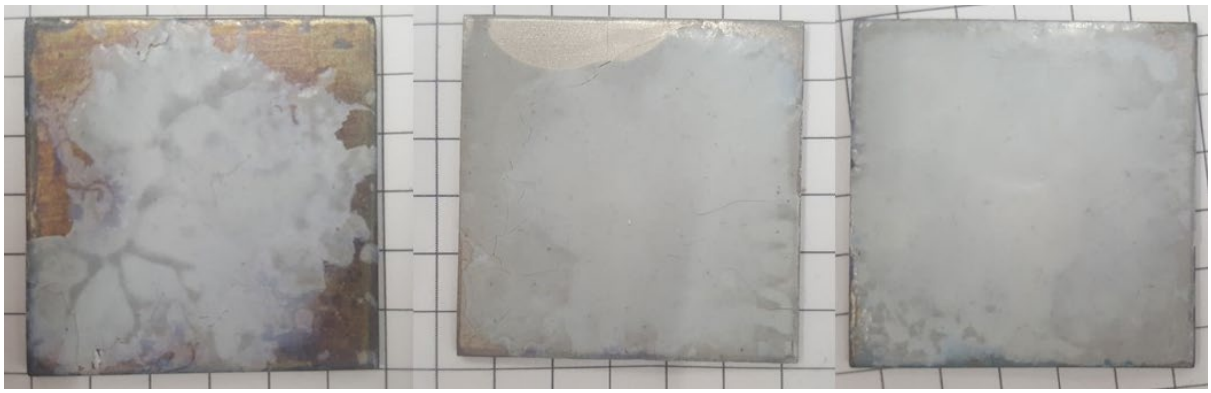

Figure 114: Optical images of Bioglass coating on Ti substrates – all samples are 3 x 3 cm

The pressure applied during cold sintering (55MPa) was not enough to ensure even distribution of the Bioglass material, leaving areas uncoated as shown in Figure 114a. This also creates variations in thickness across the material. In order to improve the uniformity, the wetted powder was subsequently placed on to the titanium and rolled out using a PTFE roller. A PTFE spacer was again to prevent adhesion to the die surface and therefore lift off during removal. Figure 114b and Figure 114c show layers in which the powder had been rolled to create a more uniform layer prior to pressing for cold sintering, a marked improvement in coverage is achieved. The edges of the titanium plate are slightly rounded and therefore the coating is not complete in these regions as the applied pressure will be lower in this region and the edges are susceptible to damage during removal from the die.

As the samples are first released from the die and the PTFE spacer is removed, the coating is a transparent brown colour, which quickly (<10 minutes) becomes translucent grey on contact with air. This colour change is also accompanied by the appearance of cracking within the coating. Examples of cracking in the Bioglass coatings of the samples show in Figure 114 can be seen in Figure 115. The cracking in Figure 115a is more prevalent in thicker regions of the sample indicating that reducing the coating thickness will lead to improvements in coating quality. By creating a

thinner, more consistent coating, as in Figure 115c, the severity of cracking is significantly reduced.

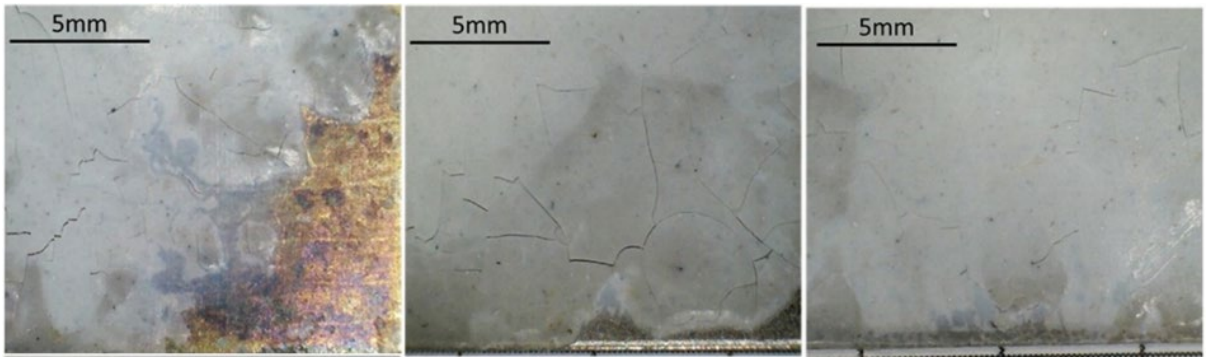

Figure 115: Optical images of Bioglass coating on Ti substrates

Cracking is a common phenomenon seen in glass and glass-ceramic glazes and coatings. It is caused when the coating material contracts (crazing) or expands (shivering) at a different rate to the underlying material. These effects can be caused by mismatched thermal expansion coefficient or expansion/contraction due to changes in the moisture content of the coating [283], [284]. In this case, the cracking occurs at room temperature after the exposure of the samples to the atmosphere. Therefore, the cracking is likely related to a change in hydration of the Bioglass coating. Reducing the thickness of the coating has been shown to reduce the extent of cracking, whilst extending the cold sintering 100 °C hold time from 60 to 120 minutes also appeared to slow the rate of crack formation and colour change within the material slightly; longer hold times giving a longer time for the removal of the water phase during the sintering process. These two factors show that the cracking of the coating is predominantly caused by loss of water from the surface causing contraction of the material, the effect of which can be mitigated by thinner coatings and removing more moisture in the sintering hold step.

The levels of adhesion between the coating and titanium were initially very variable and the cracking of the coating contributed to regions to become totally detached from the substrate. Attempts to improve the adhesion included creating a roughened surface using SiC grinding paper and heat treating to thicken the natural oxide layer. Heat treatment is the cause of the slight discoloration of the substrate surface seen in Figure 115a. The sample shown in Figure 116 had a roughened surface, the coating underwent significant cracking upon contact with the atmosphere causing loss of much of the coating material. There is cracking in the coating parallel to the substrate surface at approximately 3-5 μm from the interface, this again indicates that

a thinner layer of material would be preferable in creating a consistent, well adhered coating.

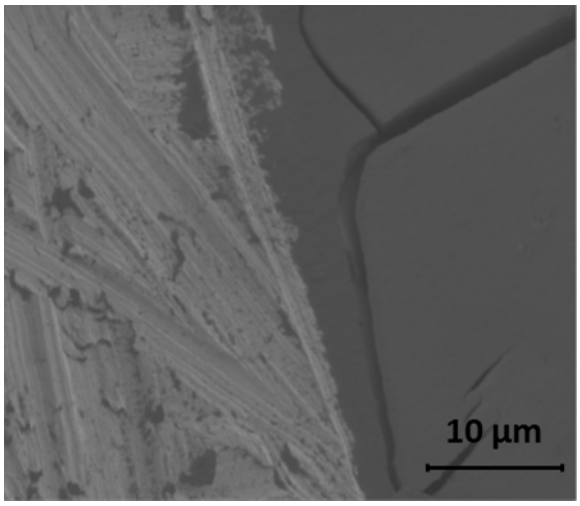

Figure 116: SEM of the coating-substrate interface – sample tilted at 45°

Figure 117 shows the surface (Figure 117a) and internal section (Figure 117b) of the Bioglass coating. It is thought that the plate-like structures are produced after the cold sintering process upon exposure to air. The change in appearance of the coating from transparent brown to a translucent grey upon exposure to air can be attributed to the development of these structures on the material surface. From the cut-through image, the levels of porosity appear to increase slightly towards the interface with the surface structures. The surface plate structures appear to emerge from a dense layer of material and themselves appear dense (Figure 117c). The increase in porosity below the surface is due to the formation of the surface structures, where the sub-surface materials act as a source of calcium, phosphorus, and sodium. It is not clear whether the carbon and oxygen in the surface structures comes from sub-surface material or the atmosphere.

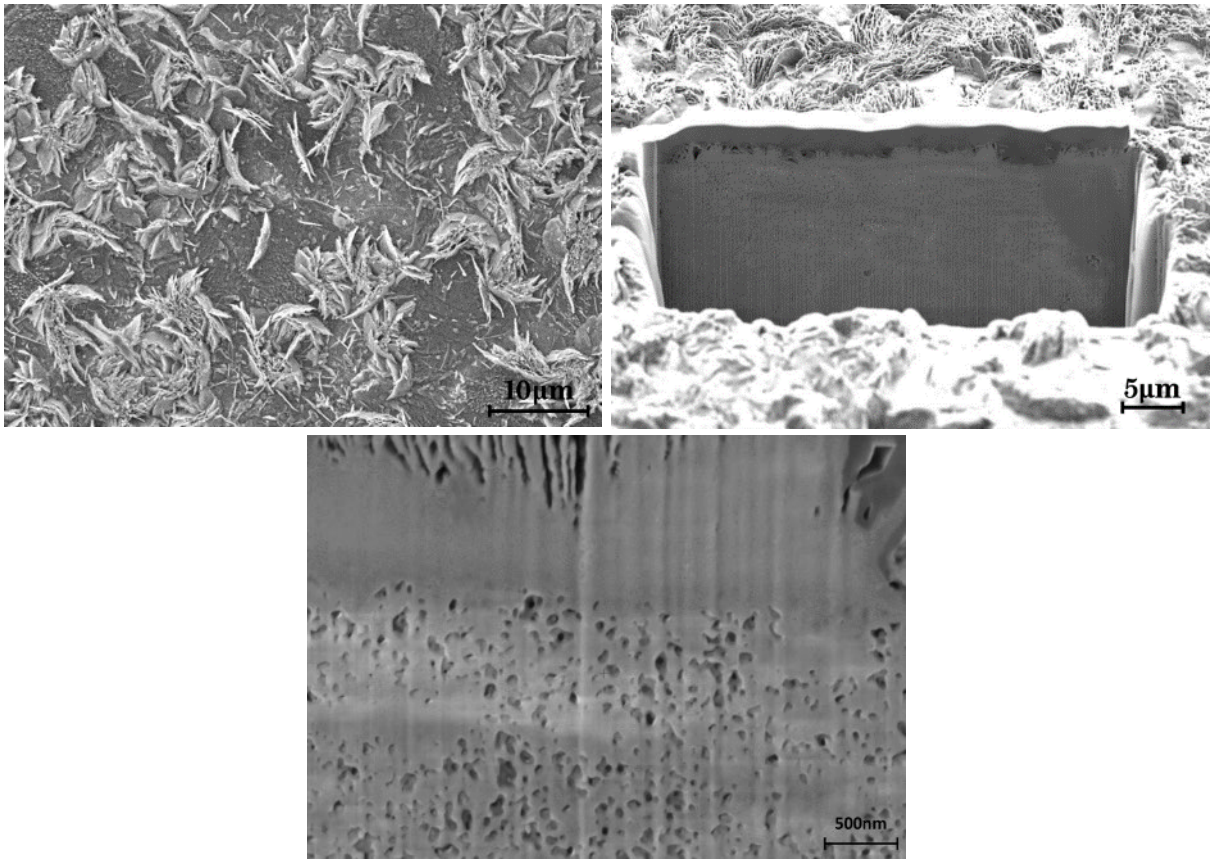

Figure 117: SEM of the surface (a), cut-through (b) and the interface between the surface strutures and sub-surface material (c) of the cold-sintered Bioglass coatings.

EDS mapping of the near surface region shown in Figure 118 allows further analysis of the surface structures seen in Figure 117. The area analysed contains two distinct regions: the surface plate-like structure and the sub-surface "bulk" material, each with a distinct chemical composition.

In the surface structures, the silicon content is significantly lower than in the sub-surface material, whereas the sodium and phosphorous levels are consistent between the two regions (Figure 118 G, D and E). The processes in Table 17 describe the repolymerisation of Si-OH leading to the formation of a silica-CaO/P_2O_5-rich layer from which HCA is mineralised. There is indication of a slight increase in silicon near the interface between the bulk and surface material (Figure 118 G), although the resolution is not sufficient to unambiguously confirm this hypothesis [172], [174]–[177], [179], [189], [191]–[193]. A gradual reduction in the oxygen content towards the surface of the material is also seen (Figure 118 C). The surface structures are shown to have high levels of both carbon and calcium compared to the sub-surface material (Figure 118 B and F). This is indicative of a carbonated calcium-based phase which also contains significant levels of phosphorus and sodium, which is encouraging for bioactivity and the formation of coating-bone bonding *in vivo*.

In the sub-surface region of the coating highlighted by a dashed white box in Figure 118, the levels of silicon are significantly depleted compared to the surrounding material. An increase in intensity indicates small increases in both sodium, calcium and phosphorus concentration can also be seen in this region. This gives evidence of some chemical inhomogeneity within the samples, which is likely to be heavily influenced by the dissolution behaviour during cold sintering.

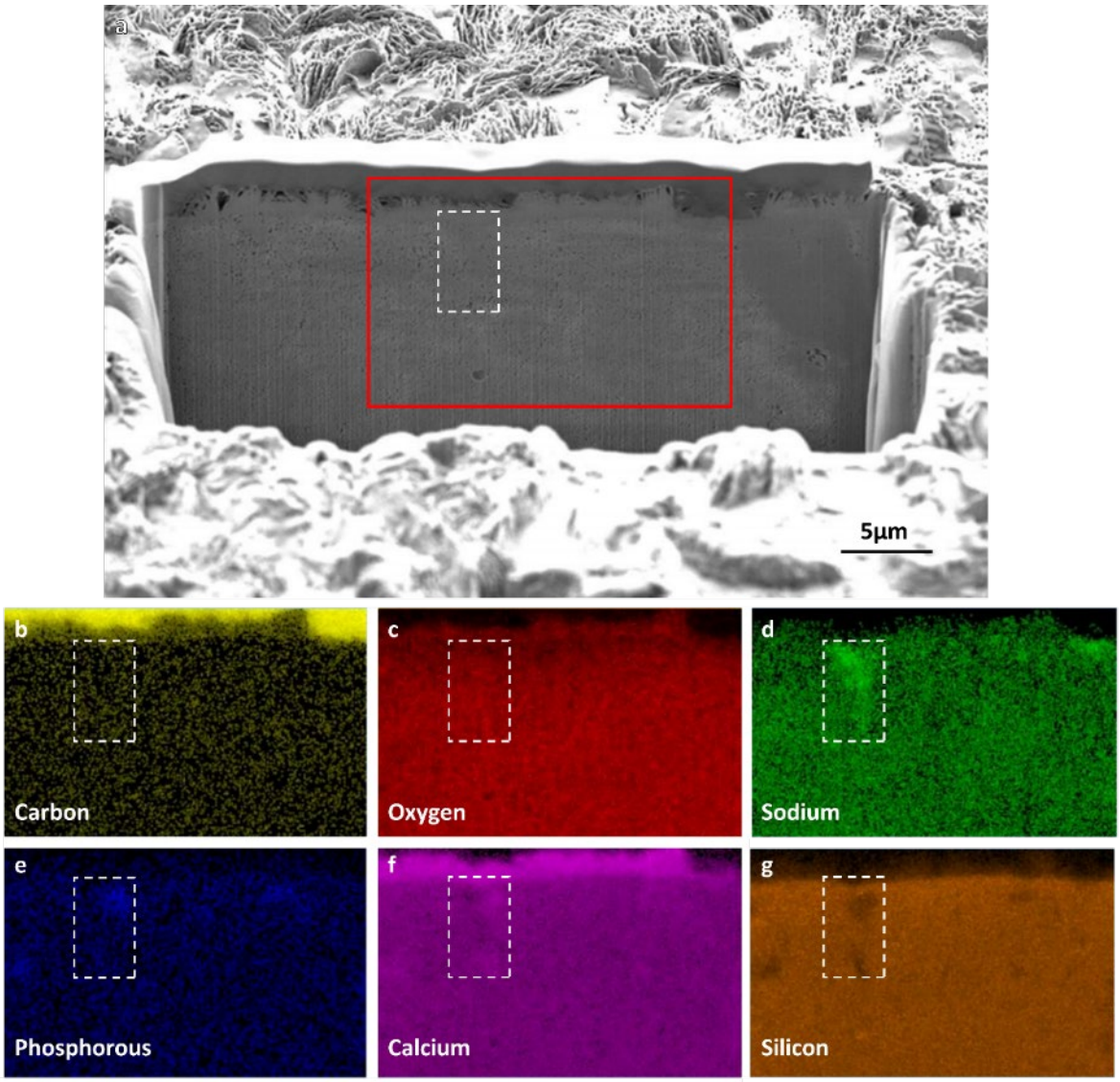

Figure 118: EDS mapping of carbon, oxygen, sodium, phosphorous, calcium, and silicon (B-G) in the near surface region, indicated by the red box in (A) of the cold sintered Bioglass coating. Scale in all sub-images is the same as (A)

7 Conclusions

Since the cold sintering process for ceramics was first described in 2016, there has been growing interesting in its potential, with over 160 papers on the topic to date [285]. Figure 119 illustrates the rapid increase in the number of published articles on the subject. The process is likely to enable the development of new technologies and a number of proof-of-concept components for various applications have already been reported.

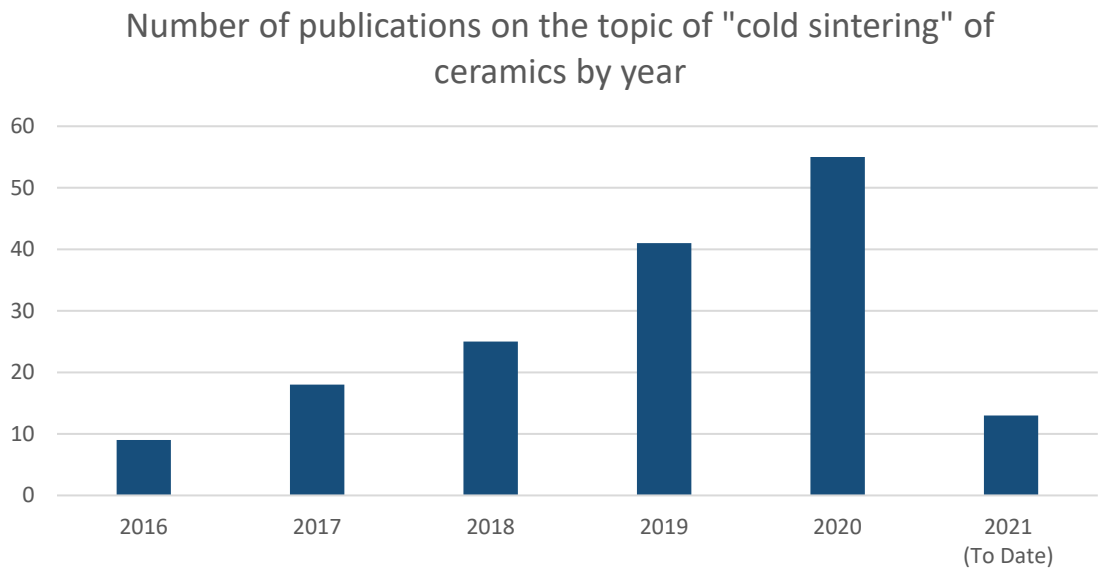

Figure 119: Number of publications on the topic of "Cold Sintering" of ceramics by year, using analytics data from Web of Science Core collection [285].

Here, the capability of cold sintering to produce composites and coatings of a number of ceramics and glasses on a range of substrates has been demonstrated. This thesis reports for the first time the densification of silicate glass components from powders at very low temperatures.

In this work, lithium molybdate was sintered to a high relative density (91-97 %) through cold sintering and achieves properties commensurate with reported values for conventionally sintered material (5.8-7.9). Through structural analysis, it has been shown that after cold sintering, no significant residual hydroxide phase remains, indicating that reductions in Qf reported in literature for cold sintered lithium molybdate are likely due to other factors such as grain size and residual amorphous phase. A cold sintered coating of lithium molybdate on a glass substrate has also been achieved. The limited grain growth observed in cold sintered layers could allow for

post-processing steps to tailor grain size. Although some issues with cracking are observed, the capability to create a well adhered layer on a glass substrate at a low temperature has been demonstrated, which could facilitate improvements in a number of technologies including microwave communications.

Work described in this thesis and within the literature confirms it is possible to densify ceramic-ceramic composites *via* cold sintering to tailor dielectric properties. Composites of lithium and bismuth molybdate have been produced *via* cold sintering at 150 °C utilising water as the transient solvent. With increasing bismuth molybdate concentration within the composite, the relative density has been shown to reduce significantly, which in turn hampers the improvement in permittivity which would be expected with the addition of a higher permittivity material into the system. Other molybdate materials, such as sodium molybdate and potassium molybdate are shown to densify via cold sintering therefore, it was expected that bismuth molybdate would also densify. There are however a number of phases of bismuth molybdate, with different Bi:Mo ratios which could potentially cold sinter but have not been explored in this work.

The potential for the cold sintering process to be applied to powdered glass silicate materials has been demonstrated and expands the current applications of the process into a new class of materials. The capability to produce dense glass components from powders at low temperatures has many advantages, allowing for "co-sintering" with a broad range of materials and the avoidance of volatilisation and high levels of crystallization. This could enable the development of new technologies or for new approaches to be taken to develop and improve existing technology.

By utilising the intrinsic solubility of JM5430F in acidic environments, it has been possible to densify pellets by cold sintering. In most cold sintering methods, the amount of liquid used is ~10 wt.%, to achieve densification of JM5430F a significantly higher concentration of acetic acid was used. The dependence of final density on liquid addition has been described and is caused by an increase in dissolution with higher volumes of liquid. Whilst the majority of applications for ceramics and glass-ceramics require very high density, the ability to tailor the density and therefore the nature of porosity could be utilised to further achieve specific properties.

The capability to use the cold sintering process to produce glass coatings and adhere dissimilar materials has been demonstrated. Significant levels of porosity remained in the coating/adhesive layers, although necking and densification had begun

during the applied cold sintering process. Improving the densification will require an understanding of how the introduction of the substrate affects the sintering process through changing the heat transfer, pressure distribution and evaporation of the transient solvent.

For the first time, Bioglass® 45S5 has been densified at temperatures significantly lower than T_g through cold sintering at 100 °C using distilled water. Using NMR, the changes in chemical structure of Bioglass as received, "wetted" and after cold sintering have been studied, allowing the potential mechanism to be revealed. The changes in structure shown by NMR shows similarities between the mechanism of cold sintering and the stages of interfacial reactions when Bioglass is implanted in the body. Although the XRD spectra of cold sintered Bioglass confirm the materials remains amorphous during sintering, Ca and P rich whiskers are seen in SEM images, indicating that hydroxyapatite may be beginning to form during cold sintering which is often an indicator of bioactivity.

Composites of Bioglass and PLA have been produced *via* cold sintering. The ability to create composites with high volume loading of Bioglass, low processing temperature and the ability to densify both phases represent significant improvements over techniques discussed in Section 2.8.2. The spontaneous development of whisker like phases, which are likely to be calcium rich in cold sintered samples when stored in ambient conditions is a positive indication that the samples remain highly reactive after cold sintering and would behave in a similar way to conventional Bioglass if used in an implant. After pre-conditioning, the cytotoxicity behaviour of the composites in this study indicated that the cold sintering method could be used to produce bioactive, composite implant materials with physical properties specifically tailored to the application.

Coatings of Bioglass on titanium plate has been demonstrated in this work. Although some crazing is observed, developing the technique further could provide a route to overcome the challenge of mismatching thermal expansion coefficients for coatings on titanium implants. On contact with air, the initially translucent coating becomes a light grey colour, which has been attributed to the formation of plate-like structures of calcium and carbon rich material which also contains phosphorous. The formation of these structure is an encouraging indicator that the bioactive behaviour of Bioglass is maintained during the cold sintering process.

Utilising cold sintering processes to densify coatings of ceramic/glass onto substrates as described in this work may be one way of limiting the effects of mismatch between thermal expansion coefficients (CTE). CTE's are commonly quoted at 20 °C, but in some materials have been shown to change with increasing temperatures, therefore staying at relatively low temperatures ensures the effect of any mismatch is minimised [286]. If significant mismatches were present within a particular material combination a variety of potential avenues could be explored to reduce the potential impact on the final components, including pre-heating the substrate and coating with a composite material to tailor CTE.

Overall, the sintering of ceramics and glasses at low temperatures has been successfully achieved through the process of cold sintering. There are numerous advantages over conventional processing for functional ceramics and glasses leading to a broad range of potential applications and developments including energy storage, communications, and biomedical devices.

8 Future Work

Following on from results presented in this thesis to develop cold sintering methods for a number of materials, with a variety of applications, there is significant scope for future work specific to *Molybdate based ceramics, Glasses and Glass Ceramics, and Bioglass® 45S5* . First reported in 2016, cold sintering remains a reasonably novel technique and there is, therefore, a very broad range of potential avenues for future work. Development in the *understanding of the cold sintering process and mechanisms* will be important in continuing to develop the technique for application to new material classes and technological areas. To date, most published work on cold sintering applies the technique to small, simple components and therefore work towards *complex geometries and upscaling* will be important for potential commercial going forward.

8.1 Molybdate based ceramics

As a material which readily cold sinters, lithium molybdate has often been used to demonstrate the potential of cold sintering, particularly as a constituent material in ceramic-ceramic composites with materials which have not yet been independently cold sintered. Where cold-sintered composites have been produced with a component material which does not itself cold sinter, the soluble component material which contributes most to densification has often been shown to have a significantly larger grain size [83], [100], [101]. Understanding the effect of the size ratio between the powders in the cold sintered matrix material and the "filler" material on the densification behaviour of ceramic-ceramic composites and their subsequent properties would be beneficial. This could allow for further tailoring of properties by achieving specific final microstructures which could utilise varying levels of homogeneity.

Bismuth molybdate ($Bi_2Mo_2O_9$) achieved a very low relative density through cold sintering. Other members of the molybdate family, such as lithium molybdate, sodium molybdate and potassium molybdate are shown to densify readily via cold sintering and it was thought the densification of bismuth molybdate would also be possible. A number of bismuth molybdate phases exist, with different Bi: Mo ratios (such as $Bi_2Mo_3O_{12}$ and Bi_2MoO_6), which could potentially cold sinter but have not been explored in this work.

A greater understanding of the causes of glass substrate fracture during the cold sintering of lithium molybdate coatings could allow for the processing to be altered to avoid fractures. This would enable the cold sintering of ceramics on glass to be further investigated, with the possibly of working towards integrating electronic components directly onto architectural or automotive glasses.

8.2 Glasses and Glass Ceramics

This work has demonstrated the ability to cold sinter glass powders into dense, mechanically stable components and coatings. To understand further the effect of the cold sintering process on the properties of JM5430F a number of experiments could be performed. Firstly, DSC/DTA could be used to determine if any reactions begin to take place as the sample is taken above 250 °C (cold sintering temperature). The secondary, crystalline phase produced during cold sintering is not fully identified in this work. An understanding of the chemical composition of this material would allow for more complete understanding of the mechanisms occurring during the cold sintering of JM5430F. The effect on properties of raising the cold sintered material above 250 °C could be further explored by holding the material at significant temperatures identified by DSC/TGA and taking a number of measurements over a prolonged period of time. The aim of demonstrating the ability to use the cold sintering of JM5430F to create a coating has been achieved. However, further understanding and refinement of the process is required to optimise the densification process including using a different steel substrate with better mechanical properties.

Technical glasses and glass ceramics are used in a variety of different industries, where the ability to produce components at low temperatures would be advantageous. The main benefits of using low temperatures for these areas are the capability to incorporate a wider variety of materials during "co-sintering" and avoid volatilisation of the material.

Glasses are commonly used and continue to be widely researched as a method to immobilise nuclear waste created during the lifetime of nuclear reactors for power generation [287], [288]. A number of studies have explored the capability of using a cold sintering process using hydroxyapatite to create a durable matrix for nuclear waste immobilisation [289]–[291]. These studies indicate that the low temperatures allow for the volatilisation of potentially harmful radioactive isotopes to be avoided, and the matrix created did not suffer high levels of leaching, indicating that the cold sintering process can be used in the immobilisation of nuclear waste. Therefore, an

interesting area of further work would be to assess the potential for the base glasses used in waste immobilisation to be cold sintered and assess their subsequent durability.

Energy storage and battery technology is going to play a large role in the decarbonisation of the world's economies [292][293]. A number of ceramic materials for use in solid-state batteries have been cold sintered [294]–[297], and a number of glass or glass-ceramic materials have been investigated for use as electrolyte materials [298]–[300]. The ability to cold sinter all-solid-state batteries could not only reduce processing temperatures and therefore cost, but also enable the use of a broader range of materials which cannot be co-sintered conventionally.

8.3 Bioglass® 45S5

The Bioglass® 45S5 starting powders used within this work were produced *via* flame spray pyrolysis, which allows for tailoring of particle size and morphology. The ability to cold sinter bioactive glasses is likely to be at least partially intrinsic, based on their chemistry and known reactions with aqueous solutions. However, the contributions of the powder manufacturing process, and the resulting particle morphologies to the reactivity has not been investigated. A study investigating commercially available bioactive glass powders of various compositions with a variety of particle size distributions would aid in understanding the contributions of chemistry and morphology to the successful densification of bioactive glasses *via* cold sintering.

It is well-reported that creating composites of polymers with Bioglass can enable the tailoring of mechanical properties to fulfil the specification of various biomedical applications. To date, no mechanical testing has been performed on cold sintered Bioglass or composites thereof; any potential effect on mechanical properties of samples made *via* the cold sintering method have therefore not been investigated. In order to study the mechanical properties in a meaningful way, the creation of composites with smaller polymer particles (of the same order as the Bioglass particles) would also be advantageous to ensure more complete and homogenous mixing of the two phases. The creation of further Bioglass composites to include other polymer materials or indeed a phase with therapeutic properties could unlock a potential avenue for the utilisation of this technique in a broader biomedical context.

Numerous studies have investigated foams and scaffolds with porous microstructures for biomedical applications [211], [212], [214], [218], [301]–[304]. Porosity levels can be utilised to tailor the rate of dissolution and subsequent bioactivity

of implant materials. A study to investigate to what extent the porosity of final components could be tailored by altering applied pressure and hold time could be used to further demonstrate the adaptability of the process.

Refinement of the process for producing Bioglass coatings on titanium and adhesion testing should be explored. It is possible that the larger dimensions of the dies used to cold sinter the Bioglass coating onto the titanium plate is hindering the escape of water at the sintering temperature, contributing to cracking upon removal. Increasing the sintering hold time or altering the shape and size of the titanium substrate and surrounding die could be investigated as a method to ensure total evaporation of the distilled water from the system. The ability to precisely and consistently control the thickness of the coating layer applied could also contribute to a reduction in the cracking phenomenon observed on exposure to the atmosphere. Once consistent coating layers can be achieved, the adhesion to the substrate should be assessed to understand the viability of using this process to create coatings for biomedical implants.

To accompany the metabolic cell activity results, SBF (simulated body fluid) testing of cold sintered Bioglass and its composites could also be pursued and the formation of HCA compared to the existing literature for [212], [218], [305]. The formation of Ca-rich and HCA-like structures has already been observed within the current work and SBF testing would give further understanding of the bioactivity of the cold-sintered sample compared to conventionally produced material. An investigation of the conditions required for formation of the internal HCA-like phases in bulk pellets and Ca-rich surface phase in the coating could enable greater understanding of the mechanisms in the cold sintering process and allow for tailoring of bioactivity.

8.4 Improving understanding of the cold sintering process and mechanisms

Fundamentally, the exact parameters required to cold sinter materials are currently uncovered by a combination of prior knowledge and a significant amount of trial and error. Developing a deeper understanding of the mechanisms responsible for densification in cold sintering could enable the creation of a set of key rules and processing parameters to provide a stronger theoretical foundation for cold sintering. Greater understanding could be achieved by extending the range of techniques typically used to study cold sintering. The wider use of (HR)TEM to study particle-particle interfaces would improve our understanding of grain growth and local

crystallisation, although we note that sample preparation is challenging. In addition, looking at the detailed density distribution throughout the sample and at the interfaces between bilayers using X-Ray Micro-CT would give a greater spatial understanding of the sintering process.

Structural studies of materials before, "wetted" and after cold sintering such as those described in chapter 0 would also enable a broader understanding of the mechanisms in cold sintering. This would allow the behaviour of the different families of cold sinterable materials to be better understood, by confirming dissolution products, formation of secondary phases during the wetting stage and how the final chemical structure is developed.

The solubility of a material is a significant factor in the success of cold sintering. There are a number of solubility scales and parameters which could be explored to identify appropriate matches more quickly between materials and potential transient liquid phases. Other key parameters in cold sintering are the applied temperature and pressure. When using the Specac Uniaxial press with heated platens to cold sinter, there is limited control over heating and cooling rates – the heating rate is fixed, and the natural cooling rate of the system is quite slow although fans can be used to increase the cooling rate. The heating rate likely to have a significant impact on the behaviour of the transient liquid and the dissolution behaviour of the material. During cold sintering, the pressure on the sample can fluctuate due to changes in the dimensions of the sintered pellet as liquid escapes or the dies expand with heat. The ability to maintain a constant applied pressure throughout the process could further increase the density of some materials, ensure a more homogeneous microstructure, and control the evaporation of the transient solvent.

8.5 Complex geometries and upscaling

Components produced *via* cold sintering currently have limited geometries and consist mainly of pellets, coatings, and structures with layers perpendicular to the applied pressure. During this work, some attempts to "robocast" the lithium molybdate slurry used during screen printing were also made. Further refinement could enable the technique to be used to create graded, composite components or coatings, with more complex structures than it is possible to produce by standard cold sintering or screen printing such as those required for graded index (GRIN) lenses [83], [306], [307]. The ability to create more complex structures by utilising dies with more intricate geometries, 3D printing, or other processes would allow a significant step to

be made towards enabling applications that require more complex net shapes. This would constitute a significant investment of time and resources and would require input from industry and effectively be a prelude to commercialisation.

Before commercialisation can occur, a number of significant challenges need to be met. Currently, the cold sintering is used to produce small scale components (a few grams of material, with dimensions less than 30 mm) and is a batch process normally producing just one sample at a time. Using taller dies with heating jackets such as those in MTI hot press does allow for the manufacture of a number of samples simultaneously by stacking alternating layers of materials to be sintered with die pieces, although this is still a very small batch process it does ensure that all samples are subjected to the same heating and pressure regimes. To increase the rate of sample production a more continuous cold sintering process could be developed utilising the capabilities of tape casting and calendaring processes to apply pressure to larger components.

As discussed in section 2.2.3, a number of processing routes have been explored to reduce sintering temperatures for ceramics such as FAST and SPS. Development of combined CSP-FAST or CSP-SPS techniques could create possibilities for further reductions in processing time and temperatures and enable further tailoring of properties and final microstructure.

8.6 Current Limitations of Cold Sintering

Cold sintering is currently very low TRL technique and there are a significant number of limitations and challenges to overcome as the technique is developed. The application of significant pressures (650MPa) is often required to encourage densification of the materials. Whilst this is readily achievable in the laboratory for small samples with dimensions less than a few centimetres, at larger scales this may prove unfeasible. Therefore, work is required to understand the interactions of the transient liquid (in terms of chemistry and volume), temperature, pressure and time is achieving densification to allow for the potential reduction in the required pressure. Inspiration for this could come from geological or biological process, which occur under a wider range of pressures and temperatures [166], [308], [309]. Temperature distributions are not often considered in the literature relating to cold sintering, as components are small and therefore temperature gradients are likely to be minimal. In larger components, however it is likely that this would become a major issue with regions densifying at different rates.

Creating more complex and large shapes will be a major step in the development of the cold sintering technique. The shape of final components is determined by the die shape, and therefore more complex tooling could allow for complex components to be made. This would need a significant amount of consideration and knowledge transfer from industries such as metal forging to understand what pressure and distributions may occur during processing. For a small component of complex geometry, it would also be necessary to understand the temperature distribution in the component to ensure the sintering parameters are met throughout the component. Components with complex geometries could suffer from inhomogeneity in density and microstructure where pressure and/or temperature gradients exist. This would need to be taken into consideration when designing components and the cold sintering process itself, where utilising different starting powder morphologies in different areas of the component or post sintering annealing steps may be necessary to achieve homogeneity after sintering.

8.7 Conclusions

In conclusion, cold sintering is still a very new technique and there are many potential avenues for future developments which could have significant impact on a broad range of industries. It is, however, highly disruptive, requiring completely different manufacturing equipment to conventional sintering, currently used for the commercial fabrication of ceramics and glass bodies from frit. Initial penetration of cold sintering into the commercial world, therefore, will most likely not be driven by the reduction in energy but because if offers a unique solution to an industrial/technical problem. The cold sintered Bioglass research presented in this thesis could provide such impetus since it demonstrates the potential to fabrication a unique group of high value products, difficult to manufacture using conventional techniques.

9 References

[1] R. M. German, "History of sintering : empirical phase," *Powder Mettalurgy*, vol. 56, no. 2, pp. 117–132, 2013, doi: 10.1179/1743290112Y.0000000025.

[2] A. Baker, H. Guo, J. Guo, and C. Randall, "Utilizing the Cold Sintering Process for Flexible-Printable Electroceramic Device Fabrication," *J. Am. Ceram. Soc.*, vol. 3, no. 38709, pp. 1–3, 2016, doi: 10.1111/jace.14467.

[3] H. Guo, A. Baker, J. Guo, and C. A. Randall, "Cold Sintering Process: A Novel Technique for Low-Temperature Ceramic Processing of Ferroelectrics," *J. Am. Ceram. Soc.*, vol. 19, no. 38863, pp. 1–19, 2016, doi: 10.1111/jace.14554.

[4] M. T. Sebastian, H. Wang, and H. Jantunen, "Low temperature co-fired ceramics with ultra-low sintering temperature: A review," *Curr. Opin. Solid State Mater. Sci.*, vol. 20, no. 3, pp. 151–170, 2016, doi: 10.1016/j.cossms.2016.02.004.

[5] M. K. Mandal, Z. N. Chen, and X. Qing, "Compact ultra-wideband filtering antennas on low temperature co-fired ceramic substrate," *APMC 2009 - Asia Pacific Microw. Conf. 2009*, pp. 2084–2087, 2009, doi: 10.1109/APMC.2009.5385267.

[6] D. Sohrabi Baba Heidary *et al.*, "Contrasting energy efficiency in various ceramic sintering processes," *J. Eur. Ceram. Soc.*, vol. 38, no. February, pp. 1018–1029, 2018, doi: 10.1016/j.jeurceramsoc.2017.10.015.

[7] K. Watari, T. Nagaoka, K. Sato, Y. Hotta, and I. P. Office, "A strategy to reduce energy usage in ceramic fabrication - novel binders and related processing technology," *Synthesiology*, vol. 2, no. 2, pp. 137–146, 2009.

[8] W. . Lee and W. . Rainforth, *Ceramic Microstructures: Property control by processing*. London: Chapman & Hall, 1994.

[9] R. M. German, *Liquid Phase Sintering*. New York: Springer US, 1985.

[10] M. N. Rahaman, *Sintering of Ceramics*. 1950.

[11] M. T. Sebastian, *Dielectric Materials for Wireless Communication*. 2008.

[12] W. D. Kingery, H. K. Bowen, and D. R. Uhlmann, *Introduction to Ceramics*, 2nd ed. John Wiley & Sons, 1975.

[13] L. C. De Jonghe and M. N. Rahaman, "Sintering of Ceramics," in *Handbook of Advanced Ceramics: Materials, Applications, Processing and Properties*, vol. 1–2, 2003, pp. 187–264.

[14] W. D. Kingery and M. Berg, "Study of the initial stages of sintering solids by viscous flow, evaporation-condensation, and self-diffusion," *J. Appl. Phys.*, vol. 26, no. 10, pp. 1205–1212, 1955, doi: 10.1063/1.1721874.

[15] L. C. De Jonghe and M. N. Rahaman, *Handbook of Advanced Ceramics*. .

[16] W. F. Hosford, *Materials Science: An Intermediate Text*. Cambridge: Cambridge University Press, 2006.

[17] T. Kimura, Q. Dong, S. Yin, T. Hashimoto, A. Sasaki, and T. Sato, "Synthesis and piezoelectric properties of Li-doped BaTiO 3 by a solvothermal approach," *J. Eur. Ceram. Soc.*, vol. 33, no. 5, pp. 1009–1015, 2013, doi: 10.1016/j.jeurceramsoc.2012.11.007.

[18] C. A. Randall, S. F. Wang, D. Laubscher, J. P. Dougherty, and W. Huebner, "Structure property relationships in core-shell BaTiO3-LiF ceramics," *J. Mater. Res.*, vol. 8, no. 4, pp. 871–879, 1993.

[19] H. I. Hsiang, C. S. Hsi, C. C. Huang, and S. L. Fu, "Sintering behavior and dielectric properties of BaTiO3 ceramics with glass addition for internal capacitor of LTCC," *J. Alloys Compd.*, vol. 459, no. 1–2, pp. 307–310, 2008, doi: 10.1016/j.jallcom.2007.04.218.

[20] C. A. Handwerker, J. E. Blendall, and W. A. Kayesser, "Sintering of Advanced Ceramics," 1990.

[21] R. Boston *et al.*, "Protocols for the fabrication, characterisation, and optimisation of n-type thermoelectric ceramic oxides," *Chem. Mater.*, vol. 29, pp. 265–280, 2017, doi: 10.1021/acs.chemmater.6b03600.

[22] J. Guo, S. S. Berbano, H. Guo, A. L. Baker, M. T. Lanagan, and C. A. Randall, "Cold Sintering Process of Composites: Bridging the Processing Temperature Gap of Ceramic and Polymer Materials," *Adv. Funct. Mater.*, 2016, doi: 10.1002/adfm.201602489.

[23] H. Yu, J. Liu, W. Zhang, and S. Zhang, "Ultra-low sintering temperature ceramics for LTCC applications: a review," *J. Mater. Sci. Mater. Electron.*, vol. 26, no. 12, pp. 9414–9423, 2015, doi: 10.1007/s10854-015-3282-y.

[24] M. T. Sebastian and H. Jantunen, "Low loss dielectric materials for LTCC applications: a review," *Int. Mater. Rev.*, vol. 53, no. 2, pp. 57–90, 2008, doi: 10.1179/174328008X277524.

[25] W. D. Kingery, "Densification during sintering in the presence of a liquid phase. I. Theory," *J. Appl. Phys.*, vol. 30, no. 3, pp. 301–306, 1959, doi: 10.1063/1.1735155.

[26] R. M. German, S. Farooq, and C. M. Kipphut, "Kinetics of liquid sintering," *Mater. Sci. Eng.*, vol. 105–106, no. PART 1, pp. 215–224, 1988, doi: 10.1016/0025-5416(88)90499-5.

[27] V. N. Eremenko, Y. V. Naidich, and I. A. Lavrienko, *Lipuid-Phase Sintering*. 1968.

[28] H. Guo, J. Guo, A. Baker, and C. A. Randall, "Cold Sintering Process for ZrO2 - Based Ceramics: Significantly Enhanced Densification Evolution in Yttria-Doped

ZrO2," *J. Am. Ceram. Soc.*, vol. 4, no. 38907, pp. 1–4, 2016, doi: 10.1111/jace.14593.

[29] J. Guo, A. L. Baker, H. Guo, M. Lanagan, and C. A. Randall, "Cold Sintering Process: A New Era for Ceramic Packaging and Microwave Device Development," *J. Am. Ceram. Soc.*, vol. 7, pp. 1–7, 2016, doi: 10.1111/jace.14603.

[30] J. G. P. Binner and B. Vaidhyanathan, "Microwave sintering of ceramics: What does it offer?," *Key Eng. Mater.*, vol. 264–268, no. I, pp. 725–730, 2004, doi: 10.4028/www.scientific.net/kem.264-268.725.

[31] D. (Microwave P. and E. C. Agrawal, "Agrawal_Microwave sintering of ceramics,composites2.pdf," vol. 65 (3). pp. 129–144, 2006.

[32] E. A. Olevsky and D. V. Dudina, "Microwave Sintering," *Field-Assisted Sinter.*, pp. 237–274, 2018, doi: 10.1007/978-3-319-76032-2_7.

[33] A. Borrell, M. D. Salvador, M. Miranda, F. L. Penaranda-Foix, and J. M. Catala-Civera, "Microwave Technique: A Powerful Tool for Sintering Ceramic Materials," *Curr. Nanosci.*, vol. 10, no. 1, pp. 32–35, 2014, doi: 10.2174/15734137096661311112250 53.

[34] N. Ivanova, V. Gugleva, M. Dobreva, I. Pehlivanov, S. Stefanov, and V. Andonova, "We are IntechOpen , the world ' s leading publisher of Open Access books Built by scientists , for scientists TOP 1 %," *Intech*, vol. i, no. tourism, p. 13, 2016.

[35] M. Oghbaei and O. Mirzaee, "Microwave versus conventional sintering: A review of fundamentals, advantages and applications," *J. Alloys Compd.*, vol. 494, no. 1–2, pp. 175–189, 2010, doi: 10.1016/j.jallcom.2010.01.068.

[36] "Microwave Sintering Fundamentals and Modeling Enhanced Reader.pdf." .

[37] M. Cologna, B. Rashkova, and R. Raj, "Flash sintering of nanograin zirconia in <5 s at 850°C," *Journal of the American Ceramic Society*, vol. 93, no. 11. pp. 3556–3559, 2010, doi: 10.1111/j.1551-2916.2010.04089.x.

[38] M. Biesuz and V. M. Sglavo, "Flash sintering of ceramics," *J. Eur. Ceram. Soc.*, vol. 39, no. 2–3, pp. 115–143, 2019, doi: 10.1016/j.jeurceramsoc.2018.08.048.

[39] K. Naik, S. K. Jha, and R. Raj, "Correlations between conductivity, electroluminescence and flash sintering," *Scr. Mater.*, vol. 118, pp. 1–4, 2016, doi: 10.1016/j.scriptamat.2016.03.001.

[40] C. E. J. Dancer, "Flash sintering of ceramic materials," *Mater. Res. Express*, vol. 3, no. 10, 2016, doi: 10.1088/2053-1591/3/10/102001.

[41] Y. Zhang, J. Il Jung, and J. Luo, "Thermal runaway, flash sintering and asymmetrical microstructural development of ZnO and ZnO-Bi2O3 under direct

currents," *Acta Mater.*, vol. 94, pp. 87–100, 2015, doi: 10.1016/j.actamat.2015.04.018.

[42] *Sintering Applications* . .

[43] Z. Shen, M. Johnsson, Z. Zhao, and M. Nygren, "Spark Plasma Sintering of Alumina."

[44] P. Cavaliere, *Spark Plasma Sintering of Materials*. Cham: Springer International Publishing, 2019.

[45] M. Suarez *et al.*, "Challenges and Opportunities for Spark Plasma Sintering: A Key Technology for a New Generation of Materials," in *Sintering Applications*, vol. i, no. tourism, InTech, 2013, p. 13.

[46] C. Elissalde *et al.*, "Single-step sintering of zirconia ceramics using hydroxide precursors and Spark Plasma Sintering below 400 °C," *Scr. Mater.*, vol. 168, pp. 134–138, 2019, doi: 10.1016/j.scriptamat.2019.04.037.

[47] Q. Z. Chen, J. L. Xu, L. G. Yu, X. Y. Fang, and K. A. Khor, "Spark plasma sintering of sol-gel derived 45S5 Bioglass®-ceramics: Mechanical properties and biocompatibility evaluation," *Mater. Sci. Eng. C*, vol. 32, no. 3, pp. 494–502, 2012, doi: 10.1016/j.msec.2011.11.023.

[48] H. Zhu *et al.*, "Effects of high pressure sintering on the microstructure and thermoelectric properties of BiCuSeO," *High Press. Res.*, vol. 37, no. 1, pp. 36–45, 2017, doi: 10.1080/08957959.2016.1273352.

[49] C. Mei, Y. Li, G. Li, M. Li, and P. Zhai, "The effect of high-pressure sintering process on the microstructure and thermoelectric properties of CoSb 3," *J. Electron. Mater.*, vol. 38, no. 7, pp. 1194–1199, 2009, doi: 10.1007/s11664-009-0736-0.

[50] "High-Pressure Sintering of Nanocrystalline γAl2O3 Enhanced Reader.pdf." .

[51] R. Lv, J. Liu, Y. Li, S. Li, Z. Kou, and D. He, "High pressure sintering of cubic boron nitride compacts with Al and AlN," *Diam. Relat. Mater.*, vol. 17, no. 12, pp. 2062–2066, 2008, doi: 10.1016/j.diamond.2008.07.002.

[52] Y. S. Ko, T. Tsurumi, O. Fukunaga, and T. Yano, "High pressure sintering of diamond-SiC composite," *J. Mater. Sci.*, vol. 36, no. 2, pp. 469–475, 2001, doi: 10.1023/A:1004840915607.

[53] R. H. Wentorf, R. C. DeVries, and F. P. Bundy, "Sintered superhard materials," *Science (80-.).*, vol. 208, no. 4446, pp. 873–880, 1980, doi: 10.1126/science.208.4446.873.

[54] S. C. Liao, Y. J. Chen, B. H. Kear, and W. E. Mayo, "High pressure/low temperature sintering of nanocrystalline alumina," *Nanostructured Mater.*, vol. 10, no. 6, pp. 1063–1079, 1998, doi: 10.1016/S0965-9773(98)00125-1.

[55] C. A. Randall, J. Guo, H. Guo, A. Baker, and M. T. Lanagan, "Cold sintering

ceramics and composites," 15/277,553, 2015.

[56] S. Funahashi *et al.*, "Demonstration of the Cold Sintering Process Study for the Densification and Grain Growth of ZnO Ceramics," *J. Am. Ceram. Soc.*, vol. 6, no. 2, pp. 1–6, 2016, doi: 10.1111/jace.14617.

[57] A. Baker, H. Guo, J. Guo, and C. Randall, "Utilizing the Cold Sintering Process for Flexible – Printable Electroceramic Device Fabrication," *J. Am. Ceram. Soc.*, no. 38709, pp. 1–3, 2016, doi: 10.1111/jace.14467.

[58] J. P. Maria *et al.*, "Cold sintering: Current status and prospects," *J. Mater. Res.*, vol. 32, no. 17, pp. 3205–3218, 2017, doi: 10.1557/jmr.2017.262.

[59] N. Yamasaki, K. Yanagisawa, M. Nishioka, and S. Kanahara, "A hydrothermal hot-pressing method: Apparatus and application," *J. Mater. Sci. Lett.*, vol. 5, no. 3, pp. 355–356, 1986, doi: 10.1007/BF01748104.

[60] K. Yanagisawa, K. Ioku, and N. Yamasaki, "Formation of Anatase Porous Ceramics by Hydrothermal Hot-Pressing of Amorphous Titania Spheres," *J. Am. Ceram. Soc.*, vol. 80, no. 5, pp. 1303–1306, 2005, doi: 10.1111/j.1151-2916.1997.tb02982.x.

[61] K. Hosoi, T. Hashida, H. Takahashi, N. Yamasaki, and T. Korenaga, "New Processing Technique for hyderoxyapatite ceramics by the hydrothermal hot-pressing method," *J. Am. Ceram. Soc.*, vol. 79, no. 10, pp. 2771–2774, 1996.

[62] J. Andrews, D. Button, and I. M. Reaney, "Advances in Cold Sintering," *Johnson Matthey Technol. Rev.*, no. 2, pp. 219–232, 2020, doi: 10.1595/205651320x15814150061554.

[63] D. Wang, H. Guo, C. S. Morandi, C. A. Randall, and S. Trolier-McKinstry, "Cold sintering and electrical characterization of lead zirconate titanate piezoelectric ceramics," *APL Mater.*, vol. 6, no. 1, 2018, doi: 10.1063/1.5004420.

[64] H. Nakaya, M. Iwasaki, T. H. de Beauvoir, and C. A. Randall, "Applying cold sintering process to a proton electrolyte material: CsH2PO4," *J. Eur. Ceram. Soc.*, vol. 39, no. 2–3, pp. 396–401, 2018, doi: 10.1016/j.jeurceramsoc.2018.09.001.

[65] H. Guo, A. Baker, J. Guo, and C. A. Randall, "Protocol for Ultralow-Temperature Ceramic Sintering: An Integration of Nanotechnology and the Cold Sintering Process," *ACS Nano*, p. acsnano.6b03800, 2016, doi: 10.1021/acsnano.6b03800.

[66] J. Guo *et al.*, "Cold Sintering: A Paradigm Shift for Processing and Integration of Ceramics," *Angew. Chemie - Int. Ed.*, vol. 16802, pp. 11629–11633, 2016, doi: 10.1002/anie.201605443.

[67] H. Kähäri, M. Teirikangas, J. Juuti, and H. Jantunen, "Improvements and modifications to room-temperature fabrication method for dielectric Li2MoO4

ceramics," *J. Am. Ceram. Soc.*, vol. 98, no. 3, pp. 687–689, 2015, doi: 10.1111/jace.13471.

[68] H. Kahari, M. Teirikangas, J. Juuti, and H. Jantunen, "Dielectric properties of lithium molybdate ceramic fabricated at room temperature," *J. Am. Ceram. Soc.*, vol. 97, no. 11, pp. 3378–3379, 2014, doi: 10.1111/jace.13277.

[69] D. L. Perry, *Handbook of Inorganic Compounds*. CRC Press, 1995.

[70] A. V. Barinova, R. K. Rastsvetaeva, and Y. V Nekrasov, "Crystal Structure of Li2MoO4," *Dokl. Chem.*, vol. 376, no. January 2001, pp. 343–346, 2001, doi: 10.1023/A.

[71] A. R. West, *Solid State Chemistry and its Applications*, 2nd editio. John Wiley & Sons, 2014.

[72] M. Moser, D. Klimm, S. Ganschow, A. Kwasniewski, and K. Jacobs, "Re-determination of the pseudobinary system Li 2 O – MoO 3," *Cryst. Res. Technol.*, vol. 43, no. 4, pp. 350–354, 2008, doi: 10.1002/crat.200711106.

[73] L. Denielou, J.-P. Petiet, and C. Tequi, "High Temperature calorimetric measurments: silver suplhate and alkali chromates, molybdates and tungstates," *J. Chem. Thermodyn.*, vol. 7, no. 9, pp. 901–902, 1970.

[74] W. S. Brower, H. S. Parker, R. S. Roth, and J. L. Waring, "Phase equilibrium and crystal growth in the system lithium oxide-molybdenum oxide," *J. Cryst. Growth*, vol. 16, no. 2, pp. 115–120, 1972, doi: 10.1016/0022-0248(72)90101-7.

[75] K. Momma and F. Izumi, "VESTA 3 for three-dimensional visualization of crystal, volumetric and morphology data," *J. Appl. Crystallogr.*, vol. 44, no. 6, pp. 1272–1276, 2011, doi: 10.1107/S0021889811038970.

[76] D. Zhou, C. a. Randall, H. Wang, L.-X. Pang, and X. Yao, "Microwave Dielectric Ceramics in Li2O-Bi2O3-MoO3 System with Ultra-Low Sintering Temperatures," *J. Am. Ceram. Soc.*, vol. 93, no. 4, pp. 1096–1100, 2010, doi: 10.1111/j.1551-2916.2009.03526.x.

[77] S. Sharma and R. N. P. Choudhary, "Phase transition in Li2MoO4 ceramics," *J. Mater. Sci. Lett.*, vol. 8, pp. 669–672, 1999.

[78] M. Inagaki, Y. Nishikawa, and M. Sakai, "Room-temperature Preparation of Li2MoO4 and its sintering," *J. Eur. Ceram. Soc.*, vol. 10, pp. 123–128, 1992.

[79] H. Zhang *et al.*, "Preparation of Li2MoO4 using aqueous solution method and microwave dielectric properties after sintering," *J. Mater. Sci. Mater. Electron.*, vol. 27, no. 5, pp. 1–5, 2016, doi: 10.1007/s10854-016-4444-2.

[80] T. W. S. Yip, Edmund J. Cussen, and C. Wilson, "Spontaneous formation of crystalline lithium molybdate from solid reagents at room temperature.," *Dalt. T3.8 (Cambridge, Engl. 2003)*, no. 2, pp. 411–7, 2010, doi:

10.1039/b908266b.

[81] A. M. P. Inc, "Sodium Molybdate Anhydrous Technical Grade | AAA Molybdenum Products, Inc," 2020. https://www.aaamolybdenum.com/mo/sodium-molybdate-anhydrous-technical-grade/ (accessed Apr. 13, 2020).

[82] I. AAA Molybdenum Products, "Potassion Molybdate | AAA Molybdenum Products, Inc," 2020. https://www.aaamolybdenum.com/mo/potassium-molybdate/.

[83] D. Wang *et al.*, "Temperature Stable Cold Sintered (Bi0.95Li0.05)(V0.9Mo0.1)O4-Na2Mo2O7 Microwave Dielectric Composites," *Materials (Basel).*, vol. 12, no. 9, p. 1370, 2019, doi: 10.3390/ma12091370.

[84] D. Wang, D. Zhou, K. Song, A. Feteira, C. A. Randall, and I. M. Reaney, "Cold-Sintered C0G Multilayer Ceramic Capacitors," *Adv. Electron. Mater.*, vol. 1900025, pp. 1–5, 2019, doi: 10.1002/aelm.201900025.

[85] D. Wang *et al.*, "Cold sintered CaTiO3-K2MoO4 microwave dielectric ceramics for integrated microstrip patch antennas," *Appl. Mater. Today*, vol. 18, p. 100519, 2020, doi: 10.1016/j.apmt.2019.100519.

[86] J. Gonzalez-julian *et al.*, "Unveiling the mechanisms of cold sintering of ZnO at 250 °C by varying applied stress and characterizing grain boundaries by Kelvin Probe Force Microscopy," *Acta Mater.*, vol. 144, pp. 116–128, 2018, doi: 10.1016/j.actamat.2017.10.055.

[87] X. Kang, E. Dickey, R. Floyd, and J. P. Maria, "Mechanism studies of hydrothermal cold sintering of zinc oxide at near room temperature," no. December 2018, pp. 1–11, 2019, doi: 10.1111/jace.16340.

[88] I. J. Induja and M. T. Sebastian, "Microwave dielectric properties of mineral sillimanite obtained by conventional and cold sintering process," *J. Eur. Ceram. Soc.*, vol. 37, no. 5, pp. 2143–2147, 2017, doi: 10.1016/j.jeurceramsoc.2017.01.007.

[89] J. Varghese, T. Siponkoski, M. Nelo, M. T. Sebastian, and H. Jantunen, "Microwave dielectric properties of low-temperature sinterable α-MoO3," *J. Eur. Ceram. Soc.*, vol. 38, no. 4, pp. 1541–1547, 2018, doi: 10.1016/j.jeurceramsoc.2017.11.027.

[90] D. Zhou, L. X. Pang, D. W. Wang, and I. M. Reaney, "Novel water-assisting low firing MoO 3 microwave dielectric ceramics," *J. Eur. Ceram. Soc.*, vol. 39, no. 7, pp. 2374–2378, 2019, doi: 10.1016/j.jeurceramsoc.2019.01.052.

[91] D. Zhou, L. Pang, D. Wang, and I. M. Reaney, "Journal of the European Ceramic Society Novel water-assisting low fi ring MoO 3 microwave dielectric ceramics," *J. Eur. Ceram. Soc.*, vol. 39, no. 7, pp. 2374–2378, 2019, doi:

10.1016/j.jeurceramsoc.2019.01.052.

[92] R. Boston *et al.*, "Reactive intermediate phase cold sintering in strontium titanate," *RSC Adv.*, vol. 8, no. 36, pp. 20372–20378, 2018, doi: 10.1039/c8ra03072c.

[93] C. Vakifahmetoglu *et al.*, "Reactive Hydrothermal Liquid-Phase Densification (rHLPD) of Ceramics - A Study of the BaTiO 3 [TiO 2] Composite System," *J. Am. Ceram. Soc.*, vol. 9, pp. 1–9, 2016, doi: 10.1111/jace.14468.

[94] J. P. Ma, X. M. Chen, W. Q. Ouyang, J. Wang, H. Li, and J. L. Fang, "Microstructure, dielectric, and energy storage properties of BaTiO3ceramics prepared via cold sintering," *Ceram. Int.*, vol. 44, no. 4, pp. 4436–4441, 2017, doi: 10.1016/j.ceramint.2017.12.044.

[95] H. Guo, J. Guo, A. Baker, and C. A. Randall, "Hydrothermal Assisted Cold Sintering Process: A New Guidance for Low Temperature Ceramic Sintering," *ACS Appl. Mater. Interfaces*, p. acsami.6b07481, 2016, doi: 10.1021/acsami.6b07481.

[96] M. C. Blanco-Lopez, B. Rand, and F. L. Riley, "The properties of aqueous phase suspensions of barium titanate," *J. Eur. Ceram. Soc.*, vol. 17, no. 2–3, pp. 281–287, 2002, doi: 10.1016/s0955-2219(96)00116-1.

[97] X. Zhu, J. Zhu, S. Zhou, Z. Liu, N. Ming, and D. Hesse, "BaTiO3 nanocrystals: Hydrothermal synthesis and structural characterization," *J. Cryst. Growth*, vol. 283, no. 3–4, pp. 553–562, 2005, doi: 10.1016/j.jcrysgro.2005.05.080.

[98] M. Bäurer, H. Kungl, and M. J. Hoffmann, "Influence of sr/ti stoichiometry on the densification behavior of strontium titanate," *J. Am. Ceram. Soc.*, vol. 92, no. 3, pp. 601–606, 2009, doi: 10.1111/j.1551-2916.2008.02920.x.

[99] H. Guo, T. J. M. Bayer, J. Guo, A. Baker, and C. A. Randall, "Current progress and perspectives of applying cold sintering process to ZrO2-based ceramics," *Scr. Mater.*, vol. 136, pp. 141–148, 2017, doi: 10.1016/j.scriptamat.2017.02.004.

[100] S. S. Faouri *et al.*, "High quality factor cold sintered Li2MoO4-BaFe12O19 composites for microwave applications," *Acta Mater.*, 2018, doi: 10.1016/j.actamat.2018.12.057.

[101] D. Wang *et al.*, "Cold-Sintered Temperature Stable Na 0.5 Bi 0.5 MoO 4 -Li 2 MoO 4 Microwave Composite Ceramics," *ACS Sustain. Chem. Eng.*, vol. 6, no. 2, pp. 2438–2444, 2018, doi: 10.1021/acssuschemeng.7b03889.

[102] D. Zhou *et al.*, "Microwave dielectric properties of (ABi)1/2MoO4 (A = Li, Na, K, Rb, Ag) type ceramics with ultra-low firing temperatures," *Mater. Chem. Phys.*, vol. 129, no. 3, pp. 688–692, 2011, doi: 10.1016/j.matchemphys.2011.05.040.

[103] I. M. Reaney, D. Iddles, F. Comtek, E. Drive, and S. S. Wv, "Microwave dielectric ceramics for resonators and filters in mobile phone networks," *J. Am. Ceram. Soc.*, vol. 89, no. 7, pp. 2063–2072, 2006, doi: 10.1111/j.1551-2916.2006.01025.X.

[104] J. Guo *et al.*, "Recent Progress in Applications of the Cold Sintering Process for Ceramic-Polymer Composites," *Adv. Funct. Mater.*, vol. 1801724, no. 2, p. 1801724, 2018, doi: 10.1002/adfm.201801724.

[105] J. Guo *et al.*, "Cold Sintering Na2Mo2O7 Ceramic with Poly(ether imide) (PEI) Polymer to Realize High-Performance Composites and Integrated Multilayer Circuits," *ACS Appl. Nano Mater.*, vol. 1, no. 8, pp. 3837–3844, 2018, doi: 10.1021/acsanm.8b00609.

[106] J. Guo, H. Guo, D. S. B. Heidary, S. Funahashi, and C. A. Randall, "Semiconducting properties of cold sintered V2O5 ceramics and Co-sintered V2O5-PEDOT:PSS composites," *J. Eur. Ceram. Soc.*, 2016, doi: 10.1016/j.jeurceramsoc.2016.11.021.

[107] Y. Zhao *et al.*, "Cold-Sintered V2O5-PEDOT:PSS Nanocomposites for Negative Temperature Coefficient Materials," *J. Eur. Ceram. Soc.*, no. August, 2018, doi: 10.1016/j.jeurceramsoc.2018.10.018.

[108] A. Sanson, D. Gardini, G. Montanari, C. Galassi, and E. Roncari, "Key role of milling in the optimization of TiO2 nanoinks," *J. Mater. Res.*, vol. 21, no. 06, pp. 1561–1569, 2011, doi: 10.1557/jmr.2006.0188.

[109] H. Wu *et al.*, "Effect of the particle size and the debinding process on the density of alumina ceramics fabricated by 3D printing based on stereolithography," *Ceram. Int.*, vol. 42, no. 15, pp. 17290–17294, 2016, doi: 10.1016/j.ceramint.2016.08.024.

[110] R. Rudež, J. Pavlič, and S. Bernik, "Preparation and influence of highly concentrated screen-printing inks on the development and characteristics of thick-film varistors," *J. Eur. Ceram. Soc.*, vol. 35, no. 11, pp. 3013–3023, 2015, doi: 10.1016/j.jeurceramsoc.2015.04.035.

[111] D. Marani, C. Gadea, J. Hjelm, P. Hjalmarsson, M. Wandel, and R. Kiebach, "Influence of hydroxyl content of binders on rheological properties of cerium-gadolinium oxide (CGO) screen printing inks," *J. Eur. Ceram. Soc.*, vol. 35, no. 5, pp. 1495–1504, 2015, doi: 10.1016/j.jeurceramsoc.2014.11.025.

[112] M. R. Somalu, V. Yufit, I. P. Shapiro, P. Xiao, and N. P. Brandon, "The impact of ink rheology on the properties of screen-printed solid oxide fuel cell anodes," *Int. J. Hydrogen Energy*, vol. 38, no. 16, pp. 6789–6801, 2013, doi: 10.1016/j.ijhydene.2013.03.108.

[113] B. Philip, E. Jewell, P. Greenwood, and C. Weirman, "Material and process

optimization screen printing carbon graphite pastes for mass production of heating elements," *J. Manuf. Process.*, vol. 22, pp. 185–191, 2016, doi: 10.1016/j.jmapro.2016.03.001.

[114] M. R. Somalu, A. Muchtar, W. R. W. Daud, and N. P. Brandon, "Screen-printing inks for the fabrication of solid oxide fuel cell films: A review," *Renew. Sustain. Energy Rev.*, vol. 75, no. October, pp. 0–1, 2016, doi: 10.1016/j.rser.2016.11.008.

[115] Y. D. Kim and J. Hone, "Screen printing of 2D semiconductors," *Nature*.

[116] H. D. Goldberg, R. B. Brown, D. P. Liu, and M. E. Meyerhoff, "Screen printing: a technology for the batch fabrication of integrated chemical-sensor arrays," *Sensors Actuators B. Chem.*, vol. 21, no. 3, pp. 171–183, 1994, doi: 10.1016/0925-4005(94)01249-0.

[117] T. Syrovy, T. Kazda, L. Syrova, J. Vondrak, L. Kubac, and M. Sedlarikova, "Cathode material for lithium ion accumulators prepared by screen printing for Smart Textile applications," *J. Power Sources*, vol. 309, pp. 192–201, 2016, doi: 10.1016/j.jpowsour.2016.01.089.

[118] H. W. Lin, C. P. Chang, W. H. Hwu, and M. Der Ger, "The rheological behaviors of screen-printing pastes," *J. Mater. Process. Technol.*, vol. 197, no. 1–3, pp. 284–291, 2008, doi: 10.1016/j.jmatprotec.2007.06.067.

[119] R. Muecke, O. Buechler, N. H. Menzler, B. Lindl, R. Va??en, and H. P. Buchkremer, "High-precision green densities of thick films and their correlation with powder, ink, and film properties," *J. Eur. Ceram. Soc.*, vol. 34, no. 15, pp. 3897–3916, 2014, doi: 10.1016/j.jeurceramsoc.2014.04.012.

[120] R. J. Cava, "Dielectric materials for applications in microwave communications," *J. Mater. Chem.*, vol. 11, no. 1, pp. 54–62, 2001, doi: 10.1039/b003681l.

[121] M. T. Sebastian, R. Ubic, and H. Jantunen, "Low-loss dielectric ceramic materials and their properties," *Int. Mater. Rev.*, vol. 60, no. 7, pp. 392–412, 2015, doi: 10.1179/1743280415Y.0000000007.

[122] D. Soren, R. Ghatak, R. K. Mishra, and D. R. Poddar, "Dielectric Resonator Antennas : Designs and Advances," *Prog. Electromagn. Res. B*, vol. 60, no. July, pp. 195–213, 2014, doi: 10.2528/PIERB14031306.

[123] S. B. Narang and S. Bahel, "Low loss dielectric ceramics for microwave applications : a review," *Ceram. Process. Res.*, vol. 11, no. 3, pp. 316–321, 2010.

[124] Z. Peng, H. Wang, and X. Yao, "Dielectric resonator antennas using high permittivity ceramics," *Ceram. Int.*, vol. 30, no. 7, pp. 1211–1214, 2004, doi: 10.1016/j.ceramint.2003.12.079.

[125] R. Freer and F. Azough, "Microstructural engineering of microwave dielectric ceramics," *J. Eur. Ceram. Soc.*, vol. 28, no. 7, pp. 1433–1441, 2008, doi: 10.1016/j.jeurceramsoc.2007.12.005.

[126] A. Petosa and A. Ittipiboon, "Dielectric Resonator Antennas: A Historical Review and the Current State of the Art," *IEEE Antennas Propag. Mag.*, vol. 52, no. 5, pp. 91–116, 2010, doi: 10.1109/MAP.2010.5687510.

[127] L. V Blake and M. W. Long, *Antennas: Fundamentals, Design, Measurement*. SciTech Publishing.

[128] R. Bancroft, *Microstrip and Printed Antenna Design*. 2009.

[129] M. D. Deshpande and N. K. Das, "Rectangular Microstrip Antenna for Circular Polarization," *IEEE Trans. Antennas Propag.*, vol. 34, no. 5, pp. 744–746, 1986.

[130] A. J. Moulson and J. M. Herbert, *Electroceramics*, 2nd ed. John Wiley & Sons, 2003.

[131] T. A. . Sulong, R. A. . Osman, and M. . Idris, "Trends of microwave dielectric materials for antenna application," in *AIP Conference Proceedings*, 2016, no. July, doi: 10.1063/1.4958779.

[132] R. D. Shannon, "Dielectric polarizabilities of ions in oxides and fluorides," *J. Appl. Phys.*, vol. 73, no. 1, pp. 348–366, 1993, doi: 10.1063/1.353856.

[133] S. J. Penn *et al.*, "Effect of Porosity and Grain Size on the Microwave Dielectric Properties of Sintered Alumina," *J. Am. Ceram. Soc.*, vol. 80, no. 7, pp. 1885–1888, 2005, doi: 10.1111/j.1151-2916.1997.tb03066.x.

[134] P. Dielectric and L. Nature, "Physical Mechanisms Determining Microwave Dielectrics Properties," *2015 IEEE 35th Int. Conf. Electron. Nanotechnol.*, pp. 29–34, 2015.

[135] J. D. Breeze, J. M. Perkins, D. W. McComb, and N. M. N. Alford, "Do grain boundaries affect microwave dielectric loss in oxides?," *J. Am. Ceram. Soc.*, vol. 92, no. 3, pp. 671–674, 2009, doi: 10.1111/j.1551-2916.2009.02932.x.

[136] H. Ohsato, T. Tsunooka, and T. S. K. Kakimoto, "Forsterite ceramics for millimeterwave dielectrics," *J. Electroceramics*, vol. 17, pp. 445–450, 2006, doi: 10.1007/s10832-006-0452-6.

[137] N. M. N. Alford *et al.*, "Dielectric loss of oxide single crystals and polycrystalline analogues from 10 to 320 K," *J. Eur. Ceram. Soc.*, vol. 21, no. 15, pp. 2605–2611, 2001, doi: 10.1016/S0955-2219(01)00324-7.

[138] N. Ichinose, "Effect of grain size and secondary phase on microwave dielectric properties of Ba(Mg1/3Ta2/3)O3 and Ba([Mg,Zn]1/3Ta2/3)O3 systems," *J. Eur. Ceram. Soc.*, vol. 26, no. 10–11, pp. 1755–1759, 2006, doi: 10.1016/j.jeurceramsoc.2005.09.032.

[139] S. Roopas Kiran, G. Sreenivasulu, V. R. K. Murthy, V. Subramanian, and B. S. Murty, "Effect of grain size on the microwave dielectric characteristics of high-energy ball-milled zinc magnesium titanate ceramics," *J. Am. Ceram. Soc.*, vol. 95, no. 6, pp. 1973–1979, 2012, doi: 10.1111/j.1551-2916.2012.05128.x.

[140] D. Kajfez and P. Guillon, *Dielectric Resonators*, 2nd ed. Atlanta: Noble Publishing Corporation, 1998.

[141] E. L. Colla, I. M. Reaney, and N. Setter, "Effect of structural changes in complex perovskites on the temperature coefficient of the relative permittivity," *J. Appl. Phys.*, vol. 74, no. 5, pp. 3414–3425, 1993, doi: 10.1063/1.354569.

[142] P. J. Harrop, "Temperature Coefficients of Capacitance of Solids," *J. Mater. Sci.*, vol. 4, pp. 370–374, 1969.

[143] H. Zheng, I. M. Reaney, D. Muir, T. Price, and D. M. Iddles, "Composite Dielectric Ceramics Based on BaO–Ln_2O_3–TiO_2 (Ln = Nd, La)," *Jpn. J. Appl. Phys.*, vol. 44, no. 5A, pp. 3087–3090, 2005, doi: 10.1143/JJAP.44.3087.

[144] K. Kinoshita and A. Yamaji, "Grain-size effects on dielectric properties in barium titanate ceramics," *J. Appl. Phys.*, vol. 47, no. 1, pp. 371–373, 1976, doi: 10.1063/1.322330.

[145] G. Arlt, D. Hennings, and G. De With, "Dielectric properties of fine-grained barium titanate ceramics," *J. Appl. Phys.*, vol. 58, no. 4, pp. 1619–1625, 1985, doi: 10.1063/1.336051.

[146] M. P. Mcneal, S. Jang, and R. E. Newnham, "The effect of grain and particle size on the microwave properties of barium titanate (BaTiO3)," *J. Appl. Phys.*, vol. 83, no. 6, pp. 3288–3297, 1998, doi: 10.1063/1.367097.

[147] H. Ohsato, "Research and Development of Microwave Dielectric Ceramics for Wireless Communications," *J. Ceram. Soc. Japan*, vol. 113, pp. 703–711, 2005, doi: 10.2109/jcersj.113.703.

[148] K. Wakino, K. Minai, and H. Tamura, "Microwave Characteristics of (Zr, Sn)TiO4 and BaO-PbO-Nd2O3--TiO2 Dielectric Resonators," *J. Am. Ceram. Soc.*, vol. 67, no. 4, pp. 278–281, 1984, doi: 10.1111/j.1151-2916.1984.tb18847.x.

[149] P. L. Wise, I. M. Reaney, W. E. Lee, D. M. Iddles, D. S. Cannell, and T. J. Price, "Tunability of tau(f) in perovskites and related compounds," *J. Mater. Res.*, vol. 17, no. 8, pp. 2033–2040, 2002, doi: Doi 10.1557/Jmr.2002.0301.

[150] R. C. KELL, A. C. GREENHAM, and G. C. E. OLDS, "High-Permittivity Temperature-Stable Ceramic Dielectrics with Low Microwave Loss," *J. Am. Ceram. Soc.*, vol. 56, no. 7, pp. 352–354, 1973, doi: 10.1111/j.1151-2916.1973.tb12684.x.

[151] I. M. Reaney and R. Ubic, "Dielectric and structural characteristics of perovskites and related materials as a function of tolerance factor," *Ferroelectrics*, vol. 228, no. 1, pp. 23–38, 1999, doi: 10.1080/00150199908226123.

[152] I. M. Reaney *et al.*, "On the temperature coefficient of resonant frequency in microwave dielectrics," *Philos. Mag. A*, vol. 81, no. 2, pp. 501–510, 2001, doi: 10.1080/01418610108214318.

[153] D. S. Brauer, "Bioactive glasses - Structure and properties," *Angew. Chemie - Int. Ed.*, vol. 54, no. 14, pp. 4160–4181, 2015, doi: 10.1002/anie.201405310.

[154] R. Hill, "An alternative view of the degradation of bioglass," *J. Mater. Sci. Lett.*, vol. 15, no. 13, pp. 1122–1125, 1996, doi: 10.1007/BF00539955.

[155] W. Bragg, "The Glassy State," in *Structural Chemistry of Glasses*, Elsevier Ltd, pp. 13–76.

[156] W. H. Zachariasen, "The atomic arrangement in glass," *J. Am. Chem. Soc.*, vol. 54, no. 10, pp. 3841–3851, 1932, doi: 10.1021/ja01349a006.

[157] F. Devreux, P. Barboux, M. Filoche, and B. Sapoval, "A simplified model for glass dissolution in water," *J. Mater. Sci.*, vol. 36, no. 6, pp. 1331–1341, 2001, doi: 10.1023/A:1017591100985.

[158] L. L. Hench and D. E. Clark, "Physical chemistry of glass surfaces," *J. Non. Cryst. Solids*, vol. 28, no. 1, pp. 83–105, 1978, doi: 10.1016/0022-3093(78)90077-7.

[159] K. G. Knauss and T. J. Wolery, "The dissolution kinetics of quartz as a function of pH and time at 70°C," *Geochim. Cosmochim. Acta*, vol. 52, no. 1, pp. 43–53, 1988, doi: 10.1016/0016-7037(88)90055-5.

[160] D.-H. Gwo, "Ultra precision and reliable bonding method," *Google Patents*, vol. 1, no. 12, 1998, [Online]. Available: https://patents.google.com/patent/US6284085B1/en.

[161] Dz-Hung Gwo, "Hydroxide-Catalyzed Bonding," vol. 1, no. 12, 2003.

[162] A. M. A. Van Veggel and C. J. Killow, "Hydroxide catalysis bonding for astronomical instruments," *Adv. Opt. Technol.*, vol. 3, no. 3, pp. 293–307, 2014, doi: 10.1515/aot-2014-0022.

[163] E. J. Elliffe *et al.*, "Hydroxide-catalysis bonding for stable optical systems for space," *Class. Quantum Gravity*, vol. 22, no. 10, 2005, doi: 10.1088/0264-9381/22/10/018.

[164] K. Haughian *et al.*, "Effect of heat treatment and aging on the mechanical loss and strength of hydroxide catalysis bonds between fused silica samples," *Phys. Rev. D*, vol. 96, no. 4, pp. 1–9, 2017, doi: 10.1103/PhysRevD.96.042003.

[165] J. Seto and P. A. Romero, "Shaping it up: Design and engineering of

biominerals and crystalline materials from the bottom up," in *Biomineralization and Biomaterials*, 2016, pp. 3–50.

[166] G. Taveri, S. Grasso, F. Gucci, J. Toušek, and I. Dlouhy, "Bio-Inspired Hydro-Pressure Consolidation of Silica," *Adv. Funct. Mater.*, vol. 28, no. 48, pp. 1–8, 2018, doi: 10.1002/adfm.201805794.

[167] D. Ke *et al.*, "Ultra-low energy joining: An invisible strong bond at room temperature," *J. Eur. Ceram. Soc.*, vol. 39, no. 16, pp. 5358–5363, 2019, doi: 10.1016/j.jeurceramsoc.2019.08.004.

[168] A. Ndayishimiye *et al.*, "Hydrothermal Sintering for Densification of Silica. Evidence for the Role of Water," *J. Eur. Ceram. Soc.*, vol. 38, no. 4, pp. 1860–1870, 2017, doi: 10.1016/j.jeurceramsoc.2017.10.011.

[169] K. Yanagisawa, M. Nishioka, K. Ioku, and N. Yamasaki, "Densification of silica gels by hydrothermal hot-pressing," *J. Mater. Sci. Lett.*, vol. 12, no. 14, pp. 1073–1075, 1993, doi: 10.1007/BF00420525.

[170] G. Kaur, *Clinical Applications of Biomaterials. State-of-the-Art Progress, Trends, and Novel Approaches*. Springer Internat, 2017.

[171] J. Huang, "Design and Development of Ceramics and Glasses," in *Biology and Engineering of Stem Cell Niches*, 2017, pp. 315–329.

[172] L. L. Hench, "Bioceramics : From Concept to Clinic," *J. Am. Ceram. Soc.*, vol. 74, no. 7, pp. 1487–1510, 1991.

[173] L. L. Hench, "Biomaterials: A forecast for the future," *Biomaterials*, vol. 19, no. 16, pp. 1419–1423, 1998, doi: 10.1016/S0142-9612(98)00133-1.

[174] I. B. Leonor, A. I. Rodrigues, and R. L. Reis, *Designing biomaterials based on biomineralization for bone repair and regeneration*. Elsevier Ltd., 2016.

[175] L. L. Fiench and J. Wilson, "Surface-Active Biomaterials," *Science (80-.).*, vol. 226, pp. 630–636, 1980.

[176] V. Krishnan and T. Lakshmi, "Bioglass : A novel biocompatible innovation," *78 J. Adv. Pharm. Technol. Res.*, vol. 4, no. 2, 2013, doi: 10.4103/2231-4040.111523.

[177] L. L. Hench, "Opening paper 2015- Some comments on Bioglass : Four Eras of Discovery and Development," *Biomed. Glas.*, vol. 1, pp. 1–11, 2015, doi: 10.1515/bglass-2015-0001.

[178] L. L. Hench, "The story of Bioglass," *J. Mater. Sci. Mater. Med.*, vol. 17, pp. 967–978, 2006, doi: 10.1007/s10856-006-0432-z.

[179] L. L. Hench, "Bioceramics," *J. Am. Ceram. Soc.*, vol. 28, 1998.

[180] J. K. Christie, R. I. Ainsworth, and N. H. De Leeuw, "Investigating structural features which control the dissolution of bioactive phosphate glasses: Beyond the network connectivity," *J. Non. Cryst. Solids*, vol. 432, pp. 31–34, 2016,

doi: 10.1016/j.jnoncrysol.2015.01.016.
[181] M. Edén, "The split network analysis for exploring composition-structure correlations in multi-component glasses: I. Rationalizing bioactivity-composition trends of bioglasses," *J. Non. Cryst. Solids*, vol. 357, no. 6, pp. 1595–1602, 2011, doi: 10.1016/j.jnoncrysol.2010.11.098.
[182] S. Zahid *et al.*, "Biological behavior of bioactive glasses and their composites," *RSC Adv.*, vol. 6, no. 74, pp. 70197–70214, 2016, doi: 10.1039/c6ra07819b.
[183] J. Chen, L. Zeng, X. Chen, T. Liao, and J. Zheng, "Preparation and characterization of bioactive glass tablets and evaluation of bioactivity and cytotoxicity in vitro," *Bioact. Mater.*, vol. 3, no. 3, pp. 315–321, 2018, doi: 10.1016/j.bioactmat.2017.11.004.
[184] M. Navarro and T. Serra, *Biomimetic mineralization of ceramics and glasses*. Elsevier Ltd., 2016.
[185] J. A. Nychka, S. L. R. Mazur, S. Kashyap, D. Li, and F. Yang, "Dissolution of bioactive glasses: The effects of crystallinity coupled with stress," *Biomed. Mater. Devices*, vol. 61, no. 9, pp. 45–51, 2009, doi: 10.1007/s11837-009-0132-5.
[186] M. Vallet-Regí and A. J. Salinas, *Ceramics as bone repair materials*, Second Edi. Elsevier Ltd, 2019.
[187] A. N. Cormack and A. Tilocca, "Structure and biological activity of glasses and ceramics," *Philos. Trans. R. Soc. A Math. Phys. Eng. Sci.*, vol. 370, no. 1963, pp. 1271–1280, 2012, doi: 10.1098/rsta.2011.0371.
[188] A. M. Gatti, T. Yamamuro, L. L. Hench, and O. H. Andersson, "In-Vivo Reactions in Some Bioactive Glasses and Glass-Ceramics Granules," *Cells Mater.*, vol. 3, no. 3, 1993.
[189] K. E. Wallace, R. G. Hill, and P. V Hatton, "Influence of sodium oxide content on bioactive glass properties," *J. Mater. Sci. Mater. Med.*, vol. 10, pp. 697–701, 1999.
[190] H. Andersson, "Calcium phosphate formation at the surface of bioactive glass in vitro," *J. Biomed. Mater. Res.*, vol. 25, pp. 1019–1030, 1991.
[191] L. Gerhardt and A. R. Boccaccini, "Bioactive Glass and Glass-Ceramic Scaffolds for Bone Tissue Engineering," no. July, pp. 3867–3910, 2010, doi: 10.3390/ma3073867.
[192] D. C. Greenspan, "Bioactive glass : mechanisms of bone bonding," *Tandläkartidningen Årk*, vol. 91, no. 8, pp. 1–32, 1999, [Online]. Available: http://www.tandlakartidningen.se/media/927/Greenspan_8_1999.pdf.
[193] Hench and Wilson, *Introduction to Bioceramics.* .
[194] J. Chen, W. Shi, A. J. Norman, and P. Ilavarasan, "Biomedical applications of

polymer-composite materials: a review," *Compos. Sci. Technol.*, no. 61, pp. 1189–1224, 2001, doi: 10.1109/isemc.2002.1032709.

[195] C. Oldani and A. Dominguez, "Titanium as a Biomaterial for Implants," in *Recent Advances in Arthroplasty*, S. Fokter, Ed. .

[196] M. Al Minnath, "7. Metals and alloys for biomedical applications," in *Fundamental Biomaterials: Metals*, Elsevier Ltd, 2018, pp. 167–174.

[197] A. T. Sidambe, "Biocompatibility of Advanced Manufactured Titanium Implants—A Review," *Materials (Basel).*, vol. 7, pp. 8168–8188, 2014, doi: 10.3390/ma7128168.

[198] J. M. Gomez-Vega, E. Saiz, A. P. Tomsia, G. W. Marshall, and S. J. Marshall, "Bioactive glass coatings with hydroxyapatite and Bioglass particles on Ti-based implants . 1 . Processing," *Biomaterials*, vol. 21, pp. 105–111, 2000.

[199] J. Wilson, "1. Metallic biomaterials: State of the art and new challenges," in *Fundamental Biomaterials: Metals*, Elsevier Ltd, pp. 1–34.

[200] F. Baino, S. Hamzehlou, and S. Kargozar, "Bioactive glasses: Where are we and where are we going?," *J. Funct. Biomater.*, vol. 9, no. 1, 2018, doi: 10.3390/jfb9010025.

[201] J. N. Oliver, D. Zhu, Y. Su, X. Lu, P. Kuo, and J. Du, "Bioactive Materials Bioactive glass coatings on metallic implants for biomedical applications," *Bioact. Mater.*, vol. 4, no. September 2019, pp. 261–270, 2020, doi: 10.1016/j.bioactmat.2019.09.002.

[202] K. De Groot, R. Geesink, and C. P. A. T. Klein, "Plasma sprayed coatings," *J. Biomed. Mater. Res.*, vol. 21, pp. 1375–1381, 1987.

[203] S. R. Radin and P. Ducheyne, "Plasma spraying induced changes of calcium phosphate ceramic characteristics and the effect on in vitro stability," *Jountal Mater. Sci. Mater. Med.*, vol. 3, pp. 33–42, 1992.

[204] L. L. Hench, R. J. Splinter, W. C. Allen, and T. K. Greenlee, "Bonding Mechanisms at the Interface of Ceramic Prosthetic Materials," *J. Biomed. Mater. Res. Symp.*, vol. 2, no. 2, p. 117/141, 1971.

[205] J. Huang, L. Di Silvio, M. Wang, I. Rehman, C. Ohtsuki, and W. Bonfield, "Evaluation of in vitro bioactivity and biocompatibility of Bioglass®-reinforced polyethylene composite," *J. Mater. Sci. Mater. Med.*, vol. 8, no. 12, pp. 809–813, 1997, doi: 10.1023/A:1018581100400.

[206] O. Tsigkou, L. L. Hench, A. R. Boccaccini, J. M. Polak, and M. M. Stevens, "Enhanced differentiation and mineralization Bioglass1 composite films in the absence of human fetal osteoblasts on PDLLA containing of osteogenic supplements," *J. Biomed. Mater. Res. Part A*, vol. 79, no. 4, pp. 963–73, 2006, doi: 10.1002/jbm.a.30910.

[207] S. Ramakrishna and Z.-M. Huang, *Biocomposites*. Elsevier, 2016.

[208] E. Fiume, J. Barberi, E. Verné, and F. Baino, "Bioactive glasses: From parent 45S5 Composition to Scaffold-Assisted Tissue-Healing Therapies," *J. Funct. Biomater.*, vol. 9, no. 1, 2018, doi: 10.3390/jfb9010024.

[209] A. Stamboulis, L. L. Hench, and A. R. Boccaccini, "Mechanical properties of biodegradable polymer sutures coated with bioactive glass," *J. Mater. Sci. Mater. Med.*, vol. 13, no. 9, pp. 843–848, 2002, doi: 10.1023/A:1016544211478.

[210] A. R. Boccaccini, A. G. Stamboulis, A. Rashid, and J. A. Roether, "Composite Surgical Sutures with Bioactive Glass Coating," *J. Biomed. Mater. Res. - Part B Appl. Biomater.*, vol. 67, no. 1, pp. 618–626, 2003, doi: 10.1002/jbm.b.10047.

[211] J. A. Roether, A. R. Boccaccini, L. L. Hench, V. Maquet, and S. Gautier, "Development and in vitro characterisation of novel bioresorbable and bioactive composite materials based on polylactide foams and Bioglass s for tissue engineering applications," *Biomaterials*, vol. 23, pp. 3871–3878, 2002.

[212] J. A. Roether, J. E. Gough, A. R. Boccaccini, L. L. Hench, V. Maquet, and R. Jérôme, "Novel bioresorbable and bioactive composites based on bioactive glass and polylactide foams for bone tissue engineering," *J. Mater. Sci. Mater. Med.*, vol. 13, no. 12, pp. 1207–1214, 2002, doi: 10.1023/A:1021166726914.

[213] X. B. Yang *et al.*, "Evaluation of human bone marrow stromal cell growth on biodegradable polymer/Bioglass® composites," *Biochem. Biophys. Res. Commun.*, vol. 342, no. 4, pp. 1098–1107, 2006, doi: 10.1016/j.bbrc.2006.02.021.

[214] J. J. Blaker, V. Maquet, R. Jérôme, A. R. Boccaccini, and S. N. Nazhat, "Mechanical properties of highly porous PDLLA/Bioglass® composite foams as scaffolds for bone tissue engineering," *Acta Biomater.*, vol. 1, no. 6, pp. 643–652, 2005, doi: 10.1016/j.actbio.2005.07.003.

[215] J. J. Blaker, J. E. Gough, V. Maquet, I. Notingher, and A. R. Boccaccini, "In vitro evaluation of novel bioactive composites based on Bioglass®-filled polylactide foams for bone tissue engineering scaffolds," *J. Biomed. Mater. Res. - Part A*, vol. 67, no. 4, pp. 1401–1411, 2003, doi: 10.1002/jbm.a.20055.

[216] A. R. Boccaccini, J. J. Blaker, V. Maquet, R. Jerome, S. Blacher, and J. A. Roether, "Biodegradable and bioactive polymer/bioglass® composite foams for tissue engineering scaffolds," *Mater. Sci. Forum*, vol. 494, pp. 499–506, 2005, doi: 10.4028/0-87849-971-7.499.

[217] G. Conoscenti, V. La Carrubba, and V. Brucato, "A Versatile Technique to Produce Porous Polymeric Scaffolds: The Thermally Induced Phase Separation

(TIPS) Method," *Arch. Chem. Res.*, vol. 01, no. 02, pp. 10–12, 2017, doi: 10.21767/2572-4657.100012.

[218] V. Maquet, A. R. Boccaccini, L. Pravata, I. Notingher, and R. Jérôme, "Preparation, characterization, and in vitro degradation of bioresorbable and bioactive composites based on Bioglass®-filled polylactide foams," *J. Biomed. Mater. Res. - Part A*, vol. 66, no. 2, pp. 335–346, 2003, doi: 10.1002/jbm.a.10587.

[219] F. Carfì Pavia, V. La Carrubba, S. Piccarolo, and V. Brucato, "Polymeric scaffolds prepared via thermally induced phase separation: Tuning of structure and morphology," *J. Biomed. Mater. Res. - Part A*, vol. 86, no. 2, pp. 459–466, 2008, doi: 10.1002/jbm.a.31621.

[220] B. D. Ratner, *The Biocompatibility of Implant Materials*. Elsevier Inc., 2015.

[221] A. A. Zadpoor, "Relationship between in vitro apatite-forming ability measured using simulated body fluid and in vivo bioactivity of biomaterials," *Mater. Sci. Eng. C*, vol. 35, no. 1, pp. 134–143, 2014, doi: 10.1016/j.msec.2013.10.026.

[222] F. Varíola *et al.*, "Improving biocompatibility of implantable metals by nanoscale modification of surfaces: An overview of strategies, fabrication methods, and challenges," *Small*, vol. 5, no. 9, pp. 996–1006, 2009, doi: 10.1002/smll.200801186.

[223] J. Wilson and G. H. Pigott, "Toxicology and biocompatibility of bioglasses," *J. Biomed. Mater. Res.*, vol. 15, pp. 805–817, 1981.

[224] F. E. Ciraldo, E. Boccardi, V. Melli, F. Westhauser, and A. R. Boccaccini, "Tackling bioactive glass excessive in vitro bioreactivity: Preconditioning approaches for cell culture tests," *Acta Biomater.*, vol. 75, pp. 3–10, 2018, doi: 10.1016/j.actbio.2018.05.019.

[225] M. Rismanchian, N. Khodaeian, L. Bahramian, M. Fathi, and H. Sadeghi-Aliabadi, "In-vitro comparison of cytotoxicity of two bioactive glasses in micropowder and nanopowder forms," *Iran. J. Pharm. Res.*, vol. 12, no. 3, pp. 437–443, 2013, doi: 10.22037/ijpr.2013.1348.

[226] B. Cowan, *Nuclear Magnetic Resonance and Relaxation*. Cambridge University Press, 1997.

[227] R. K. Harris, E. D. Becker, S. M. C. De Menezes, R. Goodfellow, and P. Granger, "NMR nomenclature: Nuclear spin properties and conventions for chemical shifts - IUPAC recommendations 2001," *Solid State Nucl. Magn. Reson.*, vol. 22, no. 4, pp. 458–483, 2002, doi: 10.1006/snmr.2002.0063.

[228] H. Kähäri, "A room-temperature fabrication method for microwave dielectric Li_2MoO_4 ceramics and their applicability for antennas," University of Oulu, 2016.

[229] Y. Ji, K. Song, X. Luo, B. Liu, H. Barzegar Bafrooei, and D. Wang, "Microwave Dielectric Properties of (1-x) Li2MoO4–xMg2SiO4 Composite Ceramics Fabricated by Cold Sintering Process," *Front. Mater.*, vol. 6, no. October, pp. 1–6, 2019, doi: 10.3389/fmats.2019.00256.

[230] G. D. Saraiva, W. Paraguassu, P. T. C. Freire, A. J. Ramiro de Castro, F. F. de Sousa, and J. Mendes Filho, "Temperature induced phase transformations on the Li2MoO4 system studied by Raman spectroscopy," *J. Mol. Struct.*, vol. 1139, pp. 119–124, Jul. 2017, doi: 10.1016/j.molstruc.2017.03.038.

[231] S. M. Baschenko and L. S. Marchenko, "On Raman spectra of water, its structure and dependence on temperature," 2011.

[232] P. C. Cross, J. Burnham, and P. A. Leighton, "The raman spectrum and structure of Water," *J. Organomet. Chem.*, vol. 59, no. 3, pp. 1134–1147, 1937, doi: 10.1016/S0022-328X(00)92067-9.

[233] V. S. Gorelik *et al.*, "Raman spectra of lithium compounds," *J. Phys. Conf. Ser.*, vol. 918, no. 1, 2017, doi: 10.1088/1742-6596/918/1/012035.

[234] J. Guo *et al.*, "Cold Sintering: Progress, Challenges, and Future Opportunities," *Annu. Rev. Mater. Res.*, vol. 49, no. 1, pp. 275–295, 2019, doi: 10.1146/annurev-matsci-070218-010041.

[235] D. Zhou, H. Wang, X. Yao, and L. X. Pang, "Microwave dielectric properties of low temperature firing Bi 2Mo2O9 ceramic," *J. Am. Ceram. Soc.*, vol. 91, no. 10, pp. 3419–3422, 2008, doi: 10.1111/j.1551-2916.2008.02596.x.

[236] R. Gheisari *et al.*, "Multi-material additive manufacturing of low sintering temperature Bi2Mo2O9 ceramics with Ag floating electrodes by selective laser burnout," *Virtual Phys. Prototyp.*, vol. 15, no. 2, pp. 133–147, 2020, doi: 10.1080/17452759.2019.1708026.

[237] D. Zhou, C. A. Randall, H. Wang, L.-X. Pang, and X. Yao, "Microwave Dielectric Ceramics in Li 2 O–Bi 2 O 3 –MoO 3 System with Ultra-Low Sintering Temperatures," *J. Am. Ceram. Soc.*, vol. 93, no. 4, pp. 1096–1100, 2010, doi: 10.1111/j.1551-2916.2009.03526.x.

[238] J. Kumar and E. Ruckenstein, "Structural changes in thin films of the 1:1 bismuth molybdate under reduction and oxidation conditions," *J. Catal.*, vol. 45, no. 2, pp. 198–215, 1976, doi: 10.1016/0021-9517(76)90135-4.

[239] S. Karlsson, B. Jonson, and C. Stålhandske, "The Technology of Chemical Glass Strengthening – A Review," *Eur. J. Glas. Sci. Technol. Part A*, vol. 51, no. 2, pp. 2–7, 2010.

[240] A. K. Varshneya, "Chemical Strengthening of Glass: Lessons Learned and Yet To Be Learned," *Int. J. Appl. Glas. Sci.*, vol. 1, no. 2, pp. 131–142, 2010, doi: 10.1111/j.2041-1294.2010.00010.x.

[241] I. W. Donald, "Methods for improving the mechanical properties of oxide glasses," *J. Mater. Sci.*, vol. 24, no. 12, pp. 4177–4208, 1989, doi: 10.1007/BF00544488.

[242] M. J. KERPER and T. G. SCUDERI, "Mechanical Properties of Chemically Strengthened Glasses at High Temperatures," *J. Am. Ceram. Soc.*, vol. 49, no. 11, pp. 613–618, 1966, doi: 10.1111/j.1151-2916.1966.tb13179.x.

[243] "Coatings on Glass - H. Pulker, H.K. Pulker - Google Books." https://books.google.co.uk/books?hl=en&lr=&id=ho2pYhOiEMcC&oi=fnd&pg=PP1&dq=coatings+for+glass&ots=vNvfnNjxiP&sig=Q3ryJWzOuchRTOkyOxh4rxF1vyc#v=onepage&q=coatings for glass&f=false (accessed Mar. 10, 2021).

[244] T. Morimoto, H. Tomonaga, and A. Mitani, "Ultraviolet ray absorbing coatings on glass for automobiles," vol. 351, pp. 1–5, 1999.

[245] J. Delgado, "Restoring Medieval Stained-Glass Transparency : Use of New Task Specific Luminescent Ionic Liquids for Corrosion Crusts Removal," 2016.

[246] E. L. Roggen, "In vitro toxicity testing in the twenty-first century," *Front. Pharmacol.*, vol. FEB, no. February, pp. 2–4, 2011, doi: 10.3389/fphar.2011.00003.

[247] N. Stone-Weiss, R. E. Youngman, R. Thorpe, N. J. Smith, E. M. Pierce, and A. Goel, "An insight into the corrosion of alkali aluminoborosilicate glasses in acidic environments," *Phys. Chem. Chem. Phys.*, vol. 22, no. 4, pp. 1881–1896, 2020, doi: 10.1039/c9cp06064b.

[248] C. Vakifahmetoglu and L. Karacasulu, "Cold sintering of ceramics and glasses: A review," *Curr. Opin. Solid State Mater. Sci.*, vol. 24, no. 1, 2020, doi: 10.1016/j.cossms.2020.100807.

[249] S. Funahashi *et al.*, "Cold sintering and co-firing of a multilayer device with thermoelectric materials," *J. Am. Ceram. Soc.*, vol. 100, no. 8, pp. 3488–3496, 2017, doi: 10.1111/jace.14852.

[250] Y. Jing *et al.*, "Remarkably improved electrical conductivity of ZnO ceramics by cold sintering and post-heat-treatment," *Ceram. Int.*, vol. 44, no. 16, pp. 20570–20574, 2018, doi: 10.1016/j.ceramint.2018.07.192.

[251] D. Pérez-Coll, E. Sánchez-López, and G. C. Mather, "Influence of porosity on the bulk and grain-boundary electrical properties of Gd-doped ceria," *Solid State Ionics*, vol. 181, no. 21–22, pp. 1033–1042, Jul. 2010, doi: 10.1016/j.ssi.2010.06.006.

[252] E. Van Besien *et al.*, "Influence of porosity on electrical properties of low-k dielectrics," *Microelectron. Eng.*, vol. 92, pp. 59–61, 2012, doi: 10.1016/j.mee.2011.04.015.

[253] J. T. S. Irvine, D. C. Sinclair, and A. R. West, "Electroceramics:

Characterization by Impedance Spectroscopy," *Adv. Mater.*, vol. 2, no. 3, pp. 132–138, 1990, doi: 10.1002/adma.19900020304.

[254] A. V. Ghule *et al.*, "In situ thermo-TOF-SIMS study of thermal decomposition of zinc acetate dihydrate," *J. Mass Spectrom.*, vol. 39, no. 10, pp. 1202–1208, 2004, doi: 10.1002/jms.721.

[255] T. Arii and A. Kishi, "The effect of humidity on thermal process of zinc acetate," *Thermochim. Acta*, vol. 400, no. 1–2, pp. 175–185, 2003, doi: 10.1016/S0040-6031(02)00487-2.

[256] R. Saravanan, E. Thirumal, V. K. Gupta, V. Narayanan, and A. Stephen, "The photocatalytic activity of ZnO prepared by simple thermal decomposition method at various temperatures," *J. Mol. Liq.*, vol. 177, pp. 394–401, 2013, doi: 10.1016/j.molliq.2012.10.018.

[257] Johnson Matthey, "Automotive Glass Enamels for Laminating applications Automotive Glass Enamels for External Press-bend Laminating applications."

[258] T. Glass, "Standard Test Method for Acid Resistance of Ceramic Decorations on Architectural-," vol. 91, no. November 1991, pp. 1–2, 2000.

[259] G. Products, "Standard Test Method for Acid Resistance of Ceramic Decorations on Glass on Architechtural-Type glass," *October*, vol. 04, no. Reapproved 2014, pp. 6–7, 2015, doi: 10.1520/C0777-04R14.2.

[260] K. M. Z. Hossain, U. Patel, and I. Ahmed, "Development of microspheres for biomedical applications: a review," *Prog. Biomater.*, vol. 4, no. 1, pp. 1–19, 2015, doi: 10.1007/s40204-014-0033-8.

[261] K. M. Z. Hossain *et al.*, "Porous calcium phosphate glass microspheres for orthobiologic applications," *Acta Biomater.*, vol. 72, pp. 396–406, 2018, doi: 10.1016/j.actbio.2018.03.040.

[262] D. Gupta, K. M. Z. Hossain, I. Ahmed, V. Sottile, and D. M. Grant, "Flame-Spheroidized Phosphate-Based Glass Particles with Improved Characteristics for Applications in Mesenchymal Stem Cell Culture Therapy and Tissue Engineering," *ACS Appl. Mater. Interfaces*, vol. 10, no. 31, pp. 25972–25982, 2018, doi: 10.1021/acsami.8b05267.

[263] A. Tilocca and A. N. Cormack, "Structural effects of phosphorus inclusion in bioactive silicate glasses," *J. Phys. Chem. B*, vol. 111, no. 51, pp. 14256–14264, 2007, doi: 10.1021/jp075677o.

[264] C. Y. Kim, A. E. Clark, and L. L. Hench, "Early stages of calcium-phosphate layer formation in bioglasses," *J. Non. Cryst. Solids*, vol. 113, no. 2–3, pp. 195–202, 1989, doi: 10.1016/0022-3093(89)90011-2.

[265] V. Cannillo and A. Sola, "Different approaches to produce coatings with bioactive glasses : Enamelling vs plasma spraying," *J. Eur. Ceram. Soc.*, vol.

30, no. 10, pp. 2031–2039, 2010, doi: 10.1016/j.jeurceramsoc.2010.04.021.

[266] A. Sola, D. Bellucci, V. Cannillo, and A. Cattini, "Bioactive glass coatings: a review," doi: 10.1179/1743294410Y.0000000008.

[267] O. P. Filho, G. P. Latorre, and L. L. Hench, "Effect of crystallization on apatite-layer formation of bioactive glass 45S5," *J. Biomed. Mater. Res.*, vol. 30, no. 4, pp. 509–514, 1996, doi: 10.1002/(SICI)1097-4636(199604)30:4<509::AID-JBM9>3.0.CO;2-T.

[268] J. Henao, C. Poblano-Salas, M. Monsalve, J. Corona-Castuera, and O. Barceinas-Sanchez, *Bio-active glass coatings manufactured by thermal spray: A status report*, vol. 8, no. 5. 2019, pp. 4965–4984.

[269] D. Bellucci, V. Cannillo, and A. Sola, "An overview of the effects of thermal processing on bioactive glasses," *Sci. Sinter.*, vol. 42, no. 3, pp. 307–320, 2010, doi: 10.2298/SOS1003307B.

[270] P. Li, Q. Yang, F. Zhang, and T. Kokubo, "The effect of residual glassy phase in a bioactive glass-ceramic on the formation of its surface apatite layer in vitro," *J. Mater. Sci. Mater. Med.*, vol. 3, no. 6, pp. 452–456, 1992, doi: 10.1007/BF00701242.

[271] P. Guanabara, "Bioactivity study of glass-ceramics with various crystalline fractions obtained by controlled crystallization," *Mater. Sci. Eng. C*, vol. 24, no. 5, pp. 689–691, 2004, doi: 10.1016/j.msec.2004.08.012.

[272] T. Tábi, I. E. Sajó, F. Szabó, A. S. Luyt, and J. G. Kovács, "Crystalline structure of annealed polylactic acid and its relation to processing," *Express Polym. Lett.*, vol. 4, no. 10, pp. 659–668, 2010, doi: 10.3144/expresspolymlett.2010.80.

[273] X. Wang, J. S. Nyman, X. Dong, H. Leng, and M. Reyes, *Fundamental Biomechanics in Bone Tissue Engineering*, vol. 2, no. 1. 2010.

[274] J. D. Currey, *Bones: Structure and mechanics*, vol. 9781400849. 2013.

[275] F. Baino, "Functionally Graded Bioactive Glass-Derived Scaffolds Mimicking Bone Tissue," in *Biomedical, Therapeutic and Clinical Applications of Bioactive Glasses*, Elsevier Ltd., 2019, pp. 443–466.

[276] R. Roop Kumar and M. Wang, "Functionally graded bioactive coatings of hydroxyapatite/titanium oxide composite system," *Mater. Lett.*, vol. 55, no. 3, pp. 133–137, 2002, doi: 10.1016/S0167-577X(01)00635-8.

[277] E. M. Inácio, M. C. Pinheiro Lima, D. H. Saboya Souza, L. Sirelli, and M. L. Dias, "Crystallization, thermal and mechanical behavior of oligosebacate plasticized poly(lactic acid) films," *Polimeros*, vol. 28, no. 5, pp. 381–388, 2018, doi: 10.1590/0104-1428.04917.

[278] O. Andrukhov *et al.*, "Proliferation, behavior, and differentiation of osteoblasts on surfaces of different microroughness," *Dent. Mater.*, vol. 32, no. 11, pp.

1374–1384, 2016, doi: 10.1016/j.dental.2016.08.217.

[279] A. Allion, J. P. Baron, and L. Boulange-Petermann, "Impact of surface energy and roughness on cell distribution and viability," *Biofouling*, vol. 22, no. 5, pp. 269–278, 2006, doi: 10.1080/08927010600902789.

[280] B. S. E. N. Iso, "Biological Evaluation of Medical Devices," *Biomed. Saf. Stand.*, vol. 26, no. 7, p. 54, 1996, doi: 10.1097/00149078-199604150-00011.

[281] N. Price, S. P. Bendall, C. Frondoza, R. H. Jinnah, and D. S. Hungerford, "Human osteoblast-like cells (MG63) proliferate on a bioactive glass surface," *J. Biomed. Mater. Res.*, vol. 37, no. 3, pp. 394–400, 1997, doi: 10.1002/(SICI)1097-4636(19971205)37:3<394::AID-JBM10>3.0.CO;2-C.

[282] I. Ahmed, P. S. Cronin, E. A. Neel, A. J. Parsons, J. C. Knowles, and C. D. Rudd, "Retention of mechanical properties and cytocompatibility of a phosphate-based glass fiber/polylactic acid composite," *J. Biomed. Mater. Res. - Part B Appl. Biomater.*, vol. 89, no. 1, pp. 18–27, 2009, doi: 10.1002/jbm.b.31182.

[283] B. Plešingerová and M. Kovalčíková, "Influence of the thermal expansion mismatch between body and glaze on the crack density of glazed ceramics," *Ceram. - Silikaty*, vol. 47, no. 3, pp. 100–107, 2003.

[284] M. Kavanová, A. Kloužková, and J. Kloužek, "Characterization of the interaction between glazes and ceramic bodies," *Ceram. - Silikaty*, vol. 61, no. 3, pp. 267–275, 2017, doi: 10.13168/cs.2017.0025.

[285] "Web of Science [v.5.35] - Citation Report." https://apps.webofknowledge.com/CitationReport.do?product=WOS&search_mode=CitationReport&SID=C64WcTzzMbK61y1g7vs&page=1&cr_pqid=12&viewType=summary&colName=WOS (accessed Mar. 23, 2021).

[286] J. A. Haynes, B. A. Pint, W. D. Porter, and I. G. Wright, "Comparison of thermal expansion and oxidation behavior of various high-temperature coating materials and superalloys," *Mater. High Temp.*, vol. 21, no. 2, pp. 87–94, 2004, doi: 10.1179/mht.2004.012.

[287] M. I. Ojovan and W. E. Lee, "Glassy wasteforms for nuclear waste immobilization," *Metall. Mater. Trans. A Phys. Metall. Mater. Sci.*, vol. 42, no. 4, pp. 837–851, 2011, doi: 10.1007/s11661-010-0525-7.

[288] J. S. McCloy and A. Goel, "Glass-ceramics for nuclear-waste immobilization," *MRS Bull.*, vol. 42, no. 3, pp. 233–238, 2017, doi: 10.1557/mrs.2017.8.

[289] S. Venkatesan, M. ul Hassan, and H. J. Ryu, "Adsorption and immobilization of radioactive ionic-corrosion-products using magnetic hydroxyapatite and cold-sintering for nuclear waste management applications," *J. Nucl. Mater.*, 2018, doi: 10.1016/J.JNUCMAT.2018.11.026.

[290] M. ul Hassan, S. Iqbal, J. Il Yun, and H. J. Ryu, "Immobilization of radioactive corrosion products by cold sintering of pure hydroxyapatite," *J. Hazard. Mater.*, vol. 374, no. April, pp. 228–237, 2019, doi: 10.1016/j.jhazmat.2019.04.038.

[291] M. ul Hassan and H. J. Ryu, "Cold sintering and durability of iodate-substituted calcium hydroxyapatite (IO-HAp) for the immobilization of radioiodine," *J. Nucl. Mater.*, 2018, doi: 10.1016/j.jnucmat.2018.11.024.

[292] M. Arbabzadeh, R. Sioshansi, J. X. Johnson, and G. A. Keoleian, "The role of energy storage in deep decarbonization of electricity production," *Nat. Commun.*, vol. 10, no. 1, 2019, doi: 10.1038/s41467-019-11161-5.

[293] D. Stampatori, P. P. Raimondi, and M. Noussan, "Li-ion batteries: A review of a key technology for transport decarbonization," *Energies*, vol. 13, no. 10, 2020, doi: 10.3390/en13102638.

[294] H. Leng, J. Huang, J. Nie, and J. Luo, "Cold sintering and ionic conductivities of Na3.256Mg0.128Zr1.872Si2PO12solid electrolytes," *J. Power Sources*, vol. 391, no. April, pp. 170–179, 2018, doi: 10.1016/j.jpowsour.2018.04.067.

[295] J. Seo, J. Guo, H. Guo, K. Verlinde, D. Sohrabi, and B. Heidary, "Cold sintering of a Li-ion cathode : LiFePO 4 -composite with high volumetric capacity," *Ceram. Int.*, no. March, 2017, doi: 10.1016/j.ceramint.2017.08.077.

[296] Y. Liu, Q. Sun, D. Wang, K. Adair, J. Liang, and X. Sun, "Development of the cold sintering process and its application in solid-state lithium batteries," *J. Power Sources*, vol. 393, no. March, pp. 193–203, 2018, doi: 10.1016/j.jpowsour.2018.05.015.

[297] W. Lee *et al.*, "Ceramic–Salt Composite Electrolytes from Cold Sintering," *Adv. Funct. Mater.*, vol. 29, no. 20, pp. 1–8, 2019, doi: 10.1002/adfm.201807872.

[298] A. Hayashi, K. Noi, N. Tanibata, M. Nagao, and M. Tatsumisago, "High sodium ion conductivity of glass-ceramic electrolytes with cubic Na3PS4," *J. Power Sources*, vol. 258, pp. 420–423, 2014, doi: 10.1016/j.jpowsour.2014.02.054.

[299] H. Tsukasaki, S. Mori, S. Shiotani, and H. Yamamura, "Ionic conductivity and crystallization process in the Li2S–P2S5 glass electrolyte," *Solid State Ionics*, vol. 317, no. November 2017, pp. 122–126, 2018, doi: 10.1016/j.ssi.2018.01.010.

[300] A. Yamauchi, A. Sakuda, A. Hayashi, and M. Tatsumisago, "Preparation and ionic conductivities of (100 - X)(0.75Li 2S·0.25P2S5)· xLiBH4 glass electrolytes," *J. Power Sources*, vol. 244, pp. 707–710, 2013, doi: 10.1016/j.jpowsour.2012.12.001.

[301] J. J. Blaker, S. N. Nazhat, V. Maquet, and A. R. Boccaccini, "Long-term in vitro degradation of PDLLA/Bioglass® bone scaffolds in acellular simulated body fluid," *Acta Biomater.*, vol. 7, no. 2, pp. 829–840, 2011, doi:

10.1016/j.actbio.2010.09.013.

[302] K. Eldesoqi *et al.*, "Safety evaluation of a bioglass-polylactic acid composite scaffold seeded with progenitor cells in a rat skull critical-size bone defect," *PLoS One*, vol. 9, no. 2, pp. 1–13, 2014, doi: 10.1371/journal.pone.0087642.

[303] D. Mohamad Yunos, O. Bretcanu, and A. R. Boccaccini, "Polymer-bioceramic composites for tissue engineering scaffolds," *J. Mater. Sci.*, vol. 43, no. 13, pp. 4433–4442, 2008, doi: 10.1007/s10853-008-2552-y.

[304] J. Kasperczyk *et al.*, "Bioactive glass/polymer composite materials with mechanical properties matching those of cortical bone Veronika," *J. Biomed. Mater. Res. Part A*, vol. 77A, no. 3, pp. 572–579, 2006, doi: 10.1002/jbm.a.

[305] A. R. Boccaccini, I. Notingher, V. Maquet, and R. Jérôme, "Bioresorbable and bioactive composite materials based on polylactide foams filled with and coated by Bioglass® particles for tissue engineering applications," *J. Mater. Sci. Mater. Med.*, vol. 14, no. 5, pp. 443–450, 2003, doi: 10.1023/A:1023266902662.

[306] S. Zhang, R. K. Arya, S. Pandey, Y. Vardaxoglou, W. Whittow, and R. Mittra, "3D-printed planar graded index lenses," *IET Microwaves, Antennas Propag.*, vol. 10, no. 13, pp. 1411–1419, 2016, doi: 10.1049/iet-map.2016.0013.

[307] S. Zhang, "Design and fabrication of 3D-printed planar Fresnel zone plate lens," *Electron. Lett.*, vol. 52, no. 10, pp. 833–835, 2016, doi: 10.1049/el.2016.0736.

[308] F. Bouville and A. R. Studart, "Geologically-inspired strong bulk ceramics made with water at room temperature," *Nat. Commun.*, vol. 8, 2017, doi: 10.1038/ncomms14655.

[309] M. Haug, F. Bouville, C. Ruiz-Agudo, J. Avaro, D. Gebauer, and A. R. Studart, "Cold densification and sintering of nanovaterite by pressing with water," *J. Eur. Ceram. Soc.*, vol. 40, no. 3, pp. 893–900, 2020, doi: 10.1016/j.jeurceramsoc.2019.10.034.